

AN ABSTRACT OF THE DISSERTATION OF

Steven G. Gaskill for the degree of Doctor of Philosophy in
Electrical and Computer Engineering presented on June 13, 2014.

Title: Equivalent Circuit Modeling of On-Chip Magnetic Devices
Based on Terminal Measurements

Abstract approved: _____

Andreas Weisshaar

The addition of thin-film alloy magnetic materials to integrated circuit processing enables a number of novel monolithic circuits. Examples include fully integrated magnetic field sensors, signal and power galvanic isolation circuits, and power supplies on chip (PwrSoC). There are several benefits to integrating these traditionally off-chip devices, including improved manufacturability, reduced cost, increased power density, better thermal management, and increase board space efficiency. Accurate circuit models are needed to enable successful circuit simulation of novel on-chip magnetic devices.

This thesis focuses on physically-motivated models extracted from terminal characteristics for three categories of devices benefiting from the inclusion of ferromagnetic alloy thin films: a microinductor, a microtransformer, and a microfluxgate. All models are well-behaved asymptotically, are guaranteed

passive, and have physical significance to elements and circuit quantities.

Measurements used to generate the models are wafer-level compatible and easily obtained with an impedance analyzer or vector network analyzer; no knowledge of the internal physics of the device (e.g. the magnetic material's magnetization behavior) is necessary. For each device an extraction algorithm is presented which obtains all model parameters within a few minutes on a 3.2 GHz Pentium[®] 4 workstation.

The resulting models not only match the measurements used to generate the model, but accurately reproduce specific determinative performance figures in their respective applications. Microinductors in buck converters accurately reproduce saturation dynamics with errors less than 2.5% and power efficiency within 0.2% when compared to field solvers. A fabricated microinductor matched the 10 MHz pulse response of the model to within 10%. A microtransformer used as a signal isolation transformer is shown to match the voltage gain to within an error $< 0.5\%$. Additionally, a microtransformer used in an isolated flyback converter captures the current with an error of 3.3% and power efficiency to within 5.6% error when compared to field solvers. The microfluxgate model exhibited accurate performance giving an error of 6.6% when compared to field solvers, and errors less than 7.5% when compared to measurements in the magnetic field sensitivity curve well beyond the linear range. Ultimately, this research enables accurate circuit simulations of novel on-chip magnetic devices potentially realizing first-pass design success.

©Copyright by Steven G. Gaskill
June 13, 2014
All Rights Reserved

Equivalent Circuit Modeling of On-Chip Magnetic Devices Based
on Terminal Measurements

by

Steven G. Gaskill

A DISSERTATION

submitted to

Oregon State University

in partial fulfillment of
the requirements for the
degree of

Doctor of Philosophy

Presented June 13, 2014
Commencement June 2015

Doctor of Philosophy dissertation of Steven G. Gaskill presented on
June 13, 2014.

APPROVED:

Major Professor, representing Electrical and Computer Engineering

Director of the School of Electrical Engineering and Computer Science

Dean of the Graduate School

I understand that my dissertation will become part of the permanent collection of Oregon State University libraries. My signature below authorizes release of my dissertation to any reader upon request.

Steven G. Gaskill, Author

ACKNOWLEDGEMENTS

My time as a graduate student at Oregon State University (OSU) will remain as a memorable part of my life. It has been a period of significant personal growth as well as intellectually and academically enriching. A large part of the thanks goes to my major adviser Professor Andreas Weisshaar. His insights into research directions, practical engineering related problems, and underlying theories have been invaluable. In addition, he has helped my growth by being a source of inspiration. I thank him for the wonderful opportunity to work under his guidance.

My committee members are well suited to the task of reviewing my work, each from their own area of interest. I would like to thank Dr. Albrecht Jander for his insights into magnetics and the many enjoyable classes I have taken from him. Thanks go to Dr. Ted Brekken, for serving on my committee as an expert in power and energy systems. I also enjoyed his class on electromechanical energy conversion. Prof. Gabor Temes also deserves my sincerest thanks for serving as an expert in network theory on my committee. His classes on analog to digital converters and network theory were among my favorite while at OSU. Finally, thanks to Dr. Karl Schilke for serving as the graduate council representative for both my preliminary and final oral exams.

Thanks go to Todd Shechter for promptly responding to IT related issues on

the many software tools and computers used in this thesis. I also appreciate the EECS office team, particularly Nicole Thompson, for their help with the administrative aspects of this work.

This thesis work has been supported by National Semiconductor (now Texas Instruments) and I would like to thank the team members there for all of their insightful reviews. Specifically thanks to Peter Hopper, Peter Smeys, Pascal Francis, and Will French for their support and technical guidance of this work. Additional thanks to Anuraag Mohan, Ann Gabrys, and Andrei Papou, for their review over the many of conference calls and aid in fabricated device measurements.

I want to thank the Center for Design of Analog-Digital Integrated Circuits (CDADIC) for their additional support of my graduate studies in general. Thanks to the Air Force Research Laboratory (AFRL) for a graduate fellowship during the 2008-2009 academic year.

I thank my colleagues Kavitha Rapolu and Erik Vernon for useful discussions and making a welcoming learning environment. Also thanks to my more recent colleagues Dyuti Sengupta, Lei Zheng, and Andy Ferrara for interesting discussions and questions. A special thanks to Vikas Shilimkar whose friendship, discussions and reviews were valuable assets to my time as a graduate student at OSU.

Finally, I thank my family and friends for their support and encouragement. Thanks to my friends David Crisman and Joe Selman for their friendship, humor, and time. Thanks to my parents, Gary and Teresa Gaskill for their financial

support and love during my time at OSU. Thanks to my siblings Sandra Wagner, Katee Horak, and Alex Gaskill for enjoyable downtime and interest in my life. An additional thanks goes to my nieces Reatta Wagner, and Reagan Wagner and nephew Isaac Horak for being sources of joy.

TABLE OF CONTENTS

	<u>Page</u>
1 Introduction	1
1.1 Background and Motivation	1
1.2 On-Chip Magnetic Devices	2
1.2.1 Microinductor	3
1.2.2 Microtransformer / Coupled Microinductor	7
1.2.3 Microfluxgate	9
1.3 The Need for Equivalent Circuit Models	11
1.4 Modeling Challenges	13
1.4.1 Physical Phenomena	14
1.4.2 On-Chip Integration	19
1.5 Research Contributions	20
1.6 Thesis Outline	22
2 General Modeling Considerations	24
2.1 What Type of Model is Desired?	25
2.1.1 Behavioral versus Physics-Based Model Comparison	28
2.1.2 Model Requirements	31
2.2 Circuit Building Blocks for Capturing Physical Effects	32
2.2.1 Saturation	32
2.2.2 Hysteresis	35
2.2.3 Ferromagnetic Relaxation/Resonance	39
2.2.4 Eddy Currents	40
2.2.5 Electric Field Effects	43
2.2.6 Physical Effects Summary	44
2.3 Conclusion	45
3 Microinductor Model	47
3.1 Introduction	47
3.2 Literature Review	48
3.2.1 Simple Linear Two-Element Model	48
3.2.2 Nonlinear Two-Element Model	49
3.2.3 First Order Eddy Current Model	49
3.2.4 Linear Frequency-Dependent Model	51
3.2.5 Higher Order Nonlinear Eddy Current Model	52

TABLE OF CONTENTS (Continued)

		Page
	3.2.6 Summary Table	53
3.3	Model Development	54
	3.3.1 Model Circuit Topology	54
	3.3.2 Nonlinear Inductors	56
	3.3.3 Measurements Employed to Generate Model	61
	3.3.4 Measurements Employed to Validate Model	64
	3.3.5 Novelty of This Model	65
3.4	Model Extraction Algorithm	67
	3.4.1 Overview	67
	3.4.2 Stage 1: Three-Bias Fitting	67
	3.4.3 Stage 2: Fit to Remaining Biases	70
	3.4.4 Stage 3: Fit Nonlinear Inductors	70
3.5	Validation	71
	3.5.1 Device 1 Simulation	73
	3.5.2 Device 2 Simulation	80
	3.5.3 Device 3 Measurements	88
	3.5.4 Discussion of Model Order	89
3.6	Future Work and Conclusions	94
	3.6.1 Adding Hysteresis	96
	3.6.2 Adding Ferromagnetic Resonance	97
	3.6.3 Conclusions	99
4	Microtransformer Model	101
	4.1 Introduction	101
	4.2 Literature Review	102
	4.2.1 Linear Models not Capturing Core Eddy Currents	102
	4.2.2 Nonlinear Models not Capturing Core Eddy Currents	104
	4.2.3 First Order Core Eddy Current Models	104
	4.2.4 Higher Order Core Eddy Current Models	106
	4.2.5 Summary Table	107
	4.3 Model Development	107
	4.3.1 Model Circuit Topology	107
	4.3.2 Nonlinear Reluctances	109
	4.3.3 Measurements Employed to Generate Model	112
	4.3.4 Measurements Employed to Validate Model	114

TABLE OF CONTENTS (Continued)

	<u>Page</u>
4.3.5 Novelty of This Model	115
4.4 Model Extraction Algorithm	116
4.4.1 Algorithm Overview	116
4.4.2 Stage 1: Zero-Bias Fitting	117
4.4.3 Stage 2: Three-Bias Fitting	118
4.4.4 Stage 3: Fit to Remaining Biases	120
4.4.5 Stage 4: Fit Nonlinear Reluctances	121
4.5 Validation	121
4.5.1 Device 1 Simulation	123
4.5.2 Device 2 Simulation	131
4.5.3 Device 3 Measurements	143
4.6 Conclusions and Future Work	144
4.6.1 Conclusions	144
4.6.2 Future Work	150
5 Microfluxgate Model	152
5.1 Introduction	152
5.2 Literature Review	154
5.2.1 Theoretical Models	154
5.2.2 Existing Circuit Models	155
5.3 Model Development	156
5.3.1 Model Circuit Topology	156
5.3.2 Nonlinear Reluctances	157
5.3.3 Measurements Employed to Generate Model	158
5.3.4 Measurements Employed to Validate Model	159
5.3.5 Novelty of This Model	160
5.4 Model Extraction Algorithm	161
5.4.1 Algorithm Overview	161
5.4.2 Stage 1: Electric Domain Extraction	162
5.4.3 Stage 2: Even Mode Magnetic Domain Extraction	163
5.4.4 Stage 3: Odd Mode Magnetic Domain Extraction	164
5.5 Validation	165
5.5.1 Device 1 Simulation	166
5.5.2 Device 2 Measurements	168
5.6 Conclusions and Future Work	175

TABLE OF CONTENTS (Continued)

	<u>Page</u>
5.6.1 Conclusions	175
5.6.2 Adding Hysteresis	175
5.6.3 Improving the Model	176
6 Summary and Future Direction	177
6.1 Summary	177
6.2 Future Direction	178
Bibliography	181
Appendices	198

LIST OF FIGURES

Figure	Page
1.1 Top down view (a), perspective view (b), and layer stackup (c) of a toroidal microinductor.	5
1.2 Top down view (a), perspective view (b), and layer stackup (c) of a solenoidal microinductor.	5
1.3 Top down view (a), perspective view (b), and layer stackup (c) of a racetrack microinductor.	6
1.4 Top down view (a), perspective view (b), and layer stackup (c) of a stripline microinductor.	6
1.5 Top down view (a), perspective view (b), and layer stackup (c) of an E-core microtransformer.	8
1.6 Top down view (a), perspective view (b), and layer stackup (c) of a dual-core microfluxgate.	10
1.7 Flow diagram of design process for ICs using micro-magnetic devices.	13
2.1 Diagram of magnetic domains in a bar magnet, when there is no magnetic field applied (a), and under the presence of an external magnetic field (b). The resultant magnetic flux density B versus magnetic field H is shown in (c).	34
2.2 LTSpice subcircuit from [87] for modeling $B(H_a)$ for Jiles-Atherton hysteresis (a), and the equations for the behavioral source (b) with a hyperbolic tangent function for anhysteretic behavior. Corresponding initial and outer magnetization behavior is shown in (c).	38
2.3 Coaxial microinductor showing partitioning of core and relevant variables (a) to approximate eddy currents as a finite order network in the magnetic domain (b). It is converted using Slemon's dual [94] to the electric domain (c)	41
2.4 Section of high order physical RC network showing connection to solenoidal microinductor geometry	44
3.1 Simple linear two-element model of a microinductor.	48
3.2 Microinductor model capturing eddy currents in the core making a low-frequency approximation	50

LIST OF FIGURES (Continued)

Figure	Page
3.3 Example of a linear frequency-dependent microinductor model. . . .	51
3.4 Example of a higher-order nonlinear eddy current model topology. .	52
3.5 Complete compact equivalent circuit model used for microinductors, with an Mth order linear ladder network, an Nth order saturating core ladder network, and parallel RC branch.	55
3.6 Plot of (3.5) versus current showing effects of α_{in} parameters. . . .	58
3.7 Example LTspice subcircuit of a nonlinear inductor described by (3.6). Inductor terminals are V_{ip} and V_{in}	59
3.8 Small-signal inductance of a tanh-based microinductor using (3.7a) with 4 different gap inductances (data points) showing the fitting performance of (3.6) (solid lines).	62
3.9 Small-signal inductance and resistance versus bias current and frequency.	64
3.10 Simplified buck converter circuit used to validate the generated models. The signal Φ controlling the switches is a pulsed rectangular wave of given duty cycle.	65
3.11 Flow chart of algorithm going from input measurements to output model with three intermediate stages.	68
3.12 COMSOL Multiphysics layout in 2-D of racetrack microinductor from [21]. The seven conductors are connected in series.	72
3.13 Small-signal inductance for L_{c1} through L_{c4} for the device 1 race-track microinductor. The data points are the optimal inductances from stages 1 and 2 of the algorithm, and the curve is (3.6) fit to these points.	75
3.14 Small-signal inductance and resistance versus frequency and bias current showing comparison between fitted Spectre models and COMSOL “measurements” for device 1.	76
3.15 The top graph shows the rise of the output voltage to steady state, the bottom graph shows the current through the microinductor in a test buck converter. Five different models are compared for device 1.	77

LIST OF FIGURES (Continued)

Figure	Page
3.16 Instantaneous power loss for different microinductor models of device 1 in a test buck converter circuit during the time 600 ns to 800 ns to approximate steady-state operation.	79
3.17 Ansys Maxwell layout in 3-D of reduced-length V-groove microinductor motivated from [97] and 2-D cross-section showing dimensions.	81
3.18 Small-signal inductance for L_{c1} through L_{c4} for the device 2 V-groove microinductor. The data points are the optimal inductances from stages 1 and 2 of the algorithm, and the curve is (3.6) fit to these points.	82
3.19 Small-signal inductance and resistance versus frequency and bias current showing comparison between fitted Spectre models and Maxwell “measurements” for device 2.	83
3.20 The top graph shows the rise of the output voltage to steady state, the bottom graph shows the current through the microinductor in a test buck converter circuit. Five different models are compared for device 2.	85
3.21 Instantaneous power loss for different microinductor models of device 2 in a test buck converter circuit during the time 594 ns to 634 ns to approximate steady-state operation.	87
3.22 Small-signal inductance for L_{c1} through L_{c4} for the device 3 measured microinductor. The data points are the optimal inductances from stages 1 and 2 of the algorithm, and the curve is (3.6) fit to these points.	90
3.23 Small-signal inductance and resistance versus frequency and bias current showing comparison between fitted Spectre model and actual measurements for device 3.	91
3.24 Top graph shows the voltage waveform applied to both models and actual device. Bottom graph compares the resulting current waveform for actual device, Fig. 3.5 model, and simple linear model. . .	92

LIST OF FIGURES (Continued)

Figure	Page
3.25 A nonlinear inductor circuit model when hysteresis is present employing subcircuit from [87]. This model is meant to serve as a replacement for the circuit of Fig. 3.7, with inductor terminals at V_{ip} and V_{in}	97
3.26 A nonlinear inductor circuit model when hysteresis and domain wall dynamics are present [87]. This is a replacement for the circuit of Fig. 3.7, with inductor terminals at V_{ip} and V_{in}	98
4.1 Example of simple linear microtransformer model without any core eddy current losses.	103
4.2 Example of nonlinear microtransformer model with core resistance modeling 1st order core eddy current losses.	105
4.3 Example of linear microtransformer model with $N+1$ th order core eddy current modeling, capturing the skin-effect in the core.	106
4.4 Compact equivalent circuit model used for microtransformers, with an M th order linear conductor ladder network and an N th order saturating core ladder network in the magnetic domain.	108
4.5 Possible LTspice subcircuit of a second order nonlinear reluctance described by (4.1). Magnetic domain terminals are V_{mp} and V_{mn}	112
4.6 The three distinct measurement setups proposed for determining the small-signal behavior of a two port microtransformer.	114
4.7 Flow chart of microtransformer extraction algorithm going from input measurements to output model with four intermediate stages.	117
4.8 Circuit diagram of the 5-element nonlinear model used in validation comparisons.	123
4.9 Circuit diagram of the linear 8th order ($N = 4, M = 2$) dynamic model used in validation comparisons.	124
4.10 Ansys Maxwell layout in 3-D of reduced-length device 1 microtransformer and 2-D cross-section showing dimensions.	125

LIST OF FIGURES (Continued)

Figure	Page
4.11 Port 1 reflected inductance for \mathcal{R}_{c1} through \mathcal{R}_{c4} for the device 1 isolation transformer. The data points are the optimal reflected inductances from stages 1 through 3 of the algorithm, and the curve is the fit to these points.	126
4.12 Small-signal impedance versus frequency and bias current for port 1 with port 2 open showing comparison between fitted Spectre model and Maxwell “measurements” for device 1.	127
4.13 Small-signal impedance versus frequency and bias current for port 2 with port 1 open showing comparison between fitted Spectre model and Maxwell “measurements” for device 1.	128
4.14 Small-signal impedance versus frequency and bias current for port 1 with port 2 shorted showing comparison between fitted Spectre model and Maxwell “measurements” for device 1.	129
4.15 The small-signal voltage gain between port 1 and port 2 of an isolation transformer versus frequency when a 50 Ω load is placed across port 2. Solid line is Spectre model, and data points are field solver simulations.	130
4.16 Large-signal input current and output voltage waveforms for the device 1 isolation transformer with 1.6 Ω load at 7 MHz with a 4 V sinusoidal input. “Linear 8th-Order Model” is simplified circuit of Fig. 4.9 and “Nonlinear 5-Element Model” is simplified circuit of Fig. 4.8.	132
4.17 Ansys Maxwell layout in 3-D of reduced-length device 2 microtransformer and 2-D cross-section showing dimensions.	133
4.18 Port 1 reflected inductance for \mathcal{R}_{c1} through \mathcal{R}_{c4} for the device 2 flyback microtransformer. The data points are the optimal reflected inductances from stages 1 through 3 of the algorithm, and the curve is the fit to these points.	134
4.19 Small-signal impedance versus frequency and bias current for port 1 with port 2 open showing comparison between fitted Spectre model and Maxwell “measurements” for device 2.	136

LIST OF FIGURES (Continued)

Figure	Page
4.20 Small-signal impedance versus frequency and bias current for port 2 with port 1 open showing comparison between fitted Spectre model and Maxwell “measurements” for device 2.	137
4.21 Small-signal impedance versus frequency and bias current for port 1 with port 2 shorted showing comparison between fitted Spectre model and Maxwell “measurements” for device 2.	138
4.22 Isolated flyback converter circuit used to validate device 2. The two switches are controlled by 50% duty cycle complementary clocks and R_{load} represents the output load.	140
4.23 Comparison of the instantaneous power loss waveform used to calculate the device 2 microtransformer efficiency in a flyback converter application. The “Linear 8th-Order Model” is simplified circuit of Fig. 4.9 and “Nonlinear 5-Element Model” is simplified circuit of Fig. 4.8.	141
4.24 Comparison of the device 2 microtransformer’s input current (top) and output current (bottom) when models are placed in a flyback converter with a $20\ \Omega$ load. The “Linear 8th-Order Model” is simplified circuit of Fig. 4.9 and “Nonlinear 5-Element Model” is simplified circuit of Fig. 4.8.	142
4.25 Port 1 reflected inductance for \mathcal{R}_{c1} through \mathcal{R}_{c4} for the device 3 microtransformer. The data points are the optimal reflected inductances from stages 1 through 3 of the algorithm, and the curve is the fit to these points.	145
4.26 Small-signal impedance versus frequency and bias current for port 1 with port 2 open showing comparison between fitted Spectre model and fabricated device measurements for device 3.	146
4.27 Small-signal impedance versus frequency and bias current for port 2 with port 1 open showing comparison between fitted Spectre model and fabricated device measurements for device 3.	147
4.28 Small-signal impedance versus frequency and bias current for port 1 with port 2 shorted showing comparison between fitted Spectre model and fabricated device measurements for device 3.	148

LIST OF FIGURES (Continued)

Figure	Page
5.1 Simplified schematic of dual-core solenoidal microfluxgate (a) and equivalent magnetic circuit based on flux paths, Φ_A and Φ_{link} (b).	153
5.2 Compact equivalent circuit model of a dual-core microfluxgate. The circuit is broken up into the electric and magnetic domains.	157
5.3 Possible LTspice subcircuit of a second order nonlinear reluctance described by (4.1). Magnetic domain terminals are Vmp and Vmn.	158
5.4 Application circuit for validating the dual-core solenoidal microfluxgate models in the time-domain using Spectre. The external voltage H_{ext} is the means by which the external field is applied to the model through a voltage-controlled voltage source with gain ℓ_c to the magnetic domain (see Fig. 5.2).	160
5.5 Flow chart of model extraction algorithm going from input measurements to output microfluxgate model with three intermediate stages.	162
5.6 Top-down view of Maxwell design of device 1 dual-core solenoidal microfluxgate and 2-D cross-section with labeled dimensions.	166
5.7 Drive coil inductance versus bias current comparing this work's model with Maxwell results (top) and likewise for sense coil (bottom).	167
5.8 Time domain voltage across drive coil (top) and sense coil (bottom) for device 1 with a 40 mA, 1 MHz current drive coil excitation in a 100 μ T external magnetic field.	169
5.9 Time domain voltage across drive coil (top) and sense coil (bottom) for device 1 with a 40 mA, 1 MHz current drive coil excitation in a 500 μ T external magnetic field.	169
5.10 Integrated absolute sense voltage versus external magnetic field for both Maxwell simulation and the model of this thesis for device 1.	170
5.11 Micrograph of device 2, fabricated dual-core solenoidal microfluxgate.	171
5.12 Drive coil (top) and sense coil (bottom) inductance versus bias current plot, comparing this work's model with measurement results for device 2.	172

LIST OF FIGURES (Continued)

<u>Figure</u>		<u>Page</u>
5.13	Time domain voltage across drive coil (top) and sense coil (bottom) for device 2 with a 80 mA, 1 MHz current drive coil excitation in a 100 μ T external magnetic field.	173
5.14	Time domain voltage across drive coil (top) and sense coil (bottom) for device 2 with a 80 mA, 1 MHz current drive coil excitation in a 500 μ T external magnetic field.	173
5.15	Integrated absolute sense voltage versus external magnetic field for both measurements and this work for device 2, showing good match for two fields.	174

LIST OF TABLES

Table	Page
2.1 Different functions to model anhysteretic $M(H)$ behavior of a saturating magnetic material, where α and β are constant fitting parameters.	33
3.1 Feature comparisons for microinductor models from literature. . . .	54
3.2 Coefficients of $M(H)$ functions (3.7a),(3.7b), and (3.7c).	60
3.3 Comparison of our model with traditional off-chip inductor models and an Intel topology model. The COMSOL simulation is used as a reference to calculate errors for device 1.	80
3.4 Comparison of our model with traditional off-chip inductor models and an Intel topology model. The COMSOL simulation is used as a reference to calculate errors for device 2.	86
3.5 Improvements in transient and small-signal errors as for different model orders for device 1. Results shown are an average of 25 algorithm runs.	94
3.6 Improvements in transient and small-signal errors as for different model orders for device 2. Results shown are an average of 25 algorithm runs.	95
3.7 Improvements in transient and small-signal errors as for different model orders for device 3. Results shown are an average of 25 algorithm runs.	95
4.1 Feature comparisons for microtransformer models from literature. .	107
4.2 Comparison of simplified microtransformer models and our model using the Maxwell simulation as a reference to calculate errors for device 1.	131
4.3 Comparison of simplified microtransformer models and our model using the Maxwell simulation as a reference to calculate errors for device 2.	140

LIST OF APPENDICES

	<u>Page</u>
A Behavioral and Physics-Based Model Examples	199
A.1 Simple Physical Structure	199
A.2 First Order Physics-Based Model	201
A.3 First Order Behavioral Model	206
B Magnetic Domain and Inductance	212
B.1 Magnetic Circuits	212
B.2 Nonlinear Inductance Definitions	219
C Passivity	222
C.1 Electric Domain	222
C.2 Magnetic Domain	223
D Sample Device Models	226
D.1 Microinductor Device Models	226
D.2 Microtransformer Device Models	229
D.3 Microfluxgate Device Models	232

LIST OF APPENDIX FIGURES

Figure	Page
A.1 Dimensional and material information for simple coaxial inductor shorted at the far end.	200
A.2 First order physics-based model of coaxial nonlinear microinductor of Fig. A.1.	205
A.3 State-function for field-solver measurements ($f(\cdot)$) (a), the polynomial fit to the state-function (f_{poly}) (b), and the difference between the two on an extended domain (c).	209
A.4 State function for field-solver measurements ($f(\cdot)$) (a), the artificial neural network fit to the state function (b), and the difference between the two on an extended domain (c).	210
A.5 State function for field-solver measurements ($f(\cdot)$) (a), the physics-based state function (b), and the difference between the two on an extended domain (c).	210
B.1 Simple diagram of a section of a microinductor (a), and its corresponding magnetic circuit (b)	214
B.2 Example of a magnetic circuit (a) being converted to an electric circuit (b).	216
B.3 Magnetoelectric differential gyrator symbol adopted from [89] (a) and an example subcircuit implementation (b).	217
B.4 Two magnetically coupled toroidal conductors with labeled fluxes. .	221

LIST OF APPENDIX TABLES

<u>Table</u>	<u>Page</u>
A.1 Element values of circuit given in Fig. A.2 for first order physics-based model.	205
B.1 Conversion of equations and elements between domains.	218
D.1 Extracted circuit element values and nonlinear inductance parameters for microinductor device 1.	226
D.2 Extracted circuit element values and nonlinear inductance parameters for microinductor device 2.	227
D.3 Extracted circuit element values and nonlinear inductance parameters for microinductor device 3.	228
D.4 Extracted circuit element values and nonlinear reluctance parameters for microtransformer device 1.	229
D.5 Extracted circuit element values and nonlinear reluctance parameters for microtransformer device 2.	230
D.6 Extracted circuit element values and nonlinear reluctance parameters for microtransformer device 3.	231
D.7 Extracted circuit element values and nonlinear reluctance parameters for microfluxgate device 1.	232
D.8 Extracted circuit element values and nonlinear reluctance parameters for microfluxgate device 2.	233

To my family

Chapter 1 – Introduction

1.1 Background and Motivation

The integrated circuit (IC) arguably made possible our modern information age. Today, ICs are found in virtually every modern electronic device such as smart phones, MP3 players, automobiles, and even greeting cards. The IC or “circuit in silicon” was invented by Jack Kilby in 1958 as a solution to a problem with the ever increasing complexity of electronic circuits. The problem was called “the tyranny of numbers” [1]. The likelihood of an assembly worker’s error, and thus the probability the circuit would not work, was dependent on the number of connections and for complex electrical circuits this was a problem. Mr. Kilby’s solution was to build even the interconnects, resistors and capacitors out of silicon. Using similar silicon processing steps Mr. Kilby built the first integrated multivibrator circuit [2]. Today, the interconnects and passive devices are constructed out of other materials during the second stage of IC fabrication known as the back end of line (BEOL), but the processing steps are in many ways similar to those of the front end of line (FEOL) and certainly compatible with it.

With the stage set for reliable circuits, IC complexity grew exponentially. In 1965, Gordon Moore noticed that the complexity for minimum component costs¹

¹For an economical design this complexity can be thought of as the number of transistors, which relates to the minimum feature size, or process node dimension.

in integrated circuits was doubling every year [3]. Although the pace has been closer to a doubling every two years, this exponential growth became known as Moore's law and continues to stimulate the electronics industry to this day. For example, Intel announced a 22 nm microprocessor in May of 2011 [4]. The benefit of Moore's law has been improved performance per cost, but this trend cannot continue forever. In fact, to extend the march of IC technology the International Technology Roadmap for Semiconductors (ITRS) has emphasized a "More-than-Moore" trend to supplement Moore's law [5]. The "More-than-Moore" trend includes adding sensors, actuators, and power/peripheral subsystems onto the IC. This means incorporating more than the traditional passives and interconnects on chip, including: devices with new materials, high-voltage components, micro-mechanical devices, or even microfluidic devices. This thesis covers the equivalent circuit modeling of devices using an innovative BEOL "More-than-Moore" process, namely the addition of magnetic materials to integrated circuits.

1.2 On-Chip Magnetic Devices

The addition of magnetic materials to integrated circuits enables many innovative monolithic devices. Although this thesis only focuses on three such device categories, this is by no means an exhaustive list, and to a large extent this work is meant to be a more general aid to equivalent-circuit modeling of on-chip magnetic devices. Relative to air-core on-chip inductive passives, monolithic devices with magnetic materials have increased inductance for a given resistance (higher quality

factors), reduced electromagnetic interference (EMI), and reduced parasitic coupling.² Relative to off-chip inductive passives, monolithic magnetic devices take up less board area, increase power density, cost less, improve reliability, have better thermal management, and offer simplified designs for IC customers [6–8].

1.2.1 Microinductor

The inductor is the most basic magnetic device category considered in this thesis. Its purpose is to store magnetic energy to be released at a later time under a different voltage. Many applications, may benefit from the addition of on-chip inductors with magnetic materials, which are referred to in this thesis as microinductors. Microinductors have been proposed to enable wireless and radio frequency circuits [9–12], as electromagnetic interference (EMI) noise filters [9, 10], to enable Power Supplies on Chip (PwrSoC) [9, 11, 13–16], and even as electromagnets in Microelectromechanical Systems (MEMS) [14, 17]. The idea of a PwrSoC is to monolithically integrate the power transistors, the output inductor and capacitor, and of course the control electronics of a modern switch-mode power supply on a single silicon die. Due to the prominence of PwrSoC-enabling microinductors in literature, and the materials and designs relevant to this thesis, we will focus on power microinductors, which typically are operated from tens of MHz to hundreds of MHz.

A primary question of microinductor design is the arrangement of the windings

²Both reduction in EMI and parasitic coupling are due to the property of the high-permeability magnetic material to contain the magnetic flux.

and the core. Some processes have two conductor layers sandwiching the magnetic material. This allows for the windings to surround the core, as in a toroidal or solenoidal microinductor. A typical toroidal microinductor is pictured in Fig. 1.1 and has many examples in literature, e.g. [11, 14, 18]. Toroidal microinductors add complexity to the processing through the need for vias between conductor layers, but allow large inductance for switching frequencies below 10 MHz [16]. A typical solenoidal microinductor is shown in Fig. 1.2 and is also found in the literature [11, 19]. Solenoidal microinductors can take advantage of anisotropic magnetic materials and are therefore useful at higher frequencies than toroidal microinductors [16].

Rather than having the windings surround the core, the core could surround the windings. The most popular of these types of arrangements are the spiral and racetrack microinductors. An example racetrack microinductor is shown in Fig. 1.3. Since the magnetic material surrounds the straight sections it can take advantage of anisotropic magnetic materials [16]. The magnetic core may be closed with magnetic vias or conformal deposition, as in [9, 10, 20–23], or it may have a gap and sandwich (rather than surround) the spiral, as in [13, 24]. Either way, spiral and racetrack microinductors are some of the most popular and can operate in PwrSoCs at 100 MHz [25].

Another microinductor arrangement with the core surrounding the conductor, is the stripline microinductor. The stripline microinductor has a single conductor with a magnetic core wrapping around it. An example stripline microinductor is shown in Fig. 1.4. They are more popular in commercial products than in the

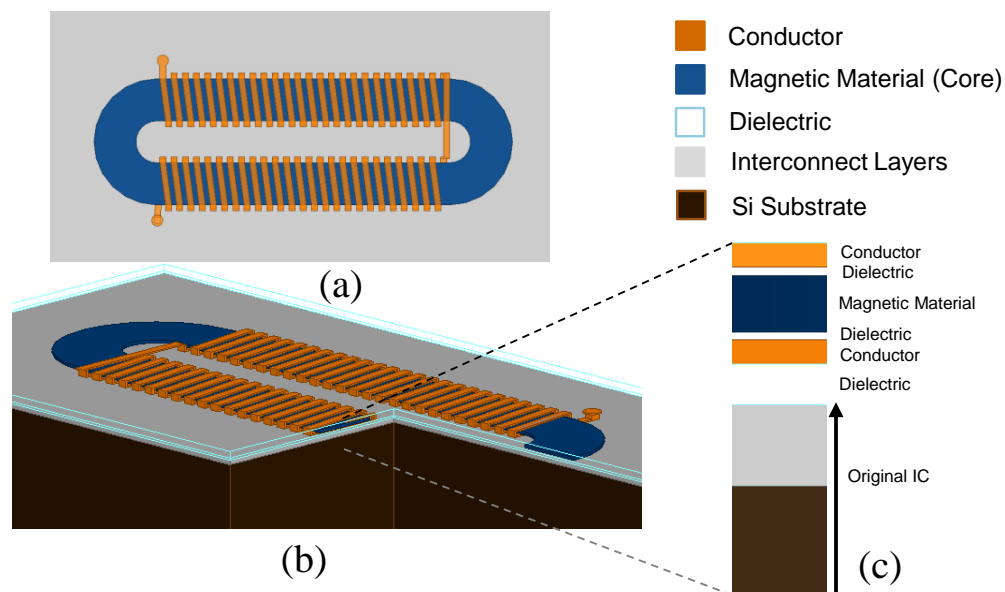


Figure 1.1: Top down view (a), perspective view (b), and layer stackup (c) of a toroidal microinductor.

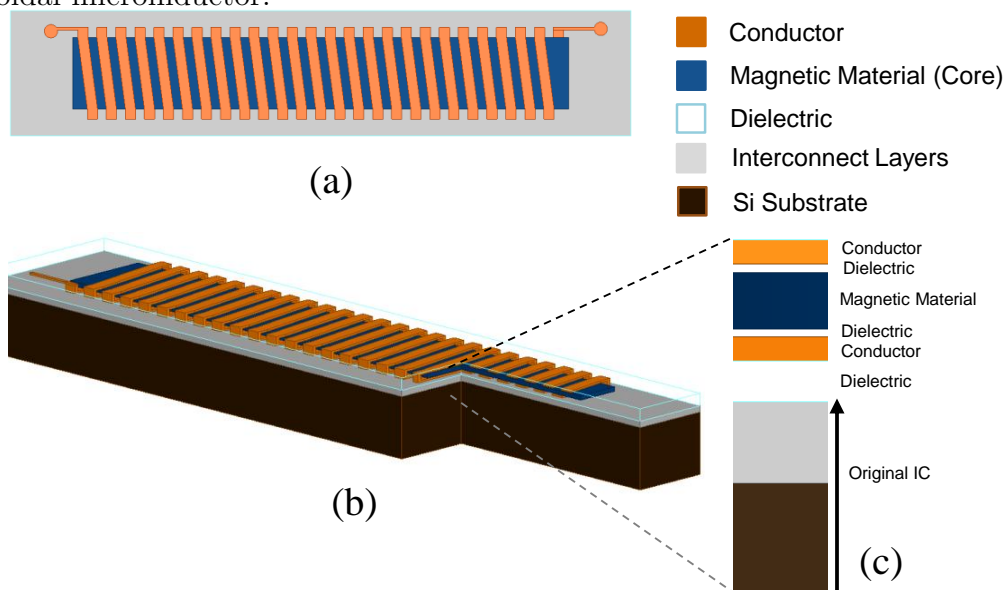


Figure 1.2: Top down view (a), perspective view (b), and layer stackup (c) of a solenoidal microinductor.

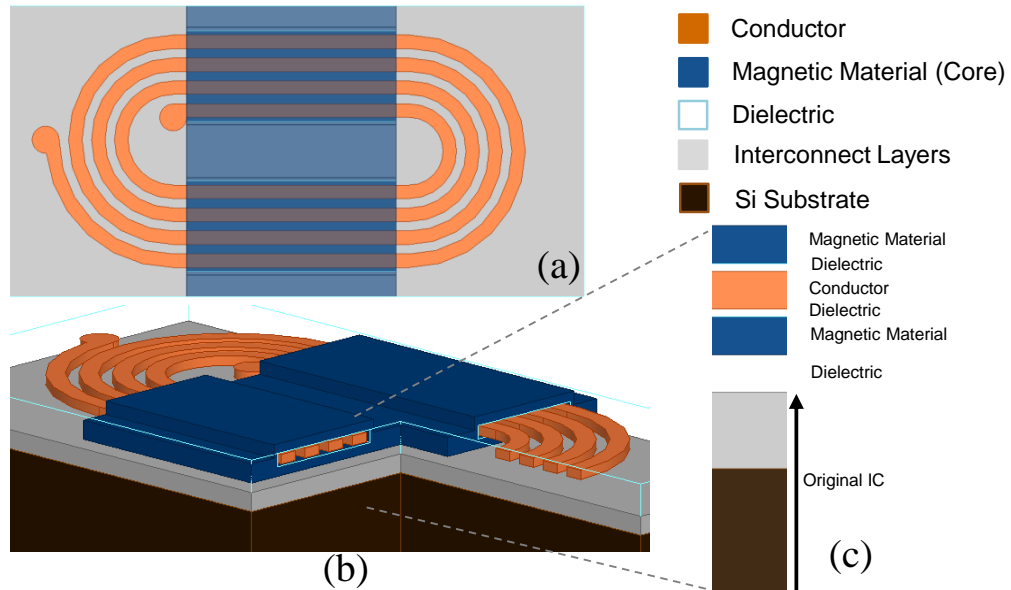


Figure 1.3: Top down view (a), perspective view (b), and layer stackup (c) of a racetrack microinductor.

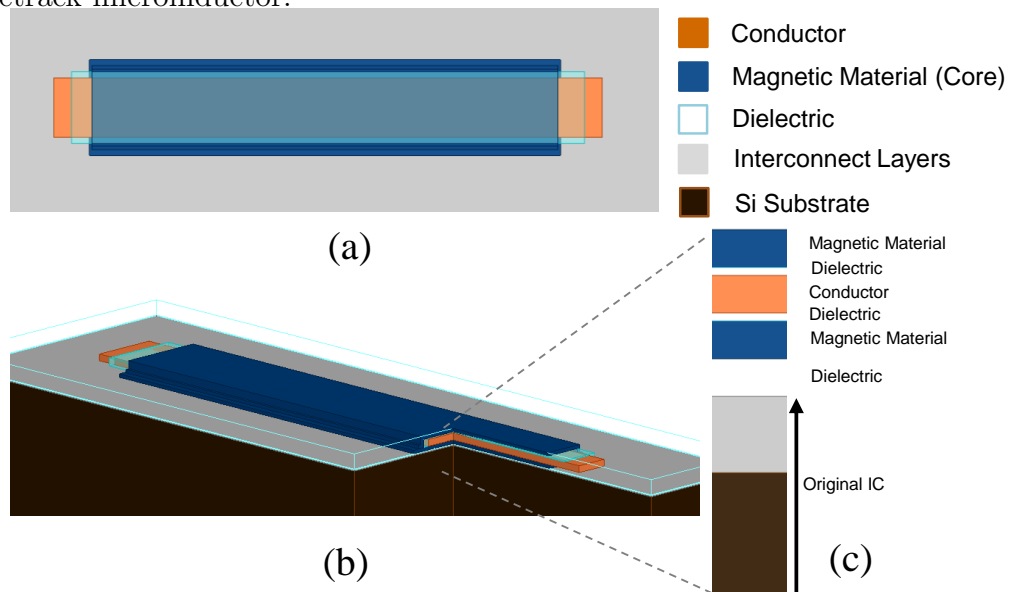


Figure 1.4: Top down view (a), perspective view (b), and layer stackup (c) of a stripline microinductor.

research literature [16]. The V-groove design [15] is an exception to this trend and features a very low resistance per length. The downside of the stripline configuration is a low inductance enhancement in the absence multiple winding turns.

1.2.2 Microtransformer / Coupled Microinductor

Transformers are galvanically isolated inductors that are magnetically coupled. They may be used to transform power or signals from one voltage to another, or store energy similar to inductors. Again, there are several applications that are capable of benefiting from on-chip transformers with magnetic materials, referred to as microtransformers. Similar to microinductors, the dominant application is the enabling of PwrSoCs [26–28]. These may be isolated DC-DC converters as in the forward converter [29] or the related flyback converter, or non-isolated DC-DC converters as in multi-output converters [30] or coupled buck converters [31]. Microtransformers, may also simply be used as a direct way to convert or isolate power and signals [32, 33]. In Chapter 4 we will consider a microtransformer designed for an isolation transformer and one designed an isolated flyback converter.

Layout/geometry considerations of planar microtransformers are very similar to those of planar microinductors. Indeed, a general method to form a microtransformer from a microinductor is to interleave N_1 primary windings with N_2 secondary windings. For example, the racetrack microinductor of Fig. 1.3 is transformed into a 2:2 E-core/racetrack microtransformer in Fig. 1.5. The racetrack microtransformer, is often referred to as an E-core microtransformer due to his-

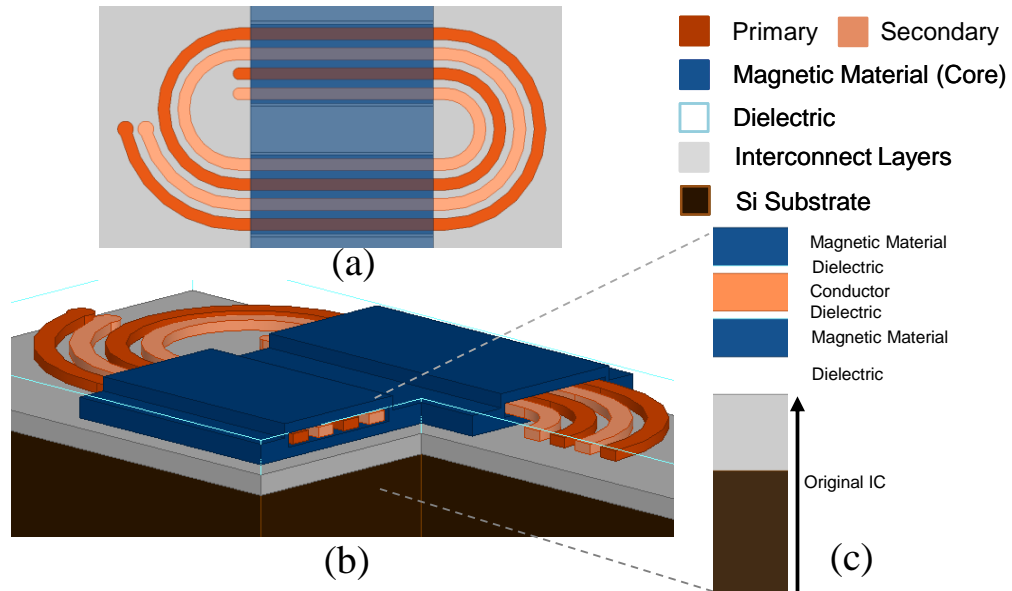


Figure 1.5: Top down view (a), perspective view (b), and layer stackup (c) of an E-core microtransformer.

torical off-chip reasons [26, 33]. While the E-core configuration allows for making use of anisotropic magnetic materials, the sandwiched spiral [30] does not. There are also solenoidal [28, 29] and toroidal [27, 32] interleaved microtransformers. By coupling two traces at a time, a complex stripline-like microtransformer can be built up as in [31]. Stacked microtransformers, e.g. [34], are not common due to the added processing steps to create two thick metal layers between the magnetic material.

1.2.3 Microfluxgate

A fluxgate sensor is a category of magnetic devices that measures a magnetic field along a highly permeable core's axis by means of the magnetic field's impact on the saturation characteristics. Fluxgates are one of the most sensitive magnetic sensors at room temperature, being able to measure down to 0.1 nT as demonstrated in recent work [35]. Apart from being a smaller/more compact solution, on-chip fluxgate sensors (microfluxgates) use less power, are more robust, and are less expensive than their off-chip counterparts. Microfluxgates find applications as eCompasses, current inspectors, and magnetometers, giving applications in physical sciences, modern aviation and space exploration [35].

One of the most compact microfluxgate layouts is the single-core design [35–38]. In this design the drive coil is excited with a periodic current transitioning the core in and out of saturation. In the absence of a magnetic field the sense coil picks up a distorted fundamental voltage with only odd harmonics. An externally applied magnetic field will effectively shift the core's saturation characteristics and generate even harmonics. Electronics then pick-up the magnitude of one of these even harmonics, which is proportional to the external field over a specified domain.

To simplify the electronics a dual-core design can be employed. This is also a popular design in microfluxgate literature [39–41] and is shown in Fig. 1.6. In this design the drive coil excites oppositely directed magnetic fields (odd-mode) for the two parallel cores and the sense coil picks up even-mode changes in flux.³ An

³based upon their relative winding orientation around each core.

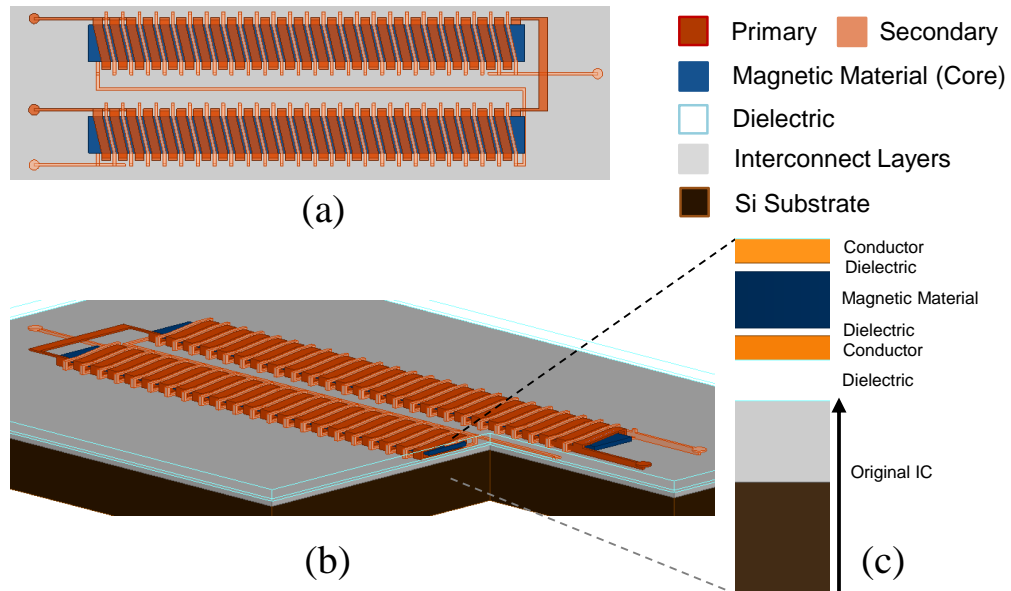


Figure 1.6: Top down view (a), perspective view (b), and layer stackup (c) of a dual-core microfluxgate.

external magnetic field will shift the core characteristics, such that there is an even-mode component to the magnetic flux in the two cores (i.e. one core is saturated due to the drive coil, but the other is not). After rectification and filtering, the sense coil's voltage is proportional to the magnetic field over a specified domain.

There are also alterations to these two designs, including toroidal [42, 43], ring-core [44–46], and a hybrid between solenoidal and spiral [47, 48]. Although the models and operation of these devices are quite similar to the two discussed in detail in the previous paragraphs, we will not be considering these additional microfluxgate designs further.

1.3 The Need for Equivalent Circuit Models

Much effort has been spent in developing models for the active devices in integrated circuits. Today, a transistor model used for circuit simulation may have ~ 75 parameters to capture all of the relevant physical effects. Contrarily, the passive device models are often oversimplified. For example, the microinductor model in a buck converter may be as simple as a linear resistor in series with a linear inductor [49–51]. However, as presented in this thesis, many complicated physical effects impact the performance of these on-chip passive magnetic devices. Ignoring these effects may lead to costly redesigns of the integrated circuit.

There are few ways to include the relevant physical effects in micro-magnetic devices without actually building the device. Due to this, a designer may (1) opt to ignore nonlinear effects, but microinductors and microtransformers are operated with currents in the saturation region of the device to boost power density. Also, power electronics often need to be modeled for over-current protection and microfluxgates rely on the nonlinear regime for operation. To include the nonlinearity, a designer may (2) use polynomials [52], empirical expressions [53], or even table-lookup [54], but these ignore dynamic losses. Currently, the only way to include all the relevant effects is to (3) use co-simulation [55] of the active circuit and the magnetic device modeled in a full wave nonlinear electromagnetic (EM) field solver.

Co-simulation uses a circuit solver and an EM field solver. Electromagnetic field solvers are numerical computer programs which first discretize or mesh the volume

or surface of a 3-D structure to be analyzed. Next, they approximate the solution to either the integral formulation, the differential formulation, or the less popular hybrid integro-differential formulation using a set of, typically, local basis functions.⁴ Finally, a matrix equation is formed that has a solution equal to the coefficients of the basis functions, thus providing an approximation of the fields. Examples, of numerical methods that use the differential equation are Finite-Difference Time-Domain (FDTD) and the Finite Element Method (FEM) [56, 57]. Examples of numerical methods that use the integral formulation are the Method of Moments (MoM) [58, 59] and Partial Element Equivalent Circuit (PEEC) [60]. One of the most popular techniques for solving the circuit problem that is linked to the field solution is Modified Nodal Analysis (MNA) [61].

Although co-simulation is accurate, it is often so memory and time consuming as to be infeasible to simulate the entire microinductor. This is partially due to the fact that the magnetic material boosts the permeability and therefore has a reduced skin-depth, leading to the need for a small mesh over a large region. If this problem could be overcome, co-simulation would likely still be too slow to allow optimization or design of the active circuits, or micro-magnetic device. The solution proposed in this thesis is to generate a compact equivalent circuit model (either through simple field-solver simulations, or actual device measurements), which allows for fast circuit simulation when the active circuit is connected. The proposed design flow, from the design of the magnetic device to the packaging

⁴Local basis functions are preferred for general numerical field-solver problems, but global basis functions may be more effective for a specific problem.

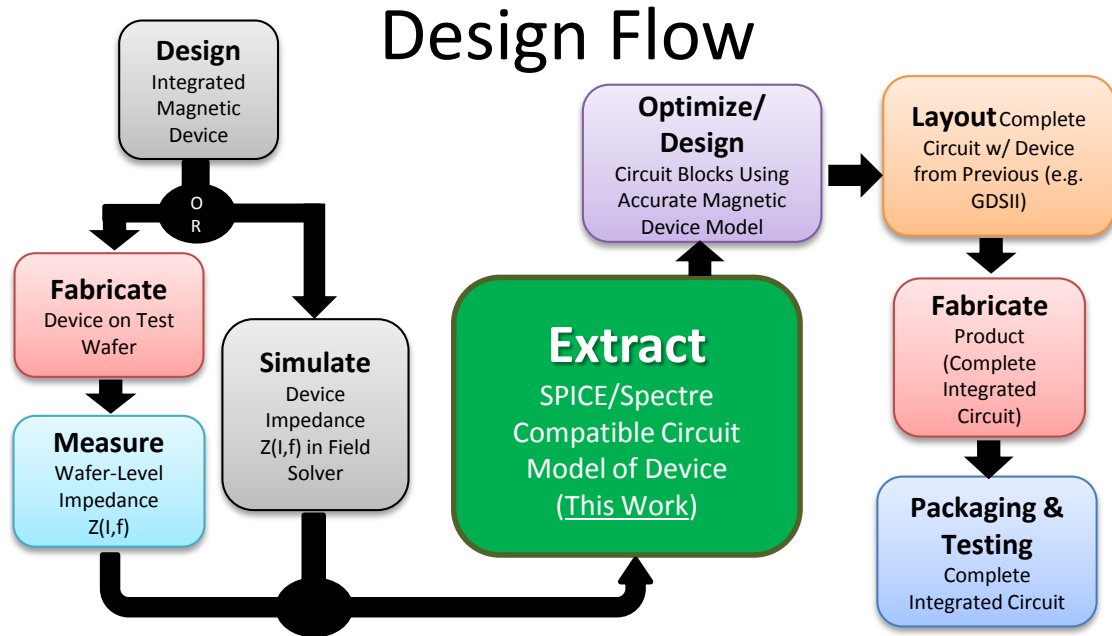


Figure 1.7: Flow diagram of design process for ICs using micro-magnetic devices.

and testing of the complete integrated circuit, is shown in Fig. 1.7. If the micro-magnetic device needs to be free to vary, the device can be selected from a library of near-optimal designs for various applications.

1.4 Modeling Challenges

Broadly speaking, there are two main challengers to modeling these types of magnetic devices. One main challenge is the need to consider a wide array of relevant physical phenomena in the magnetic and non-magnetic materials. The second main challenge discussed is the various difficulties arising from modeling a micro-sized on-chip device.

1.4.1 Physical Phenomena

Ostensibly the first modeling challenges to consider are related to the relevant physical phenomena. The phenomena we are discussing are electrical in nature, hence, they are often best described by referring to Maxwell's equations in their modern differential form:

$$\nabla \cdot \mathbf{D} = \rho_v \quad (1.1a)$$

$$\nabla \cdot \mathbf{B} = 0 \quad (1.1b)$$

$$\nabla \times \mathbf{E} = -\frac{\partial \mathbf{B}}{\partial t} \quad (1.1c)$$

$$\nabla \times \mathbf{H} = \mathbf{J} + \frac{\partial \mathbf{D}}{\partial t}, \quad (1.1d)$$

where **bold** indicates vectors and vector operators. The source terms are the volumetric charge density, ρ_v and current density, \mathbf{J} , and they are functions of space and time. The electric and magnetic fields (\mathbf{E} and \mathbf{H} , respectively), and electric and magnetic flux densities (\mathbf{D} and \mathbf{B} , respectively) are functions of space and time and related through the constitutive relations, namely,

$$\mathbf{D} = \epsilon_0 \mathbf{E} + \mathbf{P} \quad (1.2a)$$

$$\mathbf{B} = \mu_0 (\mathbf{H} + \mathbf{M}), \quad (1.2b)$$

where \mathbf{P} is the polarization, and \mathbf{M} is the magnetization, both being functions of space and time.

One phenomenon integral to the operation of magnetic devices is electromagnetic induction. Faraday's Law, (1.1c), informs us that any changing magnetic field associated with a changing current will give rise to a electromotive force (EMF); this is electromagnetic induction and it is the phenomenon that gives rise to inductance.

The flux-gate, additionally, operates based on a nonlinear relationship between the current and magnetic fields. Magnetic materials exist which are composed of tiny magnetic moments in magnetic domains. Initially, these domains are aligned without coordination so as to minimize the magnetostatic energy. As a magnetic field is impressed the domains alter so as to boost the magnetization in the direction of the field. Eventually, all of the domains, and therefore moments, point in the direction of the applied field so the magnetization does not increase further and we say the sample is in saturation.

While the domains are moving, their boundaries can get caught on lattice discontinuities and other defects giving rise to a static memory effect known as hysteresis. Hysteresis causes the magnetization, \mathbf{M} , to effectively lag the magnetic field, \mathbf{H} , and thus appears as a loss. Due to the memory being of the static type, hysteresis loss is done on a per cycle basis and, thus, is proportional to frequency.

In the absence of a conductive material, there are still dynamic memory effects. Principally, the dynamic memory effects are those related to ferromagnetic resonance/relaxation (FMR). The domain walls consist of atomic moments which do

not move instantaneously in response to a change in magnetic field. This affects the dynamics of \mathbf{M} and thus (1.2b). To first order their movement can be described by a second order differential equation. It was proposed in reference [62] to model the combined effect of FMR and hysteresis by a Hammerstein configuration, where a linear dynamic system is forced by the output of a static nonlinear system to approximate a more general nonlinear dynamic system.

When a time-varying magnetic field penetrates a conductive material, the electric field of Faraday's Law, (1.1c), gives rise to currents, known as eddy currents.⁵ From Lenz's Law we know the secondary magnetic fields produced by the eddy currents will oppose the original magnetic field and thus reduce the inductance. From Ohm's Law we know that the eddy currents represent loss. From Faraday's Law and Ohm's Law in a simple medium of conductivity σ and permeability μ excited by a time-harmonic applied magnetic field of radian frequency ω and with vector-phasor \mathbf{H}_a we have

$$\nabla \times \mathbf{J}_{eddy} = -j\omega\sigma\mu\mathbf{H}_a. \quad (1.3)$$

This is the only relationship needed to model first order eddy currents, or eddy currents at low frequencies. However, at higher frequencies the eddy currents themselves are large enough to contribute to the magnetic field, from Ampere's Law, (1.1d),

$$\nabla \times \mathbf{H}_{eddy} = \mathbf{J}_{eddy}, \quad (1.4)$$

⁵Also known as Foucault currents named after French physicist Léon Foucault.

which, in-turn, generate eddy currents described by

$$\nabla \times \mathbf{J}_{eddy} = -j\omega\sigma\mu\mathbf{H}_{eddy}. \quad (1.5)$$

Taking the curl of (1.3) combined with (1.5), and using the fact that there is no charge build up in an eddy current problem (magnetoquasistatic $\Rightarrow \nabla \cdot \mathbf{J}_{eddy} = 0$), we combine the curl of (1.5) with (1.4) and obtain the eddy current differential equation,

$$\nabla^2 \mathbf{J}_{eddy} = j\omega\sigma\mu(\nabla \times \mathbf{H}_a + \mathbf{J}_{eddy}). \quad (1.6)$$

In (1.6) ∇^2 is the Laplacian operator [59]. Another dynamic phenomenon occurring in micro-magnetic devices is capacitive self-resonance. When a voltage appears across the terminals of the micro-magnetic device, an electric field is generated. The field may pass through dielectric materials creating capacitance and through resistive materials giving rise to loss. Although this effect is distributed with the main inductance, at lower frequencies we can model it as a single canonical CG-network⁶ in parallel with the magnetic device. The frequency at which the capacitance and inductance are in resonance is referred to as the capacitive self-resonant frequency.

The previous paragraphs described the major physical phenomena we need to consider in any micro-magnetic device model. This creates a substantial modeling challenge, both in terms of the number and type of parasitics. More details

⁶Examples of canonical CG networks include, Foster and Cauer networks of network theory [63].

about each of these phenomena and how to model them in a physically-meaningful equivalent circuit model is given in Section 2.2. The devices work through EM induction, and may treat static nonlinearities, such as saturation, as parasitics or necessary for device operation. Typically static memory effects like hysteresis are considered parasitics due to their lossy nature. Nonconducting dynamic effects such as FMR also give rise to loss, as do the conductive dynamical effect of eddy currents. Finally, capacitive resonant effects can reduce the magnetic energy in place of electric field energy which has the opposite V-I phase relationship, and the device no longer behaves properly.

The devices in this thesis focus on ferromagnetic thin-film alloy magnetic materials, operated in the frequency range of 1 to 100 MHz. These materials are popular [16] due to their lower power loss density than ferrites at these frequencies [8]. Moreover, ferromagnetic thin-film alloys can be sputtered or electroplated in a fashion compatible with high volume semiconductor manufacturing [8]. Although these materials may have better saturation characteristics, saturation still needs to be considered. Hysteresis is typically not a concern since amorphous materials like Ni-Fe [16, 64], Co-Ni-Fe [16, 65], Ni-Fe-Mo, Co-Ta-Zr [66], and Fe-Co have small coercivities. Although ferromagnetic relaxation (which is the dampening portion of resonance) may be a concern at ~ 100 MHz, the actual resonance frequency is typically at GHz frequencies [67]. The most prominent physical phenomenon in these materials, besides induction, is typically eddy currents; specifically high-frequency eddy currents due to the relatively high conductivities of these alloys. Another important effect is capacitive resonance due to the large size of the final

devices.

In this thesis, the importance of including specific physical phenomena is given as follows:

- 1: magnetic induction;
- 2: magnetic saturation;
- 3: DC resistive effects;
- 4: broad-band eddy currents;
- 5: capacitive self resonance and electric field loss;
- 6: magnetic hysteresis;
- 7: ferromagnetic resonance/relaxation.

1.4.2 On-Chip Integration

Some of the challenges in modeling a micro-magnetic device come from the fact that it is on-chip. For example, if wafer-level measurements are not feasible and the device is packaged, the bond wire, package, bond pad, and trace parasitics leading to the device need to be de-embedded. The most significant challenge to modeling brought about by being on-chip is perhaps the fact that the magnetic properties are usually not the same as those of the bulk material and depend on substrate surface and demagnetization effects [11]. This makes it difficult to use the magnetic material's properties as knowns in the modeling procedure, as is typically done in off-chip magnetic device modeling.

1.5 Research Contributions

The main research contributions of this thesis are compact equivalent circuit models appropriate for micro-magnetic devices. This includes the understanding of relevant magnetic effects and theories required to build such a model. The improvements we have made to literature in this area are best described by the features of our models and extraction techniques, as listed below.

- We uniquely base our models on easily measured terminal characteristics of a particular device alone and do not rely on any independent material or device measurements. This is important in the context of on-chip modeling because setting up test structures to obtain magnetic properties can be difficult or virtually impossible, and magnetic properties can vary with layout thickness, and substrate [11].
- The measurements used are based on small-signal biased impedances, which are compatible with wafer-level measurements through vector network analyzers (VNAs) or impedance analyzers. These measurements are general enough for us to create models of a wide variety of microinductor and microtransformer topologies.
- Although the models represent complex effects that are nonlinear and dynamic, we guarantee they are passive by constraining each individual circuit element. Passivity is an important characteristic which implies both causality and stability of the model.

- Each model generated is physically motivated and has a physically meaningful circuit topology. This enables the model to provide important physical insight into the operation of the device. For example, the model could separate out physical effects such as core loss from conductor loss.
- We have developed first-of-their-kind extraction algorithms, which separate the complicated process of extracting a high-order nonlinear dynamic network from measurement data into a number of stages. The algorithms typically take a few minutes and guarantee the models generated are accurate and passive.
- The models are compact and compatible with popular circuit solvers including SPICE and Spectre[®] [68].
- We confirm that our models accurately capture key characteristics in their application domain by running simulations in the relevant application domain which is independent of the original small-signal measurement set.
- The microinductor model and extraction algorithm are suitable for a wide range of applications and layouts, and uniquely incorporate the most relevant physical phenomena, including high-frequency core eddy currents, core saturation, skin and proximity effect in the conductors, capacitive self-resonance.
- The microtransformer model and extraction algorithm are suitable for a wide range of applications and layouts. The relevant physical effects included are unique to existing literature and include high-frequency core eddy currents,

core saturation, skin and proximity effect in the conductors, capacitive self-resonance.

- Microfluxgate models are not very common in literature. Our model captures demagnetization, saturation, and their corresponding complexity in the magnetic domain. It accurately reproduces the voltage and current waveforms on both coils of a dual core solenoidal microfluxgate.

In addition to this, we have reviewed research literature summarizing relevant papers on how to incorporate higher-order effects such as ferromagnetic resonance, and hysteresis, in a physically meaningful equivalent circuit.

1.6 Thesis Outline

The scope of this thesis is on extracting accurate and physically meaningful equivalent circuit models of micro-magnetic devices from their terminal measurements. The thesis is divided into six chapters. Chapter 2 discusses the general considerations for the modeling effort and compares and contrasts the difference between behavioral and physics-based models. Once we have determined that we wish to generate physics-based models, we present techniques for including relevant physical effects using equivalent subcircuit building blocks. Chapters 3 through 5 follow a common outline, describing three different magnetic on-chip device categories. Each chapter begins with the introduction to the device category followed by a review of existing models. Necessary sub-blocks to the circuit model are then developed, followed by discussing the fitting algorithm, and validation of the model

and algorithm. Chapters 3 through 5 end with a discussion of conclusions and future work. The device category studied in Chapter 3 is a simple two-terminal microinductor. Chapter 4 adds the complexity of a four-terminal micro-device by considering coupled inductors and equivalently transformers. Finally a four-terminal device category with two separate cores is considered in Chapter 5 with the dual-core solenoidal microfluxgate. Lastly, the Conclusion in Chapter 6 summarizes the work with concluding remarks and possible future directions.

Chapter 2 – General Modeling Considerations

In this chapter we will answer many of the important initial questions that should be addressed before one ventures to make a model of a component or device. The first question we address is what type of model we should be considering for the on-chip magnetic devices in this thesis. Even within the domain of passive device modeling, the word “model” covers a wide range of different aids to design and analysis. Important considerations include: whether the model is used in design or analysis; whether there is a surrounding circuit; the speed and size of the model; how and where the model is used; and how closely the model captures the relevant physics. To aid in considering the last point, we further discuss physics-based modeling and behavioral modeling, and provide a simple coaxial microinductor example in Appendix A.

Once it is decided that the physics-based circuit modeling approach is desirable, it is important to understand how to capture the relevant physics (see Section 1.4.1). Section 2.2 answers this question by considering physically meaningful circuit building blocks for different physical phenomena. We begin with the simplest physical effect of memoryless static nonlinearities, namely magnetic saturation. Static memory effects are then added, giving rise to hysteresis. Next, dynamic memory effects in non-conducting magnetic material are considered such as ferromagnetic resonance. The magnetic material is then made conducting and an RL

ladder circuit capable of capturing nonlinear eddy currents at low and high frequencies is developed. Finally, electromagnetic dynamic effects such as capacitive self-resonance are considered through a parallel CG circuit.

2.1 What Type of Model is Desired?

A model is a representation of a physical device or system that captures its performance figures or is used in a larger circuit simulation. The focus of this thesis are models used in larger circuit simulations, where our model is a subcircuit. This is especially true since we are dealing with passive magnetic components on-chip, and such components are not isolated from their driving active devices. Performance calculations are still important, but they relate to the component in the larger circuit rather than the component alone. For example, a stand-alone model could calculate the peak quality factor of an inductor, but it wouldn't calculate the power loss in the inductor, because that depends on the surrounding circuit and its excitation.

One way to classify a model is how closely the parameters relate to design variables, such as dimensions or material properties. If one wishes to specify the design of the device from the model (or vice versa), the parameters should closely relate to the design variables. This allows optimization of the component or device given an appropriate figure of merit (FoM). There may also be a need to co-optimize the component and its surrounding circuit. To that end, one would need a circuit model with circuit elements depending on design variables; such a model is called a

scalable circuit model. Creating a scalable circuit model with accurate performance is a challenge in its own right. However, the consideration of optimum design of components is beyond the scope of this thesis. Therefore, we do not necessarily need our model parameters to relate closely to design variables.

A major trade-off in modeling is speed to obtain the results versus their accuracy. Typically solving a specific excitation of a model requires the inversion of a matrix as in numerical field solvers such as the Method of Moments (MoM) [59], or Finite Element Method (FEM) [57], or as in circuit solvers such as Modified Nodal Analysis [61]. Apart from any setup or overhead steps, the size of this matrix largely determines how long the solution will take. The general trend is the larger the matrix, the more accurate the results. However, there are ways to make smaller circuits approximate very large circuits, paying little price in terms of accuracy for a great increase in speed. For example, a class of routines to methodologically transform from a large circuit to a small circuit is Model Order Reduction (MOR) [69]. In this thesis work, we desire the accuracy and speed of such a reduced order model. That is, the developed model should closely match measurements and field solver data for the device, but be compact enough to consist of a minimum of ideal circuit elements.

Another consideration for the model is how it will be used. The model could be part of a stand-alone program used to estimate key performance figures in a simplified circuit with few parameters, or the model could be part of a more general standard simulation program, such as SPICE. One should also give forethought to the end result the user of the model desires, and the type of simulation this requires.

The end result, for this thesis work, are performance figures for the complete circuit and waveforms which inform about its operation and allow for the design of the circuit. Ultimately, this means our model should be implemented as a subcircuit in available circuit simulators and be compatible with their simulation modes, including transient simulation, DC and AC analysis, and even harmonic balance. For the model of this thesis to be implementable in most circuit simulators, two popular simulators were chosen as examples: Spectre[®] [68] and SPICE. This allows compatibility with a wide range of other models, including those used for the underlying integrated circuit's active components.

In a final consideration, we can classify models based on their level of abstraction [70]: are the circuit variables mathematical functions removed from physics, or do they represent physically meaningful quantities? Abstraction is nice when the designer of the device or circuit wants to obfuscate their design to prevent any attempts at reverse engineering. Also, typically a more mathematical/behavioral and less physical model will be more general and able to handle a wider range of physical effects. On the other hand, a physical model is beneficial to gain insight into the design processes. The user of the model can plot quantities which relate to the physical operation of the device. At the abstract end of the spectrum are black-box N-port matrix models [70]. An example of these is modeling a linear two-port reciprocal circuit by three rational impedance functions representing the frequency dependence. At the physical end of the spectrum are field-based models, by which estimates of field quantities can be obtained. Examples of field models are the Finite Element Method (FEM), mentioned previously, [57] and Partial Element

Equivalent Circuit (PEEC) Model [60]. For our purposes, we desire the generality of a mathematical model, but the design insight of a physics-based model, so we consider these options further in the following subsection.

2.1.1 Behavioral versus Physics-Based Model Comparison

We would like to further compare the trade-offs between the levels of abstraction of a compact circuit model. To this end, it is beneficial to consider a specific example. Starting with a simple coaxial line containing a nonlinear magnetic material we will discuss the benefits and costs of selecting a physics-based model or a behavioral model. The coaxial line is used to create both types of models in detail in Appendix A; here we simply compare the trade offs in selecting one over the other. The reader unfamiliar with either model, is invited to study Appendix A to help understand the reasons for the tradeoffs.

A physics-based model does not necessarily have to be based on physical parameters, as the one in Appendix A is. However, at the very least, the topology of the circuit should be consistent with the physical effects. One benefit to physics-based modeling is that typically the models have reasonable asymptotic behavior. In the coaxial model this in part means that as the circuit approaches infinite frequency both the “physical” model and the physics-based model predict a purely resistive circuit. More generally, this means there is no erratic or unexpected behavior if the model is operated far outside of the fitting region. Another benefit to physics-based modeling is that it is often easier to guarantee the model is passive,

which brings with it many desirable properties such as stability and causality [71]. For our model this is ensured by the equations of Table A.1 generating positive element values. Moreover, physics-based models may allow separating physical effects. In the model of Fig. A.2 we could separate the eddy current losses in the magnetic core, from the conduction losses in the inner conductor by observing the loss in R_1 and R_0 , respectively. A fourth benefit is that the development of a physics-based model helps to test the designer's understanding of the physics involved, thus aiding in component design. Since a physics-based model will have different pieces for differing physical effects, it may be possible to fit to the different effects independently improving the model generation algorithm (see Section 3.4). Furthermore, this partitioning of the structure may allow extending the model into a scalable circuit model for the design of the component.

There are also down-sides to using a physics-based model. The most obvious is that it is more time consuming and difficult to develop the model with all its relevant physical effects, or there may be physical effects which are ignored. In some cases, the need for more physical knowledge of the device may be looked at as a shortcoming. For example, it may be easier to simply measure the terminal characteristics, rather than uncover the complicated magnetic properties of the thin films. Finally, the model extraction algorithm may be more difficult and less well understood since it needs to be developed on a device-by-device basis rather than using the training/fitting methods for general functions as we will see in the next sub-section.

The benefits to behavioral modeling are often the shortcomings of physics-

based modeling. One benefit is the behavioral model is removed from the physics, making it difficult to reverse engineer the device parameters or material properties. Thus, if this device were to be released to the public, these important design details would be sufficiently obscured. Another important benefit to behavioral modeling is that it is more general than physics-based modeling. To add another physical effect to our physics-based model, we would need to build this into the model somehow. However, effects such as ferromagnetic resonance and hysteresis can be added to our behavioral model simply by increasing the differential equations order, and thus the number of state variables/functions. A third benefit to behavioral modeling is that the fitting procedures are often well-established and, therefore, better understood. For example, there is much work on fitting polynomials and training artificial neural networks. On the other hand, the physics-based model may need a custom extraction algorithm. Finally, the behavioral models typically can take as inputs any set of time-domain, frequency-domain, or harmonic data. A physics-based model may be better suited to a certain type of measurement, or even require geometry or material data.

As with physics-based modeling, there are also shortcomings to the behavioral modeling approach. One of the largest, is that the network is not necessarily passive. As mentioned previously, passivity is an important characteristic in regard to causality and stability, and correct behavior of a passive component. Furthermore, as we saw with both the polynomial model and artificial neural network model, behavioral models shown in Appendix A can sometimes have significantly inaccurate behavior outside of the fitting region. Another potential problem is the

inability to create accurate models of high order, as the state space functions grow in dimension with increasing differential equation's order. Finally, there is no way to test the understanding of the device through the measurements taken. This means it is possible to have an accurate behavioral model, which captures effects seen in the measurement that are not desirable. For example, bond-wires, traces and pads may be affecting the measurements, but not be removed from the model.

2.1.2 Model Requirements

The models we will be considering in this thesis are representations of on-chip magnetic devices, which fit as critical subcircuits into larger systems. We desire the model to accurately simulate performance and circuit operation waveforms and figures, in transient, DC/AC, and harmonic balance analyses in common circuit simulators. The model does not need to be scalable and therefore have parameters which allow for the design of the component, but should enable the selection from a library of devices and should allow for the design of the surrounding circuit. Our model should reproduce the performance of either measurements or physical models, but be compact enough to consist of a minimal number of ideal circuit elements. In a final consideration we would like our model to be physics-based as opposed to behavioral. The major benefits are: passivity, asymptotically well-behaved, insights gained into device operation, and possibly higher order models. The major costs to selecting a physics-based model over a behavioral model are: the need to create a unique fitting algorithm, having to consider what physical effects

are relevant, and the need to specify the types of measurements. We believe the benefits outweigh the costs. Therefore, in what follows, we will consider what is needed for the subcircuit models of the magnetic on-chip devices to be physics-based in at least their topology, and not focus any further on behavioral models.

2.2 Circuit Building Blocks for Capturing Physical Effects

Since we have decided to implement a physics-based model, we need to consider how to possibly incorporate the many physical effects that are relevant. We begin with the simplest physical effect of memoryless static nonlinearities namely magnetic saturation. Static memory effects are then added, giving rise to hysteresis. Next, dynamic memory effects in non-conducting magnetic material are considered such as ferromagnetic resonance. The magnetic material is then made conducting and an RL ladder circuit capable of capturing nonlinear eddy currents at low and high frequencies is developed. We conclude this section with a discussion of electric-field effects, which look beyond magnetic-field effects alone.

2.2.1 Saturation

Ferromagnetic materials that show saturation are composed of individual magnetic domains. These domains form in response to a balance between quantum effects, that make it favorable for individual moments to point in the same direction, and magnetostatic energy, where the energy is minimized by domains pointing

Table 2.1: Different functions to model anhysteretic $M(H)$ behavior of a saturating magnetic material, where α and β are constant fitting parameters.

Name	Function	Ref.
Hyperbolic Tangent	$M = \alpha_1 \tanh(\alpha_2 H)$	[72]
Sum of Decaying Exponentials	$M = \beta_0 - \beta_1 e^{-\alpha_1 H} - \beta_2 e^{-\alpha_2 H} - \dots$	[73]
Error Function	$M = \alpha_1 \operatorname{erf}(\alpha_2 H)$	[72]
Rational Exponential Function	$M = \frac{(1+e^{\alpha_1 H}) \dots}{(1+e^{\beta_1 H})(1+e^{\beta_2 H}) \dots}$	[74]
Langevin with Mean Field	$M = \alpha_1 \left(\coth\left(\frac{H+\alpha_2 M}{\alpha_3}\right) - \frac{\alpha_3}{H+\alpha_2 M} \right)$	[75]
Odd Polynomial	$M = \alpha_1 H + \alpha_3 H^3 + \dots$	[76]

in opposite directions. For a sufficiently large amount of material, there will be many microscopic magnetic domains. If we ignore any irreversible effects, the bulk magnetization, M , will be zero in the absence of any external field (see randomly oriented domains of Fig. 2.1(a)). Within an applied magnetic field, H_a , the total magnetostatic energy is minimized by more moments pointing in the direction of the applied field. This state is obtained by increasing the size of domains aligned with H_a and decreasing domains opposing H_a , as well as partial rotation of other domains, as shown in Fig. 2.1(b). The net effect is that the magnetization of the material becomes stronger in the direction of the applied field. As we approach the condition that all the magnetic moments are pointing in the direction of the applied field, there is no longer any means of increasing M , and we say the material saturates. Ultimately this gives rise to $M(H)$ and $B(H)$ (note: $B = \mu_0(H + M)$) behavior which exhibits a nonlinear sigmoidal shape. Fig. 2.1(c) shows an example sigmoidal curve based on a hyperbolic tangent function.

There are many functions that are capable of capturing the sigmoidal magnetization behavior when hysteresis is ignored (anhysteretic). See Table 2.1 for

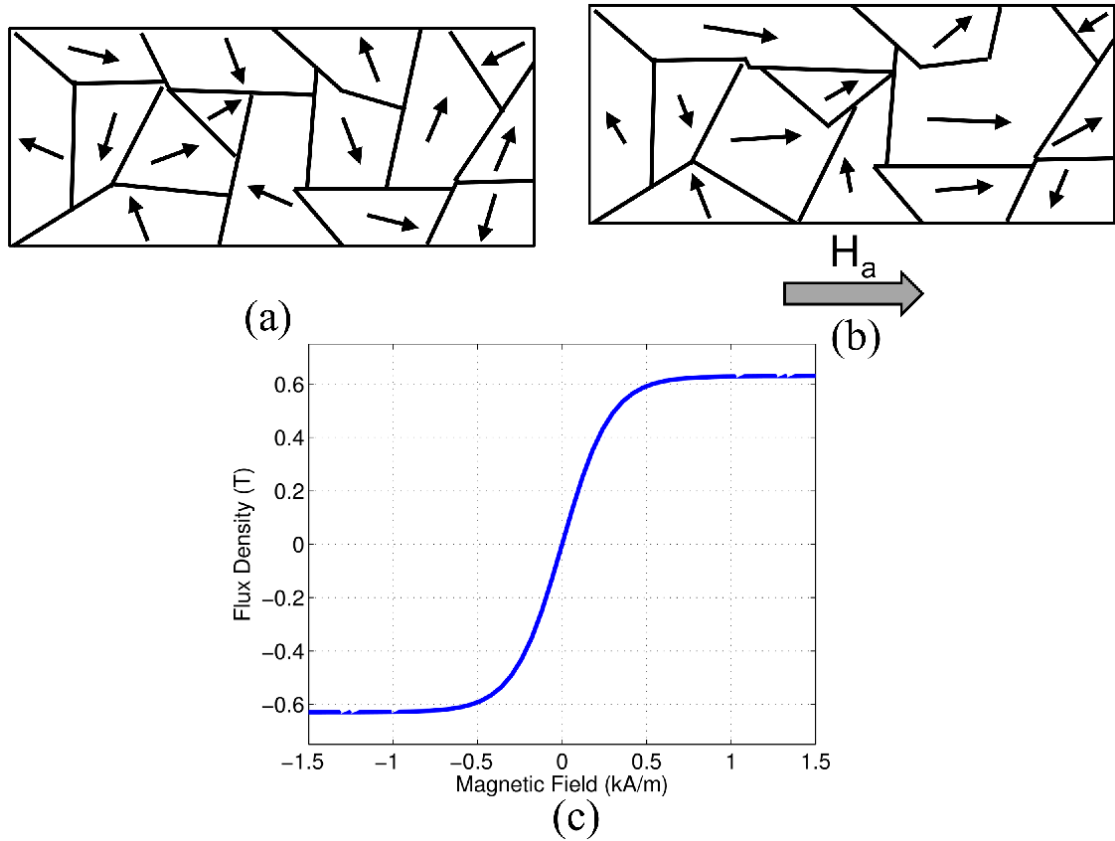


Figure 2.1: Diagram of magnetic domains in a bar magnet, when there is no magnetic field applied (a), and under the presence of an external magnetic field (b). The resultant magnetic flux density B versus magnetic field H is shown in (c).

some example functions. Using these functions requires implementing them in a circuit simulator. One approach is to recognize the saturating magnetic material is represented as an effective nonlinear inductor and then implement that inductor as a subcircuit in the electric domain. This involves taking the derivative of the flux with respect to the exciting current (see (B.12)), and thus the derivative of $M(H)$. Another approach is to implement the saturation behavior directly in the magnetic domain as a nonlinear reluctance and then perform the conversion from the electric to magnetic domains. For a discussion on electric and magnetic domains see Appendix B.1.

Although up to this point we have been using the small-signal, or incremental inductance, there is another definition of inductance, namely the large-signal or secant inductance. The secant inductance is more directly related to the magnetic domain implementation since it is used to calculate the flux directly. For a discussion of these different types of inductance see Appendix B.2.

2.2.2 Hysteresis

The anhysteretic magnetization from the previous subsection is the magnetization curve which would be achieved in the absence of a frictional force which impedes the movement of the domain walls.¹ Often a magnetic material will have a significant amount of this frictional force due to lattice discontinuities and other defects, which causes domain wall pinning at the defect sites, this causes a nonlinear memory

¹Domain walls are boundaries between different magnetization regions depicted in Fig. 2.1 as solid lines.

effect known as hysteresis. There are a number of ways to model hysteresis mathematically, including Preisach [77], StonerWohlfarth [78], and Jiles-Atherton [79] models. In this work, we do not consider individual magnetic domains, but take the average effective magnetic properties. These properties are taken to be the constitutive behavior of the material (see (1.2b)). This treatment is justified by the large number of domains in the magnetic core material as a whole.

In circuit modeling, in the early to late 80's, simple models with nonlinear capacitors, nonlinear controlled sources, or switches were used to capture the hysteresis loss [80–82]. Later, throughout the 90's, the more advanced Preisach model of hysteresis was used for lumped inductors to capture their small-signal inductance [83–86]. As mentioned in [87], SPICE analog behavioral modeling does not allow easy implementation of state behavior, making the Preisach model difficult to implement. To overcome this, in the early 2000's, there was work to implement magnetic circuits using the Jiles-Atherton model of hysteresis [87–90]. In this section we will consider implementation of the Jiles-Atherton hysteresis model. The equations that describe the Jiles-Atherton model usually make use of the Langevin expression of ferromagnetism for the anhysteretic behavior. However, we will be using the hyperbolic tangent, removing the implicit nature of the Langevin expression. The four functions describing the Jiles-Atherton hysteresis model are given as

$$\frac{dM_{irr}}{dH} = \frac{M_{an} - M_{irr}}{k\delta - \alpha(M_{an} - M_{irr})} \quad (2.1a)$$

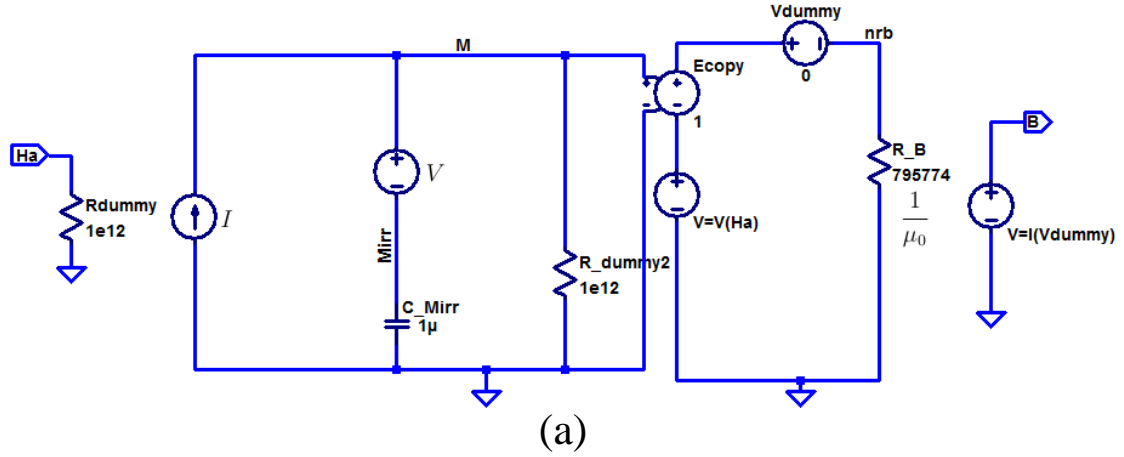
$$M_{an} = M_S \tanh(gH) \quad (2.1b)$$

$$M_{rev} = c(M_{an} - M_{irr}) \quad (2.1c)$$

$$M = M_{irr} + M_{rev}, \quad (2.1d)$$

where M is the magnetization; M_{irr} the irreversible magnetization; M_{rev} the reversible magnetization; M_{an} the anhysteretic magnetization; and H the magnetic field intensity. The five model parameters are: M_S , the saturation magnetization in A/m; α , the mean field parameter (dimensionless); c , the domain wall flexing constant (dimensionless); g , a scaling parameter of the anhysteretic $\tanh M(H)$ behavior in m/A; and k , the domain wall pinning constant in A/m which gives the width of the hysteresis loop. The term δ is a directional parameter that is defined as the sign of $\frac{dH}{dt}$.

An implementation of this form of Jiles-Atherton hysteresis is shown in Fig. 2.2(a) with behavioral source equations given in 2.2(b). More details about this implementation are provided in [87]. The basic idea is to implement these equations as behavioral controlled sources while using reactive elements to implement derivatives and integrals. In Fig. 2.2 (c) we see the initial magnetization curve and the outer hysteresis loop, which is traversed counter-clockwise. To implement the subcircuit of 2.2(a) into an inductor, we can use the subcircuit to calculate the flux versus magneto-motive force in a nonlinear reluctance in the magnetic domain, see



$$I = 1 \times 10^{-6} \frac{(V(M)/c - V(M_{irr})/c) \frac{dV(H_a)}{dt}}{k\delta - \alpha(V(M)/c - V(M_{irr})/c)}$$

$$V = c * (M_S \tanh(gV(H_a)) - V(M_{irr}))$$

(b)

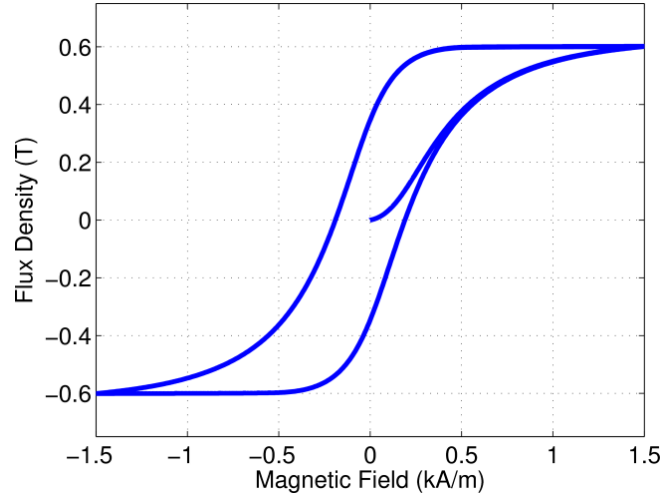


Figure 2.2: LTSpice subcircuit from [87] for modeling $B(H_a)$ for Jiles-Atherton hysteresis (a), and the equations for the behavioral source (b) with a hyperbolic tangent function for anhysteretic behavior. Corresponding initial and outer magnetization behavior is shown in (c).

Appendix B.1 and Section 3.6.1.

2.2.3 Ferromagnetic Relaxation/Resonance

Up to this point we have considered the static nonlinearities of magnetization. In this section we consider its dynamical aspect. We mentioned that as the magnetic field changes, the domain walls stretch and move and the domains undergo a partial rotation. These effects do not occur instantaneously. Even the magnetic moment of a single atom precesses around the applied field until decaying to the applied field direction, as described by the Landau-Lifshitz-Gilbert equation. These dynamic effects are known as magnetic relaxation/resonance and they impact the motion of domain walls as they approach the equilibrium position.

Jiles, in reference [62], presents a mathematical approach which models these effects via the Hammerstein configuration of nonlinear dynamical systems. The Hammerstein configuration is a cascade of a nonlinear-static block followed by a linear dynamic block. The equation presented in [62] is

$$\frac{1}{\omega_n^2} \frac{d^2 M_{dyn}(t)}{dt^2} + \frac{2\lambda}{\omega_n^2} \frac{dM_{dyn}(t)}{dt} + M_{dyn}(t) = M_\infty(t). \quad (2.2)$$

In (2.2), ω_n is the natural frequency of the domain wall dynamics and can be calculated from ferromagnetic resonance (FMR) [62], λ is the decay constant related to the decay from FMR [91, 92], M_{dyn} is the dynamic bulk magnetization, and M_∞ is the static magnetization from either hysteresis or saturation. As presented

in [87] this dynamic effect can be modeled by a second-order RLC low-pass filter² configuration connected to the magnetization output of the circuit in Fig. 2.2 (a).

2.2.4 Eddy Currents

Eddy currents are created when a time varying magnetic flux density exists in a conducting medium. From Faraday's law the flux induces an electromotive force in the conducting material. The electromotive force gives rise to conduction currents known as eddy currents, or Foucault currents.³ If these currents produce secondary magnetic fields which alter the eddy currents further, we are considering high-frequency eddy currents, since the relative strength of the currents rise with frequency. By means of Lenz's law we know the eddy currents oppose the generation of source's magnetic field and therefore reduce the inductance of the source. Also, the ohmic loss due to these currents reflects back as an additional series resistance in the main branch. These effects take place in many different locations: in the magnetic core, in each conductor, in between the conductors, and possibly in the substrate.

When considering eddy currents, one does not typically need to take into account displacement currents, since their magnitude is small when compared to the eddy currents at the frequencies of interest. Therefore, a network of resistors and inductors, can account for the effects of eddy currents in a circuit. Linear two-

²The domain-wall dynamics can be understood as a low-pass filter since the magnetization will not have the necessary time to follow a fast moving field.

³Named after French physicist Leon Foucault who first discovered them in 1851.

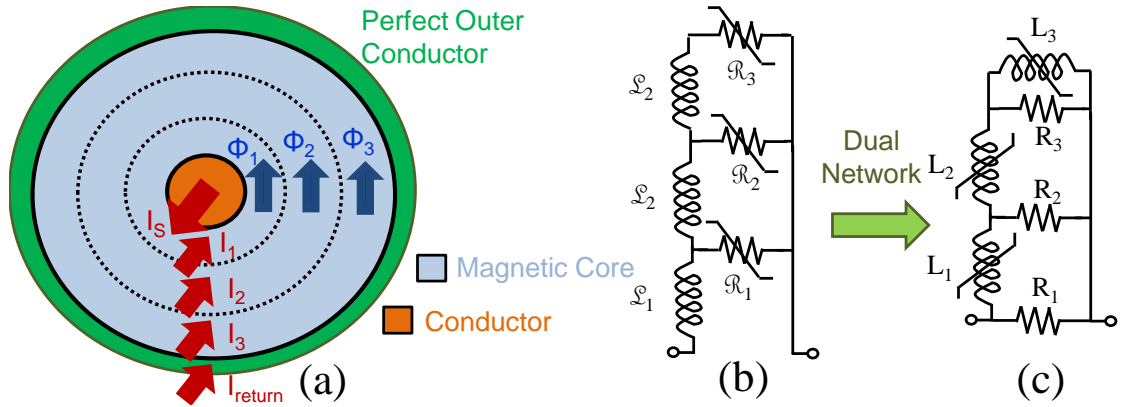


Figure 2.3: Coaxial microinductor showing partitioning of core and relevant variables (a) to approximate eddy currents as a finite order network in the magnetic domain (b). It is converted using Slemon's dual [94] to the electric domain (c)

element type networks like this can be realized by canonical circuit topologies [63], for example Foster Networks, or Cauer Networks. Other forms are also suitable, including transformer loops [93]. However, networks with nonlinear elements, behave differently for different circuit topologies. To determine what circuit is appropriate to model high-frequency eddy currents in the nonlinear core material, we will be analyzing the coaxial microinductor of Appendix A.1 in more detail.

Consider a partitioning of the coaxial core material with exaggerated thickness into three concentric regions, as shown in Fig. 2.3 (a). The fluxes and currents are considered as phasors. The outer perfect conductor acts as a return path to the currents. Thus, we can use Ampere's law to write the expressions for the fluxes, assuming the currents flow on the inner surface of their respective partition,

$$\Phi_1 = \frac{I_S - I_1}{\mathcal{R}_1} \quad (2.3a)$$

$$\Phi_2 = \frac{I_S - I_1 - I_2}{\mathcal{R}_2} \quad (2.3b)$$

$$\Phi_3 = \frac{I_S - I_1 - I_2 - I_3}{\mathcal{R}_3}, \quad (2.3c)$$

where Φ_i is the flux through the i th region, I_i is the eddy current through the i th region (See Fig. 2.3 (a)), and \mathcal{R}_i is the reluctance of the i th region (see Appendices A and B.1). From the resistance of the i th region ($R_i = 1/\mathcal{L}_i$) returning at the perfect outer conductor and from Faraday's law, we can write the expressions relating current to the fluxes

$$I_1 = j\omega\mathcal{L}_1(\Phi_1 + \Phi_2 + \Phi_3) \quad (2.4a)$$

$$I_2 = j\omega\mathcal{L}_2(\Phi_2 + \Phi_3) \quad (2.4b)$$

$$I_3 = j\omega\mathcal{L}_3\Phi_3. \quad (2.4c)$$

The six equations (2.3a-c, 2.4a-c) can be modeled by a network in the magnetic domain (noting that I is MMF or magnetic voltage and Φ is magnetic current). This network is shown in Fig. 2.3 (b). Using the dual relationship⁴ (See Appendix B.1) the magnetic domain network can be converted to an electrical network as shown in Fig. 2.3 (c). The fact that this form of Cauer Network is appropriate model

⁴Slemon's Dual (1953) [94]

for the nonlinear magnetic core's eddy currents is confirmed by the approaches in [84, 85, 88], for other geometries.

2.2.5 Electric Field Effects

When a voltage is applied across the terminals of a magnetic device, an electric field is developed. Some of the electric field passes from turn to turn through a dielectric medium, while some of the electric field passes through the conductive core. The dielectric medium gives rise to a capacitance, and the core gives rise to a resistance (or conductance). Fig. 2.4 shows an example of this for a solenoidal microinductor. The result is a distributed RC network, which, together with the inductance, gives rise to a self-resonance effect in the magnetic device. This self-resonance depends greatly on the geometry of the device, and should not be confused with material resonance effects such as ferromagnetic resonance which depends less on the device geometry⁵ (see Section 2.2.3). For the devices we are modeling, this electromagnetic self-resonance typically occurs at orders of magnitude lower frequencies than ferromagnetic resonance, and thus is more important.

Over the operating bandwidth of hundreds of MHz, we can consider distributive effects as negligible and model the electric field effects as a high-order RC networks in parallel with the main microinductor model. The high order network, would capture the change in capacitance and conductance of the parallel branch with frequency. However, we have found that over the bandwidth of interest there is

⁵This is only true since the dimensions considered are relatively large (micrometers).

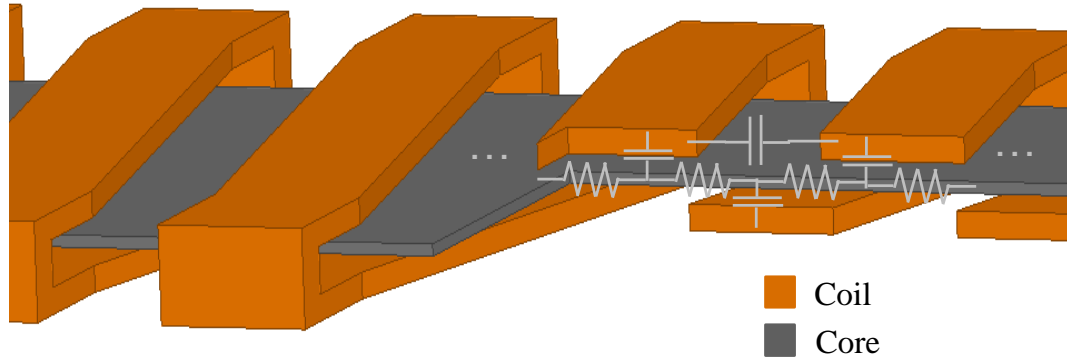


Figure 2.4: Section of high order physical RC network showing connection to solenoidal microinductor geometry

not much change in parallel capacitance and conductance, and a single simple series RC branch is sufficient. It should be noted that if higher order's are needed a canonical network such as a Foster, or Cauer network would be suitable to model the parallel two-element network [63].

2.2.6 Physical Effects Summary

As we have seen in the previous subsections, magnetic devices have several possibly relevant physical effects that need to be captured. In each of our models we will first consider what physical effects are most relevant to the operation of the device and its performance. Whether or not these effects are relevant depend on the geometry of the device, the frequency of operation, and, of course, the materials used. Static magnetic effects such as saturation and hysteresis can be implemented in the magnetic domain as nonlinear reluctances (an equation relat-

ing MMF and flux) in the magnetic domain, or a small-signal nonlinear inductor in the electric domain (if derivatives are taken). Non-conductive dynamic effects such as ferromagnetic resonance, can also be incorporated into the relevant reluctances and inductors, through the addition of low pass filters altering the constitutive relations. Some nonlinear dynamic effects cannot be implemented with the Hammerstein configuration as these effects need more general descriptions, e.g. eddy currents in nonlinear materials. For linear eddy currents, canonical RL networks are appropriate. However, linear RL canonical networks cease to be canonical for eddy currents in nonlinear mediums. For eddy currents in the nonlinear core material, we have developed a physically appropriate Cauer network which allows the inductors and resistors to represent discrete regions of the material. Finally, we have simplified the electric field effects to a simple parallel RC branch to model electromagnetic self-resonance. All of these effects are constructed so as to be capable of simultaneously being implemented in common circuit solvers if need be.

2.3 Conclusion

This chapter has answered many of the important initial questions one needs to address before making a device model. We have decided that our model does not need to be scalable, but should be compact, passive and asymptotically well-behaved. After a thoughtful consideration of the trade offs between behavioral and physics based models we have decided to design the model to be as physically meaningful as possible, while still constructing it through terminal measurements. The

physical effects that are relevant have been discussed in detail, including possible subcircuit implementations. Proceeding forward with our research, we will leverage the considerations and ideas in this chapter in generating complete modeling solutions for three unique device categories: microinductors, microtransformers, and microfluxgates in Chapters 3, 4 and 5, respectively.

Chapter 3 – Microinductor Model

3.1 Introduction

The first device category we will consider is a two-terminal inductor. Some of the first inductors were used as electromagnets in telegraph systems as early as 1840 [95]. Since then inductors have found their way into radio receivers and transmitters, a wide array of filters and oscillators, switched-mode power supplies, and more applications. In these applications, rather than creating a magnetic field to do work as in an electromagnet, energy is temporarily stored as a magnetic field to be released at a later time. Although it is conceivable that many of these applications would benefit from integration of magnetic materials on-chip, surrounding literature typically focuses on creating PwrSoCs. Integrating power supplies on chip would enable many system-level benefits along with decreased area and reduced component count; namely, improved reliability, increased manufacturability, and reduced cost [8]. As with most applications, it is important that the designed inductor have a low-loss and high reactance (high quality, Q) at the operation frequency. The trade-off between low-loss and high reactance is often benefited from boosting the inductance through a well designed magnetic material.

Microfabricated inductors with on-chip magnetics have many examples in the literature [9–11, 14, 15, 18–23, 25, 96, 97]. This chapter first reviews the current state-

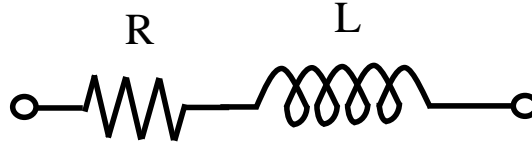


Figure 3.1: Simple linear two-element model of a microinductor.

of-the-art models for both on- and off-chip inductor modeling, showing the novelty of this thesis' work. Next, a unique microinductor model is developed in detail. In Section 3.4 a unique three stage algorithm is presented to fit the model to the measurements guaranteeing a passive and accurate fit. In Section 3.5 the model and algorithm are validated against two simulators and measurements for three different device designs. Finally, this chapter concludes by providing a section on future work and conclusions for the microinductor model.

3.2 Literature Review

3.2.1 Simple Linear Two-Element Model

Apart from having a single ideal lumped inductor, the simplest model of inductors in literature is a series combination of the linear lumped resistor and a inductor (see Fig. 3.1). The inductor's value is typically taken as the small-signal inductance at zero DC current bias and low frequencies. The resistor's value is more involved, it may be taken as the low-frequency winding/conductor resistance, or an effective resistance modeling the various loss mechanisms at the anticipated operating point.

Although this simple model is quite popular in modeling PwrSoC microinductors [49, 50], it is the least accurate model considered in this chapter. Its popularity likely comes from its ability to easily estimate parameters, and it lends itself to analytic calculation of the losses and currents.

3.2.2 Nonlinear Two-Element Model

The next simplest circuit topology often found in literature is the single lumped nonlinear inductor. Typically, these models only capture saturation effects [52–54], but they may also capture hysteresis [87]. To capture the saturation effects, polynomials [52], empirical expressions [53], or even table-lookup [54] may be used. It is not a substantial extension to add a series resistor with these models to capture either effective or DC winding loss.

3.2.3 First Order Eddy Current Model

One of the most popular circuit topologies for off-chip inductors is shown in Fig. 3.2. As we showed in Appendix A.2, the effects of eddy currents in the core material can be approximated by the parallel addition of a linear resistor (R_1) across the nonlinear core inductor ($L(i_L)$). There are many different physically meaningful ways to implement this effective parallel resistance. For example, [98,99] implement some elements in the electric domain, and others, such as the nonlinear inductor, in the magnetic domain. On the other hand, [81] is entirely in the electric domain

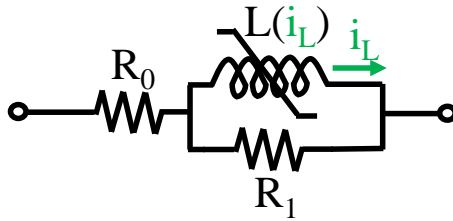


Figure 3.2: Microinductor model capturing eddy currents in the core making a low-frequency approximation

using behavioral current-controlled current source and voltage-controlled current source to model saturation and loss respectively. In [80] a domain is created where voltage represents flux and current represents magneto-motive force (MMF). The eddy current loss is then implemented as a capacitor in parallel with the saturating elements. This is equivalent to a parallel resistor in the electric domain. Another unique way of implementing the parallel resistor is to add a single resistor connected to a fictitious winding around the core [86]. Reference [82] uses a NAND-gate-based nonlinear inductor and the eddy currents are simply captured as a parallel R as in Fig. 3.2. Although more empirical than physical, this resistor can also be used to model all types of core loss using the Steinmetz equation [100,101]. If the drop in MMF/current through the nonlinear inductor is ignored, one can just take the derivative of the flux squared to find the eddy current loss as in the Simulink® model of [102].

For some off-chip inductors, the approximation of 1st order eddy-currents being proportional to frequency squared may be valid. However, as frequency increases and core dimensions become a considerable number of skin-depths, this approximation becomes invalid. All of the inductor models in the previous paragraph were

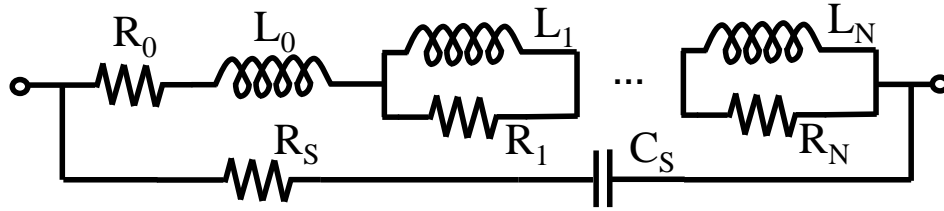


Figure 3.3: Example of a linear frequency-dependent microinductor model.

developed for off-chip inductors, except [99]. Although we have developed a model for high-frequency eddy currents in Section 2.2.4, it may not be immediately clear how to properly extend the network of Fig. 3.2 to higher orders.

3.2.4 Linear Frequency-Dependent Model

Inductors without magnetic cores have no need for nonlinear elements, and the most popular model for such inductors is a linear frequency-dependent model, like that shown in Fig. 3.3. These models capture eddy currents and capacitive effects in linear media. They may be package level inductors, such as [103], or RF on-chip inductors, such as [93, 104]. It should be noted that Fig. 3.3 is only representative, and in general two parallel two-element type networks should be able to capture the characteristics; an RC and an RL network. For example, the order of the RC network could be extended beyond one, if needed, or the RL network could be implemented as transformer loops (as in [93]), either type of Cauer network [63], or either type of Foster network [63]. The linear frequency-dependent model may also be used for inductors with magnetic materials when operated with currents far less than saturation. An off-chip example of such a linear model is [105], where

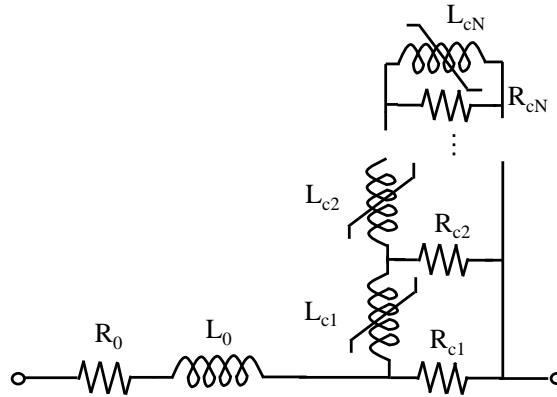


Figure 3.4: Example of a higher-order nonlinear eddy current model topology.

a behavioral frequency-dependent resistor and inductor are used rather than an RL network.

3.2.5 Higher Order Nonlinear Eddy Current Model

We mentioned previously that it may not be immediately clear how to extend the network of Fig. 3.2 to capture high-frequency eddy currents in the core. From the linear frequency-dependent model, one may think that any higher-order RL network would allow us to capture the higher-frequency eddy current effects. However, the different topologies of these networks produce different behavior when nonlinear elements are present, and only one matches the physics correctly. Early transformer models were based on the Foster topology [106] which lacks physical correlation. Fig. 3.4 shows a circuit model of an inductor able to capture high-frequency eddy currents in a nonlinear material using a physical meaningful topology. R_0 models the conductor winding resistance and L_0 models the linear

portion of inductance do to the internal inductance of the winding and the inductance external to the core. L_{cn} and R_{cn} ($n = 1, \dots, N$) are the $2N$ elements modeling the eddy currents in the core material.

We confirmed the Cauer topology of Fig. 3.4 in Section 2.2.4 using a Partial Element Equivalent Circuit (PEEC) approach. A Similar PEEC approach is used in [84, 85] for a different winding arrangement, leading to the same topology. Reference [88] uses a finite difference method to come up with the same Cauer equivalent circuit for simplified geometries. The saturation and hysteresis may be implemented with Preisach [84, 85], Jiles-Atherton [88], or simply mentioned that it is possible to include these effects [107]. Although not as physical as the approach from Section 2.2.3, references [84, 85] include anomalous losses, such as domain wall resonance due to FMR, through an adjustment to the ladder resistors.

3.2.6 Summary Table

Table 3.1 provides a quick summary of the literature review performed in this section. The features compared are considered to be the most important characteristics of the microinductor model we are trying to construct. The model presented in this chapter will cover every feature presented in Table 3.1.

Table 3.1: Feature comparisons for microinductor models from literature.

Model Section	Saturation	Linear Eddy Currents	Core Eddy Currents	Capacitive Resonance	Terminal Based	On-Chip
3.2.1	no	no	no	no	yes	yes
3.2.2	yes	no	no	no	possibly	no
3.2.3	yes	no	low-freq.	rarely	difficult	yes
3.2.4	no	yes	linear	yes	yes	yes
3.2.5	yes	no	yes	rarely	no	no

3.3 Model Development

3.3.1 Model Circuit Topology

The topology we developed for on-chip microinductors is shown in Fig. 3.5 and was initially proposed in [108] and expanded upon in [109]. One unique characteristic of this model is that it takes features from the linear frequency-dependent model and the higher-order nonlinear eddy current model. The ladder network on the left is meant to capture the skin and proximity effects in the winding conductors, as well as any other linear eddy current effects, such as in the substrate. The left ladder network has a DC resistance and high-frequency inductance (unlike the right ladder), this is to capture the DC resistance of the conductor windings and any inductance external to the conductors and core. While the left ladder is motivated by linear frequency-dependent models, the right ladder is motivated by higher order eddy current core models. The nonlinear inductors represent the saturation of the core material as the current in the winding increases (see Section 2.2.4). The right ladder only models eddy current effects which have zero DC

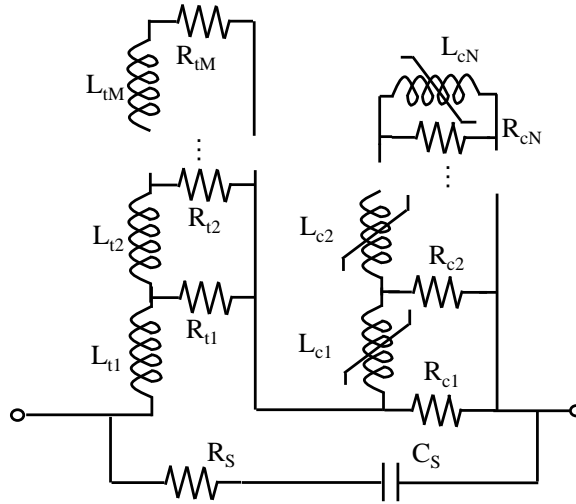


Figure 3.5: Complete compact equivalent circuit model used for microinductors, with an M th order linear ladder network, an N th order saturating core ladder network, and parallel RC branch.

resistance, due to the lack of a DC conduction path to the core, and zero high-frequency inductance, due to the high-frequency eddy currents blocking the flux from reaching the core. The physical effect of electric field coupling discussed in Section 2.2.5 also was discovered to be important in microinductors. Therefore, the RC network of that section and from the linear frequency-dependent model is included in our model. It should be noted that ferromagnetic resonance/relaxation effects are not included in the model, since we are focusing on Ni-Fe alloys with FMR frequencies in the GHz [67]. Fig. 3.5 is the first of its kind topology and is suitable for many microinductor configurations (see Sections 1.2.1 and 3.5).

3.3.2 Nonlinear Inductors

As mentioned in Section 2.2.1, the saturation effect of the nonlinear inductors of Fig. 3.5 can be implemented in either the electric domain as a small-signal characteristic or the magnetic domain as a flux-MMF relationship. Since the most useful and general expression for the nonlinear inductance was found in the electric domain and it cannot be analytically converted to a flux-MMF relationship for the magnetic domain, we chose to implement the core inductors $L_{cn}(I)$ in the electric domain as small-signal inductances. Saturation of the core is often counteracted (whether intentionally or unintentionally) through the addition of an air gap in the core or shape factor effects [8].

To keep the model physical, general, and realizable, five properties of the $L_{cn}(I)$ function are required: it should be

- 1:** an even function of current;
- 2:** monotonically decreasing for increasing $|I|$;
- 3:** guaranteed positive for all currents;
- 4:** implementable in circuit simulators;
- 5:** sufficiently general to model gaps/demagnetization and typical anhysteretic B-H curves.

The first three properties are based on physical considerations, while the last two give the function the necessary generality and ability to be implemented. The function we develop to meet these specifications is based on generalizing a bandpass filter characteristic. Starting with the natural logarithm of the magnitude of the

transfer function of a 2-pole bandpass filter we have

$$A_{filt,n}(\omega) = \ln \left| \frac{Kj\omega}{\left(1 + \frac{j\omega}{p_1}\right)\left(1 + \frac{j\omega}{p_2}\right)} \right|. \quad (3.1)$$

Specifying the poles and frequency on a linear current scale while frequency is logarithmically scaled, as in a Bode plot, we make the following substitutions:

$$\omega \mapsto e^I \quad (3.2a)$$

$$p_1 \mapsto e^{\alpha_{3n}} \quad (3.2b)$$

$$P_2 \mapsto e^{-\alpha_{3n}}. \quad (3.2c)$$

Making the substitutions and taking the magnitude of the complex terms gives

$$A_{filt,n}(I) = \ln \left(\frac{Ke^I}{\sqrt{1 + e^{2(I-\alpha_{3n})}}\sqrt{1 + e^{2(I+\alpha_{3n})}}} \right). \quad (3.3)$$

Using the laws of logarithms, (3.3) can be rewritten as

$$\begin{aligned} A_{filt,n}(I) = \ln(K) + I - \frac{1}{2} \ln \left(1 + e^{2(I-\alpha_{3n})} \right) \dots \\ - \frac{1}{2} \ln \left(1 + e^{2(I+\alpha_{3n})} \right). \end{aligned} \quad (3.4)$$

It is a simple matter of scaling the abscissa and ordinate axes to obtain the generalized form

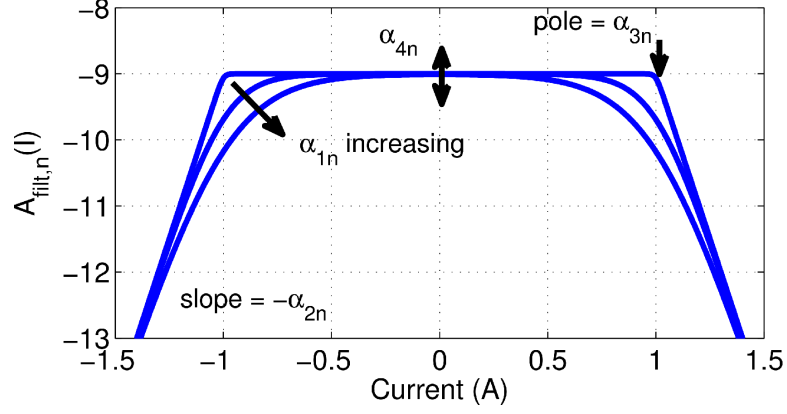


Figure 3.6: Plot of (3.5) versus current showing effects of α_{in} parameters.

$$\begin{aligned}
 A_{filt,n}(I) = & \alpha_{4n} - \alpha_{2n}I - \alpha_{1n} \ln \left(e^{-\frac{\alpha_{2n}}{\alpha_{1n}}(I+\alpha_{3n})} + 1 \right) + \dots \\
 & - \alpha_{1n} \ln \left(e^{-\frac{\alpha_{2n}}{\alpha_{1n}}(I-\alpha_{3n})} + 1 \right).
 \end{aligned} \tag{3.5}$$

The α_{in} terms are parameters of the nonlinear inductance. Fig. 3.6 shows the role of each of the α -parameters in creating (3.5). We obtain the final expression for the nonlinear inductance by taking the exponential of $A_{filt,n}$ and adding the saturated inductance, L_{0n} , as

$$L_{cn}(I) = e^{A_{filt,n}(I)} + L_{0n}. \tag{3.6}$$

There are five parameters ($\alpha_{1n}, \dots, \alpha_{4n}, L_{0n}$) in (3.6). Notice that for real parameters and positive L_{0n} , (3.6) is always positive, guaranteeing passivity (see Appendix C). A sample LTspice subcircuit for this type of nonlinear inductor is shown in Fig. 3.7. For this implementation care should be taken for large arguments to

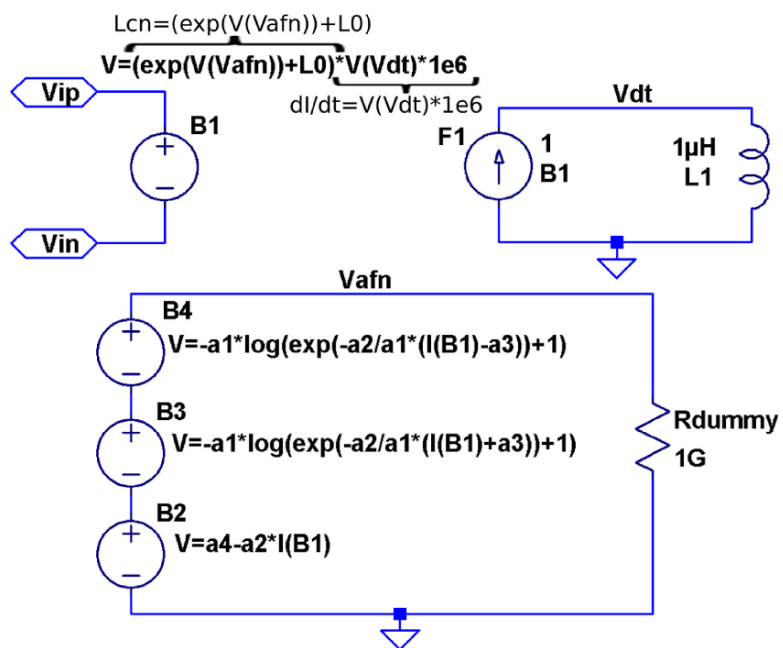


Figure 3.7: Example LTspice subcircuit of a nonlinear inductor described by (3.6). Inductor terminals are Vip and Vin.

Table 3.2: Coefficients of $M(H)$ functions (3.7a),(3.7b), and (3.7c).

$M_{S1} = 9.08 \times 10^5$ A/m	$g_1 = 3.16 \times 10^{-4}$ m/A	
$M_{S2} = 9.15 \times 10^5$ A/m	$g_2 = 2.62 \times 10^{-4}$ m/A	
$M_{S3} = 9.83 \times 10^5$ A/m	$\alpha = 3.82 \times 10^{-10}$	$a = 975$ A/m

the exponential (for example, e^{89} is beyond the bounds of single precision floating point numbers). If large arguments occur, the limit of $\ln(e^x + 1)$ can be taken as x .

We constructed (3.6) to meet properties 1-4. To confirm whether property 5 is met we consider three types of M-H curves and four different gap values. We assume an anhysteretic M-H characteristics since the materials of interest (e.g., Ni-Fe [16, 64], Co-Ni-Fe [16, 65], Co-Ta-Zr [66]) typically have small coercivities. The three M-H curves considered are: hyperbolic tangent [72], error function [72], and Langevin [75]. Their expressions are

$$M(H) = M_{S1} \tanh(g_1 H) \quad (3.7a)$$

$$M(H) = M_{S2} \operatorname{erf}(g_2 H) \quad (3.7b)$$

$$M(H) = M_{S3} \left(\coth\left(\frac{H + \alpha M}{a}\right) - \frac{a}{H + \alpha M} \right). \quad (3.7c)$$

Recall that $B(H) = \mu_0(H + M)$. The coefficients of M-H functions (3.7a),(3.7b), and (3.7c) are given in Table 3.2 with SI derived units of Tesla and A/m, as appropriate.

A zero-current-bias small-signal inductance of about 100 nH is obtained for

a one-turn microinductor using a 0.125 mm^2 magnetic flux area and a $424 \text{ }\mu\text{m}$ magnetic path length ($\mu_{r0} \approx 270$). The gap is modeled as a linear lumped reluctance appearing in series with the core reluctance. Its four values, given as permeances ($\mathcal{P} = 1/\mathcal{R}$), are $\infty \text{ H}$, 300 nH , 100 nH , and 33.3 nH , respectively. Using a global optimization algorithm to determine the five parameters of (3.6), we obtained L2-norm errors of less than 2.5%. The L2-norm error is given as

$$100\% \cdot \|\tilde{y}_k - y_k\|_2 / \|y_k\|_2, \quad (3.8)$$

where $\|\cdot\|_2$ is the L2-norm [110], \tilde{y}_k is the fitted or approximated value, and y_k is the measured or ideal value, both with the same x-value, x_k . The excellent performance of (3.6) can also be seen in Fig. 3.8. Overall, the circuit of Fig. 3.5 consists of a combination of lumped linear elements and lumped nonlinear inductors described by (3.6). The model can, thus, be readily implemented in many popular circuit simulators.

3.3.3 Measurements Employed to Generate Model

Although, in general, the complete characterization of an unspecified nonlinear dynamical circuit requires knowledge of the entire phase space, we have found it sufficient to only measure the small-signal biased impedance to generate the specific microinductor model in Fig. 3.5. Only the core model changes with respect to the bias current, and at each bias current the small-signal model of the core is an observable linear system. Therefore, the information needed to obtain the small-

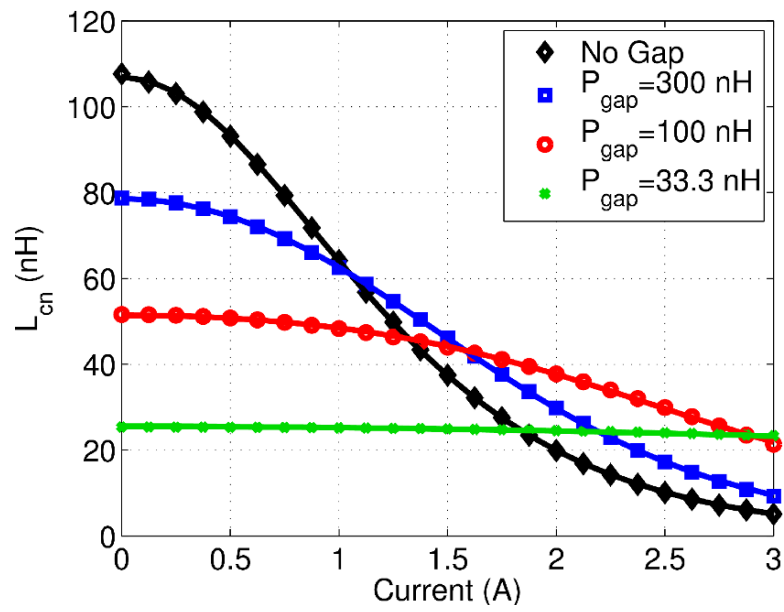


Figure 3.8: Small-signal inductance of a tanh-based microinductor using (3.7a) with 4 different gap inductances (data points) showing the fitting performance of (3.6) (solid lines).

signal impedance L_{cn} at current I_j is available in the small-signal impedance of the entire circuit, biased to current I_j .

Suppose the microinductor is biased at J unique currents ($I_1, \dots, I_j, \dots, I_J$) and the small-signal impedance is measured at K unique frequencies ($f_1, \dots, f_k, \dots, f_K$) for each of the J bias currents. These measurements are obtained either from impedance analyzer measurements on a physical device, or from field-solver simulations, depending on the design flow used. The small-signal impedance measurements could be organized into a $J \times K$ complex-valued matrix

$$Z_m(I_j, f_k) = \begin{bmatrix} Z_m(I_1, f_1) & \cdots & Z_m(I_1, f_K) \\ \vdots & \ddots & \vdots \\ Z_m(I_J, f_1) & \cdots & Z_m(I_J, f_K) \end{bmatrix}. \quad (3.9)$$

$Z_m(I_j, f_k)$ is the small-signal impedance. Referring to Fig. 3.5, we observe that a DC bias current through the microinductor model biases all the nonlinear core inductors, L_{cn} ($n = 1, \dots, N$), at the same bias current. Therefore, the unknown inductance functions L_{cn} can be sampled at bias I_j by finding the set of L_{cn} 's that best fit the impedance of the j^{th} row. We label this best fitting L_{cn} by $L_{cn,opt}$.

A sample graph of the small-signal inductance and resistance of a measured microinductor with Ni-Fe core is provided in Fig. 3.9. Notice how the bias current causes the core to saturate, lowering the inductance. This also lowers the flux-density in the core material and, thus, reduces the eddy current loss in the core, lowering the series resistance. Also, we can observe a self-resonance effect at ~ 60 MHz (under zero-bias conditions) believed to be caused by electric-field effects.

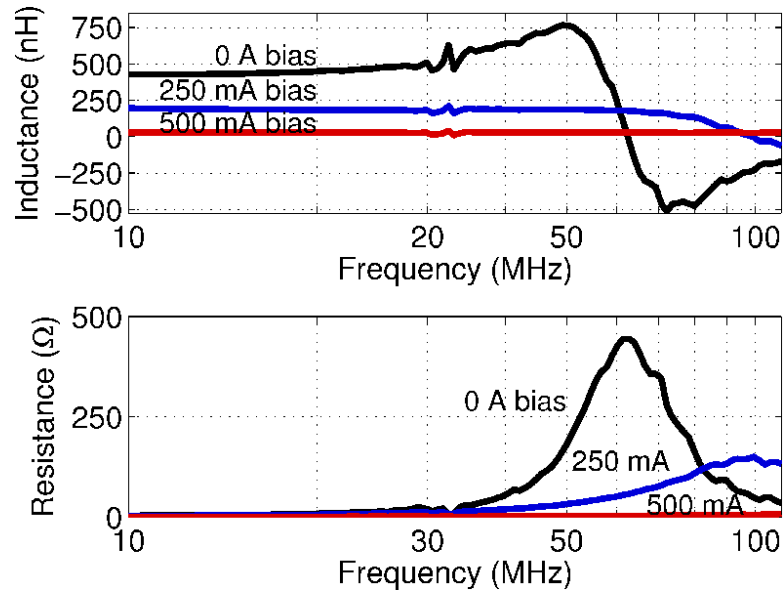


Figure 3.9: Small-signal inductance and resistance versus bias current and frequency.

3.3.4 Measurements Employed to Validate Model

To validate the model we should consider the appropriate application domain. Since PwrSoCs are the dominant application of microinductors in literature [14, 15, 21, 96, 97], we will validate our model in a PwrSoC application. Due to many ICs powering off of a reduced supply voltage, the most common type of PwrSoC is the buck converter, which is a DC-to-DC converter that steps-down the supply voltage, hopefully with higher efficiency than linear regulators.

One of the key metrics in buck converter design is delivering a large amount of power in a limited space [111]. This often means operating the microinductor near saturation, in order to boost the current that can be supplied. In light of this, we need to be able to measure key characteristics, such as the current waveform

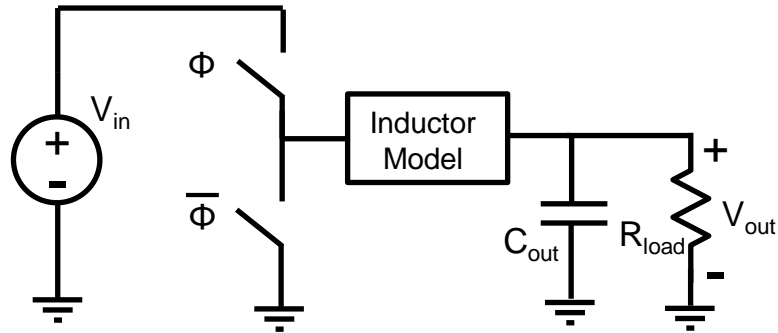


Figure 3.10: Simplified buck converter circuit used to validate the generated models. The signal Φ controlling the switches is a pulsed rectangular wave of given duty cycle.

and power loss, when operating the device in a converter as the core material saturates. Thus the two measurements we have chosen to validate the microinductor equivalent circuit model are the current waveform and the instantaneous power loss waveform in a simplified buck converter application (see Fig. 3.10).

3.3.5 Novelty of This Model

There are many features of our model, which are lacking in existing literature. The most significant of which is the ability to incorporate the core material properties without knowing them explicitly, this is not common in literature. For example, the methods described in Section 3.2.5 are created for simplified geometries or analytical solutions. The methods for off-chip inductors often suppose you have a good technique to characterize the saturation characteristics of the magnetic material, such as a cylindrical toroid. However, on-chip microinductor materials like Ni-Fe are often anisotropic [97] and contain a soft and hard axis, or vary due to

substrate surface or demagnetization [11], making toroidal analysis inappropriate. Also, in on-chip designs, the need to make multiple integrated structures (such as a separate toroid) to generate one device model can be costly. Our model and algorithm provide a way to generate a single physically-motivated equivalent-circuit device model, accurately and simply from only the terminal characteristics. Unlike off-chip inductors, we developed a simple and accurate extraction algorithm that fits terminal measurements made with an impedance analyzer or vector network analyzer (VNA) to the compact physically-motivated equivalent circuit of Fig. 3.5. The models are accurate in both the fitted and verification domains, and the algorithm guarantees passivity of the model.

The closest model to ours is the one presented in [99], which is a first order eddy current model for on-chip microinductors. In contrast, our model additionally includes electric field-effects, high-frequency core eddy-currents and linear eddy currents, which can make a significant difference in the performance of the model topologies as we will demonstrate. Specifically, there is an ability of our model to accurately capture the instantaneous power loss, and the current waveforms. Also, in [99] there is no discussion of what extraction algorithm or measurements would suitably generate their model. In what follows we have created our own extraction algorithm for the model of [99], but use their nonlinear inductor expression and circuit topology.

3.4 Model Extraction Algorithm

3.4.1 Overview

The model extraction algorithm is broken up into three main stages as shown in Fig. 3.11. First, the model is simultaneously fit to the unsaturated ($j = 1$), fully saturated ($j = J$) and moderately saturated ($j = J_{mid}$) measured impedances versus frequency ($k = 1, \dots, K$). Next, for the remaining bias currents, the measured impedance is fit to by selecting the core inductances, L_{cn} , for the particular bias current. We label this best fitting L_{cn} by $L_{cn,opt}$ ($n = 1, \dots, N$). This provides the core small-signal inductances sampled at the J bias currents of the measurement. The final stage is to fit (3.6) to $L_{cn,opt}$.

3.4.2 Stage 1: Three-Bias Fitting

This first stage is arguably the most important; it is also the most challenging due to the large number of fitting parameters. First, the model's fit is optimized to the measured impedance data versus frequency at each of the three bias currents. Only the magnetic part of the core saturates, thus only L_{cn} varies between the three circuits.

The cost function used here is the RMS combination of percentage L2-norm errors, see (3.8), of the resistance and inductance at each of the three bias currents.

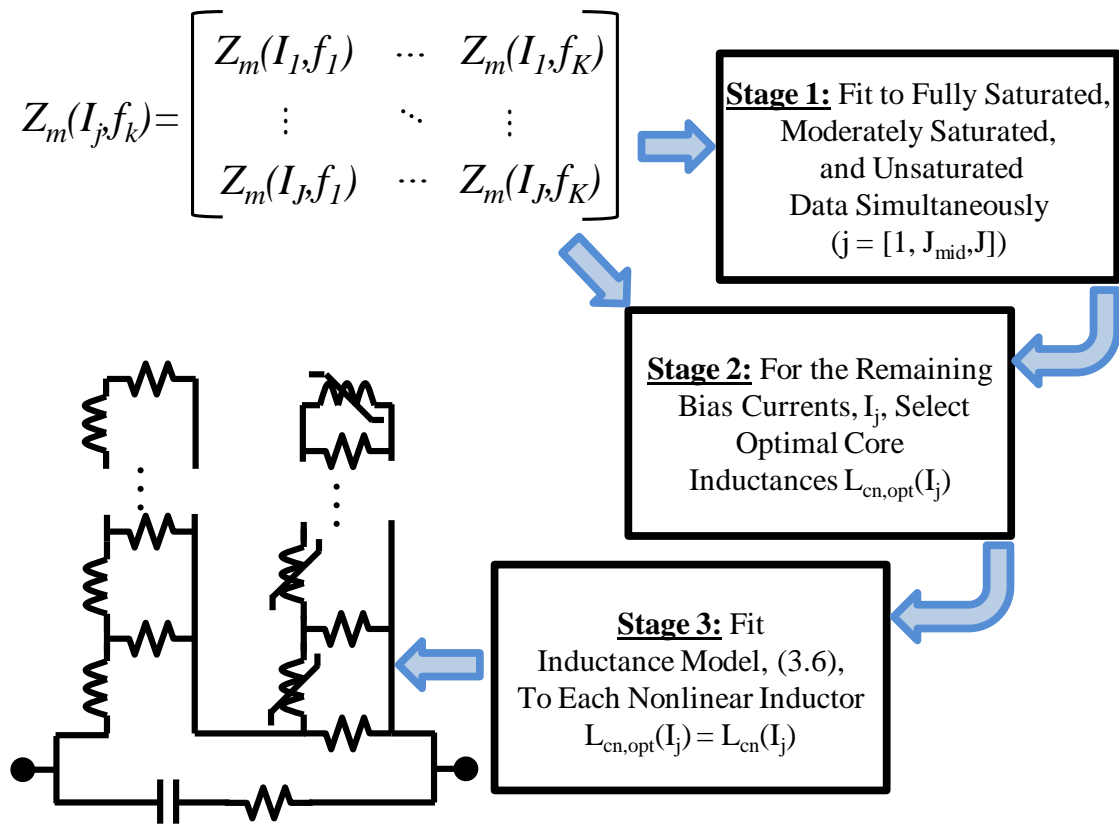


Figure 3.11: Flow chart of algorithm going from input measurements to output model with three intermediate stages.

$$f_{cost,1} = \left[\frac{1}{6} \left(E_{R,1}^2 + E_{L,1}^2 + E_{R,J_{mid}}^2 + E_{L,J_{mid}}^2 + \dots \right. \right. \\ \left. \left. E_{R,J}^2 + E_{L,J}^2 \right) \right]^{\frac{1}{2}}. \quad (3.10)$$

In (3.10), $E_{R,j}$ is the percentage L2-norm error of the model resistance versus frequency to measurements and $E_{L,j}$ is the percentage L2-norm error of the inductance versus frequency, both at bias current I_j . We can also make use of weighting various errors to emphasize certain biases, or frequencies. In total, there are $4N + 2M + 2$ parameters to the optimization: N from the linear core resistors, $3N$ from each $L_{cn,opt}(I_j)$ at each of the three bias currents (together making $4N$), $2M$ from the linear ladder resistors and inductors, and 2 from R_S and C_S (see Fig. 3.5). To limit the effective number of parameters, four constraints are applied. The first two constraints are that the DC resistance and DC zero-bias inductance of the model match the measurements at the lowest frequency. The other two constraints are that R_S and C_S guarantee a match to the zero-bias high-frequency resistance and inductance, while keeping R_S and C_S positive.

Due to the large number of parameters and fast cost function analysis, the genetic algorithm [112] can be used to solve this global optimization problem. 30 generations of population 500 were sufficient to find a good fit. To further improve the fit we used a local optimizer [113] with bounds enforcing passivity. At the end of stage 1, the optimized parameters provide every linear element and the optimized nonlinear inductance elements of the microinductor model at the three bias currents.

3.4.3 Stage 2: Fit to Remaining Biases

The next part of the algorithm is to fit to the inductance and resistance at the remaining bias currents, I_j ($j = 2, \dots, J_{mid} - 1, J_{mid} + 1, \dots, J - 1$). Since there are few (N) cost function parameters several different global optimization routines can be used to produce the values of $L_{cns}(I_j)$ that minimize the percentage error. The below pseudo code determines these optimal inductances.

```

input : Fitted linear elements, optimized nonlinear inductors at 3 biases,
          and small-signal measurements  $Z_m(I_j, f_k)$ .
output: Optimized nonlinear inductors at remaining biases.
for  $j \leftarrow 2$  to  $J - 1$  |  $j \neq J_{mid}$  do
  | optimize circuit to fit to  $Z_m(I_j, f)$  with global optimizer;
  | minimize  $f_{cost,2} = \sqrt{\frac{E_{R,j}^2 + E_{L,j}^2}{2}}$  by varying  $L_{c1,opt}(I_j), \dots, L_{cN,opt}(I_j)$ 
end

```

After stages 1 and 2 all the linear elements and the nonlinear inductors are determined at the J bias currents, $L_{cn,opt}(I_j)$.

3.4.4 Stage 3: Fit Nonlinear Inductors

Optimally selecting the nonlinear inductors at the J bias currents can be viewed as a sampling of their saturation behavior. For each nonlinear inductor element, the five parameters of (3.6) are selected to fit to the “sampled” optimized inductance versus bias current, $L_{cn,opt}(I)$, using a global optimization algorithm. The cost function to be minimized is the L2-norm error between these optimized inductances

from stages 1 and 2, and (3.6), given as

$$f_{cost,3} = 100\% \cdot \|L_{cn}(I_j) - L_{cn,opt}(I_j)\|_2 / \|L_{cn,opt}(I_j)\|_2. \quad (3.11)$$

The below pseudo code determines the five parameters of (3.6) for each of the N core inductors.

```

input :  $N$  Optimized nonlinear inductances at  $J$  measured currents,
           $L_{cn,opt}(I_j)$ .
output: Parameters for each nonlinear inductor.
for  $n \leftarrow 1$  to  $N$  do
  | optimize (3.6) to fit to  $L_{cn,opt}(I)$  with global optimizer;
  | minimize  $f_{cost,3}$  by varying  $\alpha_{1n}, \alpha_{2n}, \alpha_{3n}, \alpha_{4n}, L_{0n}$ 
end

```

3.5 Validation

In this section, we will be generating microinductor models from biased small-signal impedance measurements, and then validating the models by comparing them in the time domain using the idealized buck converter circuit discussed in Section 3.3.4 and illustrated in Fig. 3.10. For the buck converter circuit we expect our model to outperform existing simple models in terms of both AC power loss and accurately capturing the microinductor current waveforms. To make this comparison in the simulation examples, we use the device-circuit cosimulation feature available in transient field solvers. We employ the greatly simplified circuit of Fig. 3.10. The switches operate at a given frequency and duty cycle.

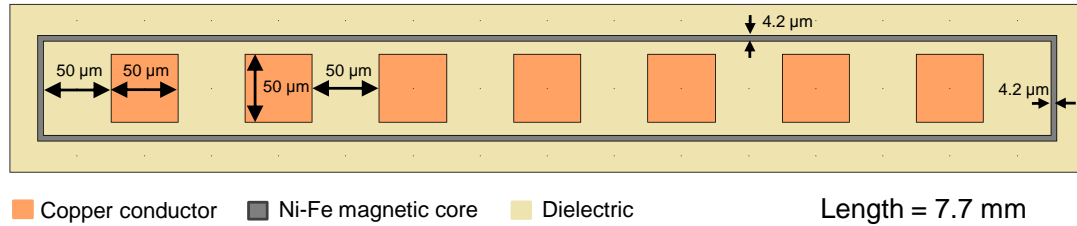


Figure 3.12: COMSOL Multiphysics layout in 2-D of racetrack microinductor from [21]. The seven conductors are connected in series.

We will be comparing the Fig. 3.5 model with two popular field solvers (COM-SOL [114] and Maxwell [115]) as well as measurements. To confirm that the model is applicable to a range of microinductor geometries, we consider three different devices: device 1 is the 2-D approximation to a racetrack microinductor, device 2 is a 3-D section of a stripline microinductor, and device 3 is a measured toroidal microinductor. We also compare our model to three other models: a linear frequency-dependent microinductor model of order four, a two-element nonlinear model consisting of a nonlinear static inductor in series with a constant resistor, and the model topology developed at Intel in [99]. The Intel topology was fit to the small-signal impedance using extraction algorithms we developed specifically for the Intel circuit topology. The linear frequency-dependent model is fit to the zero-bias impedance data, and the two element nonlinear model is fit the the low-frequency data.

3.5.1 Device 1 Simulation

The first device is a seven-turn racetrack microinductor motivated by [21]. Due to the large dimensions of this microinductor relative to skin-depth, 3-D simulation is prohibitive. However, we can approximate the racetrack by removing the bends, which are not covered by the magnetic material. Then, we essentially have a 2-D core with seven series-connected conductors representing the seven turns (See Fig. 3.12).

The microinductor's turns are made of copper and have cross-sectional size $50 \times 50 \mu\text{m}^2$ with an inter-winding separation of $50 \mu\text{m}$. The core material is assumed to have a saturation behavior of the hyperbolic tangent M-H curve of (3.7a). The core's resistivity is $45 \mu\Omega\text{cm}$ and completely surrounds the windings with a $4.2 \mu\text{m}$ thickness. The length of the microinductor is 7.7 mm . We used COMSOL Multiphysics[®] to generate the terminal characteristic and transient data.

3.5.1.1 Model Fit

Using COMSOL's multiphysics simulation we obtained the small-signal impedance at 13 bias currents from 0 to 3 A and 21 logarithmically-spaced frequencies from 100 kHz to 100 MHz. Our extraction algorithm is implemented in Matlab [116] and took less than 3 minutes to generate a complete Spectre[®] [68] model on a 3.2 GHz Pentium[®] 4 workstation. The element values returned in the fitting routine can be found in Appendix D.1. Throughout this section we use $M = 2$ and $N = 4$

for this work’s microinductor model (see Fig. 3.5).

The third stage of the algorithm is to fit (3.6) to $L_{cn,opt}$. Each of the four inductors fit within 6.5% L2-norm error. The comparison between $L_{cn,opt}$ and $L_{cn}(I)$ is shown in Fig. 3.13. The nonlinear static inductance of the Intel topology model has an L2-norm error of 7.9%. It is clear that the linear 4th order model and the nonlinear 2-element model will have substantial errors when compared to the biased small-signal impedance. The Intel topology model and this work’s model are not as clear of a case. Fig. 3.14 shows the comparison between the COMSOL field solver data, and the two fitted Spectre models: our model, and the Intel topology model. Our model captures the impedance with a 0.76% error in resistance and a 0.81% error in inductance. However, the Intel topology model makes substantial errors of 17% in resistance and 10% in inductance, due in-part to the higher order eddy current effects being present in the “measured” device.

3.5.1.2 Transient Performance

To validate the model we performed a transient simulation using the four models in Spectre and the COMSOL field-solver in a buck converter circuit. Our buck converter circuit has an input voltage of 3.6 V and an output voltage of 1.2 V giving a roughly 33% duty cycle. The switching frequency is 10 MHz and the converter has a load resistance of 1.16 Ω with 160 nF output capacitance. Fig. 3.15 shows the output voltage and microinductor current from an initially uncharged state. While the linear model has an L2-norm error of 27% in the transient current, the

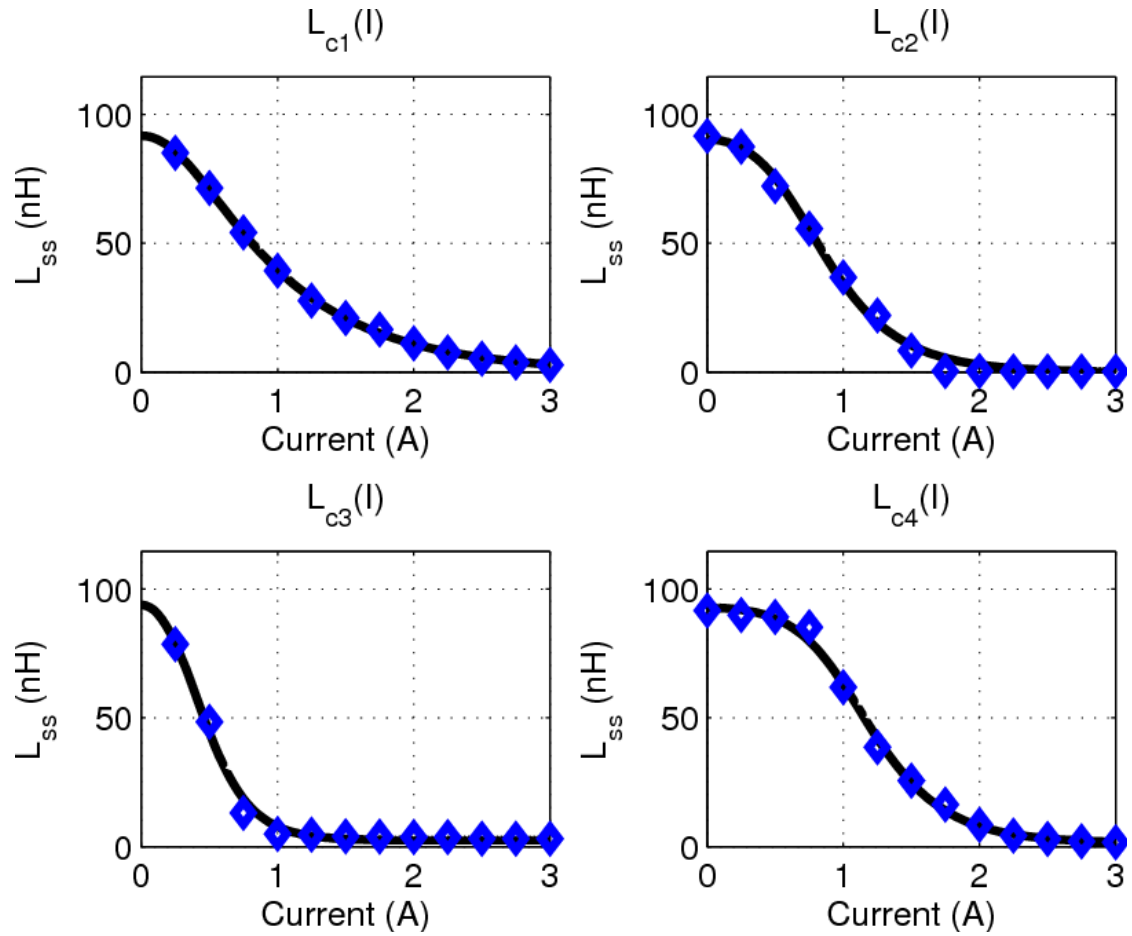


Figure 3.13: Small-signal inductance for L_{c1} through L_{c4} for the device 1 racetrack microinductor. The data points are the optimal inductances from stages 1 and 2 of the algorithm, and the curve is (3.6) fit to these points.

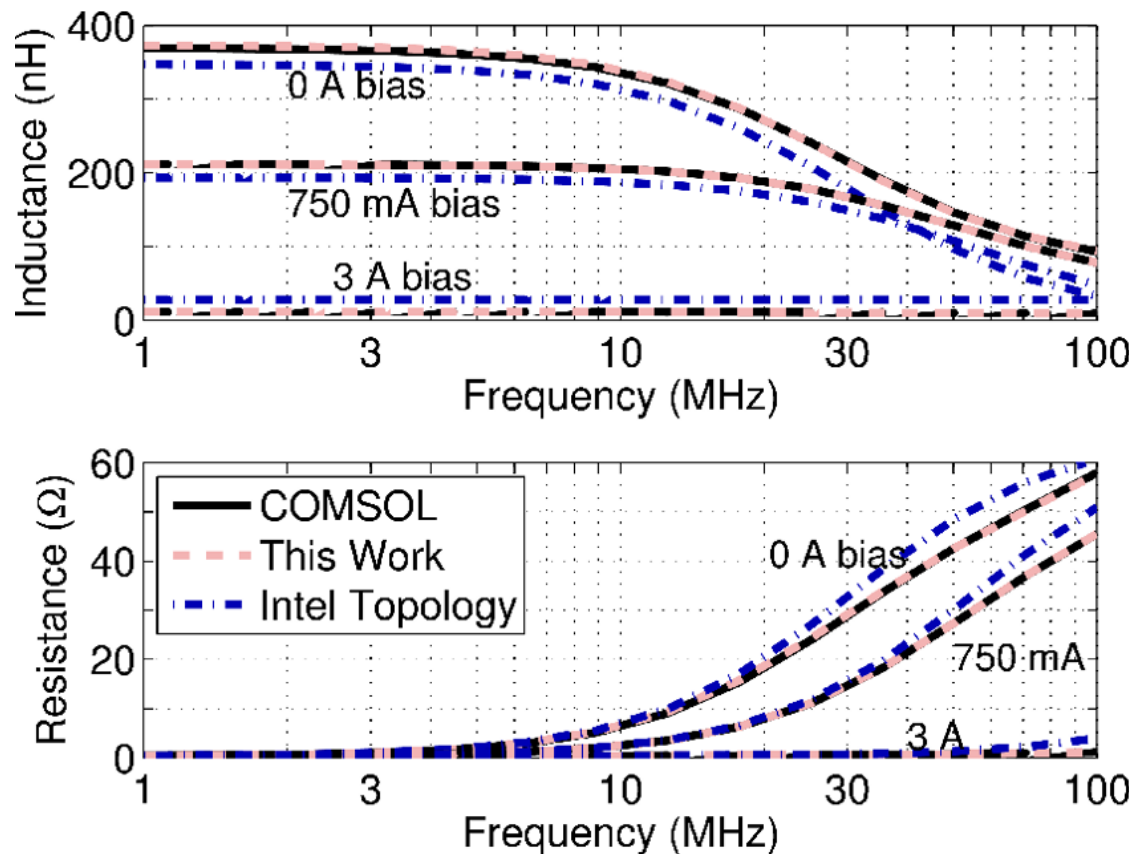


Figure 3.14: Small-signal inductance and resistance versus frequency and bias current showing comparison between fitted Spectre models and COMSOL “measurements” for device 1.

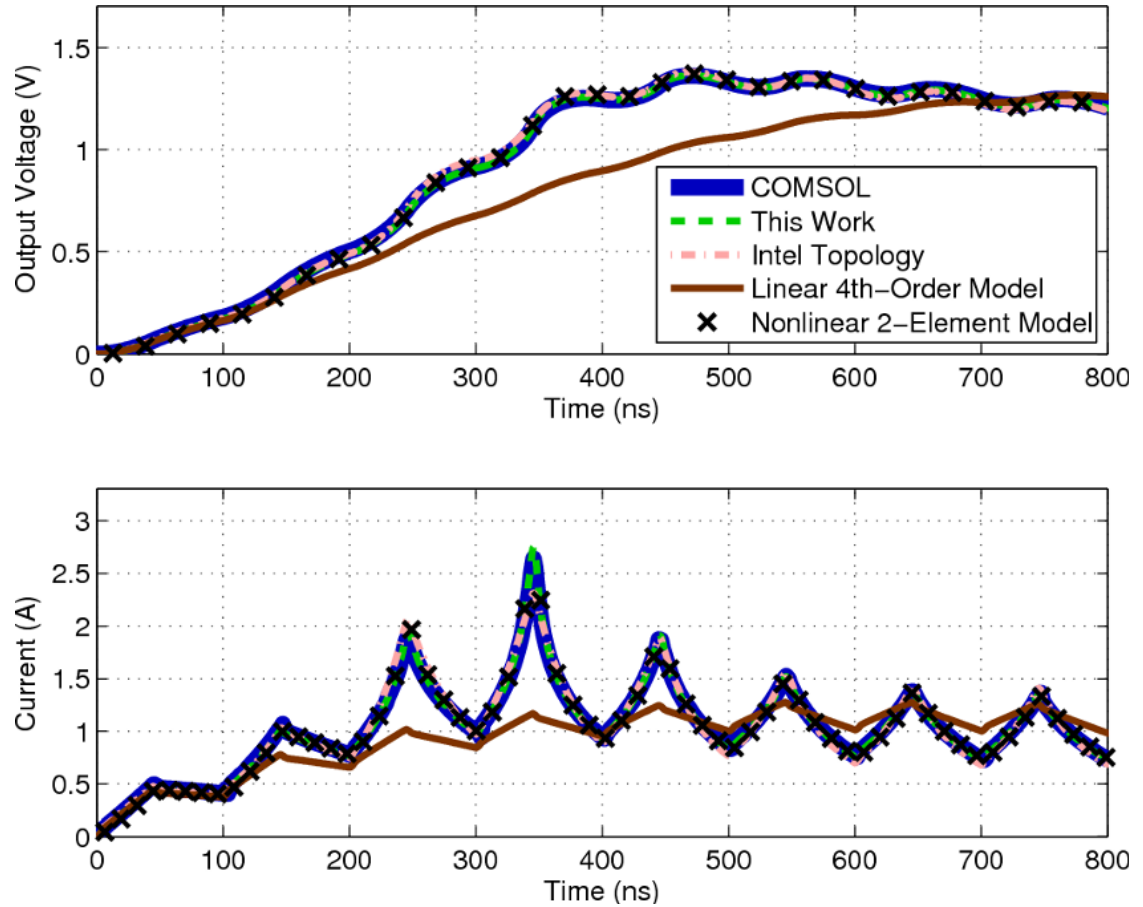


Figure 3.15: The top graph shows the rise of the output voltage to steady state, the bottom graph shows the current through the microinductor in a test buck converter. Five different models are compared for device 1.

other three models match the COMSOL simulation quite closely. The model of this thesis has the lowest L2-norm error of 2.0% in transient current. Another feature which is important to capture in a buck converter is the peak current. Similar performance characteristics are seen when comparing the peak currents (See Table 3.3).

Buck converters are used to improve efficiency over linear regulators. Therefore, the power loss of the microinductor is of particular concern in this application. Our equivalent circuit model also captures the steady-state power loss in the microinductor well. To measure the instantaneous power loss in COMSOL we integrate the instantaneous ohmic loss over the volume of the microinductor, i.e., $\int \rho |J(t)|^2 dv$. Essentially the same is done for the circuit models by adding $i(t)^2 R$ loss for each resistor. The comparison of the last two periods (an estimation of steady-state) for the power loss waveform demonstrates the good performance of the model (see Fig. 3.16). The average power loss, the power efficiency of the microinductor, and the L2-norm error in power loss waveform are shown in Table 3.3. We observe that both this work and the Intel topology model from [99] do a good job of reproducing the loss effects, making efficiency errors less than 0.4%. The other two models fail to capture the loss sufficiently. The reason the Intel topology model succeeds in estimating the power loss characteristics is that the eddy currents amount to a low percentage of the total loss which is dominated by the conductor resistance. In fact, the AC power loss for this scenario is less than 15% of the total loss. As we will see in the following section, this is not always the case and when needed, our model outperforms the others.

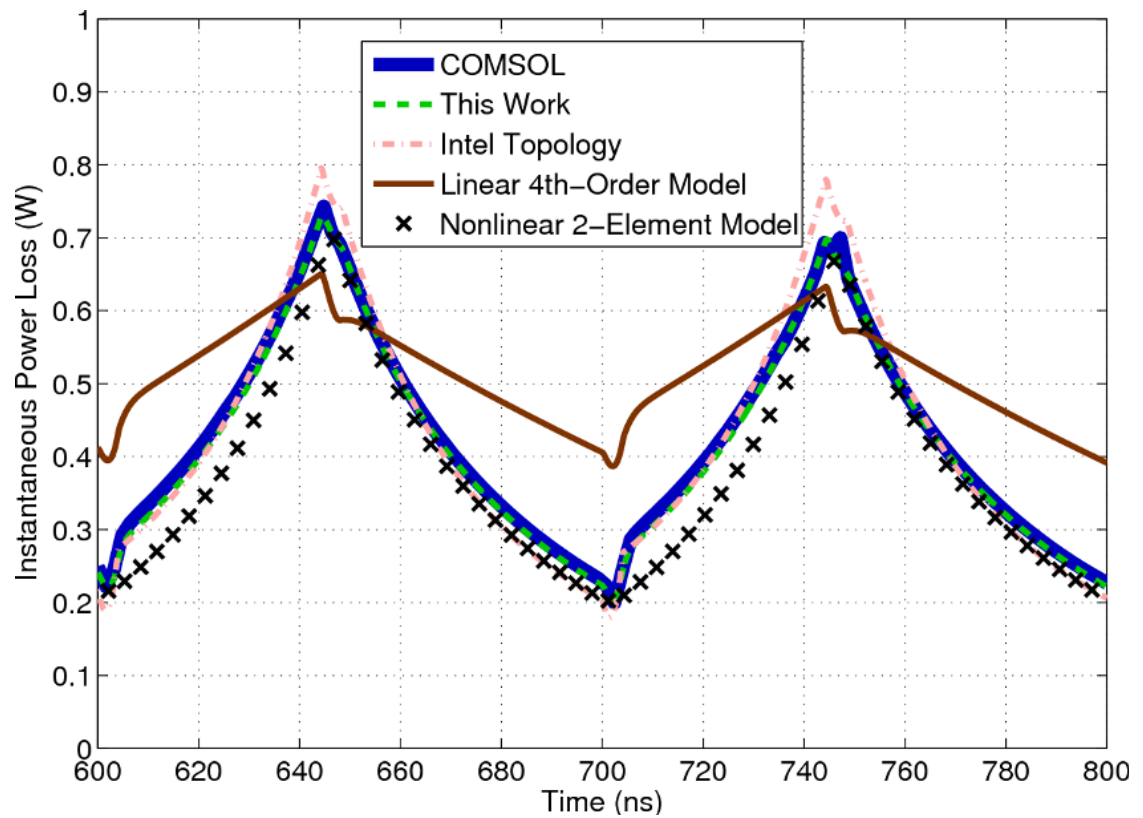


Figure 3.16: Instantaneous power loss for different microinductor models of device 1 in a test buck converter circuit during the time 600 ns to 800 ns to approximate steady-state operation.

Table 3.3: Comparison of our model with traditional off-chip inductor models and an Intel topology model. The COMSOL simulation is used as a reference to calculate errors for device 1.

	Linear 4th Order	Nonlinear 2-Element	Intel Top. Model	This Work	Comsol Ref.
$L(I, f)$ Error	N/A	N/A	10%	0.81%	0%
$R(I, f)$ Error	N/A	N/A	17%	0.76%	0%
$\max(i(t))$ Error	-52%	4.5%	5.2%	3.9%	0%
$i(t)$ Error	27%	3.7%	7.3%	2.0%	0%
$P_{loss}(t)$ Error	27%	11%	5.9%	2.1%	0%
$P_{loss,ave}$	520 mW	380 mW	420 mW	420 mW	430 mW
Efficiency	72.9%	76.5%	74.4%	75.0%	74.8%

3.5.2 Device 2 Simulation

The second device is a stripline microinductor motivated from the V-groove microinductor in [97]. It should be noted that the V-groove in [97] is only a starting point; we have altered the materials and length to be suitable for our converter. The conductor is a copper equilateral triangular bar with a $420 \mu\text{m}$ side length and 29.2 mm length. Since the problem has a large aspect ratio, we reduced the microinductor length by a factor of 91.7 to $318 \mu\text{m}$ and scaled the circuit appropriately (see Fig. 3.17). The core material has saturation behavior in the form of the hyperbolic tangent M-H curve of (3.7a). Its resistivity is $17.2 \mu\Omega\text{cm}$, and completely surrounds the conductor with a $10 \mu\text{m}$ thickness. In this case, we chose the resistivity to be consistent with a measured Ni-Fe material, rather than the material in the paper. All values shown in the following sections are scaled back up to be relevant to the designed microinductor, rather than the reduced-length

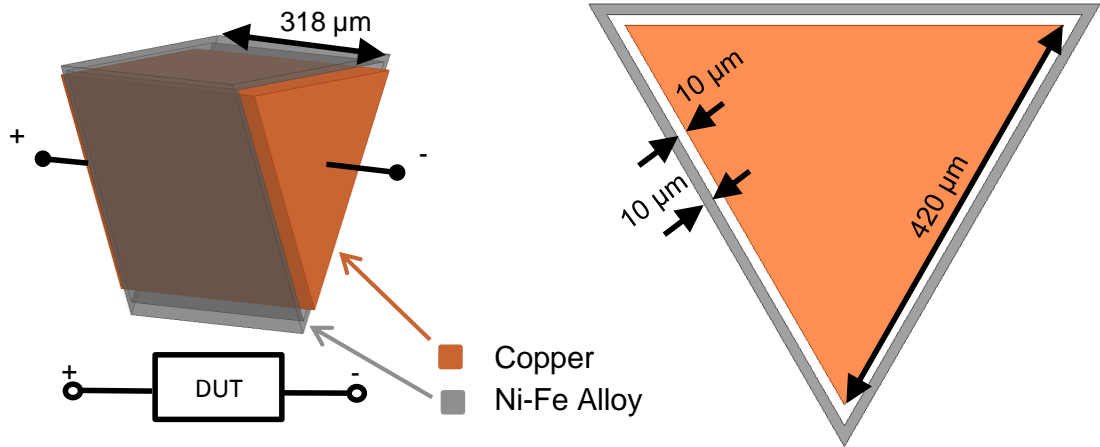


Figure 3.17: Ansys Maxwell layout in 3-D of reduced-length V-groove microinductor motivated from [97] and 2-D cross-section showing dimensions.

simulated microinductor.

3.5.2.1 Model Fit

The small signal impedance data was obtained via the Maxwell field solver [115] at 31 frequencies logarithmically spaced from 100 kHz to 100 MHz and 9 bias currents from 0 to 8 A. Since a biased small-signal analysis was not available in Maxwell, we approximated the core as saturating uniformly and simulated nine individual eddy current analyses with different permeabilities to the core. This approximation is justified by the small core thickness relative to its magnetic path length.

Our extraction algorithm took 2 minutes 40 seconds to generate the complete Spectre model from the field solver data. The element values and nonlinear inductor parameters are provided in Appendix D.1. The four static nonlinear inductances fit their optimum values with L2-norm errors less than 6.6% (See Fig.

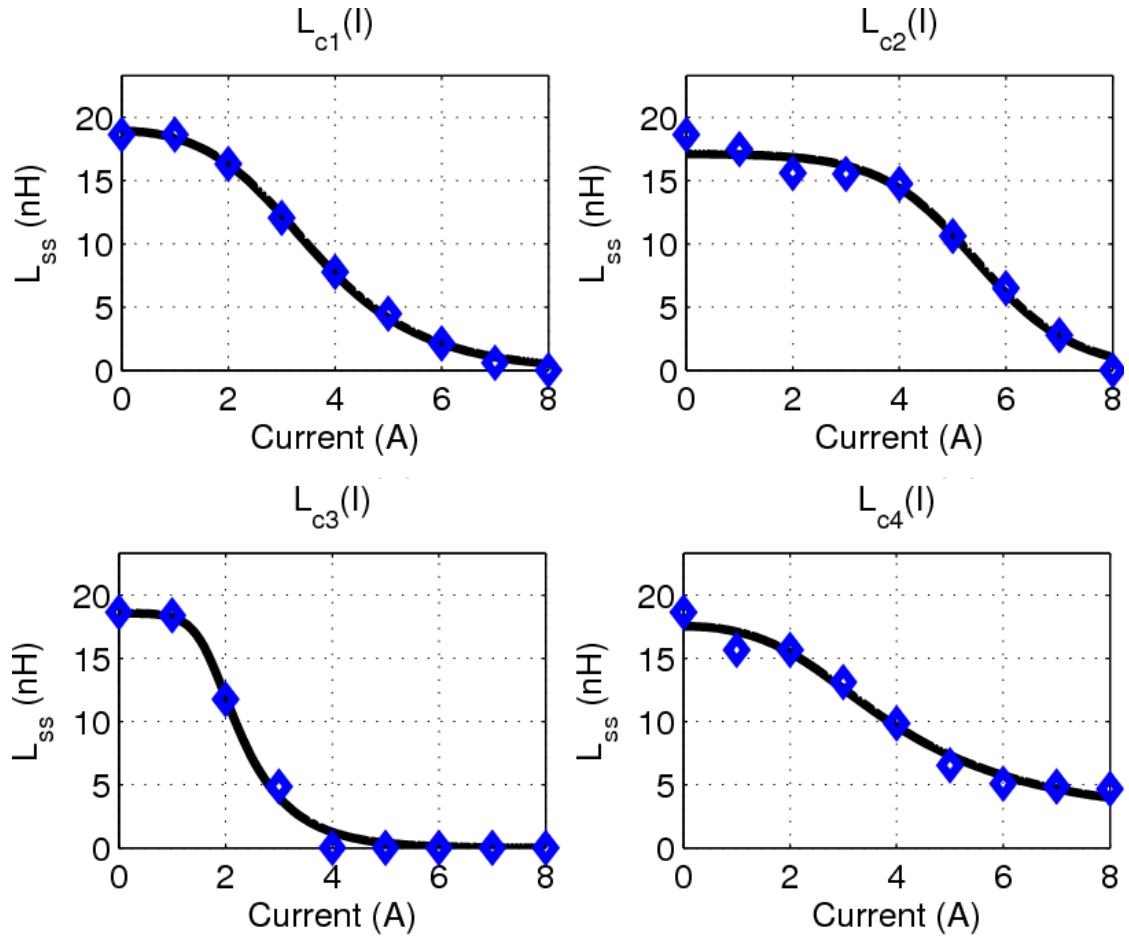


Figure 3.18: Small-signal inductance for L_{c1} through L_{c4} for the device 2 V-groove microinductor. The data points are the optimal inductances from stages 1 and 2 of the algorithm, and the curve is (3.6) fit to these points.

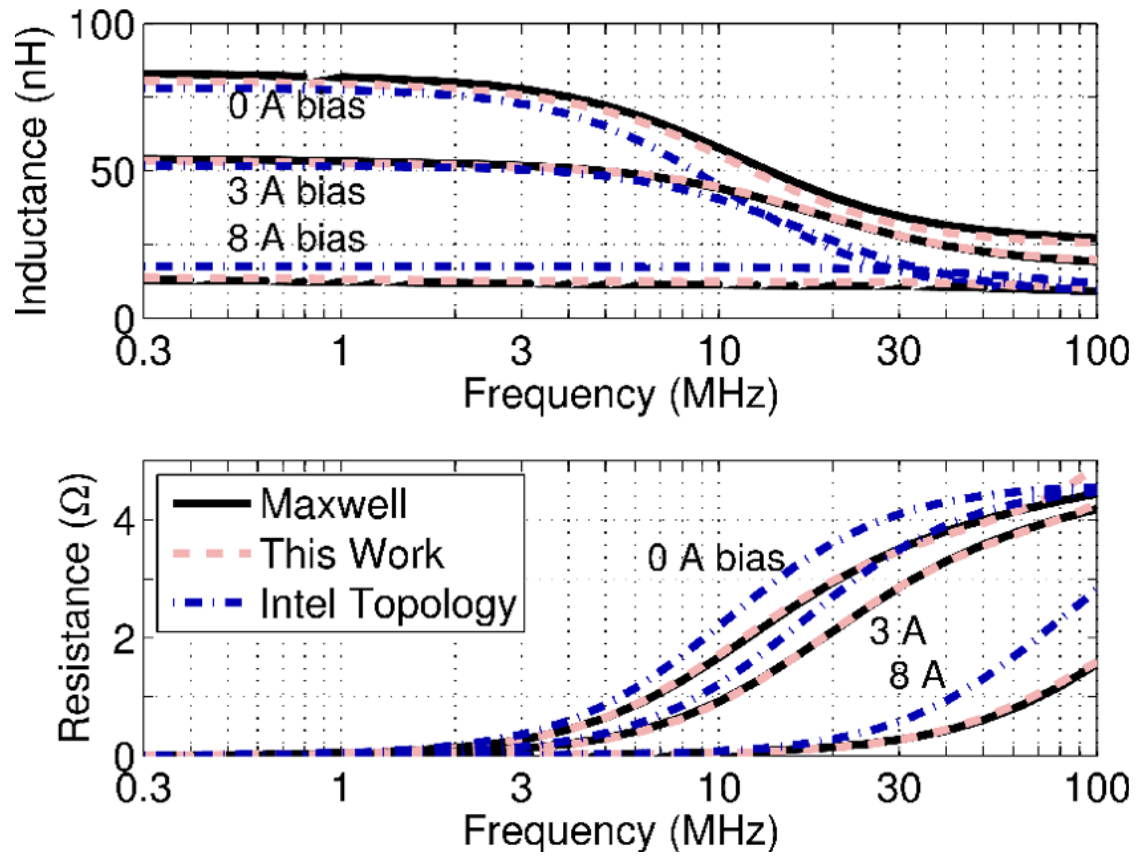


Figure 3.19: Small-signal inductance and resistance versus frequency and bias current showing comparison between fitted Spectre models and Maxwell “measurements” for device 2.

3.18). The Intel topology model had a static error of 7.0% for its single nonlinear inductor. A large difference between the Intel topology model and this work is in the small-signal impedance versus bias and frequency. In resistance, our model's L2-norm error with respect to the Maxwell simulation was 3.8%, but the Intel topology model resulted in an error of 18%. Likewise, in small-signal inductance, the L2-norm was 2.4% using our model and 14.8% using the Intel topology model (See Table 3.4). The Intel topology model errors are not due to inaccuracy of the extraction algorithm, but rather the inability to capture nonlinear high-frequency eddy currents, do to the reduced topology. The comparison of the small-signal impedance of the device 2 model to Maxwell simulations is shown in Fig. 3.19.

3.5.2.2 Transient Performance

Similar to device 1, we placed the Maxwell model and our compact model implemented in Spectre[®] [68], as well as the competing models, in a buck converter circuit. The buck converter stepped 6 V down to 3 V at 50.5 MHz. The load resistor was 1 Ω and the output capacitance was 100 nF. These values were properly scaled by 91.7 to be applied to the co-simulation of the shortened Maxwell model. The resulting start-up current and output voltage are shown in Fig. 3.20. In terms of maximum current, both the Intel topology model and this work, match Maxwell within 2.5% (See Table 3.4). Similarly, the L2-norm error in the current waveform is 2.2% for this work, and 5.5% for the Intel topology model. The linear 4th order model and nonlinear 2-element model give errors greater than 10%.

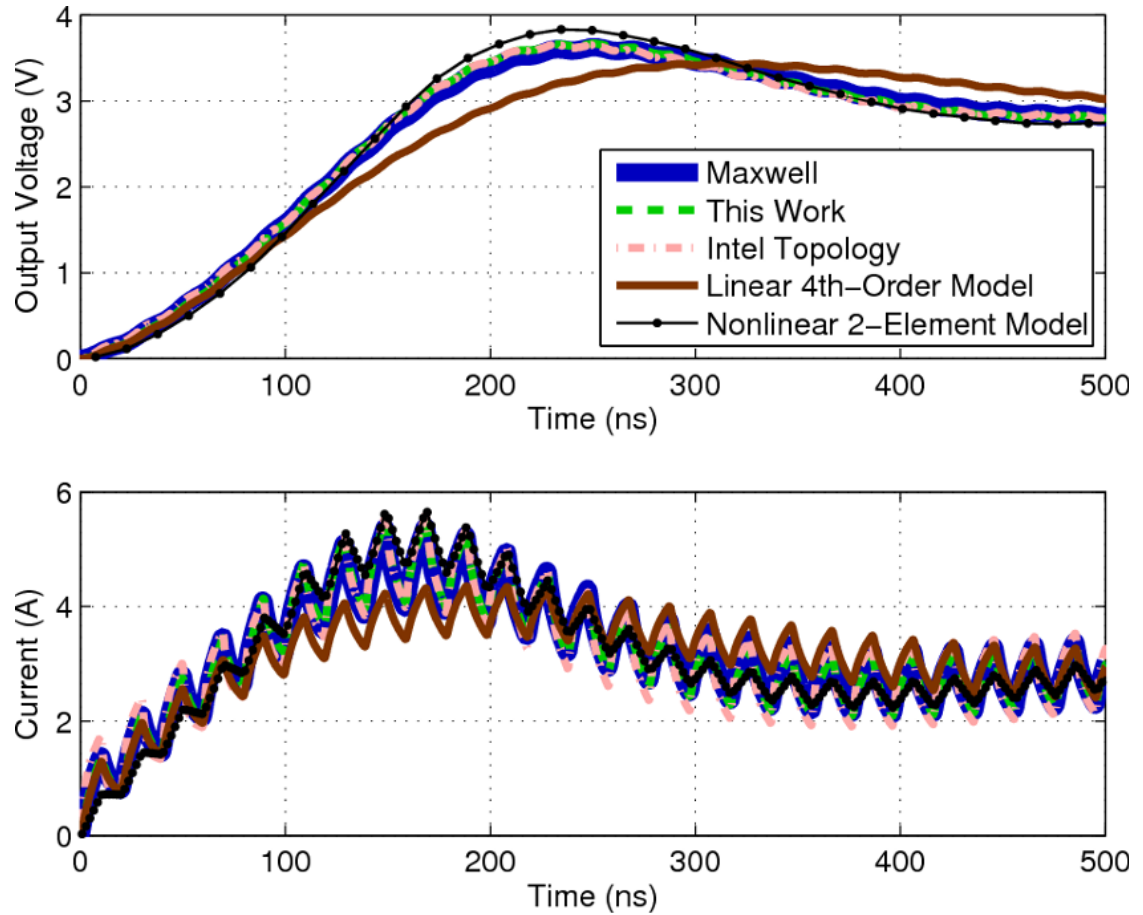


Figure 3.20: The top graph shows the rise of the output voltage to steady state, the bottom graph shows the current through the microinductor in a test buck converter circuit. Five different models are compared for device 2.

Table 3.4: Comparison of our model with traditional off-chip inductor models and an Intel topology model. The COMSOL simulation is used as a reference to calculate errors for device 2.

	Linear 4th Order	Nonlinear 2-Element	Intel Top. Model	This Work	Maxwell Ref.
$L(I, f)$ Error	N/A	N/A	15%	2.5%	0%
$R(I, f)$ Error	N/A	N/A	18%	3.8%	0%
$\max(i(t))$ Error	-19%	5.3%	2.4%	2.3%	0%
$i(t)$ Error	12%	10%	5.5%	2.2%	0%
$P_{loss}(t)$ Error	34%	88%	110%	9.3%	0%
$P_{loss,ave}$	330 mW	76 mW	1.0 W	490 mW	490 mW
Efficiency	96.2%	99.2%	89.6%	94.8%	94.9%

In buck converter applications, we are also concerned with the power loss. Since the power loss is roughly split 50/50 between AC and DC components, the eddy currents are more pronounced in this example over the previous. The only model which can predict the steady-state power loss with less than 30% error for this setup is the model presented in this thesis, which gives an error of just 1.4%. The instantaneous power-loss waveforms shown in Fig. 3.21 are indicative of this. Table 3.4 shows a numerical comparison summary including the L2-norm in the power loss waveforms. The Intel topology model over estimates the eddy current loss and thus makes an error of over 100% in power loss leading to a 5.3% lower efficiency. Only our model can capture the critical efficiency parameter to within 1%.

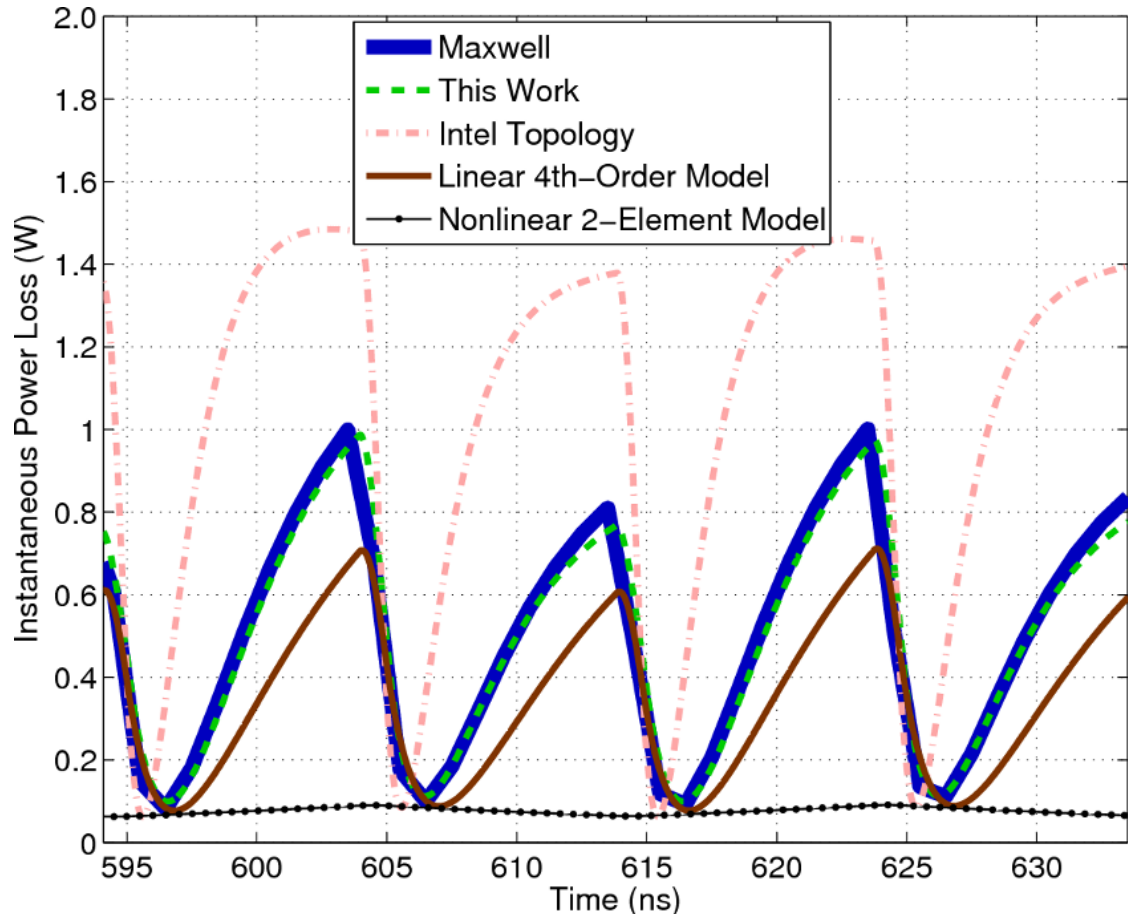


Figure 3.21: Instantaneous power loss for different microinductor models of device 2 in a test buck converter circuit during the time 594 ns to 634 ns to approximate steady-state operation.

3.5.3 Device 3 Measurements

The previous small-signal data has been obtained with magnetoquasistatic field solvers. This ignores the effect of displacement currents and the capacitive part of the model. To consider all relevant effects, we used actual device measurements to generate the model. We measured the small-signal impedance for a device made from a thin film alloy with low coercivity, and having a small saturation current, using an Agilent 4294A precision impedance analyzer. The microinductor was biased through an Agilent 16200B external DC bias adapter using a Keithley 2410 1100V source meter. Overall, we measured small-signal R and L from 2 to 110 MHz and for eight bias currents ranging from 0 to 60 mA. Since this device showed resonant behavior, the three models we previously used as comparisons to are insufficient to capture the characteristics. Instead, we compare this model only in the transient domain to a reduced 1st order linear model with a lumped inductor and resistor.

3.5.3.1 Model Fit

Our algorithm took less than 3 minutes and produced a model capturing the resonance sufficiently well. The element values and nonlinear inductor parameters can be found in Appendix D.1. Although the L2-norm errors in resistance and inductance were rather large (14% and 11% for R and L, respectively), (3.6) fitting performances for the optimized inductances were good with errors around 5%. The fit to the optimized inductances is shown in Fig. 3.5.3.1. The small-signal

impedance of the measurements compared to the fitted model is shown in Fig. 3.23.

3.5.3.2 Transient Performance

We applied an approximately 7 V, 10 MHz square-wave to this microinductor and measured the resulting current. We also compared the results to a two-element linear model generated at zero bias current and low frequencies. The transient current waveform obtained with our model had an L2-norm error of 10%, whereas the simple linear model gave a much larger L2-norm error of 60%. The maximum current comparison showed similar results with 3.6% error in our model, and 53% in maximum current in the simple linear model. These results can be seen in Fig. 3.24 and show the improved performance with the proposed model. We can also estimate the average power loss from the measurements and the models. We see that while our model underestimates the power loss of 300 mW by only 1.4%, the simple linear model gives a much larger error of 60% with a 120 mW power loss estimate.

3.5.4 Discussion of Model Order

In the previous sections we only considered our work to have a fourth order core model and a second order linear model ($N = 4$ and $M = 2$; see Fig. 3.5). Determining these values is often an exercise in trial and error. To accommodate order

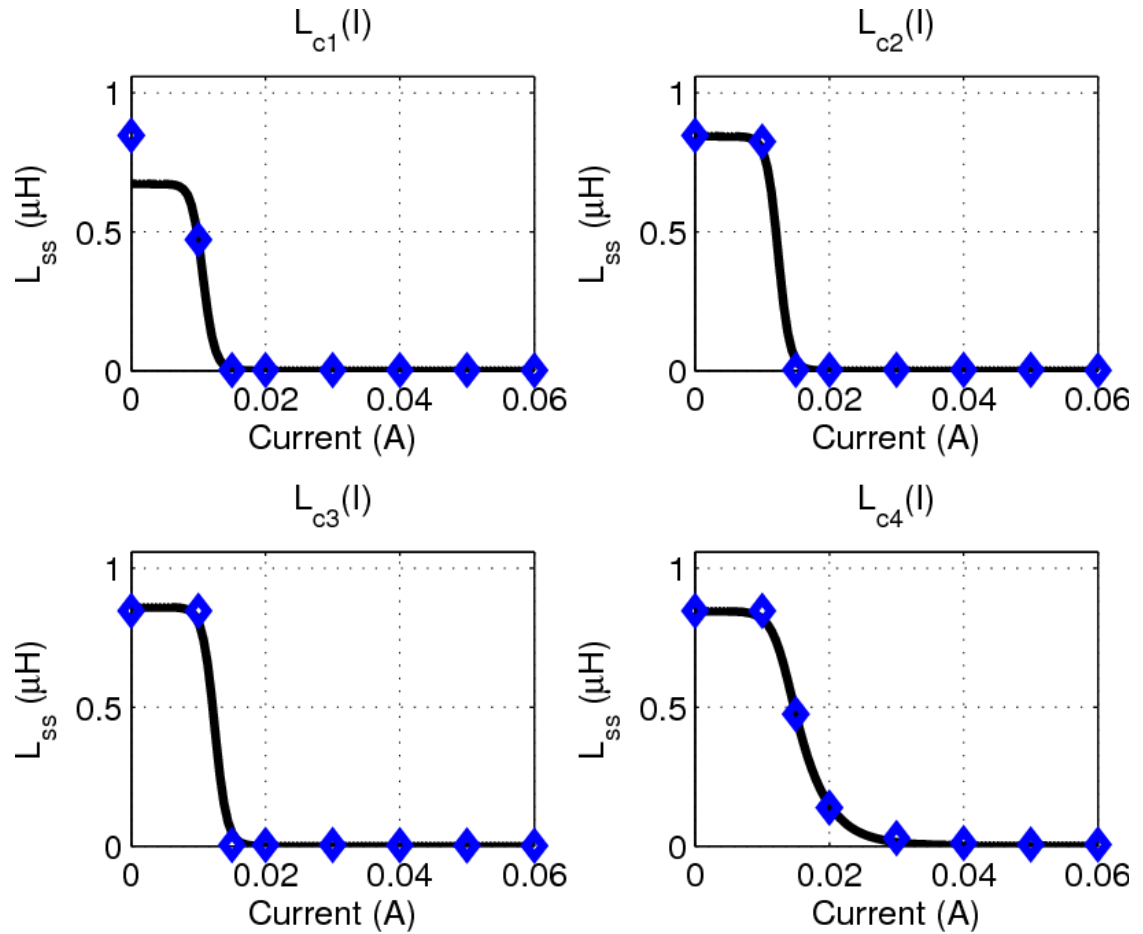


Figure 3.22: Small-signal inductance for L_{c1} through L_{c4} for the device 3 measured microinductor. The data points are the optimal inductances from stages 1 and 2 of the algorithm, and the curve is (3.6) fit to these points.

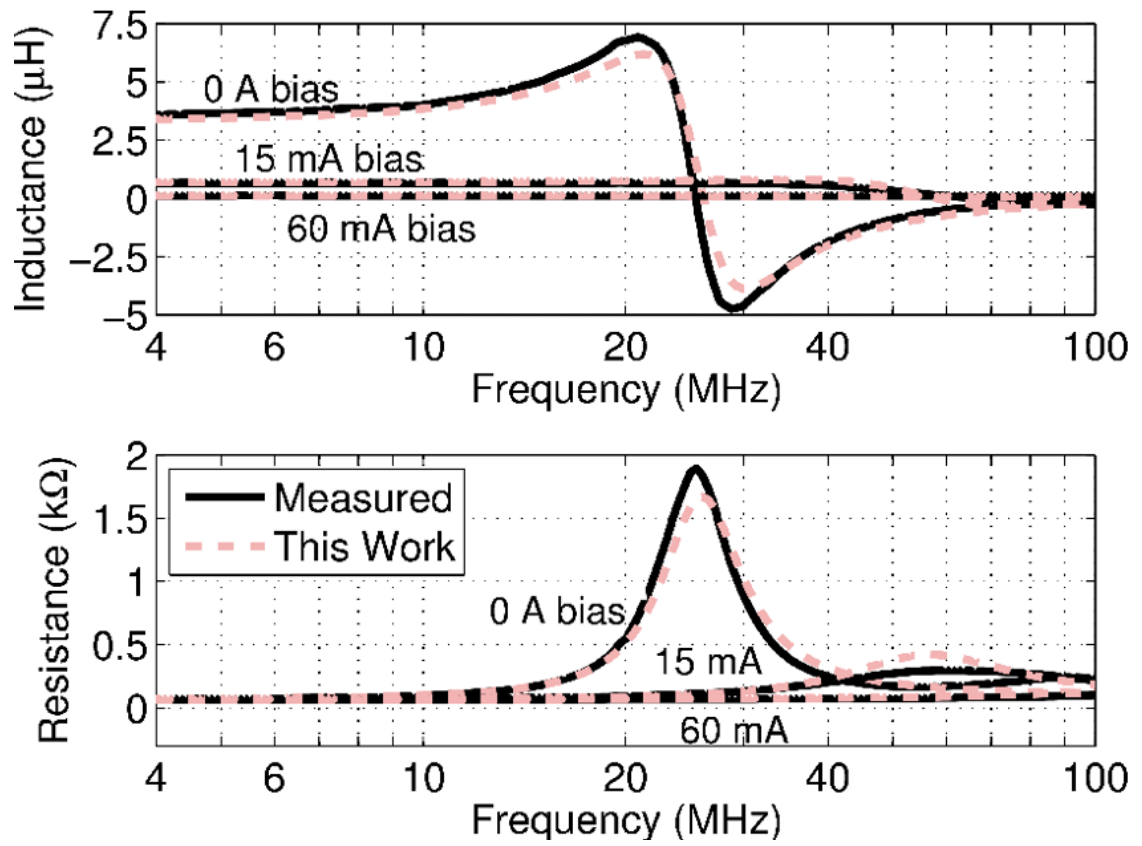


Figure 3.23: Small-signal inductance and resistance versus frequency and bias current showing comparison between fitted Spectre model and actual measurements for device 3.

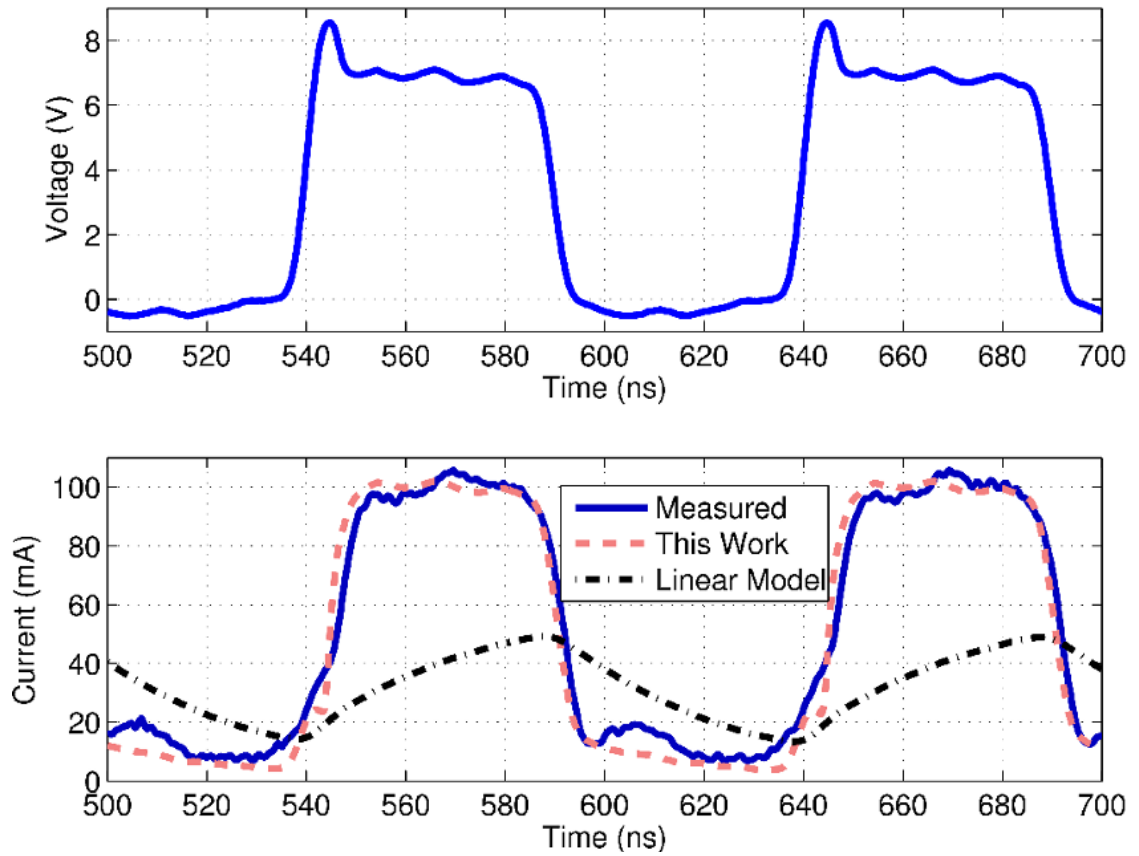


Figure 3.24: Top graph shows the voltage waveform applied to both models and actual device. Bottom graph compares the resulting current waveform for actual device, Fig. 3.5 model, and simple linear model.

selection of the model, the algorithm presented in Section 3.4 allows the order to be an input parameter. In this section, we present a study of the impact of model order on model performance.

We first consider the device 1 microinductor. Since the genetic algorithm we used starts with a random population, we take the average of 25 trials for each model order. Initially we do not include eddy currents at all and the error in small-signal impedance is large (see Table 3.5). The error in AC power loss is 72%. We then add the 1st order eddy current R and the errors improve significantly. The errors continue to improve as we raise the order of the core network, especially the AC power loss, until we get to 4th order, after which they roughly remain constant. Adding another order to the linear network, only improves the AC power loss slightly. Therefore, we conclude the proper order for this device is either $N = 3, M = 2$, or $N = 4, M = 2$, without the need for the RC branch. Adding an RC branch actually makes the performance worse since the device is strictly based on magnetoquasistatic simulations, which ignore capacitive effects.

Since the device 2 microinductor is also a magnetoquasistatic simulation, similar results hold for its order analysis (see Table 3.6). However, device 2 has more pronounced eddy current loss, and the AC loss is therefore more prominent. The errors are smallest when using $N = 4$ and $M = 1$ without the RC branch. Increasing the order of the linear eddy current branch may make the fitting procedure more complicated and therefore lead to larger errors.

The order analysis of the fabricated and measured microinductor, device 3, is shown in Table 3.7. The order of this measured device is mainly determined by the

Table 3.5: Improvements in transient and small-signal errors as for different model orders for device 1. Results shown are an average of 25 algorithm runs.

Device 1	$R(I, f)$ Error	$L(I, f)$ Error	$i(t)$ Error	$P_{loss,ac}$ Error	$P_{loss}(t)$ Error
No RC, L_{c1} Alone, $M = 1$	99%	27%	10%	72%	13%
No RC, $N = 1$, $M = 1$	15%	6.9%	3.3%	10%	2.4%
No RC, $N = 2$, $M = 1$	6.5%	1.7%	1.9%	0.32%	1.3%
No RC, $N = 3$, $M = 1$	4.4%	2.4%	2.4%	3.0%	1.8%
No RC, $N = 4$, $M = 1$	2.9%	2.4%	3.8%	5.8%	1.7%
No RC, $N = 4$, $M = 2$	3.3%	2.3%	3.1%	3.4%	1.8%
With RC, $N = 4$, $M = 2$	5.2%	2.9%	3.2%	3.7%	3.0%

match to small-signal biased impedance measurements. Therefore, these are the only parameters we show in Table 3.7. The addition of the RC branch in parallel is the most significant improvement in the model. As we add more elements to the core branch, the error becomes larger, possible due to the difficulty of optimizing the three-bias stage of fitting. The optimal order for the device 3 microinductor appears to be $N = 2$, $M = 1$, with the parallel RC branch present. Nonetheless, we get acceptable results with the higher order network used in Section 3.5.3.

3.6 Future Work and Conclusions

In this section we propose the possibility of adding hysteresis and ferromagnetic resonance to the model. These effects may be important depending on the core material choice and the frequency of operation. Although not all of the details to implementing these physical effects are determined at this time, we discuss the

Table 3.6: Improvements in transient and small-signal errors as for different model orders for device 2. Results shown are an average of 25 algorithm runs.

Device 2	$R(I, f)$ Error	$L(I, f)$ Error	$i(t)$ Error	$P_{loss,ac}$ Error	$P_{loss}(t)$ Error
No RC, L_{c1} Alone, $M = 1$	100%	32%	20%	31%	88%
No RC, $N = 1, M = 1$	17%	14%	5.4%	233%	104%
No RC, $N = 2, M = 1$	21%	6.4%	3.0%	58%	37%
No RC, $N = 3, M = 1$	7.8%	3.5%	1.8%	29%	19%
No RC, $N = 4, M = 1$	4.2%	2.0%	2.2%	3.3%	9.9%
No RC, $N = 4, M = 2$	4.5%	2.3%	2.2%	8.9%	10%
With RC, $N = 4, M = 2$	4.7%	2.5%	2.2%	6.6%	10%

Table 3.7: Improvements in transient and small-signal errors as for different model orders for device 3. Results shown are an average of 25 algorithm runs.

Device 3	$R(I, f)$ Error	$L(I, f)$ Error
No RC, L_{c1} Alone, $M = 1$	87%	85%
With RC, L_{c1} Alone, $M = 1$	24%	19%
With RC, $N = 1, M = 1$	27%	21%
With RC, $N = 2, M = 1$	16%	11%
With RC, $N = 3, M = 1$	18%	15%
With RC, $N = 4, M = 1$	21%	18%
With RC, $N = 4, M = 2$	18%	14%

circuit topology and some of the extraction algorithm challenges. The final part of this section are the conclusions we can draw from this chapter.

3.6.1 Adding Hysteresis

Many ferromagnetic materials exhibit hysteresis. Hysteresis is the next most significant effect to include in the compact microinductor model presented in this thesis. While eddy current loss at low frequencies is proportional to the square of frequency, hysteresis loss without FMR is proportional to frequency. One way to estimate whether hysteresis loss is significant is to measure the magnetic material's coercivity. As described in Section 2.2.2, hysteresis is caused by defects and discontinuities pinning the domain walls. This means that the effect is dependent on how the material is deposited and should be captured for the specific thin-film microinductor in question.

Using the information presented in Section 2.2.2 and Fig. 3.7, it is fairly straight forward to augment the circuit in Fig. 3.5 to include a Jiles-Atherton type hysteresis. Fig. 3.25 shows an appropriate SPICE model for the nonlinear inductors when hysteresis is present. This model is meant to replace the model of Fig. 3.7 and has six parameters for the hyperbolic tangent anhysteretic function ($M_S, g, k, c, A_{core}, L_{core}$). More parameters would possibly be required for other anhysteretic functions (see Table 2.1).

The hysteresis loss is negligible for small magnetic flux densities. Therefore, the small-signal effects of hysteresis are non-existent if the bias current places

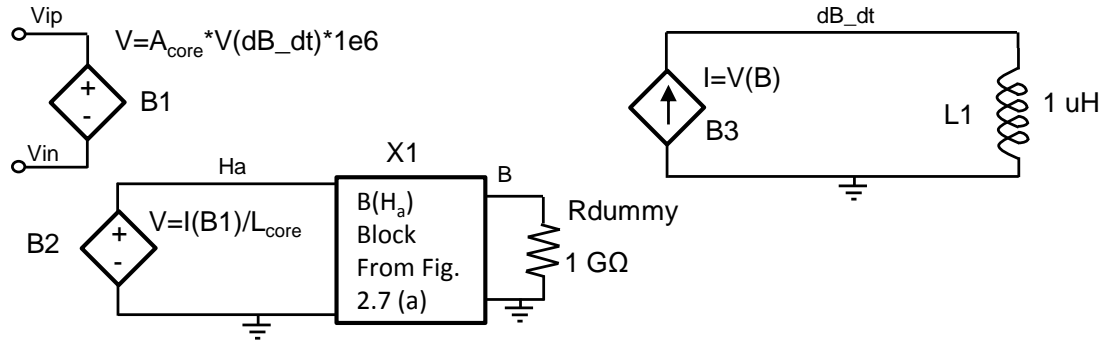


Figure 3.25: A nonlinear inductor circuit model when hysteresis is present employing subcircuit from [87]. This model is meant to serve as a replacement for the circuit of Fig. 3.7, with inductor terminals at V_{ip} and V_{in} .

the material along the anhysteretic curve. If, however, the bias current can be used to sweep the outer hysteresis loop, a biased measurement of the small-signal characteristics would yield the effects of hysteresis, particularly in the small-signal inductance. These two measurements provide a way to separate out the effects of hysteresis from the fitted model. This would possibly allow our existing extraction algorithm to be employed, and then an additional algorithm could augment the anhysteretic model and capture the effects of hysteresis. We envision an algorithm that separates the effects to be more effective than optimizing all the parameters in one routine, since more parameters make finding the global optimum difficult.

3.6.2 Adding Ferromagnetic Resonance

The Hammerstein configuration of a second order linear network and the nonlinear hysteresis network, can be modeled by the simple addition of a RLC low-pass

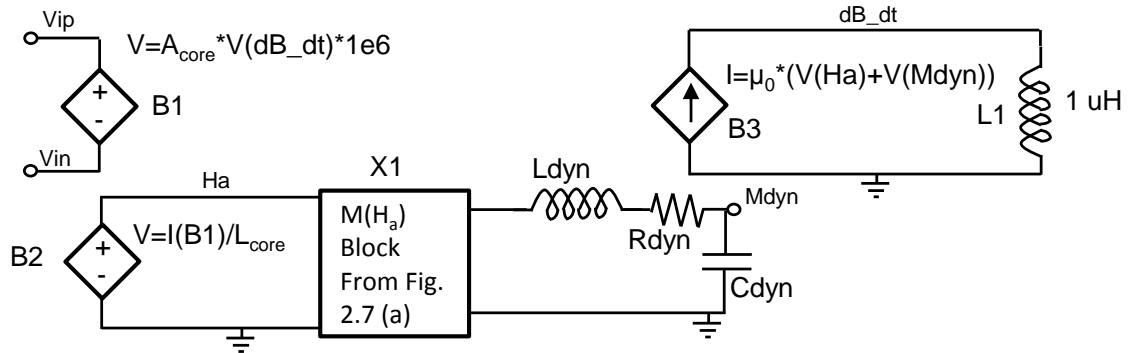


Figure 3.26: A nonlinear inductor circuit model when hysteresis and domain wall dynamics are present [87]. This is a replacement for the circuit of Fig. 3.7, with inductor terminals at V_{ip} and V_{in} .

filter [87]. This was done in Fig. 3.26 where the hysteresis core subcircuit is now an $M(H_a)$ block rather than $B(H_a)$ block. If each of the nonlinear core inductors of the circuit in Fig. 3.5 is replaced with the circuit of Fig. 3.26, then both hysteresis and the effects of ferromagnetic resonance are present in a physically meaningful, spatially distributed manner. If the model should capture FMR, but does not need to include hysteresis, the $M(H_a)$ block of Fig. 3.26 can be replaced by an appropriate saturating controlled source modeling the susceptibility of the material.

As described in Section 2.2.3 and as is exposed in [62], the resonance frequency of the domain walls is related to the ferromagnetic resonance frequency. The dampening factor is more complicated to estimate. Ultimately, the inclusion of ferromagnetic resonance into the dynamics of a nonlinear microinductor, with many other effects occurring is a challenging problem. It would be best if the FMR effects for the material were measured before the device is modeled, and the FMR

characteristics translated into the domain-wall motion dynamics (both ω_n and λ , from (2.2)).

3.6.3 Conclusions

We have presented a physically motivated nonlinear frequency-dependent model for microinductors with alloy thin-film cores and compared it with literature and simplified models. The model is obtained from terminal characteristics rather than knowledge of material parameters and geometry, giving a unique advantage since thin-film magnetic properties are process and dimension dependent. This allows using wafer-level compatible measurements (or a field solver) to generate an accurate model. The measurements are simply small-signal impedance measurements with an applied DC current bias. We have also presented a unique, fast algorithm capable of generating the compact model in Spectre or SPICE from these measurements. Since commercial circuit simulation tools (e.g. those from Cadence [68]) directly simulate behavioral models, the presented methodology is compatible with most commercially available circuit simulators. Using the proposed algorithm and nonlinear static inductance expression, the model is guaranteed passive.

To demonstrate the performance and applicability of our model to PwrSoCs we have placed two field-solver-based models in simplified buck converter circuits. The results indicate that we are able to capture core eddy currents and saturation behavior accurately. The peak current using a linear frequency-dependent model can be in error by as much as 50%, whereas our model captures the peak current at

startup to within 4%. The biased small-signal impedance is captured by our model within 4%, however, the model from [99] consistently has impedance errors around 15%. For the V-groove device, Maxwell simulations predicted 94.9% efficiency, and our model had an error in efficiency of 0.1%. The model from [99] gave an error of 5.3% in efficiency. This is a considerable difference in the estimated efficiency and could mean the difference between a viable PwrSoC design and a unfeasible one. The model of this chapter is also compared favorably to actual device measurements, where the RMS error in current is less than 7.1%. To the authors' best knowledge, this is the first time a measurement generated model of a microinductor has been compared to large-signal time-domain measurements. Our model is physically motivated and should be amenable to the addition of other effects, including ferromagnetic resonance and hysteresis.

Chapter 4 – Microtransformer Model

4.1 Introduction

With the second device category we add the complexity of an additional winding and four terminals. That is, the device can be considered to be a set of two coupled inductors, or equivalently a transformer. The transformer is often employed in AC power conversion. For example, AC power can be transmitted at a high voltage to reduce I^2R losses and then easily stepped-down using a transformer. In addition to voltage conversion the transformer has current conversion and impedance conversion properties that find uses at a wide range of frequencies and applications. Another useful property of transformers is the ability to provide galvanic isolation, that is, there is no direct current conduction path from input to output. Microtransformer with magnetic materials can be used in an isolation fashion for either signal or power. In this application there may be separate voltage domains on the same chip or printed circuit board, and the microtransformer allows safe transfer of power and signals across the domain boundary. Similarly, microtransformers may be used in isolated Power Supplies on Chip (PwrSoCs) such as the flyback step-down converter, or as coupled inductors in a multi-phase buck converter. On-chip integration provides many of the benefits listed for microinductors including, decreased area, reduced component count, improved reliability, and reduced cost [8].

In these applications, the magnetic material provides a boost to the quality factor especially at frequencies of 1 to 100 MHz.

Microfabricated transformers with on-chip magnetics have many examples in the literature [26–34]. This chapter reviews the current state-of-the-art models for both on- and off-chip transformer modeling, showing the novelty of this thesis’ work. Next, the model is developed in detail and a unique nonlinear reluctance block is presented. In Section 4.4 a unique four stage algorithm, similar to that of Section 3.4 is presented to fit the model to a unique set of easily made measurements. The algorithm ensures an accurate and passive model, ensuring proper device behavior. In Section 4.5 the model and algorithm are validated against two simulators and measurements for three different sample devices. Finally, this chapter concludes by providing suggestions for future work and conclusions for the microtransformer model.

4.2 Literature Review

4.2.1 Linear Models not Capturing Core Eddy Currents

One of the simplest transformer models is the linear model not capturing core losses. This model includes the effects of linear magnetic coupling through an ideal transformer and three additional linear parasitic inductances: two leakage inductances for ports 1 and 2 in series with the ideal transformer, and a magnetizing inductance in parallel with the ideal transformer, as illustrated in Fig. 4.1. The

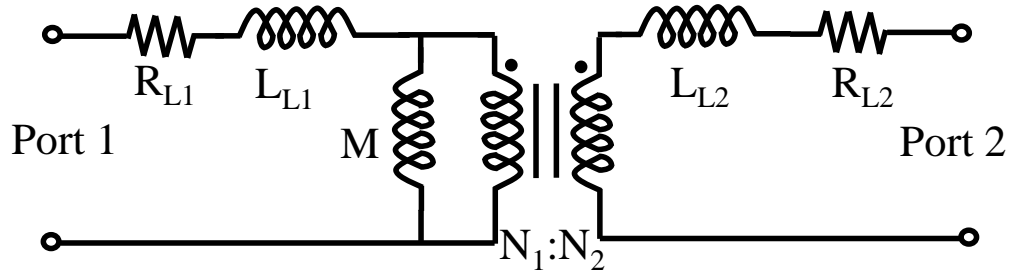


Figure 4.1: Example of simple linear microtransformer model without any core eddy current losses.

ideal transformer itself is recovered if the leakage inductances, L_{L1} and L_{L2} , are zero and the magnetizing inductance, M , is infinite. This model can be considered equivalent to the coupled inductor model available in many circuit simulators. It also finds application in literature [31, 117–120]. Additionally, the conductor resistance may be added as in Fig. 4.1 and [121]. Capacitive self-resonance is also often included in research literature models of this type [29, 122–125]. The leakage impedances may even include conductor skin/proximity effects through RL networks as in [126–128]. Many of these models are designed for microtransformers, but only two of these include magnetic materials [29, 31]. Due to the fact that this type of transformer model is strictly linear, it is not suitable to capture saturation effects or hysteresis, which is important in PwrSoCs and isolation transformers. Moreover, the loss is an important consumer exposed parameter in PwrSoCs, and these models ignore the important eddy current losses in the core material. Nonetheless, the simplicity and ease of implementation of these models make them attractive for first order approximations of device operation.

4.2.2 Nonlinear Models not Capturing Core Eddy Currents

The nonlinear version of the transformer model not capturing eddy currents is very similar to the linear version. The only difference is the magnetizing inductance includes the effects of saturation and/or hysteresis. As in the linear version, the nonlinear transformer model may have DC resistance in the leakage terms [129, 130], or it may exclude the DC resistances [53]. The examples mentioned so far only include saturation, but another nonlinear effect often relevant is hysteresis. References [80, 87, 131, 132] all include the effects of hysteresis. The effects of capacitive resonance may also be included as shown in [82, 133]. Although none of these models discussed in this section are for microtransformers, it is not too difficult to imagine a microtransformer for which they may be appropriate, namely one where saturation matters, but core eddy currents are not dominant. For example, [87] models ferromagnetic resonance in the core material, which would dominate over eddy currents in some materials, such as ferrites.

4.2.3 First Order Core Eddy Current Models

We have seen in Appendix A that the low-frequency eddy current losses¹ in the core are proportional to $(d\Phi/dt)^2$ and, therefore, appear as a resistor in parallel with the core inductance. The physics-based model presented in Appendix A.1 adds the effect of low-frequency eddy current losses and, thus, adds this parallel

¹By low-frequency losses we mean those not altered by the skin effect, and proportional to frequency squared.

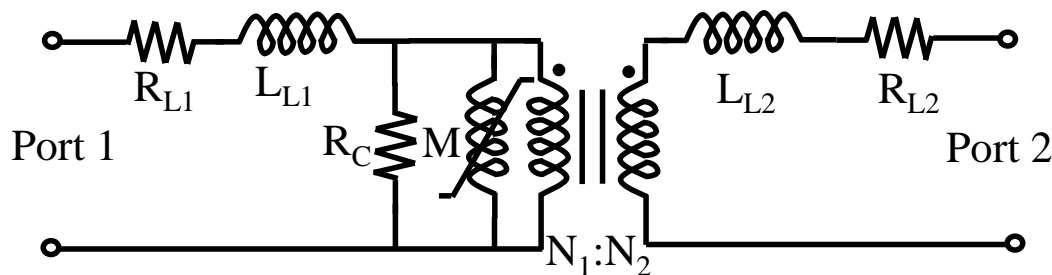


Figure 4.2: Example of nonlinear microtransformer model with core resistance modeling 1st order core eddy current losses.

resistor (see Fig. 4.2). Some of these models are purely linear and do not include saturation or hysteresis [33, 34, 134, 135]. Others include saturation in the magnetizing inductor [130, 136–138]. Still others include hysteresis as well [139–144]. The low-frequency core eddy current model, can certainly include capacitive resonance effects through the addition of capacitors, as some of the referenced models do, namely, [33, 134, 140–143]. Three of the above models make use of the concept of a gyrator or differential gyrator [138, 141, 144] (see Appendix B.1 for discussion of this device). While modeling microtransformers with magnetic materials is relatively new, four of the above models are explicitly intended for microtransformers, i.e. [33, 34, 135, 138]. The ability to include core eddy current effects is important, thus the prevalence of the type of model discussed in this section. Furthermore, many microinductors are operated at frequencies where their skin-depth is a fraction of a single lamination’s thickness. This creates the need to model eddy currents in a regime needing higher order eddy current models for the core.

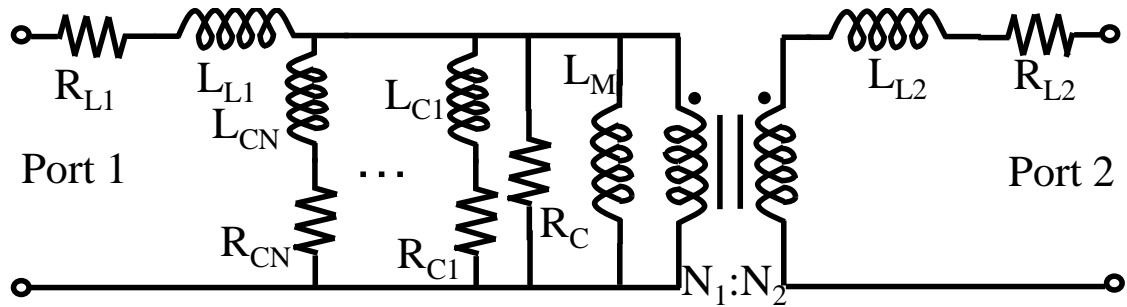


Figure 4.3: Example of linear microtransformer model with $N+1$ th order core eddy current modeling, capturing the skin-effect in the core.

4.2.4 Higher Order Core Eddy Current Models

Higher order models of eddy current core loss allow the capture of eddy currents at frequencies where skin-effect is relevant. When the skin-effect in the eddy currents is pronounced the losses are proportional to the square-root of frequency, and we refer to these eddy currents as being “high-frequency.” Similar to the previous models, the magnetizing inductances can either be linear, as in [145, 146] and Fig. 4.3, or nonlinear, as in [90, 106, 147]. It should be noted that while many different magnetizing RL networks are suitable in the linear case (such as the Foster network in Fig. 4.3), only the Cauer network is suitable for the nonlinear case (similar to the microinductor). This is because with nonlinear inductances the networks with different topologies behave differently, whereas linear networks can create the same impedance functions. The high-frequency core eddy current model discussed here is the most appropriate so far for microtransformers with thin-film ferromagnetic alloys as the core material, which at frequencies of 10-100 MHz have skin depths smaller than the core thickness.

Table 4.1: Feature comparisons for microtransformer models from literature.

Model Section	Saturation	Linear Eddy Currents	Core Eddy Currents	Capacitive Resonance	Terminal Based	On-Chip
4.2.1	no	rarely	no	often	possibly	yes
4.2.2	yes	no	no	rarely	no	no
4.2.3	some	no	low-freq.	often	possibly	yes
4.2.4	some	few	yes	rarely	possibly	yes

4.2.5 Summary Table

Table 4.1 provides a quick summary of the literature review performed in this section. The features compared are considered to be the most important characteristics of the microtransformer model we are trying to construct. The model presented in this chapter will cover every feature presented in Table 4.1.

4.3 Model Development

4.3.1 Model Circuit Topology

The topology we developed for on-chip microtransformers is shown in Fig. 4.4. The outer connections are the RC branches associated with the capacitive self-resonance effects of large on-chip microtransformers. The ladder networks on the left and right are the M th order leakage impedances of port 1 and port 2, respectively. They include the DC resistance as well as any linear eddy current effects resulting only from a single conductor, including skin-effect and substrate eddy currents. There are two differential gyrators (see Appendix B.1) to make the two conductors

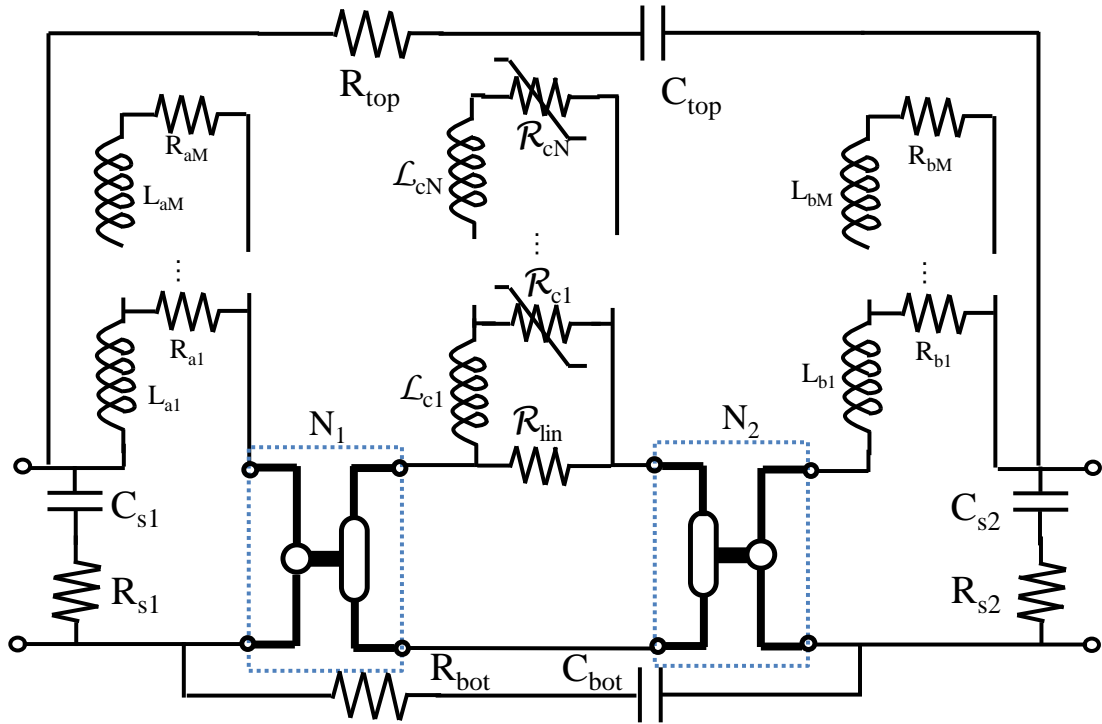


Figure 4.4: Compact equivalent circuit model used for microtransformers, with an M th order linear conductor ladder network and an N th order saturating core ladder network in the magnetic domain.

connect to the magnetic domain, where the core is modeled by an N th order nonlinear ladder network. The first linear reluctance, \mathcal{R}_{lin} , makes the network one order higher. It is used to capture any coupling between the two conductors external to the core material.

4.3.2 Nonlinear Reluctances

Unlike the microinductor core network, the microtransformer core network was best implemented in the magnetic domain. This allows for an intuitive understanding of the major topology of the magnetic circuit. If, for example, we wanted to capture the even-mode saturation of [138], we would split the magnetic ladder in two and add a shunt reluctance to the magnetic ground. Also, nonlinear reluctances become dependent only on the flux through them, whereas a nonlinear magnetizing inductance would have to be dependent on the two port currents separated by a transformer. In the magnetic domain, we implement the nonlinear reluctance, \mathcal{R}_{cn} , as a flux-MMF relationship ($\Phi_{cn}(\mathcal{V}_{cn})$).

To keep the model physical, general, and realizable, six properties of the $\Phi_{cn}(\mathcal{V}_{cn})$ function implementing the nonlinear reluctance \mathcal{R}_{cn} are required: it should be

- 1:** an odd function of MMF, \mathcal{V}_{cn} ;
- 2:** monotonically increasing;
- 3:** only present in quadrants I and III of Φ_{cn} vs \mathcal{V}_{cn} ;
- 4:** a one-to-one mapping;
- 5:** implementable in circuit simulators;
- 6:** sufficiently general to model gaps/demagnetization and typical anhysteretic B-H curves.

It should be noted that properties 3 and 4 are consequences of 1 and 2; however, they are more directly related to the properties we specify in Appendix C to

guarantee passivity. These four properties together are based on physical considerations, while the last two give the function the necessary generality and ability to be implemented. The function we develop to meet these specifications is based on the hyperbolic tangent anhysteretic function (see Table 2.1). To make the function general enough to capture the variety of Φ - \mathcal{V} behaviors, additional hyperbolic tangent terms were added. These were added in pairs of equal positive and negative shifted and scaled versions, so as to preserve the oddness/antisymmetry of the overall function.

The $\Phi_{c,n}(\mathcal{V}_{c,n})$ function is defined as

$$\begin{aligned} \Phi_{c,n}(\mathcal{V}_{c,n}) = & \beta_{0,n}\mathcal{V}_{c,n} + \beta_{1,n} \tanh\left(\frac{\beta_{2,n}}{\beta_{1,n}}\mathcal{V}_{c,n}\right) \\ & + \sum_{i=1}^I \left(\beta_{3i,n} \tanh\left(\frac{\beta_{3i+1,n}}{\beta_{3i,n}}(\mathcal{V}_{c,n} - \beta_{3i+2,n})\right) \right. \\ & \left. + \beta_{3i,n} \tanh\left(\frac{\beta_{3i+1,n}}{\beta_{3i,n}}(\mathcal{V}_{c,n} + \beta_{3i+2,n})\right) \right). \end{aligned} \quad (4.1)$$

This can be converted through differentiation to a small-signal permeance expression ($\mathcal{P}(\mathcal{V}) = \frac{d\Phi}{d\mathcal{V}}$) as

$$\begin{aligned} \mathcal{P}_{c,n}(\mathcal{V}_{c,n}) = & \beta_{0,n} + \beta_{2,n} \operatorname{sech}^2\left(\frac{\beta_{2,n}}{\beta_{1,n}}\mathcal{V}_{c,n}\right) \\ & + \sum_{i=1}^I \left(\beta_{3i+1,n} \operatorname{sech}^2\left(\frac{\beta_{3i+1,n}}{\beta_{3i,n}}(\mathcal{V}_{c,n} - \beta_{3i+2,n})\right) \right. \\ & \left. + \beta_{3i+1,n} \operatorname{sech}^2\left(\frac{\beta_{3i+1,n}}{\beta_{3i,n}}(\mathcal{V}_{c,n} + \beta_{3i+2,n})\right) \right). \end{aligned} \quad (4.2)$$

In (4.1) and (4.2) the order is the number of uniquely defined $\tanh/\operatorname{sech}^2$ terms, i.e. $1 + I$, and there are $3 + 3I$ parameters for the n th reluctance, namely, $\beta_{0,n}, \dots, \beta_{3I+2,n}$. Consider a second order form of (4.1) with three hyperbolic tangent terms. The first term is a constant slope $\beta_{0,n}$ representing the non-saturating effect of free space permeability. The first \tanh term is centered at the origin with no shift. This term contributes a saturation flux of $\beta_{1,n}$ and has a slope of $\beta_{2,n}$ at the origin.² The second and third \tanh terms are centered at $\pm\beta_{5,n}$, respectively. Combined they saturate at $2\beta_{3,n}$. With higher orders come more degrees of freedom and the ability to fit to a wider range of $\Phi(\mathcal{V}_m)$ behaviors, including gaps and demagnetization effects.

The nonlinear permeance model described here can simply be implemented as controlled sources. Either as a single behavioral voltage controlled current source, or a parallel combination of such sources as shown in Fig. 4.5. Due to the generality of (4.1) we expect with sufficient order, it can match any odd, monotonically increasing function to arbitrary accuracy, and thus it should be able to capture demagnetization effects and the addition of gaps in the core. For the addition of magnetic material effects such as ferromagnetic resonance and hysteresis a more advanced circuit is necessary. This will be discussed in detail in the future work.

²This slope is also the small-signal inductance of this term at zero current bias considering a 1-turn differential gyrator.

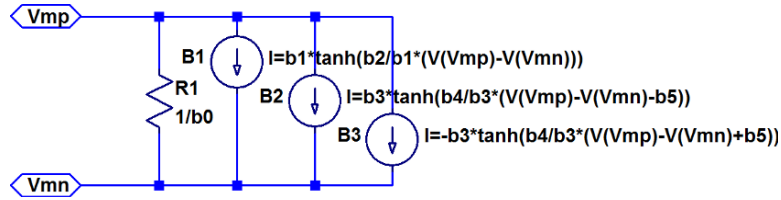


Figure 4.5: Possible LTspice subcircuit of a second order nonlinear reluctance described by (4.1). Magnetic domain terminals are Vmp and Vmn.

4.3.3 Measurements Employed to Generate Model

Transformers and coupled inductors are, at the very least, two port devices. A reciprocal two port device at every bias current and frequency has 3 degrees of freedom (since immittance matrices are symmetric for a reciprocal device). Therefore, we need at least three separate small-signal impedance measurements versus frequency and versus the two bias currents to form the impedance matrix

$$\mathbf{Z}_{ss}(f, I_1, I_2) = \begin{bmatrix} Z_{11}(f, I_1, I_2) & Z_m(f, I_1, I_2) \\ Z_m(f, I_1, I_2) & Z_{22}(f, I_1, I_2) \end{bmatrix}. \quad (4.3)$$

The circuit model in Fig. 4.4 has only a single nonlinear magnetic impedance branch, thus the nonlinear reluctance is dependent on $N_1 I_1 - N_2 I_2$. Therefore, the circuit dependence on I_2 can be derived from its dependence on I_1 and vice versa.

We chose to measure the small-signal port impedance versus frequency and bias for the primary port while the secondary is open or shorted with the bias applied to the primary port and the same for the secondary port while the primary is open with the bias again applied to the primary port. These measurement setups are illustrated in Fig. 4.6. After performing these measurements, the results are

three impedance values specified at K frequencies and J currents, namely the complex-valued matrices

$$Z_{open1}(I_j, f_k) \quad (4.4a)$$

$$Z_{open2}(I_j, f_k) \quad (4.4b)$$

$$Z_{short1}(I_j, f_k). \quad (4.4c)$$

At each bias current and frequency measurement point, we can convert these measurements into the corresponding impedance matrix via

$$Z_m = \sqrt{(Z_{open1} - Z_{short1}) Z_{open2}} \quad (4.5a)$$

$$Z_{11} = Z_{open1} \quad (4.5b)$$

$$Z_{22} = Z_{open2}. \quad (4.5c)$$

Similar to the microinductor the measurements are strictly terminal based, and use either an impedance analyzer or vector network analyzer and bias tee. Thus, the measurements are simple to perform and compatible with wafer-level probing.

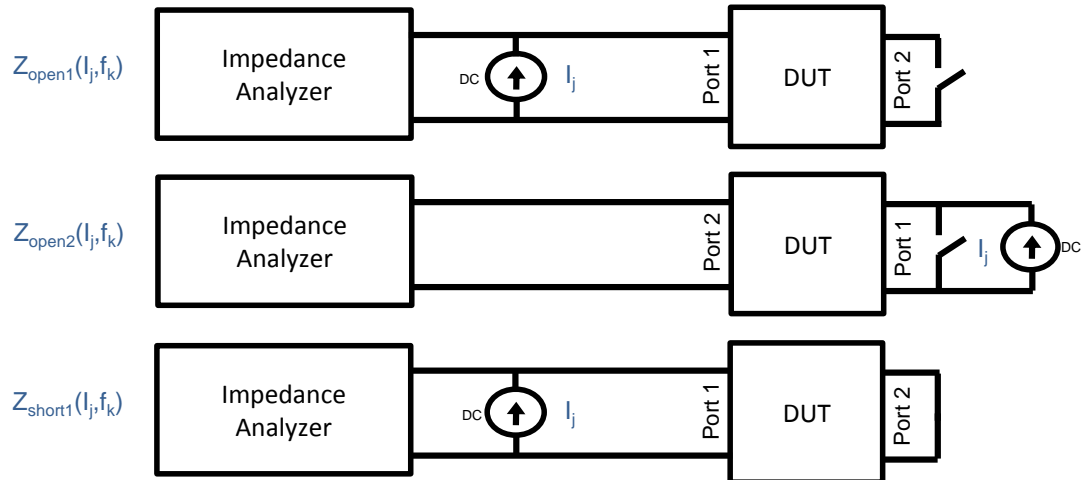


Figure 4.6: The three distinct measurement setups proposed for determining the small-signal behavior of a two port microtransformer.

4.3.4 Measurements Employed to Validate Model

Two application domains were selected to validate the microtransformer model developed. The first application is an isolation transformer for transferring signals and/or power from one electrically isolated domain to another. The second application is an isolated step-down converter of flyback topology for isolated DC-to-DC voltage conversion. Both of these domains stress the model.

It is desirable for isolation transformers to be able to transfer substantial power at high frequencies. This application stresses the saturation behavior of our model due to large currents, and the eddy current behavior due to high frequencies. The input current and output voltage time-domain waveforms matching for a sinusoidal input voltage will be the validating test for the designed isolation transformer. Similar to the buck converter, in the flyback topology, power density should be

high, so we need to operate close to saturation to boost output current. The most important design criteria of a DC-to-DC converter typically is efficiency, so the model should accurately capture the average power loss and, more specifically, the instantaneous power loss time-domain waveform. Thus, the matching of these two power figures will be the validating test for the flyback application.

4.3.5 Novelty of This Model

The model developed in this thesis has some rarely used features from literature. Firstly, there are few models that are meant for microtransformers with on-chip magnetic materials. Secondly, few models make use of the differential gyrator concept (see Appendix B.1), which allows the use of the intuitive magnetic domain and its automatic galvanic isolation. Thirdly, only one other reference was found that implemented the skin-effect in the conductors and saturation in the core, namely, [126]. The effects included in the core are high-frequency eddy currents and saturation. It should be noted that ferromagnetic resonance/relaxation effects are currently not included in this chapter's model, since we are focusing on Ni-Fe alloys with FMR frequencies in the GHz [67]. Hysteresis is also not included as the Ni-Fe alloys also have a low coercivity [16, 64]. Figure 4.4 is the first of its kind topology and is suitable for many microtransformer configurations (see Section 1.2.2).

There are other features of our model, which are lacking in existing literature. The most significant of which is the ability to incorporate the core material

properties without knowing them explicitly. For example, the methods described in the literature review, are created for simplified geometries or analytical solutions. On-chip magnetic materials like Ni-Fe are often anisotropic [97] and contain a soft and hard axis, or vary due to substrate surface or demagnetization [11], making the measurement of properties prohibitive. Also, in on-chip designs, the need to make multiple integrated structures to generate a single device model can be costly. Our model and algorithm provide a way to generate one physically-motivated equivalent-circuit device model, accurately and simply from only the terminal characteristics. Unlike off-chip transformers, we generated a simple and accurate extraction algorithm that generates the compact, physically-motivated, equivalent circuit of Fig. 4.4 by means of terminal measurements made with an impedance analyzer or vector network analyzer (VNA). The models are accurate in both the fitted and verification domains, and the algorithm guarantees passivity.

4.4 Model Extraction Algorithm

4.4.1 Algorithm Overview

The model extraction algorithm is broken up into four main stages as shown in Fig. 4.7. First, the model's element values are extracted from the measurements made without any bias currents ($j = 1$); this provides appropriate parameter bounds for the next stage. Next, the model's elements are simultaneously fit to match the unsaturated ($j = 1$), fully saturated ($j = J$), and moderately saturated

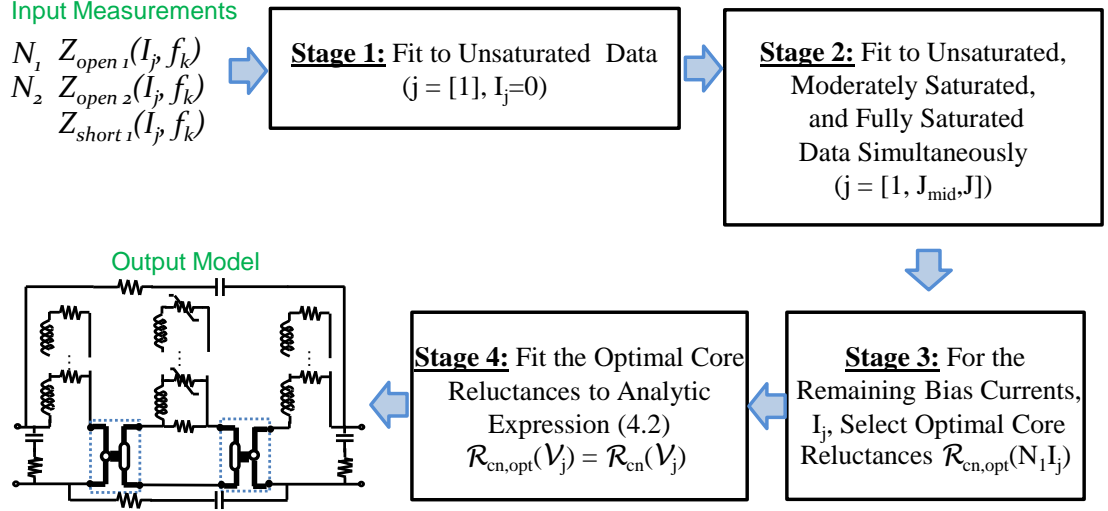


Figure 4.7: Flow chart of microtransformer extraction algorithm going from input measurements to output model with four intermediate stages.

($j = J_{mid}$) small-signal impedance measurements versus frequency ($k = 1, \dots, K$). Third, the nonlinear core reluctances, \mathcal{R}_{cn} , at the remaining bias currents are extracted by fitting to each bias current's small-signal impedance measurements. The optimal small-signal core reluctances from stages 2 and 3 are referred to as $\mathcal{R}_{cn,opt}$, ($n = 1, \dots, N$). The final stage is to fit (4.2) to the optimized small-signal permeances, $1/\mathcal{R}_{cn,opt}$.

4.4.2 Stage 1: Zero-Bias Fitting

This first stage attempts to find a good fit using only parameters relevant to the zero-bias measurements. This is done in order to ease the burden on the next stage with its many fitting parameters by transforming it from a wide optimization

region to a more narrow region. The parameters in stage 1 are the value of every element in Fig. 4.4 with the nonlinear reluctances, \mathcal{R}_{cn} , taking on a single value. Since there are few parameters it is feasible to use a larger optimization region and thus cover a wider array of microtransformers. We make sure that the upper limit for each resistor and inductor is larger than the largest measured inductance and resistance. The cost function of the fitting procedure is given by

$$f_{cost,1} = \left[\frac{1}{6} \left(E_{R,o1}^2 + E_{R,o2}^2 + E_{R,s1}^2 + E_{L,o1}^2 + E_{L,o2}^2 + E_{L,s1}^2 \right) \right]^{\frac{1}{2}}, \quad (4.6)$$

where $E_{R,o1}$ is the percentage L2-norm error in the frequency-dependent resistance of the open measurement at port 1, $E_{R,o2}$ is the error for the resistance of the open measurement at port 2, and $E_{R,s1}$ is the error for the resistance of the shorted measurement at port 1. The ‘L’ subscript indicates the errors are for the inductance. This cost function doesn’t overemphasize small inductances and resistances in the frequency domain by using the L2-norm error over frequency. It also provides relatively equal weight to the contribution from $R(f)$ and $L(f)$ under different measurement setups by combining them in the RMS sense.

4.4.3 Stage 2: Three-Bias Fitting

The second stage of the extraction procedure is the most important and most challenging. Both aspects arise from the large number of fitting parameters. The model parameters are optimized to the measured impedance data versus frequency for three bias currents. To aid in getting a good fit, the parameter values obtained

from stage 1 are leveraged to reduce the range of values for this stage. Only the magnetic permeability of the core saturates, thus only \mathcal{R}_{cn} vary between the three circuits.

The cost function is a weighted RMS combination of the L2-norm errors for each bias current

$$f_{cost,2} = \left[\frac{W_1 E_1^2 + W_{J_{mid}} E_{J_{mid}}^2 + W_J E_J^2}{W_1 + W_{J_{mid}} + W_J} \right]^{\frac{1}{2}}. \quad (4.7)$$

In (4.7), E_j is the cost function of stage 1 applied to bias current j and W_j is its weight. In total, there are $4N + 4M + 9$ parameters to the optimization: $3N$ from the N nonlinear core reluctances at the three bias currents, N from the linear core magnetic inductances (together making $4N$), $4M$ from the two linear leakage branches in the electric domain, 8 from the surrounding R/C network, and 1 from \mathcal{R}_{lin} . To reduce the problem complexity, constraints are applied and the parameter region is reduced. At zero bias the DC inductance is constrained to match the measurements, and all of the core inductances are made equal.³ This reduces the parameters by N . Furthermore, R_{top} and C_{top} are constrained to equal R_{bot} and C_{bot} , respectively. This is an assumption that the interwinding capacitance and loss are evenly distributed with the inductive portions and are thus lumped equally on either side in a sort of Π configuration.

Due to the large number of parameters and fast cost function analysis, the genetic algorithm [112] is employed to solve this global optimization problem. 30

³Equal inductance values were found to aid in the transient performance when going well into saturation where eddy currents penetrate deeper into the core material.

generations of population 500 were sufficient to find a good fit. To further improve the fit a local optimizer [113] with bounds enforcing passivity was employed. At the end of stage 2, the optimized parameters provide every linear element and the optimized nonlinear core reluctance elements, $\mathcal{R}_{cn,opt}$, of the microtransformer model at the three bias currents.

4.4.4 Stage 3: Fit to Remaining Biases

The next part of the model extraction procedure is to fit to the inductance/reluctance and resistance measurements at the remaining bias currents, I_j ($j = 2, \dots, J_{mid} - 1, J_{mid} + 1, \dots, J - 1$). Since there are few (N) cost function parameters several different global optimization routines can be used to produce the values of $L_{cns}(I_j)$ that minimize the percentage error. The below pseudo code determines these optimal inductances/reluctances.

input : Fitted linear elements, optimized nonlinear core reluctances at 3 biases, and small-signal measurements Z_{open1} , Z_{open2} , and Z_{short1} .
output: Optimized nonlinear reluctances at remaining biases.

for $j \leftarrow 2$ **to** $J - 1$ | $j \neq J_{mid}$ **do**
 optimize circuit to fit to $Z_{open1}(I_j, f)$, $Z_{open2}(I_j, f)$, and $Z_{short1}(I_j, f)$ with global optimizer;
 minimize $f_{cost,3} = \left[\frac{1}{6} \left(E_{R,o1}^2 + E_{R,o2}^2 + E_{R,s1}^2 + E_{L,o1}^2 + E_{L,o2}^2 + E_{L,s1}^2 \right) \right]^{\frac{1}{2}}$
 by varying $\mathcal{R}_{c1,opt}(I_j), \dots, \mathcal{R}_{cN,opt}(I_j)$
end

After stages 1 through 3 all the linear elements and the nonlinear reluctances' small-signal reluctance are optimized at the J bias currents, $\mathcal{R}_{cn,opt}(I_j)$.

4.4.5 Stage 4: Fit Nonlinear Reluctances

The nonlinear reluctances optimized at the J bias currents can be viewed as a sampling of their saturation behavior. For each nonlinear reluctance element, the parameters of (4.2) are selected to fit to the “sampled” optimized permeance versus bias current, $1/\mathcal{R}_{cn,opt}(I)$, using a global optimization algorithm. The cost function to be minimized is the L2-norm error between these optimized reluctances from stages 1 through 3, and (4.2), given as

$$f_{cost,4} = 100\% \cdot \|\mathcal{P}_{cn}(I_j) - 1/\mathcal{R}_{cn,opt}(I_j)\|_2 / \|1/\mathcal{R}_{cn,opt}(I_j)\|_2. \quad (4.8)$$

The below pseudo code determines the parameters of (4.2) for each of the N core reluctances.

```

input :  $N$  Optimized nonlinear reluctances at  $J$  measured currents,
           $\mathcal{R}_{cn,opt}(I_j)$ .
output: Parameters for each nonlinear reluctance.
for  $n \leftarrow 1$  to  $N$  do
  | optimize (4.2) of order  $1 + I$  to fit to  $1/\mathcal{R}_{cn,opt}(I)$  with global optimizer;
  | minimize  $f_{cost,4}$  by varying  $\beta_{1,n}, \dots, \beta_{3I+2,n}$ 
end

```

4.5 Validation

In this section, microtransformer models are generated from the three small-signal biased impedance measurements. The models are then validated using the ide-

alized application circuit for which the microtransformer was designed. When relevant, time domain comparisons are performed using the device-circuit cosimulation feature available in Maxwell.

Device 1 is a Maxwell [115] simulation of a 2:2 signal isolation transformer used to transfer voltage signals between two galvanically isolated circuit domains. The model should accurately capture the frequency dependent gain of the microtransformer and be able to replicate waveforms under low impedance loads. Device 2 is a Maxwell simulation of a microtransformer used in a flyback isolated step-down DC-to-DC converter. The model should capture both AC and DC power loss under heavy load conditions and reproduce any transient peaks in current waveforms. These two devices are simulated as a single section of an interleaved microtransformer to allow accurately capturing of eddy currents. As a measurement example, a 18:18 solenoidal microtransformer was fabricated, measured, and a model extracted. No validation measurements were able to be performed for this microtransformer, but the biased small-signal data should match well.

Where appropriate, the necessity of the fully nonlinear dynamic model of Fig. 4.4 will be presented by comparing the validation results with two simplified models. The first simplified model is a 5-element nonlinear model intended to ignore the dynamic effects of eddy currents. This model reduces the magnetic network to a single nonlinear reluctance \mathcal{R}_{core} and reduces the leakage models to single series combinations of a linear resistor and inductor. The topology of the 5-element nonlinear model is shown in Fig. 4.8. The other simplified model is a linear dynamic model intended to ignore the nonlinear effects of core saturation. The magnetic

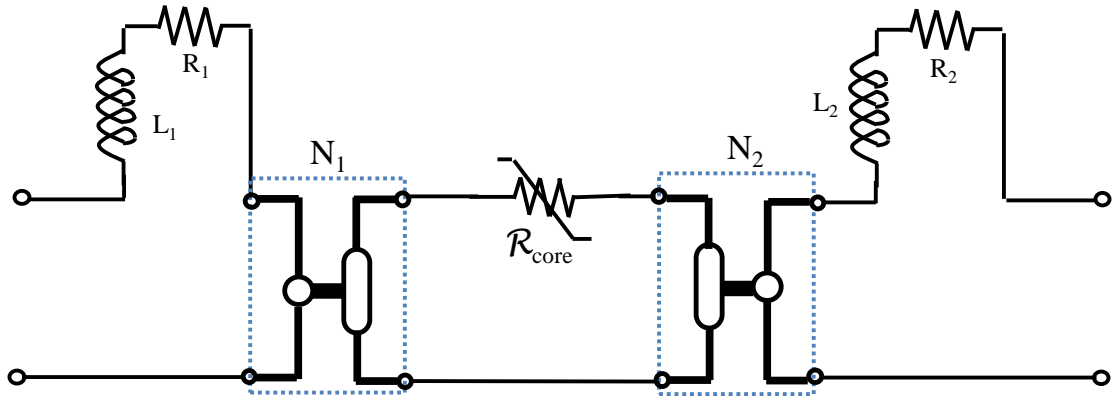


Figure 4.8: Circuit diagram of the 5-element nonlinear model used in validation comparisons.

network is reduced to a linear 4th order ladder network ($N = 4$) and the leakage networks are linear 2nd order ladder networks ($M = 2$). The topology of the 8th order linear model is shown in Fig. 4.9. Since the magnetoquasistatic simulations in Maxwell necessarily ignore displacement currents, the RC networks have been removed from both of these reduced models.

4.5.1 Device 1 Simulation

The first test device is a 2:2 interleaved racetrack microtransformer. Due to the large dimensions of this microtransformer relative to the skin-depth in the core, simulation of the full microtransformer is prohibitive. However, we can approximate the microtransformer by removing the bends not covered by magnetic material, and then simulate a short section of the straightaway. To estimate the characteristics of the full racetrack we then multiply the impedance by the frac-

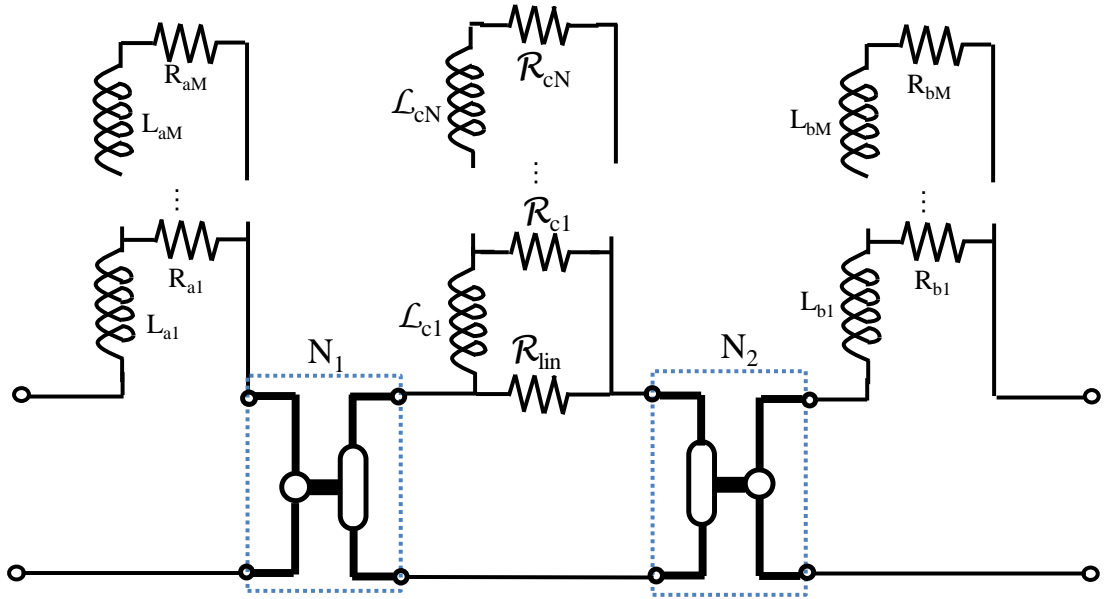


Figure 4.9: Circuit diagram of the linear 8th order ($N = 4$, $M = 2$) dynamic model used in validation comparisons.

tional ratio. Figure 4.10 shows a perspective view for the Maxwell [115] simulation of the section, and a 2-D cross-section showing the dimensions. The conductors are made of copper, and the core material is a Ni-Fe alloy with resistivity $17 \mu\Omega\text{cm}$ and a hyperbolic tangent M-H behavior as in (3.7a), with $M_S = 9.08 \times 10^5 \text{ A/m}$ and $g = 3.16 \times 10^{-4} \text{ m/A}$. The overall length of the microtransformer is 4.2 mm, which was scaled by a factor of 200 to simulate in the field solver.

4.5.1.1 Model Fit

The three small signal impedance measurements of Fig. 4.6 were obtained via the Maxwell field solver [115] at 31 frequencies logarithmically spaced from 1 kHz to 50

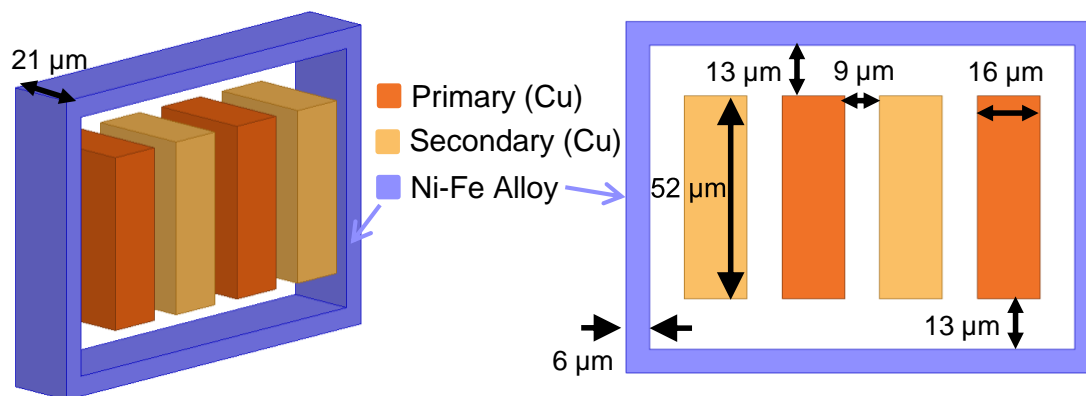


Figure 4.10: Ansys Maxwell layout in 3-D of reduced-length device 1 microtransformer and 2-D cross-section showing dimensions.

MHz and 13 bias currents from 0 to 3 A. Since a biased small-signal analysis was not available in Maxwell, we approximated the core as saturating uniformly and simulated 13 individual eddy current analyses with different permeabilities to the core. This approximation is justified by the core thickness relative to its magnetic path length.

The developed extraction algorithm from Section 4.4 took 3 minutes 36 seconds on a 3.2 GHz Pentium[®] 4 workstation to generate the complete Spectre model from the field solver data. The element values and nonlinear reluctance parameters can be found in Appendix D.2. The four static nonlinear core inductances fit their optimum values with L2-norm errors less than 8% (See Fig. 4.11). Combining the L2-norm errors in resistance and inductance at each bias current in a root-mean-square sense gives an error in the “open 1” measurement of 6.2%, an error in the “open 2” measurement of 6.9%, and an error in the “short 1” measurement of 6.6%. (see Table 4.2). The comparison of the small-signal impedance of the model

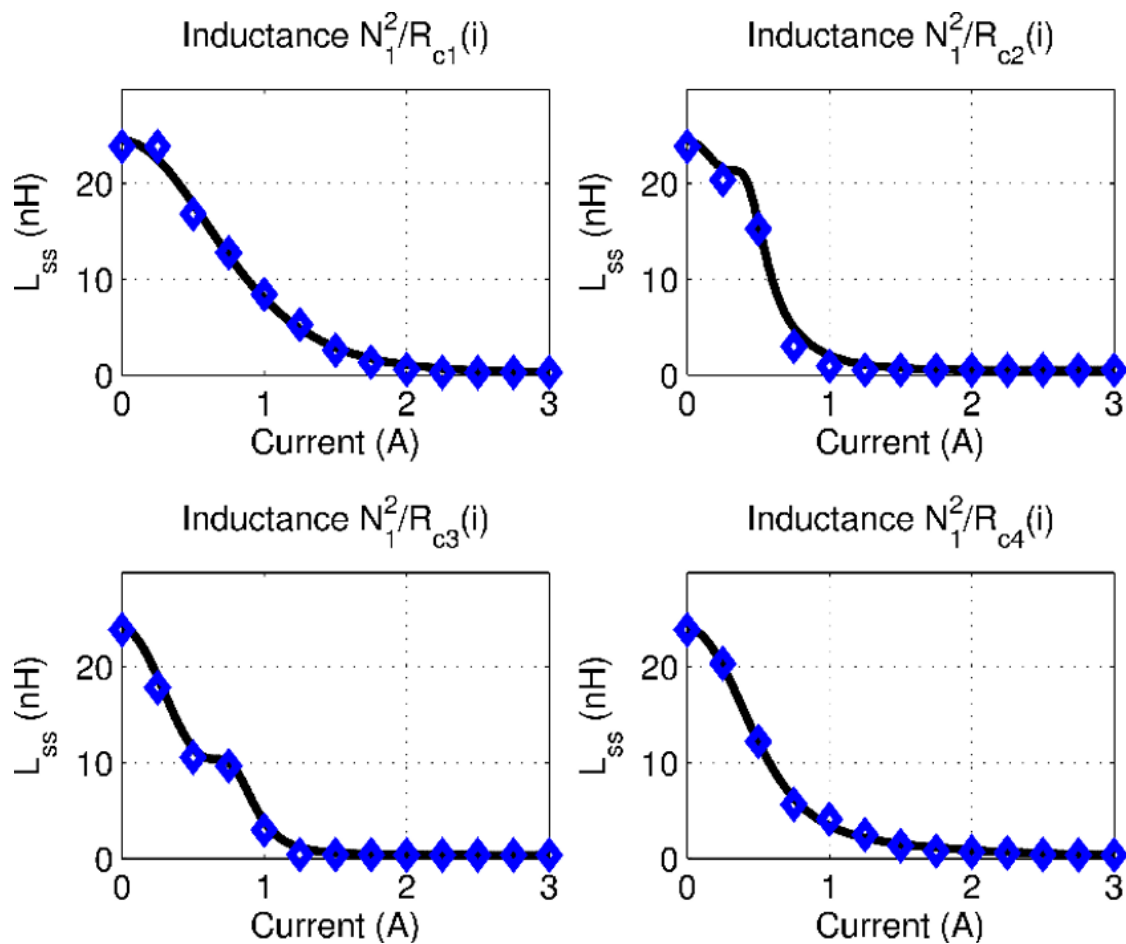


Figure 4.11: Port 1 reflected inductance for \mathcal{R}_{c1} through \mathcal{R}_{c4} for the device 1 isolation transformer. The data points are the optimal reflected inductances from stages 1 through 3 of the algorithm, and the curve is the fit to these points.

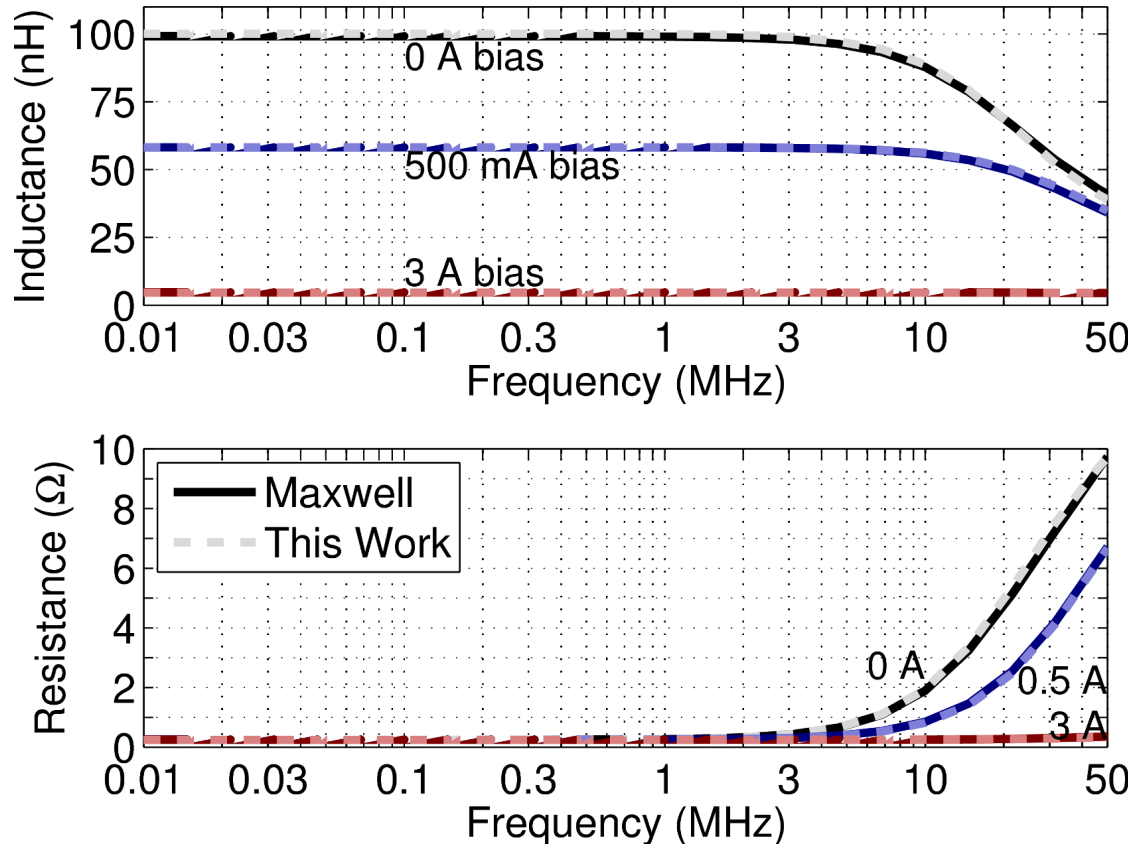


Figure 4.12: Small-signal impedance versus frequency and bias current for port 1 with port 2 open showing comparison between fitted Spectre model and Maxwell “measurements” for device 1.

to Maxwell is shown in Figs. 4.12, 4.13, and 4.14.

4.5.1.2 Validation Performance

The application of device 1 is galvanic isolation of voltage signals between circuit domains. A small-signal sinusoidal voltage was applied directly to the port 1 terminals and a $50\ \Omega$ load was placed across the port 2 terminals. The plot of

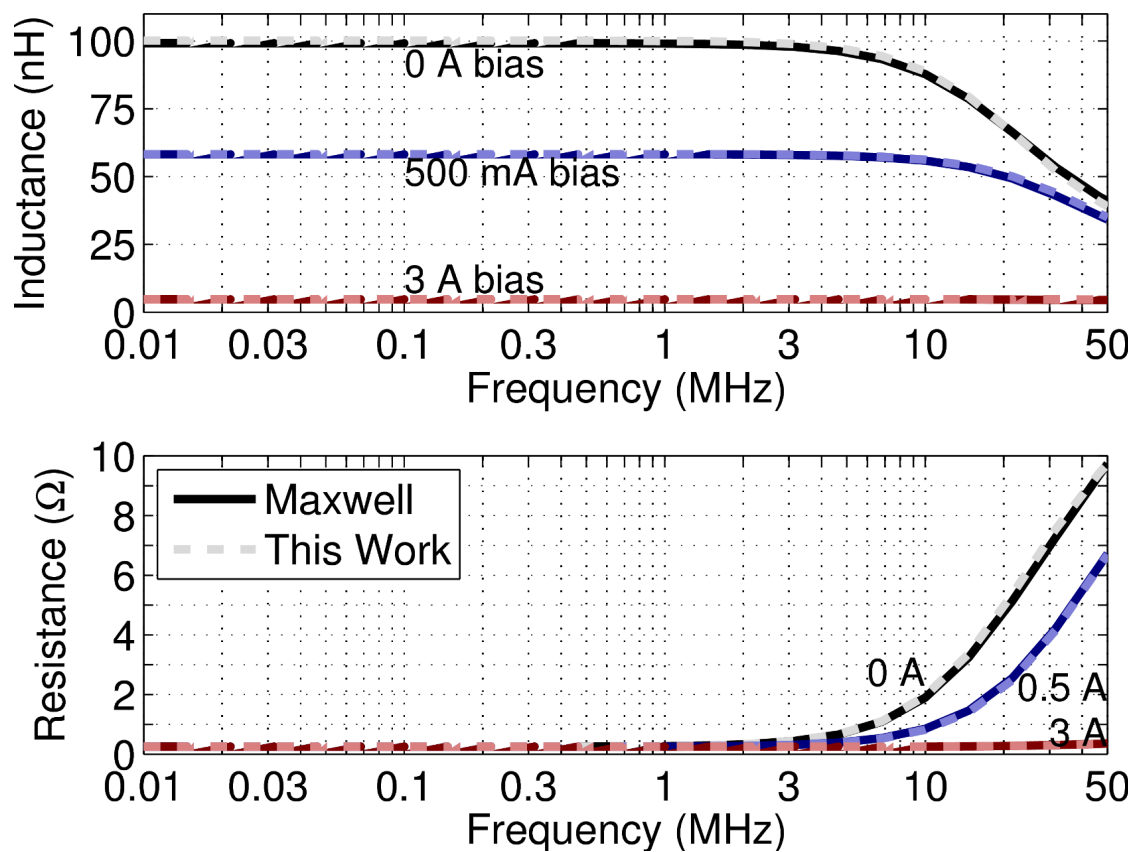


Figure 4.13: Small-signal impedance versus frequency and bias current for port 2 with port 1 open showing comparison between fitted Spectre model and Maxwell “measurements” for device 1.

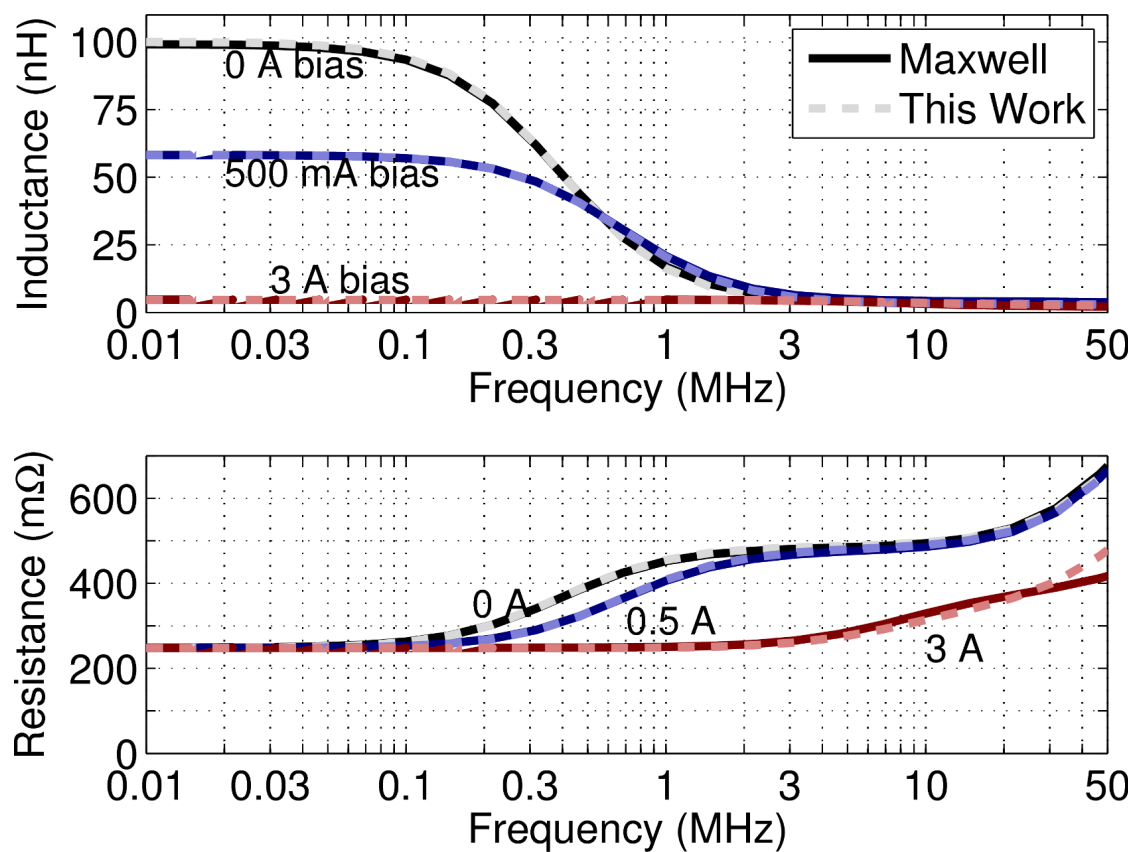


Figure 4.14: Small-signal impedance versus frequency and bias current for port 1 with port 2 shorted showing comparison between fitted Spectre model and Maxwell “measurements” for device 1.

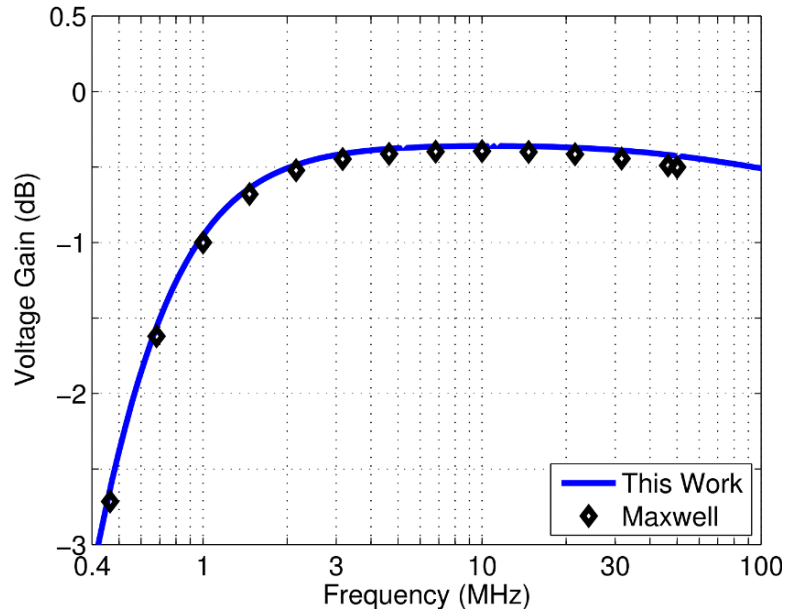


Figure 4.15: The small-signal voltage gain between port 1 and port 2 of an isolation transformer versus frequency when a $50\ \Omega$ load is placed across port 2. Solid line is Spectre model, and data points are field solver simulations.

the voltage gain in dB for both the Spectre model and the Maxwell simulation are shown in Fig. 4.15 for frequencies from 400 kHz to 100 MHz. The gain is greater than -0.5 dB for 2.5 to 80 MHz, and this gain is matched to within 0.49% by the Spectre Model.

The load was reduced to $1.6\ \Omega$ to test if the model still accurately predicts the transient terminal characteristics under heavy load. With a 4 V amplitude sinusoidal input voltage at 7 MHz, the peak transient current was simulated with the field solver to be 10 A which was reproduced by the Spectre model. The large signal input current and port 2 output voltage are shown in Fig. 4.16 for the initial two periods. This work's model matches the field solver output voltage waveform

Table 4.2: Comparison of simplified microtransformer models and our model using the Maxwell simulation as a reference to calculate errors for device 1.

	Linear 8th Order	Nonlinear 5-Element	This Work	Maxwell Ref.
Open 1 $Z(I, f)$ Error	N/A	N/A	6.2%	0%
Open 2 $Z(I, f)$ Error	N/A	N/A	6.9%	0%
Open 1 $Z(I, f)$ Error	N/A	N/A	6.6%	0%
$i_{in}(t)$ Error	65%	23%	13%	0%
$v_{out}(t)$ Error	32%	17%	4.1%	0%
$max(i(t))$	3 A	12 A	10 A	10 A

with 4.1% error, whereas the linear 8th order model of Fig. 4.9 is in error by 32% and the nonlinear 5-element model of Fig. 4.8 is in error by 17%. Table 4.2 summarizes the performance of device 1.

4.5.2 Device 2 Simulation

The second test device is a 3:3 interleaved racetrack microtransformer, similar to the previous device 1 microtransformer. The application is an isolated DC-to-DC converter known as a flyback converter rather than the isolation transformer of device 1. Similar to device 1, we can approximate the microtransformer by removing the bends not covered by magnetic material, and then simulate a short section of the straightaway. This is again due to the large dimensions of the whole device relative to skin depth. To estimate the characteristics of the full racetrack we then multiply the impedance by the fractional ratio. Figure 4.17 shows a perspective view for the Maxwell [115] simulation of the section, and a

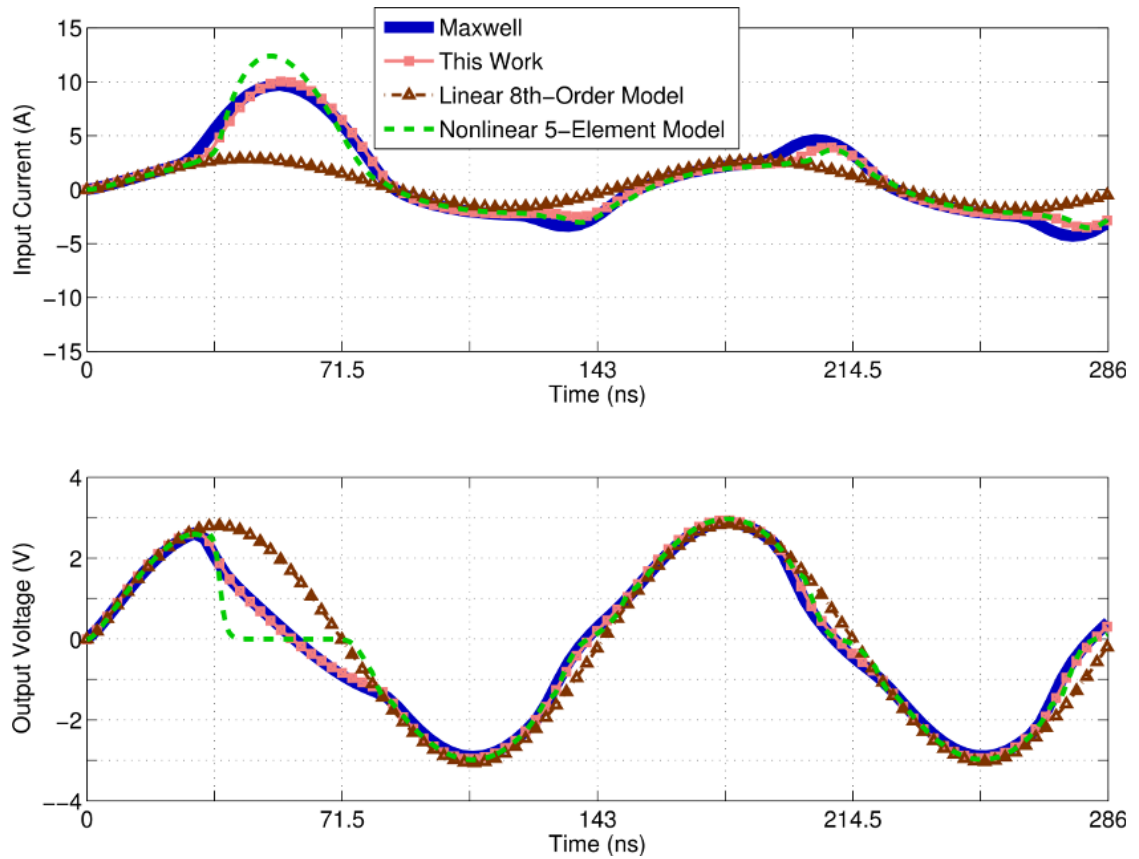


Figure 4.16: Large-signal input current and output voltage waveforms for the device 1 isolation transformer with 1.6Ω load at 7 MHz with a 4 V sinusoidal input. “Linear 8th-Order Model” is simplified circuit of Fig. 4.9 and “Nonlinear 5-Element Model” is simplified circuit of Fig. 4.8.

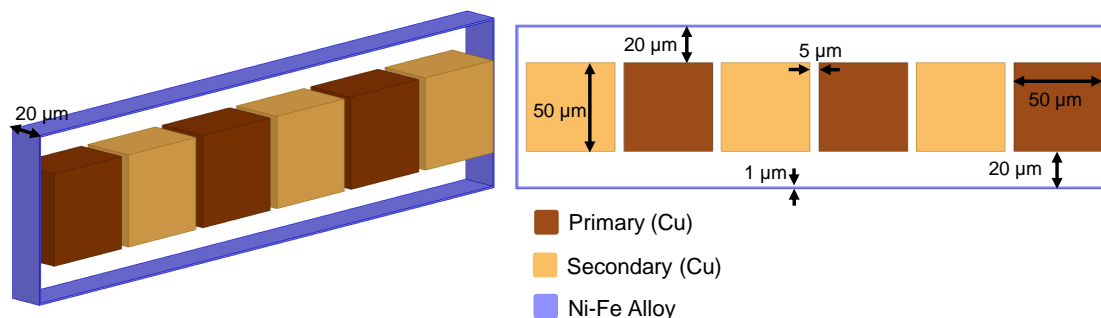


Figure 4.17: Ansys Maxwell layout in 3-D of reduced-length device 2 microtransformer and 2-D cross-section showing dimensions.

2-D cross-section showing the dimensions. The separation between the conductors may be difficult to manufacture in practice, regardless, the results here should be extendable to more realistic designs. The conductors are made of copper, and the core material is a Ni-Fe alloy with resistivity $17 \mu\Omega\text{cm}$ and a hyperbolic tangent M-H behavior as in (3.7a), with $M_S = 9.08 \times 10^5 \text{ A/m}$ and $g = 3.16 \times 10^{-4} \text{ m/A}$. The overall length of the microtransformer is 20 mm, which was scaled by a factor of 1000 to simulate in the field solver.

4.5.2.1 Model Fit

The three small signal impedance measurements of Fig. 4.6 were obtained via the Maxwell field solver [115] at 24 frequencies logarithmically spaced from 1 kHz to 500 MHz and 12 bias currents from 0 to 3 A. Similar to device 1, we approximated the core as saturating uniformly and simulated 12 individual eddy current analyses having different permeabilities to the core. This approximation is justified by the thin core thickness relative to its long magnetic path length.

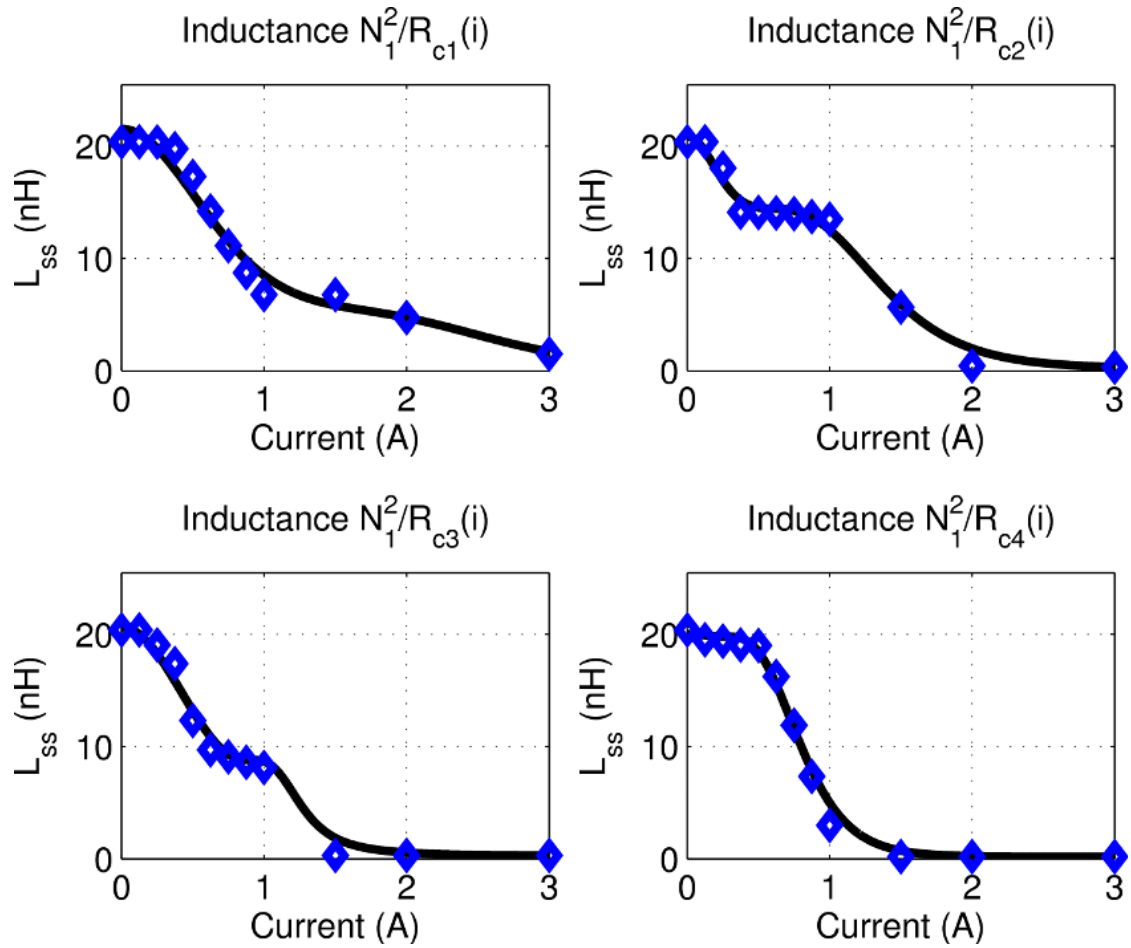


Figure 4.18: Port 1 reflected inductance for \mathcal{R}_{c1} through \mathcal{R}_{c4} for the device 2 flyback microtransformer. The data points are the optimal reflected inductances from stages 1 through 3 of the algorithm, and the curve is the fit to these points.

The developed extraction algorithm from Section 4.4 took 5 minutes on a 3.2 GHz Pentium[®] 4 workstation to generate the complete Spectre model from the field solver data. The element values and nonlinear reluctance parameters can be found in Appendix D.2. The four static nonlinear core inductances fit their optimum values with L2-norm errors less than 7.5% (See Fig. 4.18). Combining the L2-norm errors in resistance and inductance at each bias current in a root-mean-square sense gives an error in the “open 1” measurement of 6.7%, an error in the “open 2” measurement of 7.9%, and an error in the “short 1” measurement of 9.8%. (see Table 4.3). The larger error in the “short 1” performance is likely do to the leakage inductance varying at larger bias currents, which isn’t captured by the model of Fig. 4.4. The comparison of the small-signal impedance of the model to Maxwell is shown in Figs. 4.19, 4.20, and 4.21.

4.5.2.2 Validation Performance

The application of device 2 is the isolated converter known as a flyback converter. This converter is a DC-to-DC switching converter and the basic flyback circuit topology used to validate device 2 is provided in Fig. 4.22. For the device 2 microtransformer we found an acceptable efficiency converting from 4.5 V to 2.25 V at 140 MHz with a 20 ohm load resistance. To smooth the output voltage ripple, C_{out} was 5 nF. Both the circuit model and the Maxwell field solver model were placed in a time domain simulation of the flyback converter. The converter reached steady-state after about 250 ns, after which the current and power loss waveforms

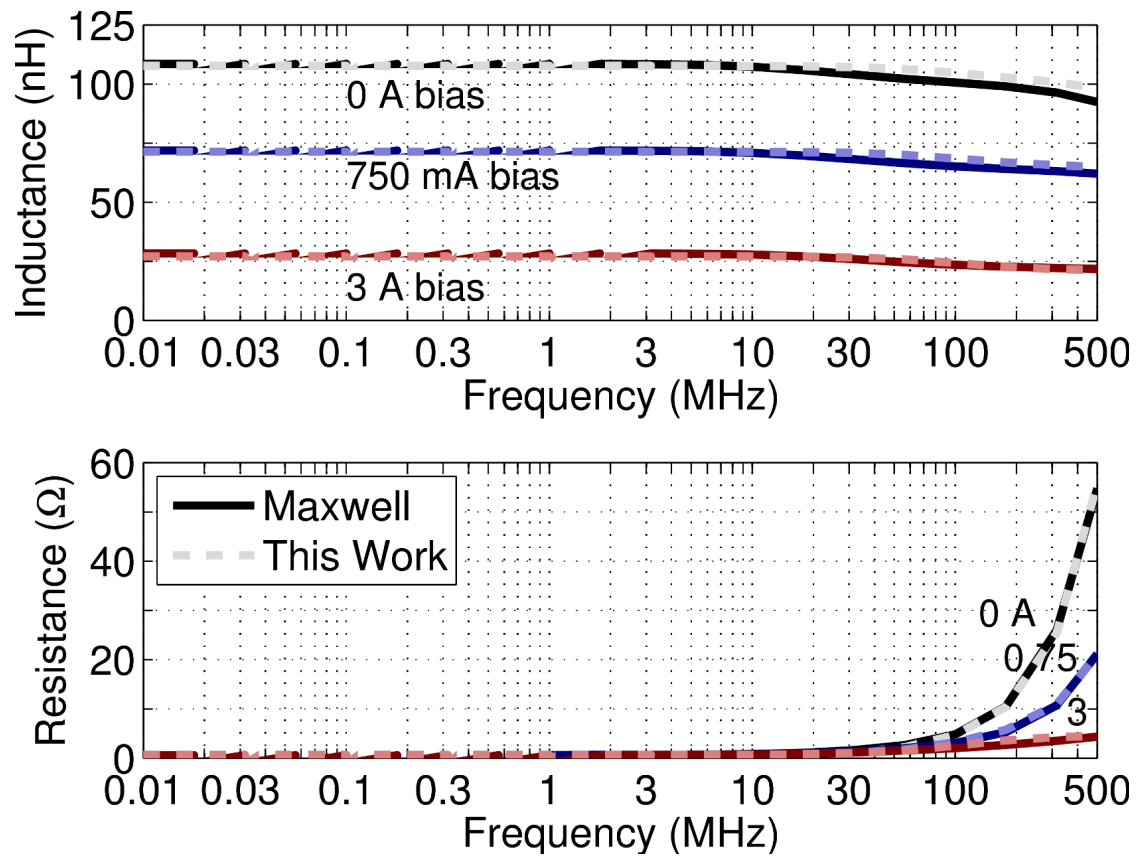


Figure 4.19: Small-signal impedance versus frequency and bias current for port 1 with port 2 open showing comparison between fitted Spectre model and Maxwell “measurements” for device 2.

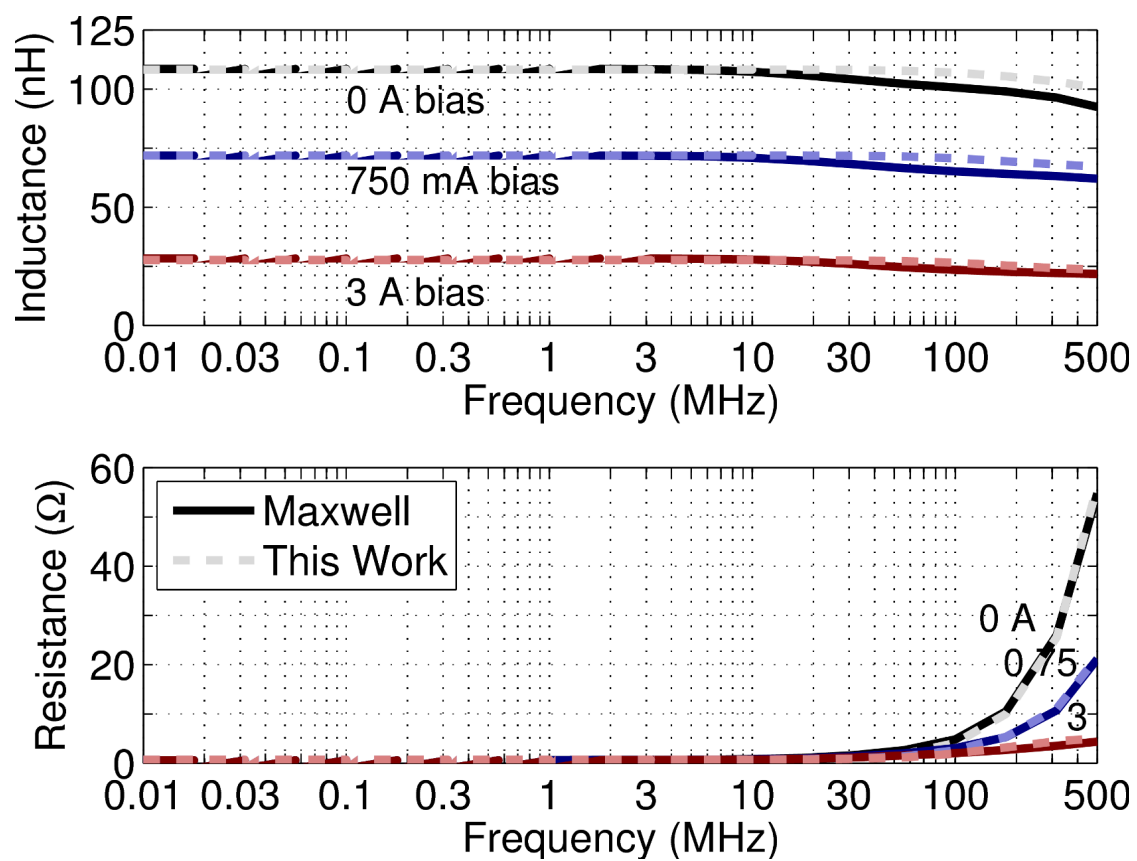


Figure 4.20: Small-signal impedance versus frequency and bias current for port 2 with port 1 open showing comparison between fitted Spectre model and Maxwell “measurements” for device 2.

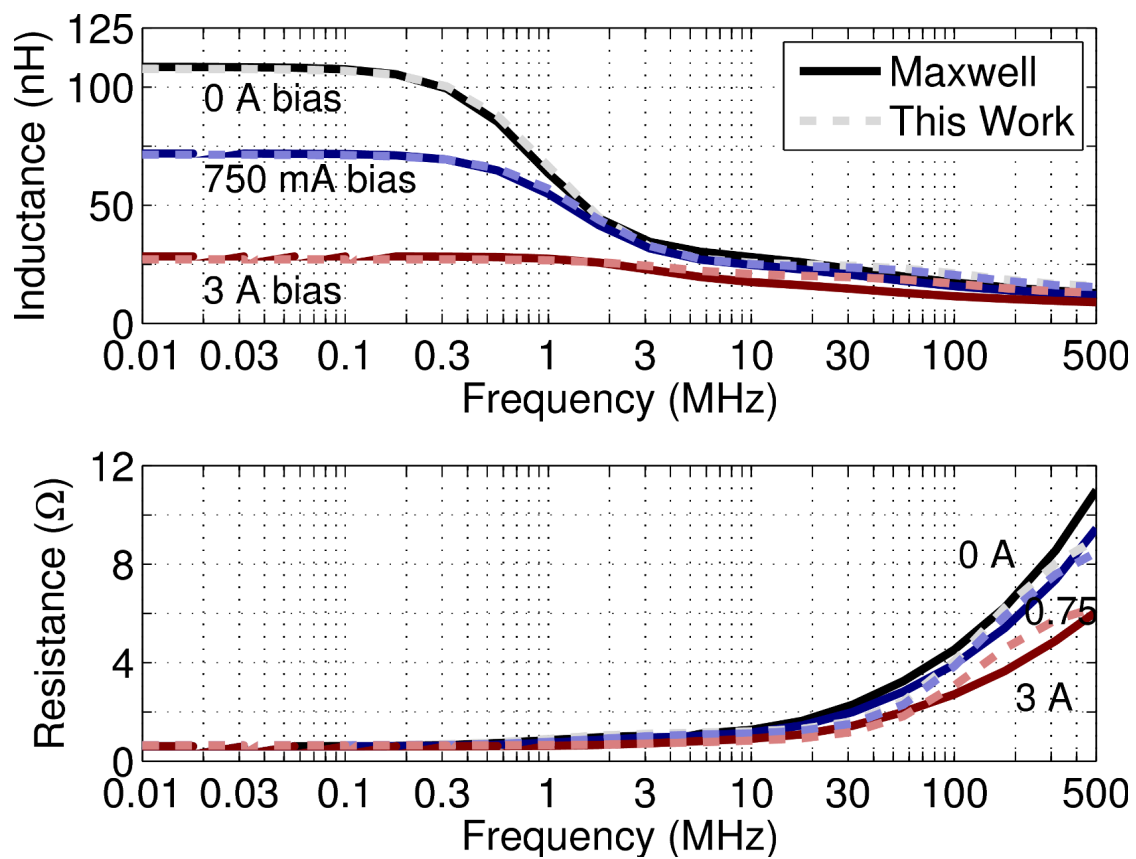


Figure 4.21: Small-signal impedance versus frequency and bias current for port 1 with port 2 shorted showing comparison between fitted Spectre model and Maxwell “measurements” for device 2.

were recorded.

Due to time constraints, the field solver simulation had a course mesh (34 μm RMS edge length in core material) and a large time step of 100 ps. We believe these factors contribute to the errors present in the following comparison, during the last two periods from 256 to 271 ns. The average output power from Maxwell was 320 mW, which this thesis's model captured within 10%, the nonlinear 5-element model of Fig. 4.8 was in error by 27%. The linear model of Fig. 4.9 performed well with just 4.7 % error in output power, but this is believed to be an indication of the inaccurate field solver solution. The efficiency of the field solver was likely over estimated at 70.3% and we believe a more accurate field solver simulation would produce an efficiency more similar to this thesis's model of 64.7%. The efficiency is calculated through the average instantaneous power loss waveform, and the average output power. A comparison of the instantaneous power loss waveform for the last two periods is provided in Fig. 4.23. The field solver simulation, this thesis' model, the linear model and the nonlinear 5-element model all accurately captured the microtransformer's output current waveform well with none having an L2-norm error greater than 4.5%⁴ (see Fig. 4.24). For a summary of these number and more comparisons refer to Table 4.3.

⁴The reference is taken to be the Maxwell field solver measurements.

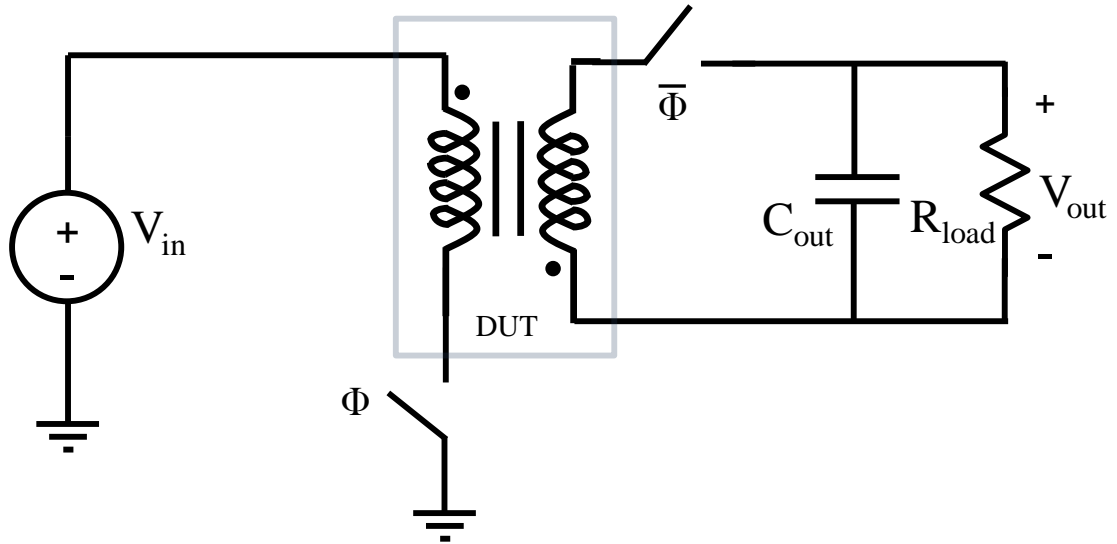


Figure 4.22: Isolated flyback converter circuit used to validate device 2. The two switches are controlled by 50% duty cycle complementary clocks and R_{load} represents the output load.

Table 4.3: Comparison of simplified microtransformer models and our model using the Maxwell simulation as a reference to calculate errors for device 2.

	Linear 8th Order	Nonlinear 5-Element	This Work	Maxwell Ref.
Open 1 $Z(I, f)$ Error	N/A	N/A	6.7%	0%
Open 2 $Z(I, f)$ Error	N/A	N/A	7.9%	0%
Open 1 $Z(I, f)$ Error	N/A	N/A	9.8%	0%
$i_{out}(t)$ Error	3.2%	4.2%	3.3%	0%
$P_{out,ave}$	304 mW	233 mW	287 mW	320 mW
$P_{loss,ave}$	141 mW	33.2 mW	157 mW	135 mW
Efficiency	68.4%	87.5%	64.7%	70.3%

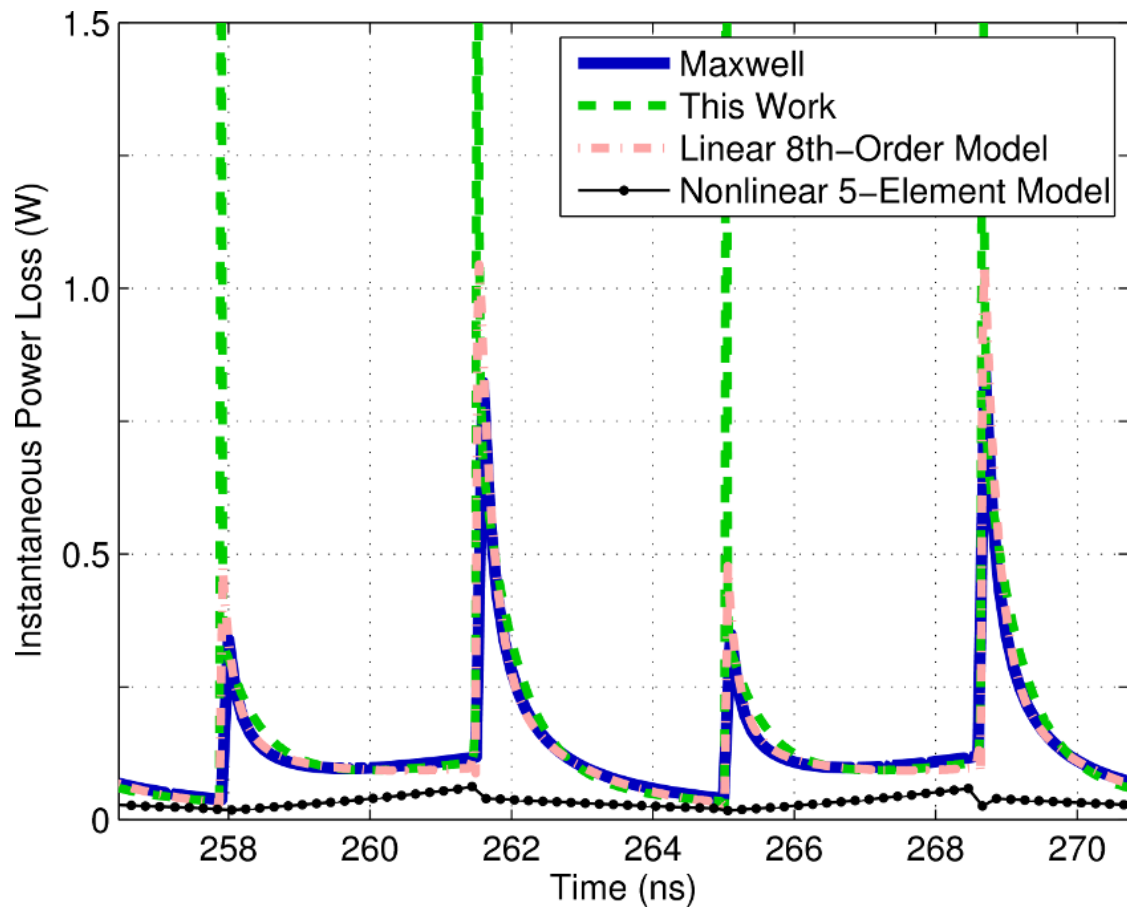


Figure 4.23: Comparison of the instantaneous power loss waveform used to calculate the device 2 microtransformer efficiency in a flyback converter application. The “Linear 8th-Order Model” is simplified circuit of Fig. 4.9 and “Nonlinear 5-Element Model” is simplified circuit of Fig. 4.8.

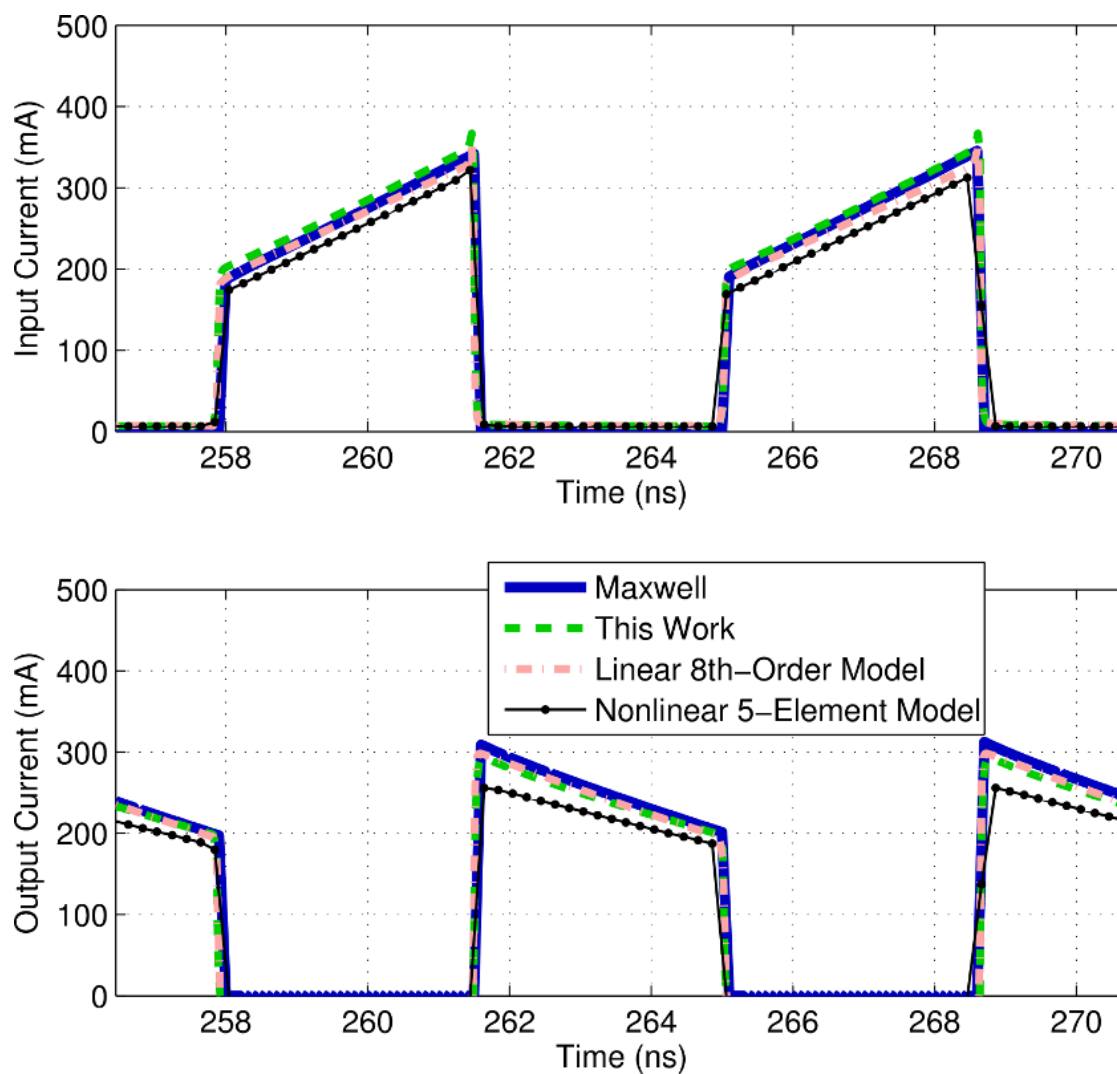


Figure 4.24: Comparison of the device 2 microtransformer’s input current (top) and output current (bottom) when models are placed in a flyback converter with a $20\ \Omega$ load. The “Linear 8th-Order Model” is simplified circuit of Fig. 4.9 and “Nonlinear 5-Element Model” is simplified circuit of Fig. 4.8.

4.5.3 Device 3 Measurements

The previous biased small-signal data have been obtained with magnetoquasistatic field solvers. This ignores the effect of displacement currents and the capacitive portion of the model. To confirm the model works when all relevant effects are present, actual device measurements were used to generate the model. The three measurement configurations from Fig. 4.6 were setup for a packaged 18:18 microtransformer with a thin film alloy with a low coercivity. Small-signal impedance measurements were performed with an Agilent 4294A precision impedance analyzer, and the microtransformer was biased through an Agilent 16200B external DC bias adapter using a Keithley 2410 1100V source meter. For each setup, 201 logarithmically-spaced frequency points from 2 to 110 MHz were measured at 6 bias currents from 0 to 500 mA. Unfortunately we have no verification measurements for this microtransformer, therefore we can only judge the model performance on how well we match the measurements used to generate the model.

4.5.3.1 Model Fit

Altogether the four stages of the fitting algorithm took less than 8 minutes for $N = 4$ and $M = 2$, with 35 generations of population 500 for each use of the genetic algorithm. The computer used was a 3.2 GHz Pentium[®] 4 workstation. The element values and nonlinear reluctance parameters can be found in Appendix D.2. The fit of the shifted hyperbolic tangent nonlinear core reluctances as inductances reflected to the primary side is shown in Fig. 4.25. The errors in these inductors

range from 4% to 12%, but could be reduced with a higher number of unique hyperbolic tangent functions than the three used. Combining the L2-norm errors in resistance and inductance at each bias current in a root-mean-square sense, gives an error in the “open 1” measurement of 8.6%, an error in the “open 2” measurement of 10%, and an error in the “short 1” measurement of 8.4%. The comparison of the small-signal impedance of the model to the measurements is shown in Figs. 4.26, 4.27, and 4.28.

4.6 Conclusions and Future Work

In this section we first present the conclusions of this chapter on microtransformer modeling. Next, improvements of the model that verify more rigorously the performance and enable the use of a wider range of materials are proposed. These improvements fall under the category of future work to be accomplished on the model.

4.6.1 Conclusions

We have presented a physically motivated nonlinear frequency-dependent model for microtransformers with alloy thin-film cores in the context of current literature. The model is obtained from terminal characteristics rather than knowledge of material parameters and geometry, giving a unique advantage since thin-film magnetic properties are process and dimension dependent. This allows using wafer-

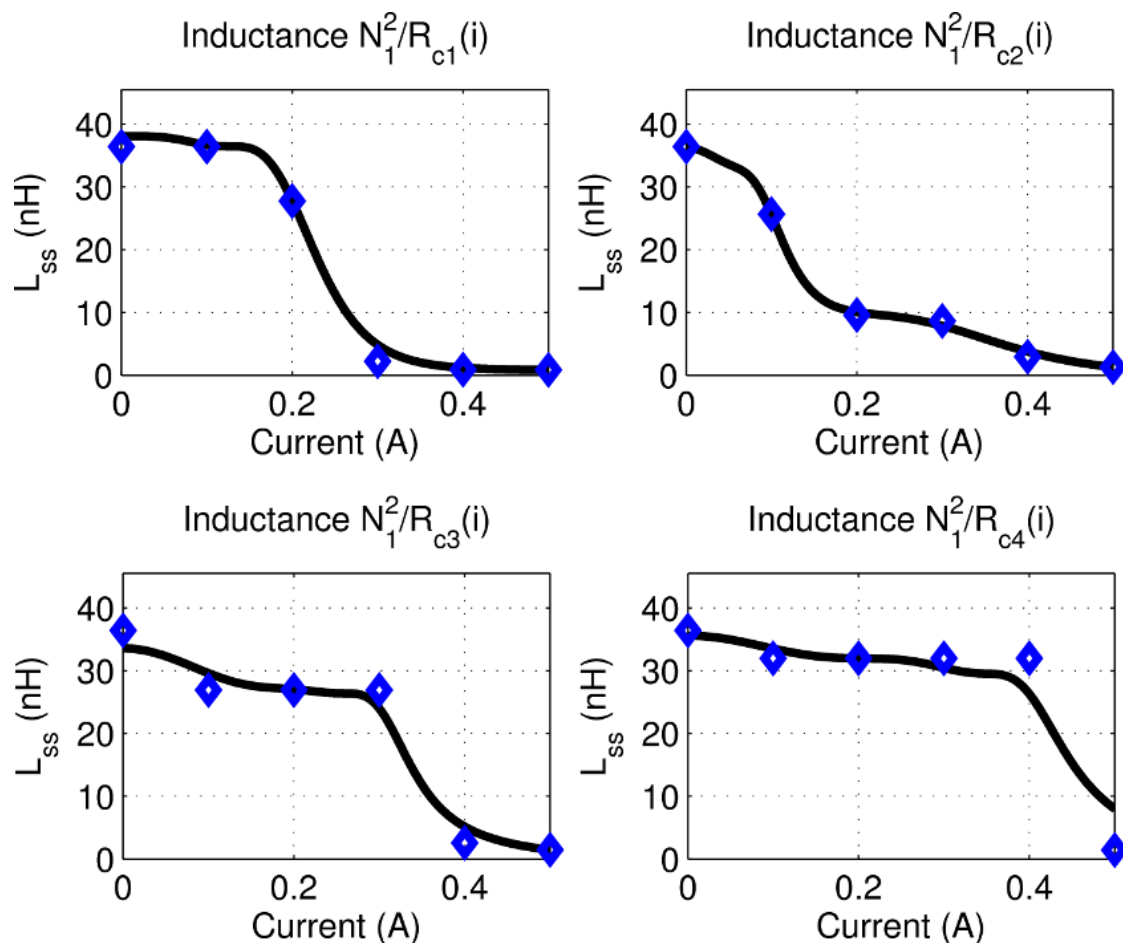


Figure 4.25: Port 1 reflected inductance for \mathcal{R}_{c1} through \mathcal{R}_{c4} for the device 3 microtransformer. The data points are the optimal reflected inductances from stages 1 through 3 of the algorithm, and the curve is the fit to these points.

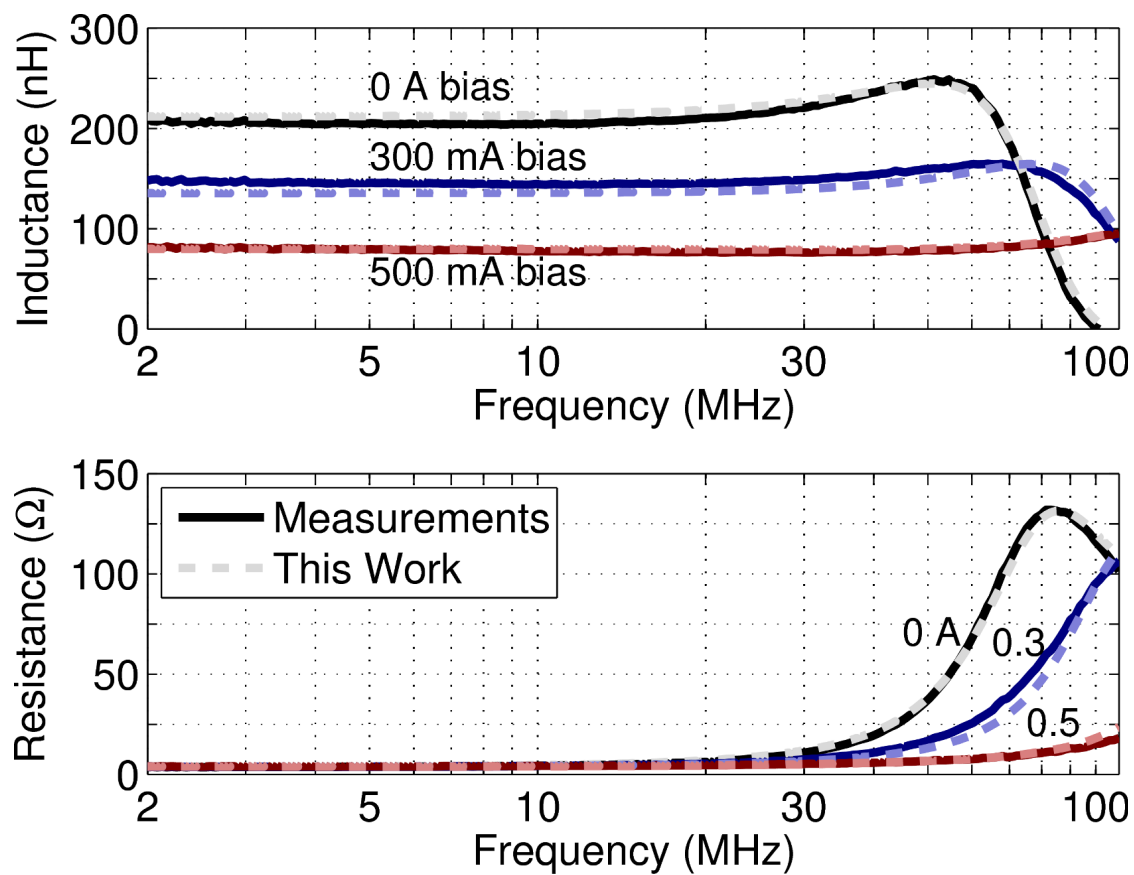


Figure 4.26: Small-signal impedance versus frequency and bias current for port 1 with port 2 open showing comparison between fitted Spectre model and fabricated device measurements for device 3.

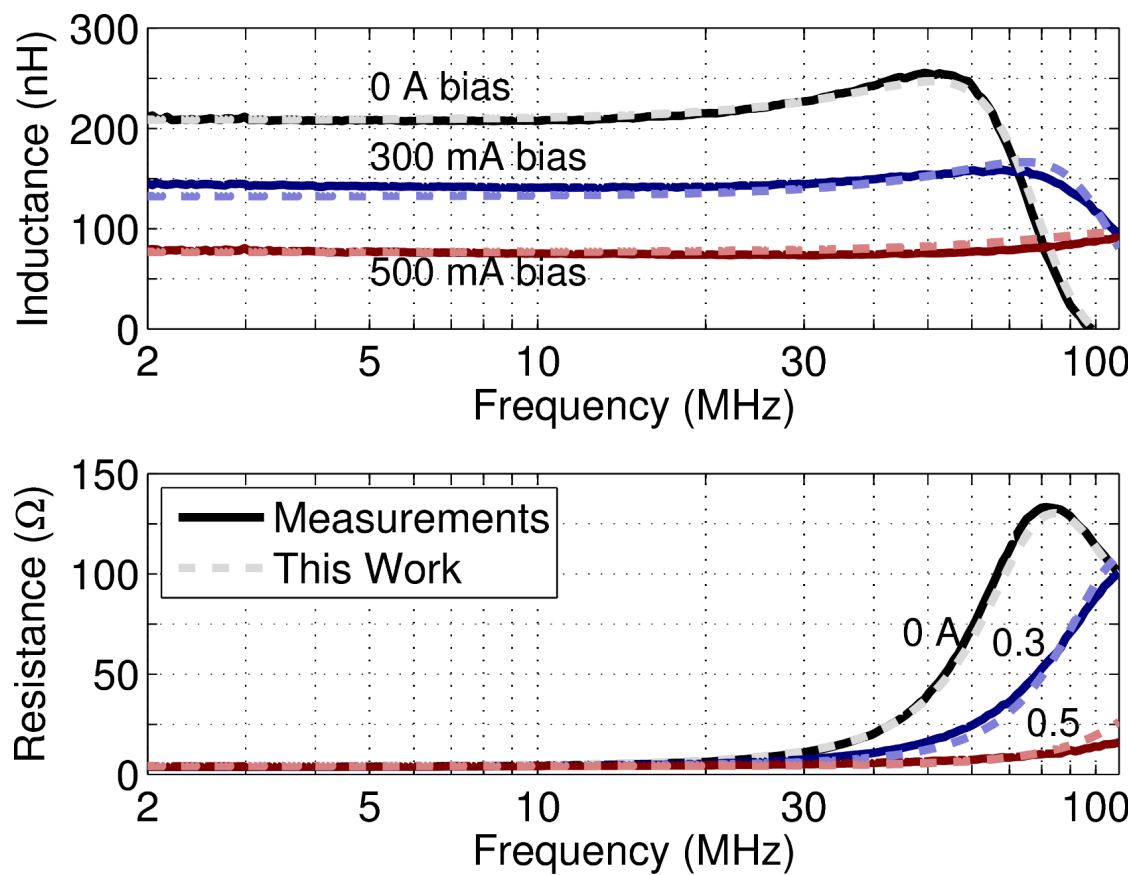


Figure 4.27: Small-signal impedance versus frequency and bias current for port 2 with port 1 open showing comparison between fitted Spectre model and fabricated device measurements for device 3.

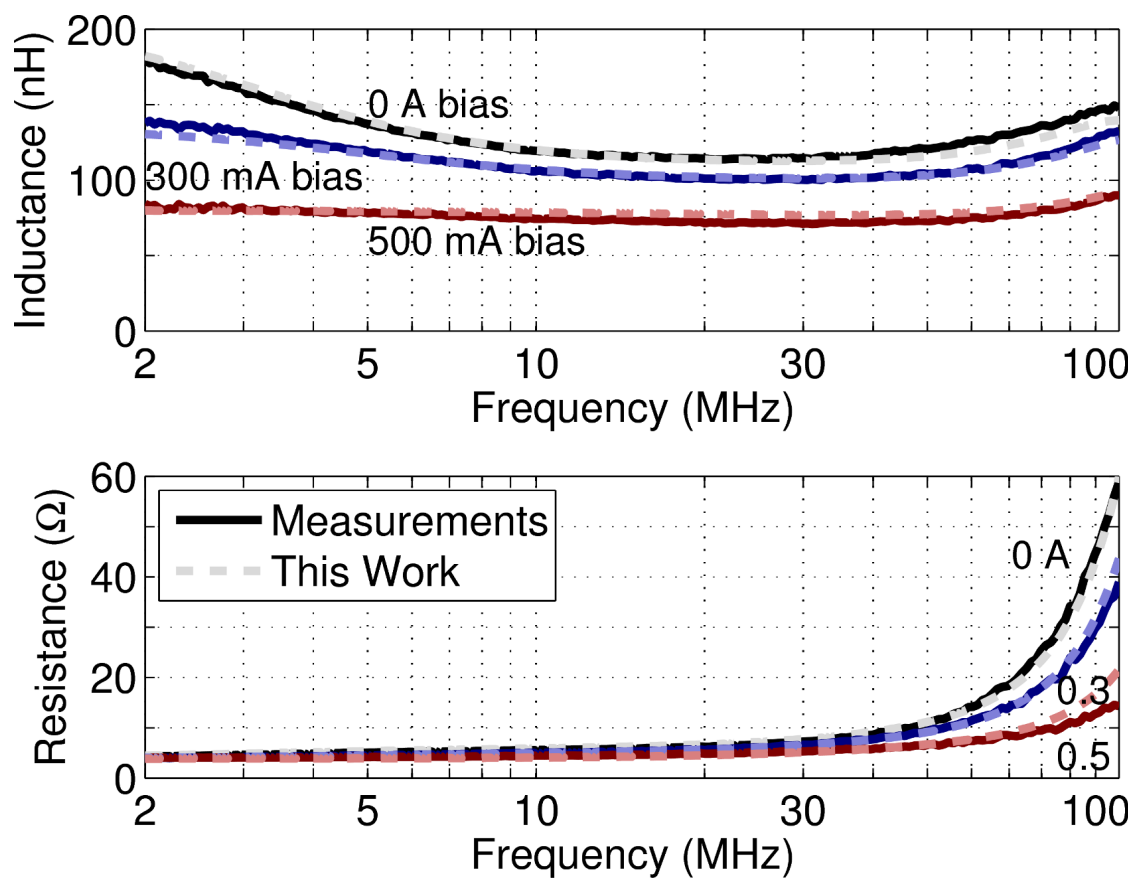


Figure 4.28: Small-signal impedance versus frequency and bias current for port 1 with port 2 shorted showing comparison between fitted Spectre model and fabricated device measurements for device 3.

level compatible measurements (or a field solver) to generate an accurate model. The measurements are the accessible small-signal impedance measurements with an applied DC current bias, and ideal loads applied to the unmeasured port. We have also presented a unique, fast algorithm capable of generating the compact model in Spectre or SPICE from these measurements. Since commercial circuit simulation tools (e.g. those from Cadence [68]) directly simulate behavioral circuit elements, the presented methodology is compatible with most commercially available circuit simulators. Using the proposed algorithm and nonlinear static inductance expression, the model is guaranteed passive.

To demonstrate the performance and applicability of our model to complete circuit solutions we have simulated a 2:2 microtransformer in a signal isolation circuit and a 3:3 microtransformer in a flyback converter circuit. Both models accurately capture the biased small-signal measurements with errors less than 10%. The isolation microtransformer accurately captured the small-signal frequency-dependent voltage gain, the output voltage waveform, and the peak input current with errors under 4.2%. Other simpler microtransformer models, failed to capture the behavior of this device correctly. The flyback converter estimated the power loss to within 10% and the efficiency to within 5.7%. However, we believe more accurate could be obtained with finer discretization and time step. Our model is physically motivated and should be amenable to the addition of other effects, including ferromagnetic resonance and hysteresis.

4.6.2 Future Work

There are several steps that could be undertaken to improve and further validate the model. For example, no time-domain application measurements were available for the fabricated microtransformer topology to confirm its accurate behavior. Performing such measurements is the most important future work to be accomplished. Additionally, a rather coarse time-domain field solver analysis was used to validate device 2 microtransformer. Improving the mesh and time step of the field solver simulation, making the design easier to fabricate, and providing transient data under heavy load would all aid in validating the model presented in this chapter.

To enable the use of materials with a significant coercivity, the addition of hysteresis needs to be made. The Jiles-Atherton implementation of hysteresis discussed in Section 2.2.2 can be implemented with our shifted hyperbolic tangent function as the anhysteretic magnetization behavior. If accurate large-signal M-H plots showing the hysteresis of the material could be made, we simply need to add the domain wall flexing constant, c , and domain wall pinning constant, k , from [79]. Another approach is a more significant alteration on the work presented here. Since the effects of hysteresis may not show up in the small-signal analysis, additional measurements, where hysteresis is included, could enable a new extraction algorithm. Large signal sinusoidal terminal measurements could possibly serve as the needed additional measurements.

If the frequency or material is altered it may be necessary to include the effects of ferromagnetic relaxation/resonance (FMR) from Section 2.2.3. As was shown

in that section, the Hammerstein configuration of a second order linear block after the M-H block, would enable the inclusion of FMR into each nonlinear reluctance, \mathcal{R}_{cn} of our model in Fig. 4.4. However, there maybe a way to transform FMR to its effects on domain-wall dynamics [62, 91, 92]. In general, we need to add the two FMR parameters (ω_n and λ) to our fitting procedure. Fortunately, FMR impacts biased small-signal measurements, and should be distinguishable form the capacitive resonance already included.

Chapter 5 – Microfluxgate Model

5.1 Introduction

The third device category considered in this thesis adds the complexity over the transformer of two cores and an externally applied field in a dual-core fluxgate. The interaction between the nonlinear cores and the externally applied field is integral as this is how a fluxgate senses the magnitude of the external field in a certain direction. If two fluxgates are used (or one two-axis fluxgate), they can together be used as an electronic compass, or eCompass. They can also sense the strength of the magnetic field once properly calibrated and thus be used as magnetometers. This, together with their use as indirect current inspectors, gives them applications in physical sciences, modern aviation, space exploration, and even consumer electronics [35].

The design for which a circuit model will be generated is the dual-core solenoidal design. Dual-core microfluxgates have a number of examples in literature [39–41], and a simplified diagram is shown in Fig. 5.1(a). In this design the drive coil excites oppositely directed magnetic fields (odd mode) for the two parallel cores and the sense coil picks up even mode changes in core flux. Two fluxes are shown for a combination of even and odd mode excitations in Fig. 5.1: Φ_A , that passes through either core and its air/dielectric surrounding, and Φ_{link} , that links the two

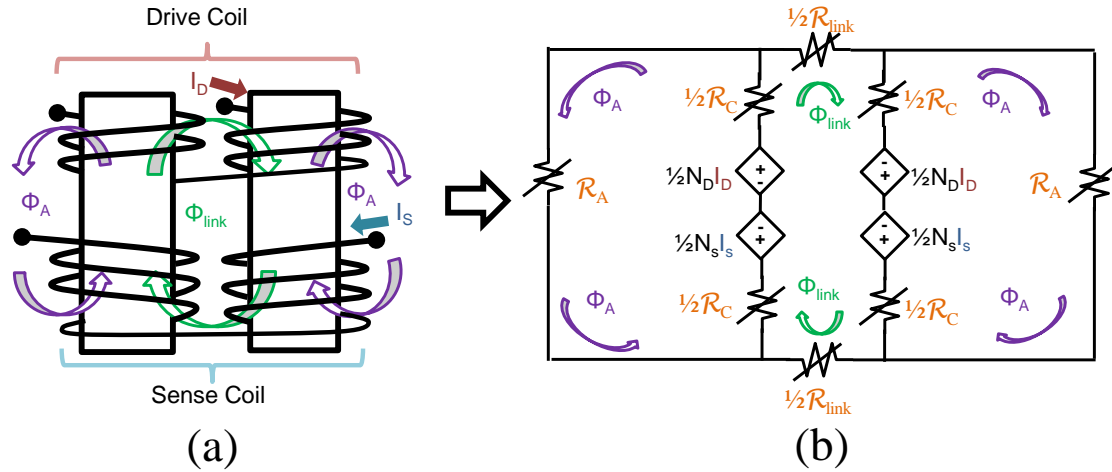


Figure 5.1: Simplified schematic of dual-core solenoidal microfluxgate (a) and equivalent magnetic circuit based on flux paths, Φ_A and Φ_{link} (b).

cores together through the surrounding air/dielectric. The reluctance \mathcal{R}_C has both Φ_A and Φ_{link} flowing through it and is mainly in the core material. Reluctance \mathcal{R}_A (\mathcal{R}_{link}) carries flux Φ_A (Φ_{link}) alone, and both include some air/dielectric reluctance. Considering this we can develop an expanded magnetic model as provided in Fig. 5.1(b). An additional external magnetic field will behave as an even mode magnetomotive force similar to the sense coil's current.

This chapter reviews the current state-of-the-art modeling techniques applicable to dual core flux-gates, showing the novelty of the model in this thesis. Next, the model's circuit topology is developed in detail, including the novel magnetic domain circuit, which is simplified from Fig. 5.1(b). In Section 5.4 a simple algorithm is presented to fit the model to a unique set of easily made measurements, guaranteeing an accurate and passive model. In Section 5.5 the model is validated by reproducing the terminal characteristics in the time-domain when an external

field is present for both a simulation and actual device measurements. Finally, this chapter provides a section on future work and conclusions for the microfluxgate model.

5.2 Literature Review

5.2.1 Theoretical Models

For off-chip fluxgates their behavior, to first order, can be described by theoretical analysis of the nonlinearity in the core. A analytic model from 1967 [148] initially performs perturbation analysis on a single core fluxgate. Then, with the aid of a simple power function for $\mu_r(H)$, the authors calculate the sense coil voltage for a square wave excitation on the drive coil. Another theoretical analysis was performed in [149] for a ring-core fluxgate. Making use of Heavyside step functions to approximate $\mu_r(H)$ and a sinusoidal voltage on the drive coil, [149] proceeds to derive a formula for the second harmonic voltage amplitude on the sense coil.

Both of these types of theoretical models can be extended to the dual-core fluxgate with the addition of a demagnetization effect, and a second core. However, they are not suitable for creating a circuit model. Moreover, these models do not calculate the input current to the drive coil, the effect of a load on the sense coil, or any resistive impacts.

5.2.2 Existing Circuit Models

As fluxgates have transitioned to microfluxgates (on chip), more modern models of microfluxgates have become available. Reference [150] developed a circuit model in the magnetic domain for a ring-core microfluxgate. Although hysteresis is included in the core, many effects are still ignored. For one, it is not a full four-terminal model and does not calculate the effect of any loading on the sense coil. Moreover, the drive coil is assumed to be linear, although when the core saturates during normal operation the effective inductance should decrease. Ignoring these effects make the model in [150] physically inconsistent.

Another, more recent microfluxgate model is presented in [151]. The model is implemented in SPICE and is a true four-terminal device model of a dual-core solenoidal flux-gate, similar to this work. The model is implemented entirely in the electric domain making the addition of any higher order magnetic effects difficult to include, and the effect of magnetic field less intuitive. Moreover, the terminal measurements of the device is not directly used in the model extraction, but rather an estimate of the core's $\mu_r(i)$ is used. No general extraction algorithm is presented.

5.3 Model Development

5.3.1 Model Circuit Topology

The model proposed in this thesis for dual-core microfluxgates is presented in Fig. 5.2. The model is separated into the electric domain and the magnetic domain. Although Fig. 5.2 uses behavioral controlled sources to couple the two domains, four differential gyrators (see Appendix B.1) could also be used. The number of turns relate the two domains, and N_D (N_S) is the total number of turns to the drive (sense) coil around both cores. The electric domain consists of the DC conductor resistances and the linear leakage¹ inductances of the drive and sense coils at their respective ports. The controlled sources in the electric domain couple the time derivative of the odd flux linkage for the drive coil and the even flux linkage for the sense coil. The magnetic domain is a simplification of the circuit in Fig. 5.1(b) representing the physical topology of the dual core microfluxgate. For even mode excitations,² the half circuit consists of the series combination of \mathcal{R}_C and \mathcal{R}_A together these form the effect of the core and its demagnetization, which is nonlinear. For odd mode excitations, the core has flux flowing mutually between the two cores, this is modeled by the nonlinear reluctance, \mathcal{R}_{link} which partially links the two cores. All of the nonlinear reluctances are implemented with the same behavioral function but having different parameter values (see Section 5.3.2).

¹The linear leakage inductance is any inductance that does not pass through the core material.

²Even mode excitations include the external magnetic field, H_{ext} , which is scaled by the length of the coil around one core, ℓ_c (See Fig. 5.2), to generate a magnetomotive force.

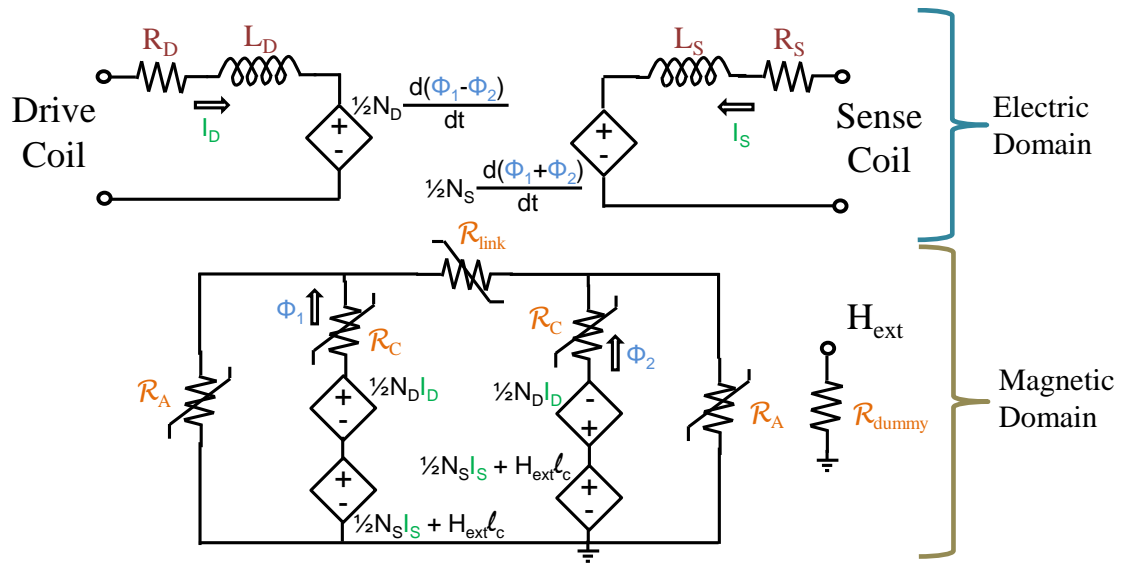


Figure 5.2: Compact equivalent circuit model of a dual-core microfluxgate. The circuit is broken up into the electric and magnetic domains.

5.3.2 Nonlinear Reluctances

The microfluxgate core network was best implemented in the magnetic domain. This allows an intuitive understanding of the major topology of the magnetic circuit. Also, nonlinear reluctances become dependent only on the flux through them, whereas, a nonlinear magnetizing inductance would have to be dependent on both the drive and sense coil currents separated by ideal transformers. In the magnetic domain, we implement the nonlinear reluctance, \mathcal{R}_{cn} , as a flux-MMF relationship.

The nonlinear reluctance model used for the microfluxgate is the same as that for the microtransformer from Section 4.3.2. The same benefits and key characteristics are desirable for the nonlinear reluctances of this chapter. For reference we

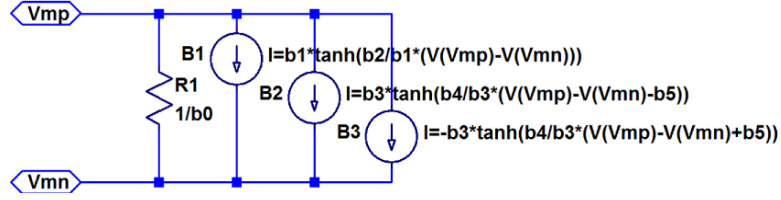


Figure 5.3: Possible LTspice subcircuit of a second order nonlinear reluctance described by (4.1). Magnetic domain terminals are Vmp and Vmn.

reproduce the permeance expression (4.2) as (5.1) below. Additionally the LTspice subcircuit implementing this behavior is reproduced in Fig. 5.3.

$$\begin{aligned}
 \mathcal{P}_{cn}(\mathcal{V}_{cn}) = & \beta_{0,n} + \beta_{2,n} \operatorname{sech}^2\left(\frac{\beta_{2,n}}{\beta_{1,n}} \mathcal{V}_{cn}\right) \\
 & + \sum_{i=1}^I \left(\beta_{3i+1,n} \operatorname{sech}^2\left(\frac{\beta_{3i+1,n}}{\beta_{3i,n}} (\mathcal{V}_{cn} - \beta_{3i+2,n})\right) \right. \\
 & \left. + \beta_{3i+1,n} \operatorname{sech}^2\left(\frac{\beta_{3i+1,n}}{\beta_{3i,n}} (\mathcal{V}_{cn} + \beta_{3i+2,n})\right) \right). \quad (5.1)
 \end{aligned}$$

5.3.3 Measurements Employed to Generate Model

Given that the microfluxgate is operated at a low frequency, we can ignore eddy-current effects as implied by the lack of ladder circuits in Fig. 5.2. To capture the behavior in the magnetic domain, we need to measure the nonlinear inductance versus bias current for the drive and sense coils. It is important that the bias current be applied to the same coil at which the inductance is measured. The electric domain can be obtained from the DC resistance of each coil and the assumption

that the linear leakage inductance is the measured inductance at core saturation.

The primary measurements needed are

$$Z_{drive}(I_{drive,j}) \Big|_{\text{low-frequency}} \quad (5.2a)$$

$$Z_{sense}(I_{sense,j}) \Big|_{\text{low-frequency}} \quad (5.2b)$$

If the device is to have physically meaningful magnetic circuit parameters, the number of turns for each coil should also be provided. Furthermore, if measurements in an external field³ are not possible, then the length of the coil around a single core needs to be provided (see ℓ_c parameter of Fig. 5.2).

5.3.4 Measurements Employed to Validate Model

A fluxgate is intended to measure the strength of the magnetic field. For a dual-core microfluxgate the average magnitude of the sense voltage should be proportional to the magnetic field applied along its axis. To validate our models we applied a sinusoidal drive coil current and observe the time-domain voltage across drive coil (See Fig. 5.4), and, more importantly, the sense coil making sure they both match for various applied magnetic fields. Additionally, the sensitivity plot of the average sense voltage magnitude for varying external magnetic fields will be

³External magnetic fields can be applied by placing the whole device in a Helmholtz coil.

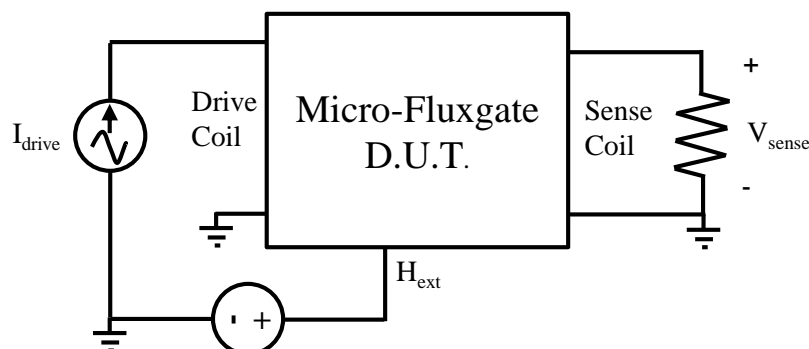


Figure 5.4: Application circuit for validating the dual-core solenoidal microfluxgate models in the time-domain using Spectre. The external voltage H_{ext} is the means by which the external field is applied to the model through a voltage-controlled voltage source with gain ℓ_c to the magnetic domain (see Fig. 5.2).

compared between our model and the target device.⁴

5.3.5 Novelty of This Model

The model of Fig. 5.2 has many advantages over the existing literature. When compared to theoretical models, this work does not need measurements of the actual demagnetization factor for a complicated nonlinear material, nor measurements of the nonlinear permeability. Moreover, this chapter’s model is physically consistent in that an input current in the drive coil is necessary to drive the device into saturation. Additionally, the resistive effects of both coils and the loading effects of the sense coil are accurately reproduced.

When compared to state-of-the-art circuit models [150, 151], there are also ad-

⁴Target device refers to either the measured fabricated device in a Helmholtz coil, or the field-solver simulated device.

vantages to using the approach of this chapter. The model of this chapter includes the effects of loading and resistance on each coil, unlike [150]. Furthermore, reference [150] uses a linear model of the drive coil, which is physically inconsistent with the operation of a fluxgate. Unlike [151], if higher order magnetic effects need to be included, the magnetic domain implementation of Fig: 5.2 makes it intuitive. Finally, the model proposed here is easily obtained from device terminal measurements, and does not require detailed knowledge of the magnetic material. To generate the model a simple extraction algorithm obtaining a passive and accurate fit is provided.

5.4 Model Extraction Algorithm

5.4.1 Algorithm Overview

There are 5 inputs to the model extraction algorithm: the coil length around a single core, the number of turns for the drive and sense coil around both cores, and the biased small-signal impedance measurements for each coil at low frequencies. The algorithm is broken up into three main stages as shown in Fig. 5.5. The first stage (Section 5.4.2) is the simplest and requires no optimization algorithm; it is the extraction of the electric domain parameters. The second stage (Section 5.4.3) is to model the sense coil's small-signal inductance versus bias current. This is done by approximating $\mathcal{R}_C + \mathcal{R}_A$ as a single nonlinear reluctance since \mathcal{R}_{link} is irrelevant to the sense coil's even mode excitation (see Fig. 5.2). The final stage

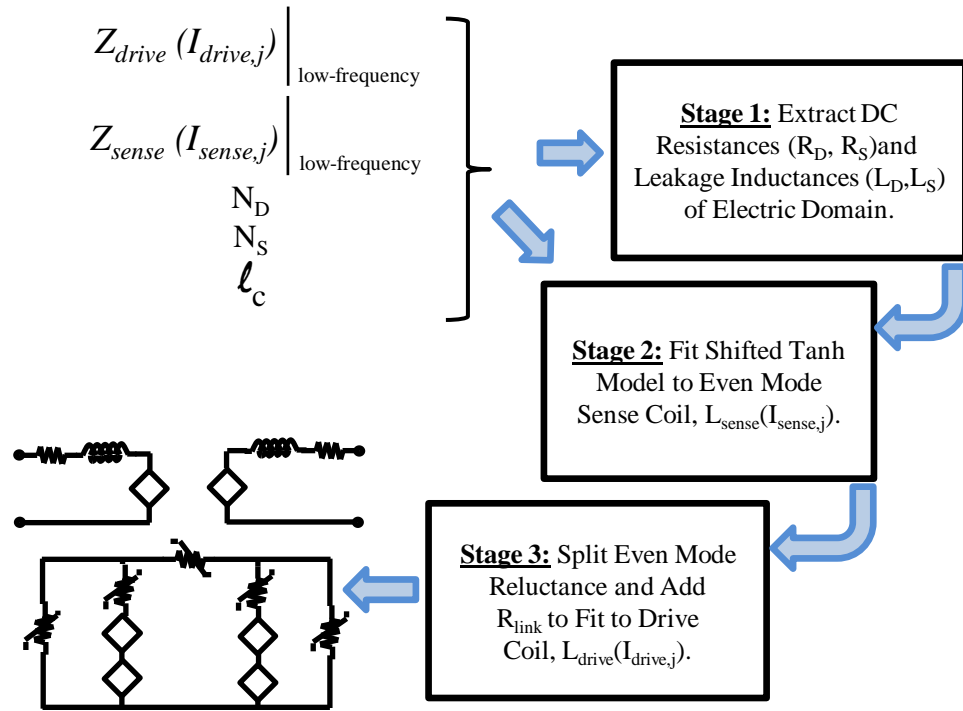


Figure 5.5: Flow chart of model extraction algorithm going from input measurements to output microfluxgate model with three intermediate stages.

(Section 5.4.4) is most involved. The drive coil's small-signal nonlinear inductance is used to find the optimal splitting of $\mathcal{R}_C + \mathcal{R}_A$ and the parameters that describe \mathcal{R}_{link} , thus completing the description of the magnetic domain.

5.4.2 Stage 1: Electric Domain Extraction

In this first stage we obtain the electric domain parameters, namely the DC coil resistances, R_D and R_S , and the linear leakage inductances, L_D and L_S (see Fig. 5.2). The conductor resistance does not change with bias, so the real part of

$Z_{drive}(I_{drive,j})$ is taken as R_D ; likewise, the real part of $Z_{sense}(I_{sense,j})$ is taken as R_S . A fluxgate operates by taking the core in and out of saturation. This means we need to measure the small-signal impedances beyond saturation. If we assume there is little coupling to the coils outside of the core material, and the core has negligible inductance in saturation, then the linear leakage inductances, L_D and L_S , can be taken to be the respective measured small-signal coil inductance at the highest bias current. These assumptions are validated by the good performance of the model in Section 5.5.

5.4.3 Stage 2: Even Mode Magnetic Domain Extraction

The second stage captures the even mode characteristics of the sense coil, through the magnetic domain model. Using the biased small-signal inductance of the sense coil and removing the leakage inductance, the permeance versus magnetomotive force, $\mathcal{P}(\mathcal{V})$, of the even mode half-circuit is obtained. The half circuit is composed of the series combination of \mathcal{R}_C and \mathcal{R}_A , we call this combination \mathcal{R}_{eq} (or in permeance \mathcal{P}_{eq}). Using a global optimizer with positive bounds, we fit $\mathcal{P}_{eq}(\mathcal{V})$ to the permeance model, (5.1). That is we obtain $\beta_{0,eq}, \dots, \beta_{3I+2,eq}$ through the following algorithm.

input : Biased small-signal impedance of sense coil $Z_{sense}(I_{sense,j})$, number of sense coil turns, N_S , extracted sense coil leakage inductance, L_S , number of unique tanh terms to fit, $I + 1$.

output: Parameters for equivalent nonlinear permeance.

obtain magnetic domain half-circuit permeance and MMF;

for $j \leftarrow 1$ **to** J **do**

| $\mathcal{P}_{eq}[j] = 2 [\text{Im} \{Z_{sense}(I_{sense,j})\}] / (2\pi f) - L_S / N_S^2$;

| $\mathcal{V}[j] = (N_S/2) \cdot I_{sense,j}$;

end

optimize (5.1) to fit to $\mathcal{P}_{eq}(\mathcal{V})$ with global optimizer;

minimize $100\% \cdot \|\mathcal{P}_{cn} - \mathcal{P}_{eq}\|_2 / \|\mathcal{P}_{eq}\|_2$ *by varying $\beta_{0,eq}, \dots, \beta_{3I+2,eq}$;*

5.4.4 Stage 3: Odd Mode Magnetic Domain Extraction

The final stage of the extraction algorithm captures the odd mode nonlinear characteristics of the drive coil. In fitting to the biased small-signal inductance of the drive coil, \mathcal{R}_{eq} of the previous stage is split into \mathcal{R}_C and \mathcal{R}_A and the $3I + 3$ parameters of $\mathcal{R}_{link} / \mathcal{P}_{link}$ are obtained. Assuming the portion of reluctance that creates \mathcal{R}_A is k_A , then the portion for \mathcal{R}_C is $k_C = 1 - k_A$. Parameters k_A and k_C scale the MMF of the series reluctances but not the flux, and thus scale certain parameters of (5.1), namely $\beta_{0,eq}$, $\beta_{2,eq}$, $\beta_{3i+1,eq}$, and $\beta_{3i+2,eq}$. The following algorithm is used to obtain k_A and the parameters of the nonlinear linkage reluctance, such that the odd mode half circuit permeance is fit.

```

input : Biased small-signal impedance of drive coil  $Z_{drive}(I_{drive,j})$ , number
          of drive coil turns,  $N_D$ , extracted drive coil leakage inductance,  $L_D$ ,
          number of unique tanh terms to fit,  $I + 1$ .
output: Parameters for nonlinear permeance  $\mathcal{P}_{link}$  and  $k_A$ .
obtain magnetic domain half-circuit permeance and MMF;
for  $j \leftarrow 1$  to  $J$  do
  |  $\mathcal{P}_{targ}[j] = 2 [\text{Im} \{Z_{drive}(I_{drive,j})\}] / (2\pi f) - L_D] / N_D^2$ ;
  |  $\mathcal{V}[j] = (N_D/2) \cdot I_{drive,j}$ ;
end
optimize (5.1) and  $k_A$  to fit the half circuit permeance,  $\mathcal{P}_{half}(\mathcal{V})$  to  $\mathcal{P}_{targ}(\mathcal{V})$ 
with global optimizer;
minimize  $100\% \cdot \|\mathcal{P}_{half} - \mathcal{P}_{targ}\|_2 / \|\mathcal{P}_{targ}\|_2$  by varying  $k_A$ ,
           $\beta_{0,link}, \dots, \beta_{3I+2,link}$ ;

```

5.5 Validation

In this section, two microfluxgate models are generated from the biased nonlinear drive and sense coil inductances, using the extraction algorithm from Section 5.4. One model is based on field-solver simulations, and the other is a fabricated on-chip device, with physical measurements made using an impedance analyzer. The models are then validated as magnetometers (see section 5.3.4). Comparisons are made with both the sensitivity curve and the time domain voltages across both coils. Time domain measurement are made using an oscilloscope and sinusoidal current source with the device in a Helmholtz coil. Simulation-based comparisons are performed using the device-circuit cosimulation feature available in Maxwell [115].

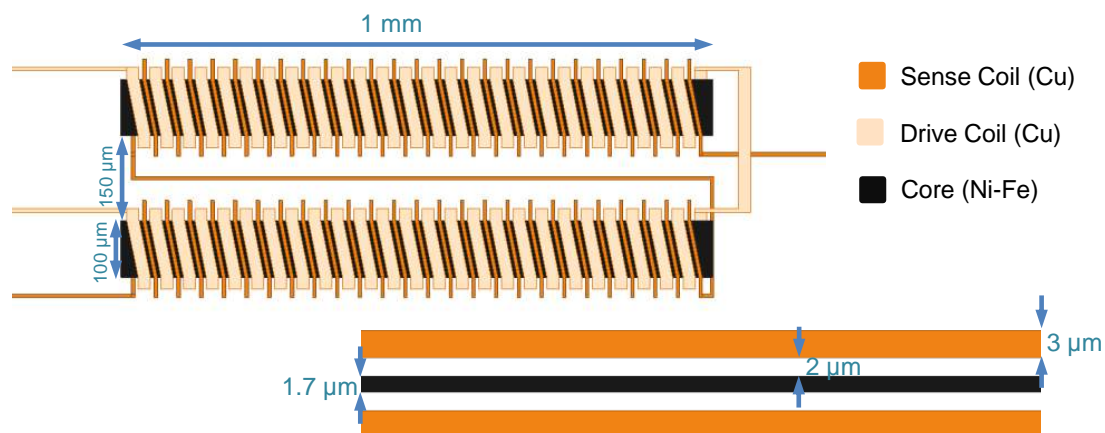


Figure 5.6: Top-down view of Maxwell design of device 1 dual-core solenoidal microfluxgate and 2-D cross-section with labeled dimensions.

5.5.1 Device 1 Simulation

Device 1 is a field solver simulation of a 1 mm long microfluxgate with 50^5 turns to the drive and sense coils around both cores. Figure 5.6 shows the design of the microfluxgate in Maxwell.

5.5.1.1 Model Fit

The extraction algorithm took 2 minutes and 43 seconds to complete on a 3.2 GHz Pentium[®] 4 workstation. The L2-norm error in the measured nonlinear drive coil inductance was 6.2% and that for the sense coil was 0.64%. The better performance in the sense coil is likely due to the fact that there are fewer constraints on this inductance; the drive coil inductance is constrained to match the series combination

⁵In this work, reference is always made to the total number of turns around both cores. In this case 50: 25 turns around one core and 25 around the other core.

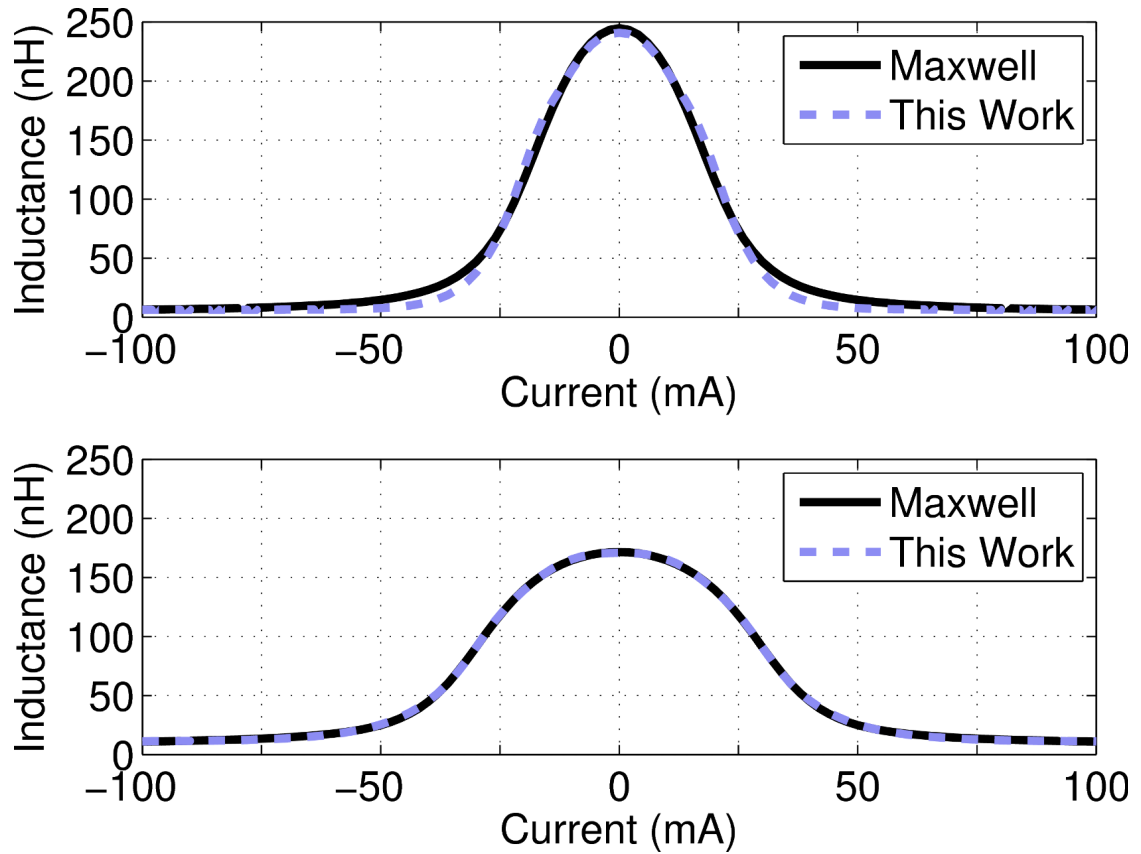


Figure 5.7: Drive coil inductance versus bias current comparing this work’s model with Maxwell results (top) and likewise for sense coil (bottom).

of \mathcal{R}_C and \mathcal{R}_A . Both sense and drive coil inductance match closely as shown by the curve comparison in Fig. 5.7.

5.5.1.2 Transient Performance

To validate the model, a time domain simulation was performed with a 40 mA amplitude sinusoidal drive current at 1 MHz. To emulate the effect of an exter-

nal field, the sense coil was biased with the corresponding DC current, a proper Helmholtz coil configuration would be used with more time. The drive and sense coil voltage were recorded under a $1\text{ M}\Omega$ load on the sense coil. Comparisons between this work's model and the Maxwell field solver measurements are shown for $100\ \mu\text{T}$ and $500\ \mu\text{T}$ in Fig. 5.8 and Fig. 5.9, respectively.

Eight time domain simulations were performed under fields ranging from 0 to 1.5 mT . The amplitude of the sense voltage should be an indication of the field strength. The circuit that performs this calculation integrates the sense voltage magnitude. Plotting this signal voltage versus the external magnetic field for both Maxwell and the model produced curves which matched with an L2-norm error of 6.6% (see Fig. 5.10).

5.5.2 Device 2 Measurements

Device 2 is a fabricated dual-core solenoidal microfluxgate. There are 50 turns to each the drive and sense coil, and the core length is $\sim 1\text{ mm}$. Figure 5.11 shows a micrograph of the microfluxgate.

5.5.2.1 Model Fit

Measurements of the biased small-signal inductance, for both the drive and sense coils, were made using an impedance analyzer operating at 1 MHz . The extraction algorithm took 3 minutes and 37 seconds to complete on a 3.2 GHz Pentium[®] 4

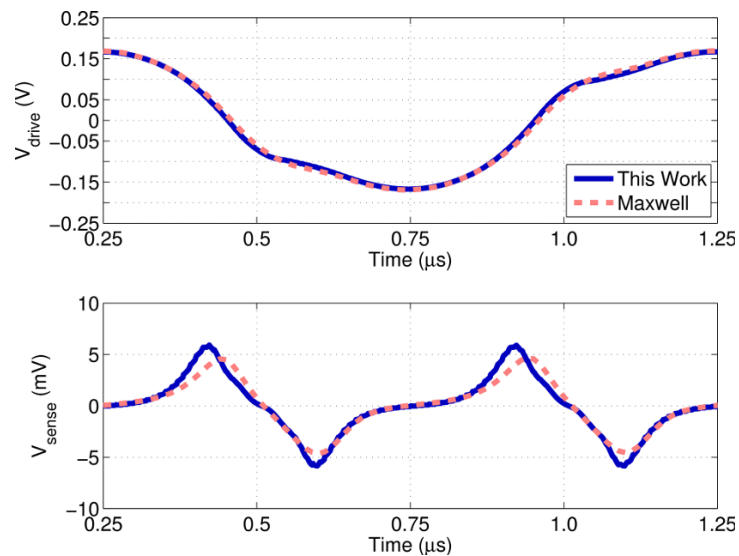


Figure 5.8: Time domain voltage across drive coil (top) and sense coil (bottom) for device 1 with a 40 mA, 1 MHz current drive coil excitation in a $100 \mu\text{T}$ external magnetic field.

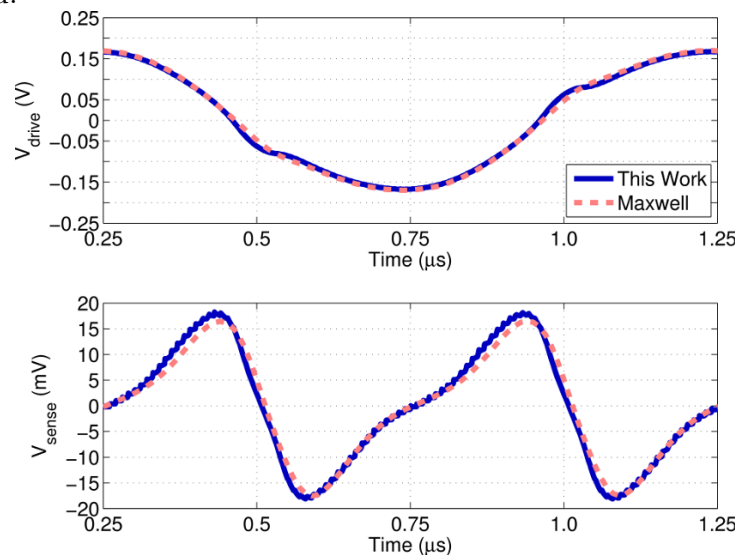


Figure 5.9: Time domain voltage across drive coil (top) and sense coil (bottom) for device 1 with a 40 mA, 1 MHz current drive coil excitation in a $500 \mu\text{T}$ external magnetic field.

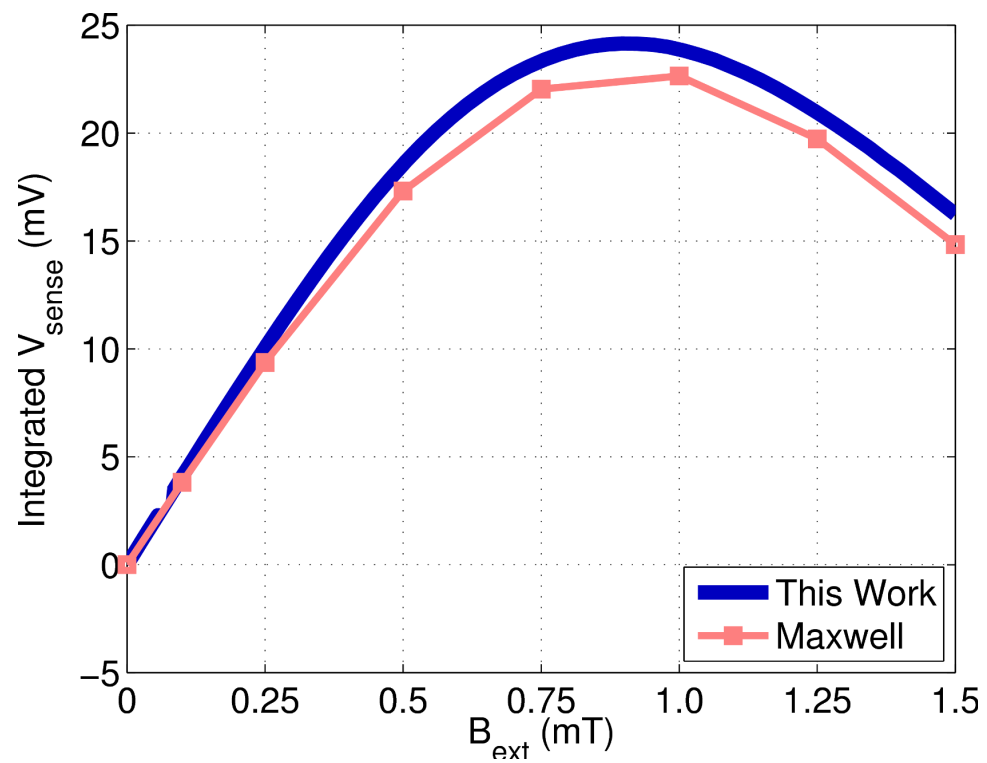


Figure 5.10: Integrated absolute sense voltage versus external magnetic field for both Maxwell simulation and the model of this thesis for device 1.

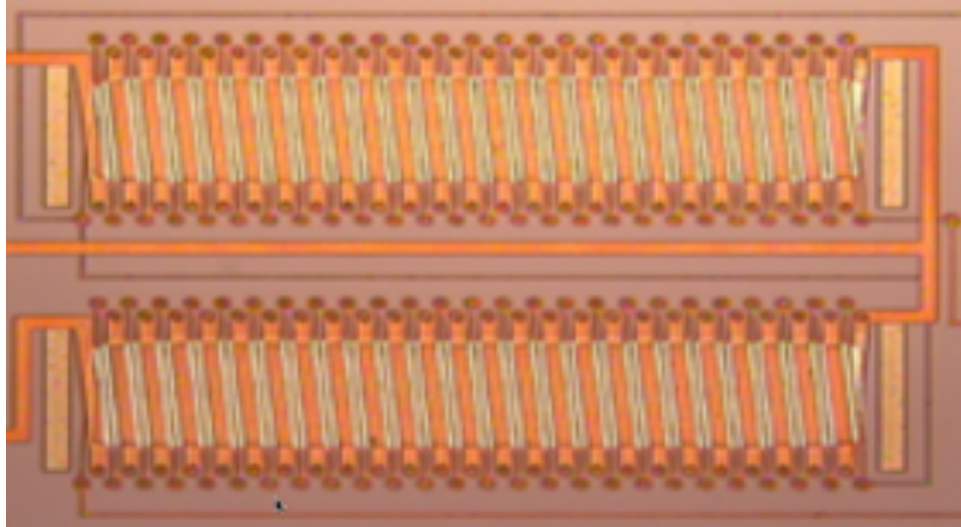


Figure 5.11: Micrograph of device 2, fabricated dual-core solenoidal microfluxgate.

workstation. The L2-norm error in the measured nonlinear drive coil inductance was 2.1% and that for the sense coil was 1.9%. Both fits match relatively well as shown by the curve comparison in Fig. 5.12.

5.5.2.2 Transient Performance

To validate the model, time domain oscilloscope measurements were performed with an 80 mA amplitude sinusoidal drive current at 1 MHz. A Helmholtz coil was used to generate the external magnetic field. The drive and sense coil voltage were recorded under a 1 M Ω load on the sense coil. Comparisons between this work's model and the measurements are shown for 100 μ T and 500 μ T in Fig. 5.13 and Fig. 5.14, respectively.

Do to certain obstacles we were unable to measure the time domain response for

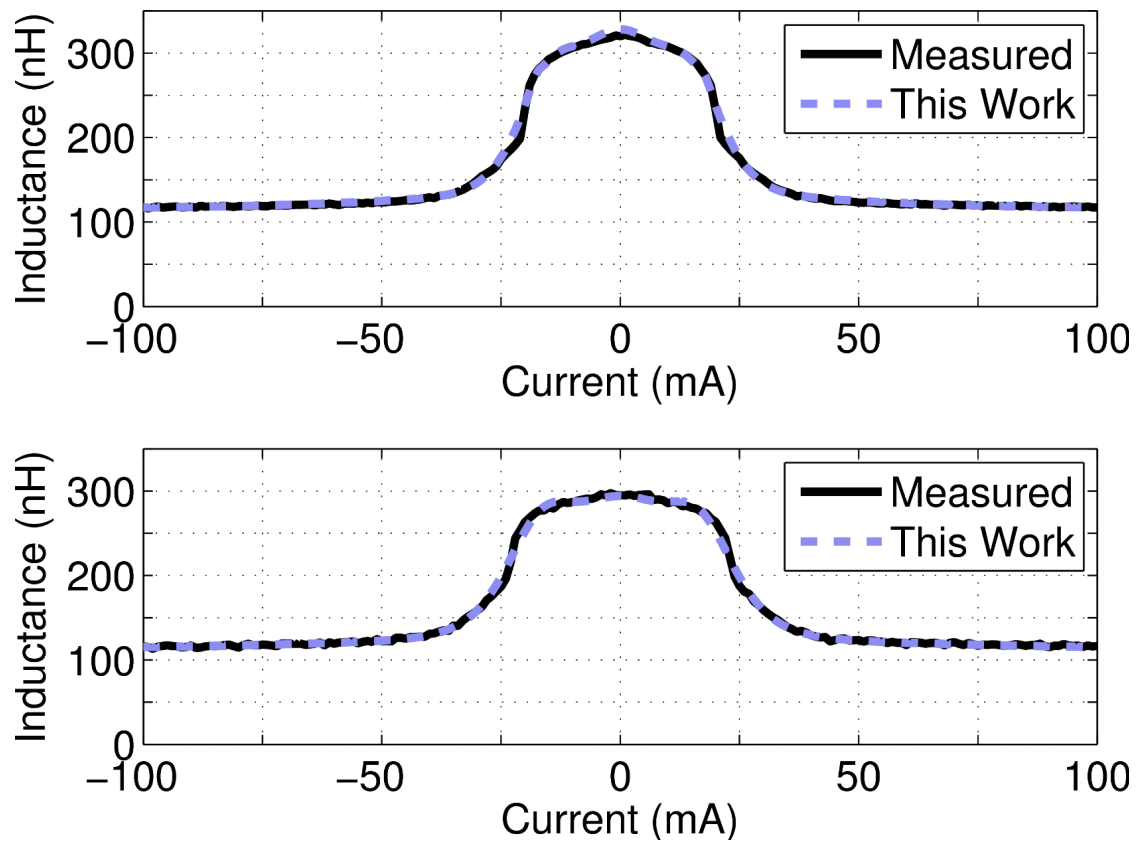


Figure 5.12: Drive coil (top) and sense coil (bottom) inductance versus bias current plot, comparing this work's model with measurement results for device 2.

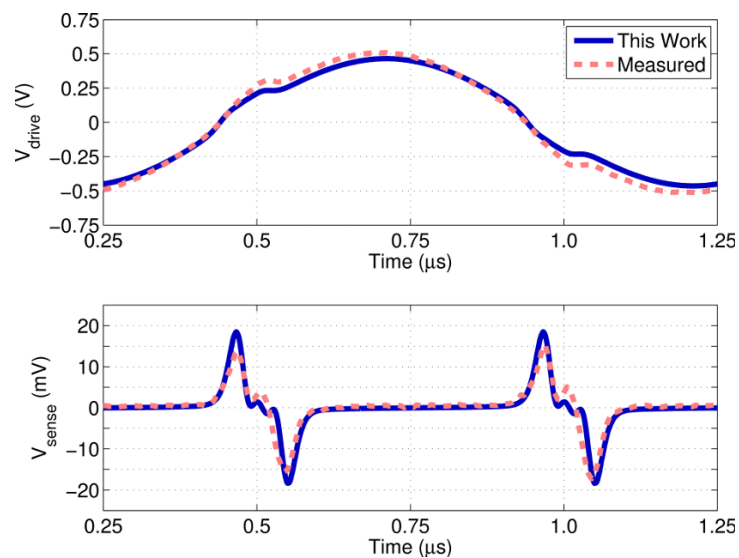


Figure 5.13: Time domain voltage across drive coil (top) and sense coil (bottom) for device 2 with a 80 mA, 1 MHz current drive coil excitation in a $100 \mu\text{T}$ external magnetic field.

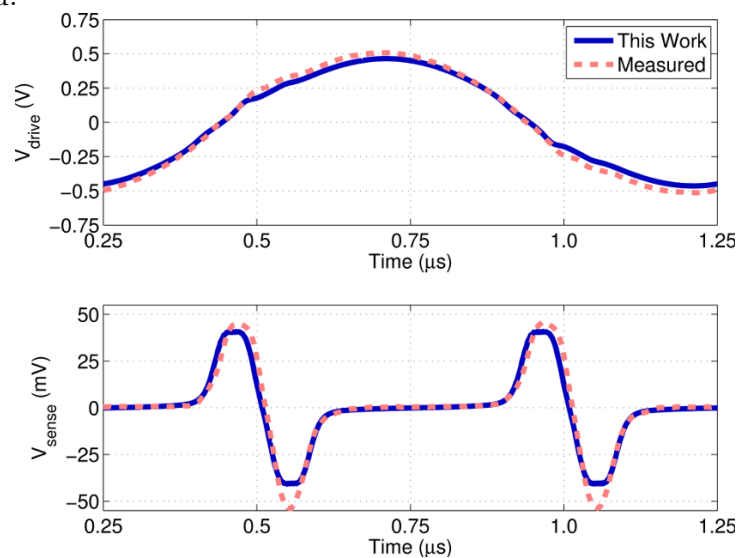


Figure 5.14: Time domain voltage across drive coil (top) and sense coil (bottom) for device 2 with a 80 mA, 1 MHz current drive coil excitation in a $500 \mu\text{T}$ external magnetic field.

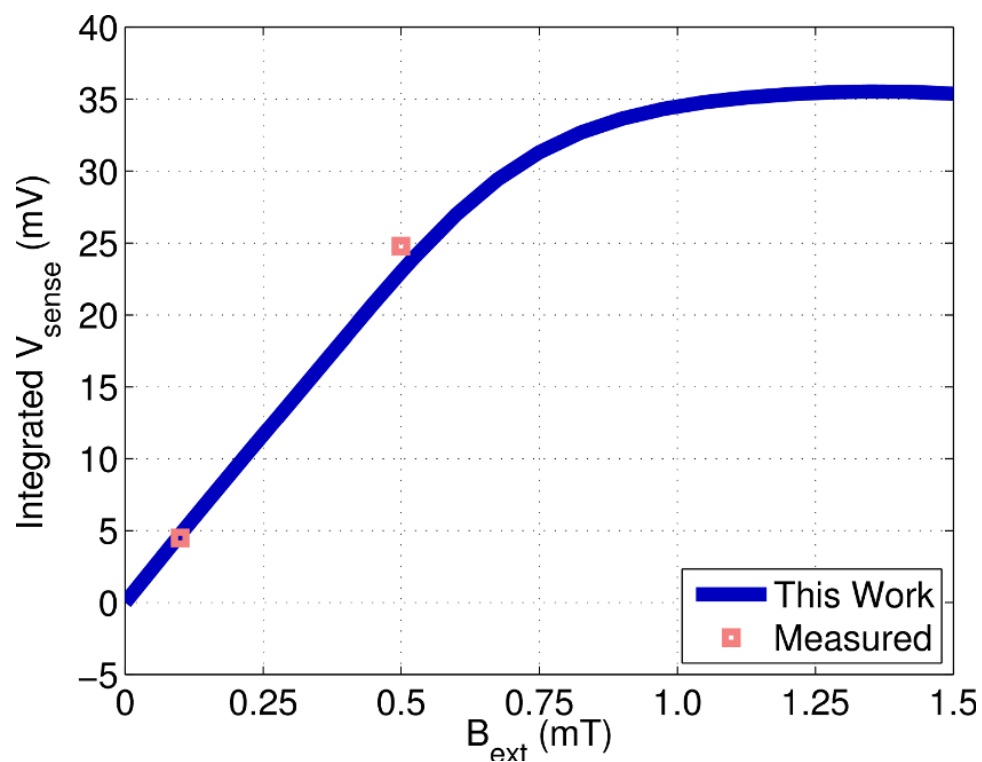


Figure 5.15: Integrated absolute sense voltage versus external magnetic field for both measurements and this work for device 2, showing good match for two fields.

more than the two applied fields. We continue with the available measurements. Plotting the integrated signal voltage versus the external magnetic field for both the two measurements and the model produced data points which matched to within a maximum error of 7.2% (see Fig. 5.15).

5.6 Conclusions and Future Work

5.6.1 Conclusions

In this chapter we have extended our modeling effort to a two core device with the addition of an external magnetic field by modeling a dual-core solenoidal magnetometer. Our circuit model correctly provides the resulting non-sinusoidal voltage response to the drive coil and any losses due to low-frequency resistance of the coils. A modeling extraction algorithm is provided to create an accurate and passive model in the absence of direct magnetic core characterization. The model is physically consistent in that nonlinearities of the core translate to nonlinearities in both coil responses and includes a physically meaningful magnetic subcircuit. The accuracy of our model used as a magnetometer beyond its linear range is demonstrated both through a field solver and actual fabricated device measurements. The L2-norm error of the sense signal is 6.6% when compared to the field-solver, and the maximum error is 7.2% when compared to measurements.

5.6.2 Adding Hysteresis

To allow the use of materials with a significant coercivity, hysteresis should be considered in the model. The Jiles-Atherton implementation of hysteresis discussed in Section 2.2.2 can be implemented with the shifted hyperbolic tangent function approach as the anhysteretic magnetization behavior. If the biased small-signal measurements of inductance are made with both an increasing and decreasing bias

current, then an indication of the outer hysteresis loop is present in the measurements. In stages 2 and 3 of the algorithm, the domain wall flexing constant, c , and domain wall pinning constant, k , from [79] could be added to the optimization and thus include the effects of hysteresis.

5.6.3 Improving the Model

We have noticed with a microfluxgate $\sim 50\%$ longer in core length that the model of Fig. 5.2 is not suitable to capture the nonlinear magnetic circuit behavior. For example, there are currents where the half-circuit flux for the odd mode is less than for the even mode, but this is not possible with the magnetic domain arrangement in the circuit model of Fig. 5.2. Currently, it is not clear what is causing this behavior, so part of the future work would be to reproduce this behavior in a field solver to aid in building a suitable circuit. One hypothesis is that there is a component of the magnetic flux due to the odd mode which saturates the core, but does not contribute to the flux seen by the coil. This flux would have to be orthogonal to the solenoid's axis, and would reduce the small-signal permeance of the core, without adding to the flux seen by the MMF. Ultimately, more consideration of why the circuit model presented in this chapter is not suitable for some dual-core solenoidal microfluxgate layouts of larger physical size needs to be determined.

Chapter 6 – Summary and Future Direction

6.1 Summary

In this thesis, we have presented techniques to enable equivalent circuit modeling of on-chip magnetic devices based on terminal measurements. Describing the specific details of models, algorithms, and performance benefits for three example devices: a microinductor, a microtransformer, and a microfluxgate.

Chapter 1, exposed the benefits to adding more features to the back end of line (BEOL) for integrated circuit (IC) manufacturing and put it in the context of traditional IC scaling and Moore’s Law. Specifically, in this thesis the BEOL “More-than-Moore” process of adding magnetic materials to integrated circuits is focused on. The devices were seen to benefit in increased power density, decreased cost, improved reliability, better thermal management, and simplified designs for IC customers. However, there is a need to model these passive devices accurately.

In Chapter 2, we first discussed the benefits to the modeling effort chosen in this thesis. Numerical field solvers were seen to be too time and memory expensive to simulate the entire relevant system. We specifically compare behavioral models to physics-based models, deciding that the benefits of proper operation outside of the region of interest, the ability to enforce passivity and the design insight obtained from physically meaningful elements and circuit topology, along with the

ability to have higher orders, outweigh the costs of more complicated algorithm and model development. To enable physically meaningful circuits capturing the relevant physics, how to model individual physical effects in circuit simulators is discussed, before transitioning into the specific device solutions of the following chapters.

Chapters 3 through 5 are complete solutions to the three device categories from Chapter 1: the microinductor, the microtransformer, and the microfluxgate, respectively. For each device, a literature review is performed considering both on and off chip examples. In this context, the novelty of this thesis' model is discussed. Next, the details of the nonlinear implementation and measurements used to generate and validate the model are discussed in each chapter. The details of extracting the complete circuit from the measurements is provided through an extraction algorithm. Finally, each chapter shows that for the relevant application, our model can accurately reproduce the important behaviors and parameters; whereas other models may have inaccuracies.

6.2 Future Direction

This thesis has addressed the challenge of modeling on-chip magnetic devices with compact equivalent circuits. The future direction of this research includes the addition of other magnetic effects such as hysteresis and ferromagnetic resonance to the modeling tools, further validation of the models and augmenting the models to account for a wide range of designs. The tools will help enable the design of

novel integrated circuits employing magnetic materials.

For the microinductor we have included the dominant effects for ferromagnetic alloys of eddy currents (both in the core and conductors), saturation, and capacitive resonance. However, other popular materials may require inclusion of hysteresis, or ferromagnetic resonance. The microinductor was validated with a single excitation for a strongly nonlinear microinductor. Although the model of this thesis performed well, not every modeled effect was significant in the measurement. Further measurement validation of our model when capacitive resonance, conductor loss, or core loss is dominant would be important future work.

The microtransformer model included the same physical phenomena dominant in the microinductor model. This was done since the same material was employed. There are popular materials which may require the inclusion of hysteresis and/or ferromagnetic resonance. Research into extending the model to include these effects would widen the application domain of this thesis. The microtransformer model was confirmed via a fabricated microtransformer to be able to reproduce the biased small-signal impedance measurements. Ideally, there would also be time-domain verification in the domain of application for fabricated devices.

The microfluxgate model included magnetic saturation, external magnetic field, and resistances. These are the dominant effects, however, at higher frequencies it may be important to capture the core eddy currents. Future research on including effects such as hysteresis, or core eddy currents would be a valuable contribution. The fabricated dual-core microfluxgate was measured in the presence of two external fields, adding more field points (especially larger external fields) would verify

if the model is correct in this regime. It is also recommended there be future research into why the microfluxgate model presented in this thesis was inadequate to capture some behaviors present in fabricated microfluxgates.

Bibliography

- [1] (2003) The history of the integrated circuit. [Online]. Available: http://www.nobelprize.org/educational/physics/integrated_circuit/history/
- [2] S. Deffree. (2013) Kilby demos all-semiconductor circuit, august 28, 1958. [Online]. Available: <http://www.edn.com/electronics-blogs/edn-moments/4394864/Kilby-demos-all-semiconductor-circuit-August-28-1958>
- [3] G. Moore, “Cramming more components onto integrated circuits,” pp. 114–117, April 19 1965.
- [4] (2011) Intel 22nm 3-d tri-gate transistor technology. [Online]. Available: <http://newsroom.intel.com/docs/DOC-2032>
- [5] W. Arden, M. Brillout, P. Coge, M. Graef, B. Huizing, and R. Mahnkopf. (2013) More than moore white paper. [Online]. Available: <http://www.itrs.net/LINKS/2010ITRS/IRC-ITRS-MtM-v2%203.pdf>
- [6] J. Y. Park, S. Han, and M. Allen, “Batch-fabricated microinductors with electroplated magnetically anisotropic and laminated alloy cores,” *Magnetics, IEEE Transactions on*, vol. 35, no. 5, pp. 4291–4300, Sep 1999.
- [7] R. Foley, F. Waldron, J. Slowey, A. Alderman, B. Narveson, and S. O’Mathuna, “Technology roadmapping for power supply in package (psip) and power supply on chip (pwrSOC),” pp. 525–532, 2010.
- [8] S. Mathúna, T. O’Donnell, N. Wang, and K. Rinne, “Magnetics on silicon: an enabling technology for power supply on chip,” *Power Electronics, IEEE Transactions on*, vol. 20, no. 3, pp. 585–592, 2005.
- [9] D. Gardner, G. Schrom, P. Hazucha, F. Paillet, T. Karnik, S. Borkar, J. Saulter, J. Owens, and J. Wetzels, “Integrated on-chip inductors with magnetic films,” in *Electron Devices Meeting, 2006. IEDM ’06. International*, Dec 2006, pp. 1–4.

- [10] D. Gardner, G. Schrom, P. Hazucha, F. Paillet, T. Karnik, S. Borkar, R. Hallstein, T. Dambrauskas, C. Hill, C. Linde, W. Worwag, R. Baresel, and S. Muthukumar, "Integrated on-chip inductors using magnetic material (invited)," *Journal of Applied Physics*, vol. 103, no. 7, pp. 07E927–07E927–6, Apr 2008.
- [11] D. W. Lee, K.-P. Hwang, and S. X. Wang, "Fabrication and analysis of high-performance integrated solenoid inductor with magnetic core," *Magnetics, IEEE Transactions on*, vol. 44, no. 11, pp. 4089–4095, Nov 2008.
- [12] W. Ni, J. Kim, and E. Kan, "Permalloy patterning effects on rf inductors," *Magnetics, IEEE Transactions on*, vol. 42, no. 10, pp. 2827–2829, Oct 2006.
- [13] K. H. Kim, J. Kim, H.-J. Kim, S. H. Han, and H. J. Kim, "A megahertz switching dc/dc converter using febn thin film inductor," *Magnetics, IEEE Transactions on*, vol. 38, no. 5, pp. 3162–3164, Sep 2002.
- [14] T. Liakopoulos and C. Ahn, "3-d microfabricated toroidal planar inductors with different magnetic core schemes for mems and power electronic applications," *Magnetics, IEEE Transactions on*, vol. 35, no. 5, pp. 3679–3681, 1999.
- [15] D. Yao, C. Levey, R. Tian, and C. Sullivan, "Microfabricated v-groove power inductors using multilayer co-zr-o thin films for very-high-frequency dc-dc converters," *Power Electronics, IEEE Transactions on*, vol. 28, no. 9, pp. 4384–4394, 2013.
- [16] C. Mathuna, N. Wang, S. Kulkarni, and S. Roy, "Review of integrated magnetics for power supply on chip (pwrSOC)," *Power Electronics, IEEE Transactions on*, vol. 27, no. 11, pp. 4799–4816, 2012.
- [17] C. H. Ahn and M. Allen, "Micromachined planar inductors on silicon wafers for mems applications," *Industrial Electronics, IEEE Transactions on*, vol. 45, no. 6, pp. 866–876, Dec 1998.
- [18] ———, "A new toroidal-meander type integrated inductor with a multilevel meander magnetic core," *Magnetics, IEEE Transactions on*, vol. 30, no. 1, pp. 73–79, Jan 1994.
- [19] J. Lu, H. Jia, X. Wang, K. Padmanabhan, W. Hurley, and Z. Shen, "Modeling, design, and characterization of multiturn bondwire inductors with ferrite

epoxy glob cores for power supply system-on-chip or system-in-package applications,” *Power Electronics, IEEE Transactions on*, vol. 25, no. 8, pp. 2010–2017, Aug 2010.

- [20] M. Mino, K. Tsukamoto, K. Yanagisawa, A. Tago, and T. Yachi, “A compact buck-converter using a thin-film inductor,” in *Applied Power Electronics Conference and Exposition, 1996. APEC '96. Conference Proceedings 1996., Eleventh Annual*, vol. 1, Mar 1996, pp. 422–426 vol.1.
- [21] N. Wang, T. O'Donnell, R. Meere, F. M. F. Rhen, S. Roy, and S. O'Mathuna, “Thin-film-integrated power inductor on si and its performance in an 8-mhz buck converter,” *Magnetics, IEEE Transactions on*, vol. 44, no. 11, pp. 4096–4099, 2008.
- [22] L. Daniel, C. Sullivan, and S. Sanders, “Design of microfabricated inductors,” in *Power Electronics Specialists Conference, 1996. PESC '96 Record., 27th Annual IEEE*, vol. 2, Jun 1996, pp. 1447–1455 vol.2.
- [23] R. Meere, T. O'Donnell, N. Wang, N. Achotte, S. Kulkarni, and S. O'Mathuna, “Size and performance tradeoffs in micro-inductors for high frequency dc-dc conversion,” *Magnetics, IEEE Transactions on*, vol. 45, no. 10, pp. 4234–4237, Oct 2009.
- [24] T. Sato, H. Tomita, A. Sawabe, T. Inoue, T. Mizoguchi, and M. Sahashi, “A magnetic thin film inductor and its application to a mhz switching dc-dc converter,” *Magnetics, IEEE Transactions on*, vol. 30, no. 2, pp. 217–223, Mar 1994.
- [25] N. Wang, J. Hannon, R. Foley, K. Mccarthy, T. O'Donnell, K. Rodgers, F. Waldron, and C. Mathuna, “Integrated magnetics on silicon for power supply in package (psip) and power supply on chip (pwrSOC),” in *Electronic System-Integration Technology Conference (ESTC), 2010 3rd*, Sept 2010, pp. 1–6.
- [26] M. Brunet, T. O'Donnell, L. Baud, N. Wang, J. O'Brien, P. McCloskey, and S. O'Mathuna, “Electrical performance of microtransformers for dc-dc converter applications,” *Magnetics, IEEE Transactions on*, vol. 38, no. 5, pp. 3174–3176, Sep 2002.

- [27] R. Rassel, C. Hiatt, J. DeCramer, and S. A. Campbell, "Fabrication and characterization of a solenoid-type microtransformer," *Magnetics, IEEE Transactions on*, vol. 39, no. 1, pp. 553–558, Jan 2003.
- [28] E.-J. Yun, M. Jung, C. I. Cheon, and H. G. Nam, "Microfabrication and characteristics of low-power high-performance magnetic thin-film transformers," *Magnetics, IEEE Transactions on*, vol. 40, no. 1, pp. 65–70, Jan 2004.
- [29] M. Mino, T. Yachi, A. Tago, K. Yanagisawa, and K. Sakakibara, "A new planar microtransformer for use in micro-switching converters," *Magnetics, IEEE Transactions on*, vol. 28, no. 4, pp. 1969–1973, Jul 1992.
- [30] K. Yamasawa, K. Maruyama, I. Hirohama, and P. Biringer, "High-frequency operation of a planar-type microtransformer and its application to multilayered switching regulators," *Magnetics, IEEE Transactions on*, vol. 26, no. 3, pp. 1204–1209, May 1990.
- [31] S. Prabhakaran, C. Sullivan, T. O'Donnell, M. Brunet, and S. Roy, "Microfabricated coupled inductors for dc-dc converters for microprocessor power delivery," in *Power Electronics Specialists Conference, 2004. PESC 04. 2004 IEEE 35th Annual*, vol. 6, June 2004, pp. 4467–4472 Vol.6.
- [32] M. Xu, T. Liakopoulos, C. H. Ahn, S. H. Han, and H. J. Kim, "A microfabricated transformer for high-frequency power or signal conversion," *Magnetics, IEEE Transactions on*, vol. 34, no. 4, pp. 1369–1371, Jul 1998.
- [33] N. Wang, T. O'Donnell, S. Roy, S. Kulkarni, P. McCloskey, and C. O'Mathuna, "Thin film microtransformer integrated on silicon for signal isolation," *Magnetics, IEEE Transactions on*, vol. 43, no. 6, pp. 2719–2721, June 2007.
- [34] K. Yamaguchi, E. Sugawara, O. Nakajima, H. Matsuki, and K. Murakami, "Load characteristics of a spiral coil type thin film microtransformer," *Magnetics, IEEE Transactions on*, vol. 29, no. 6, pp. 3207–3209, Nov 1993.
- [35] W.-S. Huang, C.-C. Lu, and J.-T. Jeng, "Multiple frequency characterizations of a cmos planar fluxgate magnetic sensor," in *Mechanical and Electronics Engineering (ICMEE), 2010 2nd International Conference on*, vol. 1, Aug 2010, pp. V1–409–V1–412.

- [36] O. Zorlu, P. Kejik, and R. Popovic, "Fluxgate-type magnetic microsensors for wide linear measuring range," in *Sensors Applications Symposium, 2007. SAS '07. IEEE*, Feb 2007, pp. 1–4.
- [37] C. Maier, S. Kawahito, M. Schneider, M. Zimmermann, and H. Baltes, "2d magnetic micro fluxgate system with digital signal output," in *Solid-State Circuits Conference, 1999. Digest of Technical Papers. ISSCC. 1999 IEEE International*, Feb 1999, pp. 130–131.
- [38] S. Kawahito, A. Cerman, K. Aramaki, and Y. Tadokoro, "A weak magnetic field measurement system using micro-fluxgate sensors and delta-sigma interface," *Instrumentation and Measurement, IEEE Transactions on*, vol. 52, no. 1, pp. 103–110, Feb 2003.
- [39] C.-C. Lu, W.-S. Huang, Y.-T. Liu, and J.-T. Jeng, "Design, fabrication, and characterization of a 3-d cmos fluxgate magnetometer," *Magnetics, IEEE Transactions on*, vol. 47, no. 10, pp. 3752–3755, Oct 2011.
- [40] Liangjintao, Liushibin, and L. Wei, "Study on silicon-based micro-fluxgate permalloy core film," in *Industrial Electronics and Applications, 2009. ICIEA 2009. 4th IEEE Conference on*, May 2009, pp. 1196–1198.
- [41] R. Gottfried-Gottfried, W. Budde, R. Mae, H. Mick, B. Sauer, S. Ulbricht, and U. Wende, "A miniaturized magnetic field sensor system consisting of a planar fluxgate sensor and a cmos readout circuitry," in *Solid-State Sensors and Actuators, 1995 and Eurosensors IX.. Transducers '95. The 8th International Conference on*, vol. 2, June 1995, pp. 229–232.
- [42] D.-S. Shim, H.-S. Park, K.-W. Na, W.-Y. Choi, J.-S. Hwang, and S.-O. Choi, "Micro fluxgate sensor using solenoid driving and sensing coils," in *Optoelectronic and Microelectronic Materials and Devices, 2002 Conference on*, Dec 2002, pp. 237–240.
- [43] H.-S. Park, D.-S. Shim, J.-S. Hwang, and S.-O. Choi, "Micro-fluxgate sensor incorporating solenoid coil and bcb dielectric," in *Sensors, 2004. Proceedings of IEEE*, Oct 2004, pp. 1133–1136 vol.3.
- [44] N. Sharafi and M. Nekoui, "Analyzing optimization of fluxgate sensor," in *Electronic Design, 2008. ICED 2008. International Conference on*, Dec 2008, pp. 1–4.

- [45] P.-M. Wu and C. H. Ahn, "Design of a low-power micromachined fluxgate sensor using localized core saturation method," *Sensors Journal, IEEE*, vol. 8, no. 3, pp. 308–313, March 2008.
- [46] C. Lei, L. Chen, Y. Zhou, and Z. Zhou, "Ultra low power solenoid mems fluxgate sensor with amorphous alloy core," in *Solid-State and Integrated Circuit Technology (ICSICT), 2010 10th IEEE International Conference on*, Nov 2010, pp. 1471–1473.
- [47] W.-S. Huang, C.-C. Lu, and J.-T. Jeng, "A novel 3d cmos micro-fluxgate magnetic sensor for low magnetic field detection," in *Sensors, 2010 IEEE*, Nov 2010, pp. 1791–1794.
- [48] A. Baschiroto, E. Dallago, P. Malcovati, M. Marchesi, E. Melissano, M. Morelli, P. Siciliano, and G. Venchi, "An integrated micro-fluxgate magnetic sensor with front-end circuitry," *Instrumentation and Measurement, IEEE Transactions on*, vol. 58, no. 9, pp. 3269–3275, Sept 2009.
- [49] V. Kursun, S. Narendra, V. De, and E. Friedman, "Analysis of buck converters for on-chip integration with a dual supply voltage microprocessor," *Very Large Scale Integration (VLSI) Systems, IEEE Transactions on*, vol. 11, no. 3, pp. 514–522, 2003.
- [50] J. Lee, G. Hatcher, L. Vandenberghe, and C.-K. Yang, "Evaluation of fully-integrated switching regulators for cmos process technologies," *Very Large Scale Integration (VLSI) Systems, IEEE Transactions on*, vol. 15, no. 9, pp. 1017–1027, 2007.
- [51] T. Andersen, C. Zingerli, F. Krismer, J. Kolar, N. Wang, and C. Mathuna, "Modeling and pareto optimization of microfabricated inductors for power supply on chip," *Power Electronics, IEEE Transactions on*, vol. 28, no. 9, pp. 4422–4430, 2013.
- [52] C. C. Kuo, M. Y. Kuo, and M. S. Kuo, "Modeling of capacitors and nonlinear inductors using piecewise curve fitting technique," in *Computers in Power Electronics, 1994., IEEE 4th Workshop on*, 1994, pp. 133–138.
- [53] D.-W. Cheng, W. Leung-Pong, and Y. S. Lee, "Design, modeling, and analysis of integrated magnetics for power converters," in *Power Electronics Specialists Conference, 2000. PESC 00. 2000 IEEE 31st Annual*, vol. 1, 2000, pp. 320–325 vol.1.

- [54] E. Rozanov and S. Ben-Yaakov, "A spice behavioral model for current-controlled magnetic inductors," in *Electrical and Electronics Engineers in Israel, 2004. Proceedings. 2004 23rd IEEE Convention of*, 2004, pp. 338–341.
- [55] P. Zhou, D. Lin, W. N. Fu, B. Ionescu, and Z. Cendes, "A general cosimulation approach for coupled field-circuit problems," *Magnetics, IEEE Transactions on*, vol. 42, no. 4, pp. 1051–1054, April 2006.
- [56] A. Ruehli and A. Cangellaris, "Progress in the methodologies for the electrical modeling of interconnects and electronic packages," *Proceedings of the IEEE*, vol. 89, no. 5, pp. 740–771, May 2001.
- [57] J. Jin, *The Finite Element Method in Electromagnetics*. New York, NY: Wiley, 2002.
- [58] R. F. Harrington, *Field Computation by Moment Methods (IEEE Press Series on Electromagnetic Wave Theory)*. Wiley-IEEE Press, 1993.
- [59] J. R. W. Simon Ramo and T. V. Duzer, *Fields and Waves in Communication Electronics Third Ed.* Hoboken, NJ: John Wiley & Sons, Inc., 1994.
- [60] A. E. Ruehli, "Equivalent circuit models for three-dimensional multiconductor systems," *Microwave Theory and Techniques, IEEE Transactions on*, vol. 22, no. 3, pp. 216–221, 1974.
- [61] C.-W. Ho, A. E. Ruehli, and P. A. Brennan, "The modified nodal approach to network analysis," *Circuits and Systems, IEEE Transactions on*, vol. 22, no. 6, pp. 504–509, 1975.
- [62] D. Jiles, "Frequency dependence of hysteresis curves in 'non-conducting' magnetic materials," *Magnetics, IEEE Transactions on*, vol. 29, no. 6, pp. 3490–3492, 1993.
- [63] L. Weinberg, *Network Analysis and Synthesis*. New York, NY: McGraw-Hill, 1962.
- [64] E. J. Brandon, E. Wesseling, V. White, C. Ramsey, L. Del Castillo, and U. Lieneweg, "Fabrication and characterization of microinductors for distributed power converters," *Magnetics, IEEE Transactions on*, vol. 39, no. 4, pp. 2049–2056, 2003.

- [65] T. Osaka, "Electrodeposition of highly functional thin films for magnetic recording devices of the next century," *Electrochimica Acta*, vol. 45, pp. 3311–3321, 2000.
- [66] A. Crawford, D. Gardner, and S. X. Wang, "High-frequency microinductors with amorphous magnetic ground planes," *Magnetics, IEEE Transactions on*, vol. 38, no. 5, pp. 3168–3170, 2002.
- [67] J. Youssef, P.-M. Jacquart, N. Vukadinovic, and H. Le Gall, "Frequency-dependent complex permeability in zr-substituted permalloy thin films," *Magnetics, IEEE Transactions on*, vol. 38, no. 5, pp. 3141–3143, Sep 2002.
- [68] *Virtuoso Spectre Circuit Simulator Version 6.2.1.170*, Cadence Design Systems Inc., San Jose, CA 95134, USA.
- [69] Z.-Q. Qu, *Model Order Reduction Techniques: With Applications in Finite Element Analysis*. New York, NY: Springer, 2004.
- [70] R. Leventhal and L. Green, *Semiconductor Modeling : For Simulating Signal, Power, and Electromagnetic Integrity*. New York, NY: Springer, 2007.
- [71] P. Triverio, S. Grivet-Talocia, M. Nakhla, F. Canavero, and R. Achar, "Stability, causality, and passivity in electrical interconnect models," *Advanced Packaging, IEEE Transactions on*, vol. 30, no. 4, pp. 795–808, 2007.
- [72] J. Takacs, *Mathematics of Hysteretic Phenomena: The $T(x)$ Model for the Description of Hysteresis*. New York, NY: Wiley, 2003.
- [73] M. El-Sherbiny, "Representation of the magnetization characteristic by a sum of exponentials," *Magnetics, IEEE Transactions on*, vol. 9, no. 1, pp. 60–61, 1973.
- [74] D. Grimaldi, L. Michaeli, and A. Palumbo, "Automatic and accurate evaluation of the parameters of a magnetic hysteresis model," *Instrumentation and Measurement, IEEE Transactions on*, vol. 49, no. 1, pp. 154–160, 2000.
- [75] E. P. Furlani, *Permanent Magnet and Electromechanical Devices*. San Diego, CA: Academic Press, 2001.
- [76] J. R. Brauer, "Simple equations for the magnetization and reluctivity curves of steel," *Magnetics, IEEE Transactions on*, vol. 11, no. 1, pp. 81–81, 1975.

- [77] I. Mayergoyz and G. Friedman, "Generalized preisach model of hysteresis," *Magnetics, IEEE Transactions on*, vol. 24, no. 1, pp. 212–217, 1988.
- [78] B. Phelps and D. Atherton, "Pinning and minor loops in an inclusive model of ferromagnetic hysteresis," *Magnetics, IEEE Transactions on*, vol. 37, no. 1, pp. 517–521, 2001.
- [79] D. Jiles and D. Atherton, "Theory of ferromagnetic hysteresis," *Journal of Magnetism and Magnetic Materials*, vol. 61, pp. 48–60, 1986.
- [80] L. Meares, "New simulation techniques using spice," *Applied Power Electronics Conference (APEC), IEEE*, pp. 198–205, 1986.
- [81] D. Pei and P. O. Lauritzen, "A computer model of magnetic saturation and hysteresis for use on spice2," *Power Electronics, IEEE Transactions on*, vol. PE-1, no. 2, pp. 101–110, 1986.
- [82] G. P. Muyschondt and W. Portnoy, "Circuit level modeling of inductive elements," in *Energy Conversion Engineering Conference, 1989. IECEC-89., Proceedings of the 24th Intersociety*, 1989, pp. 93–97 vol.1.
- [83] S. Naidu, "Time domain model for the ferromagnetic core, including the effects of hysteresis and eddy currents," *Science, Measurement and Technology, IEE Proceedings A*, vol. 138, no. 1, pp. 44–50, 1991.
- [84] J. Zhu, S. Hui, and V. Ramsden, "A dynamic equivalent circuit model for solid magnetic cores for high switching frequency operations," *Power Electronics, IEEE Transactions on*, vol. 10, no. 6, pp. 791–795, 1995.
- [85] S. Hui, J. Zhu, and V. Ramsden, "A generalized dynamic circuit model of magnetic cores for low- and high-frequency applications. ii. circuit model formulation and implementation," *Power Electronics, IEEE Transactions on*, vol. 11, no. 2, pp. 251–259, 1996.
- [86] P. Tenant and J.-J. Rousseau, "Dynamic model of magnetic materials applied on soft ferrites," *Power Electronics, IEEE Transactions on*, vol. 13, no. 2, pp. 372–379, 1998.
- [87] K. Ngo, "Subcircuit modeling of magnetic cores with hysteresis in pspice," *Aerospace and Electronic Systems, IEEE Transactions on*, vol. 38, no. 4, pp. 1425–1434, 2002.

- [88] H.-G. Brachtendorf and R. Laur, "Simulation of skin effects and hysteresis phenomena in the time domain," *Magnetics, IEEE Transactions on*, vol. 37, no. 5, pp. 3781–3789, 2001.
- [89] A. Brown, J. Ross, and K. G. Nichols, "Time-domain simulation of mixed nonlinear magnetic and electronic systems," *Magnetics, IEEE Transactions on*, vol. 37, no. 1, pp. 522–532, 2001.
- [90] W. Chandrasena, P. McLaren, U. Annakkage, R. Jayasinghe, and E. Dirks, "Simulation of eddy current effects in transformers," in *Electrical and Computer Engineering, 2002. IEEE CCECE 2002. Canadian Conference on*, vol. 1, 2002, pp. 122–126 vol.1.
- [91] C. E. Patton and F. B. Humphrey, "A comparison of the losses for domain-wall motion and ferromagnetic resonance in thin ni-fe alloy films," *Journal of Applied Physics*, vol. 39, no. 2, pp. 857–858, Feb 1968.
- [92] G. T. Rado, "Magnetic spectra of ferrites," *Rev. Mod. Phys.*, vol. 25, pp. 81–89, Jan 1953. [Online]. Available: <http://link.aps.org/doi/10.1103/RevModPhys.25.81>
- [93] D. Melendy, P. Francis, C. Pichler, K. Hwang, G. Srinivasan, and A. Weishaar, "A new wideband compact model for spiral inductors in rfics," *Electron Device Letters, IEEE*, vol. 23, no. 5, pp. 273–275, 2002.
- [94] G. Slemon, "Equivalent circuits for transformers and machines including nonlinear effects," *Proceedings of the IEE - Part II: Power Engineering*, vol. 100, no. 77, pp. 577–581, October 1953.
- [95] S. F. B. Morse, "Improvement in the mode of communicating information by signals by the application of electro-magnetism," U.S. Patent 1647, June 20, 1840.
- [96] D. Gardner, G. Schrom, P. Hazucha, F. Paillet, T. Karnik, and S. Borkar, "Integrated on-chip inductors with magnetic films," *Magnetics, IEEE Transactions on*, vol. 43, no. 6, pp. 2615–2617, 2007.
- [97] G. Mehas, K. Coonley, and C. Sullivan, "Design of microfabricated inductors for microprocessor power delivery," in *Applied Power Electronics Conference and Exposition, 1999. APEC '99. Fourteenth Annual*, vol. 2, 1999, pp. 1181–1187 vol.2.

- [98] L. Mandache, D. Topan, M. Iordache, L. Dumitriu, and I. Sirbu, "On the time-domain analysis of analog circuits containing nonlinear inductors," in *Circuit Theory and Design (ECCTD), 2011 20th European Conference on*, 2011, pp. 98–101.
- [99] A. Elsherbini, H. Braunisch, and K. O'Brien, "Circuit modeling of nonlinear lossy frequency dependent thin-film magnetic inductors," in *Electrical Performance of Electronic Packaging and Systems (EPEPS), 2012 IEEE 21st Conference on*, 2012, pp. 105–108.
- [100] L.-C. Yeh, "A flexible dynamic behavior model of inductors to link time domain simulation with empirical loss equations that is instantaneous db/dt and $b(t)$ dependent for spice simulation," in *Power Electronics and Drive Systems (PEDS), 2011 IEEE Ninth International Conference on*, 2011, pp. 517–522.
- [101] Z. Liu, A. Abou-Alfotouh, and M. Wilkowski, "Nonlinear inductor modeling for power converter," in *Applied Power Electronics Conference and Exposition (APEC), 2012 Twenty-Seventh Annual IEEE*, 2012, pp. 1868–1871.
- [102] L. Mandache and D. Topan, "Managing eddy current losses and ferromagnetic material nonlinearities in distorting regimes," in *Electric Machines and Drives Conference, 2009. IEMDC '09. IEEE International*, 2009, pp. 1449–1454.
- [103] G. Sizikov, A. Kolodny, E. Fridman, and M. Zelikson, "Efficiency optimization of integrated dc-dc buck converters," in *Electronics, Circuits, and Systems (ICECS), 2010 17th IEEE International Conference on*, 2010, pp. 1208–1211.
- [104] A. Niknejad and R. Meyer, "Analysis and optimization of monolithic inductors and transformers for rf ics," in *Custom Integrated Circuits Conference, 1997., Proceedings of the IEEE 1997*, 1997, pp. 375–378.
- [105] C. Inc. (2013) Spice model-0603ps. [Online]. Available: <http://www.coilcraft.com/models.cfm>
- [106] J. Avila-Rosales and F. Alvarado, "Nonlinear frequency dependent transformer model for electromagnetic transient studies in power systems," *Power Apparatus and Systems, IEEE Transactions on*, vol. PAS-101, no. 11, pp. 4281–4288, 1982.

- [107] J. Krah, "Optimum discretization of a physical cauer circuit," *Magnetics, IEEE Transactions on*, vol. 41, no. 5, pp. 1444–1447, 2005.
- [108] S. Gaskill, A. Papou, A. Mohan, W. French, and A. Weisshaar, "Nonlinear frequency-dependent model for microinductors with magnetic core," *Electron Device Letters, IEEE*, vol. 34, no. 2, pp. 304–306, Feb 2013.
- [109] —, "Modeling microinductors with thin-film alloy magnetic cores," *Power Electronics, IEEE Transactions on*, vol. 29, no. 9, pp. 4901–4910, Sept 2014.
- [110] E. W. Weisstein. (2014) " l^2 -norm." from mathworld--a wolfram web resource. [Online]. Available: <http://mathworld.wolfram.com/L2-Norm.html>
- [111] P. Herget, N. Wang, E. O'Sullivan, B. Webb, L. Romankiw, R. Fontana, X. Hu, G. Decad, and W. Gallagher, "A study of current density limits due to saturation in thin film magnetic inductors for on-chip power conversion," *Magnetics, IEEE Transactions on*, vol. 48, no. 11, pp. 4119–4122, 2012.
- [112] C. Karr, D. Stanley, and B. Scheiner, "Genetic algorithm applied to least squares curve fitting," U.S. Dept. of the Interior, Bureau of Mines, Tech. Rep. RI-9339, Feb. 1991.
- [113] T. Coleman and Y. Li, "An interior, trust region approach for nonlinear minimization subject to bounds," *SIAM Journal on Optimization*, vol. 6, pp. 418–445, 1996.
- [114] *COMSOL Multiphysics Version 3.5a*, COMSOL AB, Stockholm, Sweden.
- [115] *Maxwell 3D Version 15.0.0*, Ansys, Inc., Canonsburg, PA, USA.
- [116] *MATLAB*, The MathWorks Inc., Natick, MA, USA.
- [117] S. El-Hamamsy and E. Chang, "Magnetics modeling for computer-aided design of power electronics circuits," in *Power Electronics Specialists Conference, 1989. PESC '89 Record., 20th Annual IEEE*, Jun 1989, pp. 635–645 vol.2.
- [118] J. Hayes, N. O'Donovan, and M. Egan, "The extended t model of the multiwinding transformer," in *Power Electronics Specialists Conference, 2004. PESC 04. 2004 IEEE 35th Annual*, vol. 3, June 2004, pp. 1812–1817 Vol.3.

- [119] M. Xu, J. Zhou, K. Yao, and F. Lee, "Small signal modeling of a high bandwidth voltage regulator using coupled inductors," *Power Electronics, IEEE Transactions on*, vol. 22, no. 2, pp. 399–406, March 2007.
- [120] J. Pejtersen, J. Dollner Monster, and A. Knott, "Development and verification of printed circuit board toroidal transformer model," in *Applied Power Electronics Conference and Exposition (APEC), 2013 Twenty-Eighth Annual IEEE*, March 2013, pp. 1654–1659.
- [121] H. B. Shin, E.-S. Jang, J. G. Park, H. W. Lee, and T. Lipo, "Small-signal analysis of multiphase interleaved boost converter with coupled inductors," *Electric Power Applications, IEE Proceedings -*, vol. 152, no. 5, pp. 1161–1170, Sept 2005.
- [122] J. Long and M. Copeland, "Modeling of monolithic inductors and transformers for silicon rfc design," in *Technologies for Wireless Applications Digest, 1995., MTT-S Symposium on*, Feb 1995, pp. 129–134.
- [123] J. Norhuzaimin, S. P. Chew, and A. H. Kharuddin, "The design of integrated monolithic transformer for power ic," in *Applied Electromagnetics, 2005. APACE 2005. Asia-Pacific Conference on*, Dec 2005, pp. 5 pp.–.
- [124] E.-S. Hasaneen, "Compact circuit simulation model for on-chip inductor and transformer for rf integrated circuits," in *Design and Test Workshop, 2007. IDT 2007. 2nd International*, Dec 2007, pp. 265–269.
- [125] B. A. McDonald and D. Freeman, "Practical transformer modeling and characterization for a high performance llc converter," in *Applied Power Electronics Conference and Exposition (APEC), 2013 Twenty-Eighth Annual IEEE*, March 2013, pp. 2582–2589.
- [126] P. Okyere and E. Habiger, "A novel physically-based pspice-compatible-model for common-mode chokes," in *Electromagnetic Compatibility, 1999 International Symposium on*, 1999, pp. 33–36.
- [127] S. Kythakyapuzha and W. Kuhn, "Modeling of inductors and transformers," in *Radio Frequency Integrated Circuits (RFIC) Symposium, 2001. Digest of Papers. 2001 IEEE*, May 2001, pp. 283–286.

- [128] J. Long and M. Danesh, "A uniform compact model for planar rf/mmhc interconnect, inductors and transformers," in *Bipolar/BiCMOS Circuits and Technology Meeting, Proceedings of the 2001*, 2001, pp. 167–170.
- [129] A. Narang and R. H. Brierley, "Topology based magnetic model for steady-state and transient studies for three-phase core type transformers," *Power Systems, IEEE Transactions on*, vol. 9, no. 3, pp. 1337–1349, Aug 1994.
- [130] J. Pedra, F. Corcoles, L. Sainz, and R. Lopez, "Harmonic nonlinear transformer modeling," *Power Delivery, IEEE Transactions on*, vol. 19, no. 2, pp. 884–890, April 2004.
- [131] L. Pierrat, T. Tran-Quoc, and A. Montmeat, "Nonlinear transient simulation of transformers," in *Industry Applications Conference, 1995. Thirtieth IAS Annual Meeting, IAS '95., Conference Record of the 1995 IEEE*, vol. 2, Oct 1995, pp. 1193–1198 vol.2.
- [132] M. Bloech and M. Rashid, "Pspice modeling of three-phase transformer," in *Power Symposium, 2007. NAPS '07. 39th North American*, Sept 2007, pp. 76–79.
- [133] M. Vakilian and R. Degeneff, "A method for modeling nonlinear core characteristics of transformers during transients," *Power Delivery, IEEE Transactions on*, vol. 9, no. 4, pp. 1916–1925, Oct 1994.
- [134] J. Pleite, R. Prieto, R. Asensi, J. Cobos, and E. Olias, "Obtaining a frequency-dependent and distributed-effects model of magnetic components from actual measurements," *Magnetics, IEEE Transactions on*, vol. 35, no. 6, pp. 4490–4502, Nov 1999.
- [135] J. Hayes, M. Egan, N. Wang, and T. O'Donnell, "Series-coupling test characterization of on-chip silicon-integrated and pwb-integrated transformers," in *Applied Power Electronics Conference, APEC 2007 - Twenty Second Annual IEEE*, Feb 2007, pp. 97–103.
- [136] M. Lind, W. Xiao, and W. Dunford, "Modeling of a constant voltage transformer," *Circuits and Systems I: Regular Papers, IEEE Transactions on*, vol. 53, no. 2, pp. 409–418, Feb 2006.
- [137] L. Xiaoping, W. Xishan, L. Lei, and F. Yadong, "Harmonics study for three-phase transformer under dc inrushing," in *Electromagnetic Compatibility*,

2006. *EMC-Zurich 2006. 17th International Zurich Symposium on*, Feb 2006, pp. 227–230.
- [138] A. Elsherbini, H. Braunisch, K. O’Brien, and M. Hill, “Circuit modeling of nonlinear lossy frequency-dependent thin-film magnetic inductors,” *Components, Packaging and Manufacturing Technology, IEEE Transactions on*, vol. 4, no. 1, pp. 145–152, Jan 2014.
 - [139] D. Maclean, “The mspice simulation of a saturating transformer,” in *Energy Conversion Engineering Conference, 1989. IECEC-89., Proceedings of the 24th Intersociety*, Aug 1989, pp. 105–110 vol.1.
 - [140] W. Archer, M. Deveney, and R. Nagel, “Non-linear transformer modeling and simulation,” in *Circuits and Systems, 1994., Proceedings of the 37th Midwest Symposium on*, vol. 1, Aug 1994, pp. 665–669 vol.1.
 - [141] E. Dallago, G. Sassone, and G. Venchi, “High-frequency power transformer model for circuit simulation,” *Power Electronics, IEEE Transactions on*, vol. 12, no. 4, pp. 664–670, Jul 1997.
 - [142] A. Maxim, D. Andreu, and J. Boucher, “A new analog behavioral spice macromodel of magnetic components,” in *Industrial Electronics, 1997. ISIE ’97., Proceedings of the IEEE International Symposium on*, vol. 2, Jul 1997, pp. 183–188 vol.2.
 - [143] T. Vu, S. O’Driscoll, and J. Ringwood, “Nonlinear dynamic transformer time-domain identification for power converter applications,” *Power Electronics, IEEE Transactions on*, vol. 29, no. 1, pp. 318–327, Jan 2014.
 - [144] L. Mandache, D. Topan, M. Iordache, and I. Sirbu, “Spice model for effective and accurate time domain simulation of power transformers,” in *Nonlinear Dynamics and Synchronization (INDS) 16th Int’l Symposium on Theoretical Electrical Engineering (ISTET), 2011 Joint 3rd Int’l Workshop on*, July 2011, pp. 1–6.
 - [145] L. Heinemann, “A novel spice compatible high frequency multiwinding transformer model,” in *Industry Applications Conference, 1998. Thirty-Third IAS Annual Meeting. The 1998 IEEE*, vol. 2, Oct 1998, pp. 929–936 vol.2.
 - [146] Y. Mayevskiy, A. Watson, P. Francis, K. Hwang, and A. Weisshaar, “A new compact model for monolithic transformers in silicon-based rfics,” *Microwave*

- and Wireless Components Letters, IEEE*, vol. 15, no. 6, pp. 419–421, June 2005.
- [147] P. Okyere and L. Heinemann, “An advanced spice-compatible model for high frequency multiwinding transformers,” in *Power Electronics Specialists Conference, 1999. PESC 99. 30th Annual IEEE*, vol. 1, Aug 1999, pp. 592–597 vol.1.
- [148] S. Marshall, “An analytic model for the fluxgate magnetometer,” *Magnetics, IEEE Transactions on*, vol. 3, no. 3, pp. 459–463, September 1967.
- [149] J. Burger, “The theoretical output of a ring core fluxgate sensor,” *Magnetics, IEEE Transactions on*, vol. 8, no. 4, pp. 791–796, Dec 1972.
- [150] S. Gupta, C. H. Ahn, and I. Park, J., “Electromagnetic modeling and harmonic analysis of micro-machined ring-type magnetic fluxgate sensor using spice,” in *Sensors, 2003. Proceedings of IEEE*, vol. 1, Oct 2003, pp. 622–625 Vol.1.
- [151] S. Yang, S. Liu, W. Feng, B. Guo, X. Hou, and J. Li, “Spice circuit model of voltage excitation fluxgate sensor,” *Science, Measurement Technology, IET*, vol. 7, no. 3, pp. 145–150, May 2013.
- [152] D. K. Cheng, *Field and Wave Electromagnetics 2nd edition*. Reading, MA: Addison-Wesley, 1989.
- [153] L. Hunt, D. Linebarger, and R. DeGroat, “Nonlinear system identification and characterization,” in *Acoustics, Speech, and Signal Processing, 1989. ICASSP-89., 1989 International Conference on*, May 1989, pp. 2117–2120 vol.4.
- [154] Y. Cao and Q.-J. Zhang, “State-space dynamic neural network technique for high-speed ic buffer modeling,” in *Signals, Systems and Electronics, 2007. ISSSE '07. International Symposium on*, 2007, pp. 71–74.
- [155] Q. Zhang and K. Gupta, *Neural Networks for RF and Microwave Design*. Norwood, MA: Artech House, 2000.
- [156] G. C. Temes and J. W. LaPatra, *Introduction to Circuit Synthesis and Design*. New York, NY: McGraw-Hill, Inc., 1977.

- [157] L.-P. Wong, Y. S. Lee, and D.-W. Cheng, “A new approach to the analysis and design of integrated magnetics,” in *Applied Power Electronics Conference and Exposition, 2001. APEC 2001. Sixteenth Annual IEEE*, vol. 2, 2001, pp. 1196–1202 vol.2.
- [158] I. Gyimesi and D. Ostergaard, “Inductance computation by incremental finite element analysis,” *Magnetics, IEEE Transactions on*, vol. 35, no. 3, pp. 1119–1122, May 1999.

APPENDICES

Appendix A – Behavioral and Physics-Based Model Examples

This appendix discusses a specific example of a comparison between a physics-based and behavioral model of a simplified physical stripline microinductor. It is used to aid in the understanding of the differences between these two types of modeling approaches and help elucidate the costs and benefits discussed in Section 2.1.1

A.1 Simple Physical Structure

We cannot construct an actual microinductor which is as simple as we would like, so we will use a PEEC field solver to obtain “measurement” data. The simple physical structure is a coaxial line shorted at the far end¹ with a nonlinear magnetic material, as shown in Fig. A.1. The inner conductor is made of copper (relative permeability, $\mu_r = 1$, conductivity, $\sigma = 6 \times 10^7$ S/m) with a radius of $r_i = 150 \mu\text{m}$, and the outer shield is a perfect electric conductor ($\sigma = \infty$). The thin cylinder between inner and outer conductors is a $10\mu\text{m}$ thick nonlinear magnetic material with conductivity $\sigma_{core} = 1 \times 10^6$ S/m and a magnetization that is a specific function² of the magnetic field, i.e.

¹The length is sufficiently longer than the cross-sectional dimensions, so end effects are negligible.

²For an example plot of this tanh form, see Fig. 2.1(c).

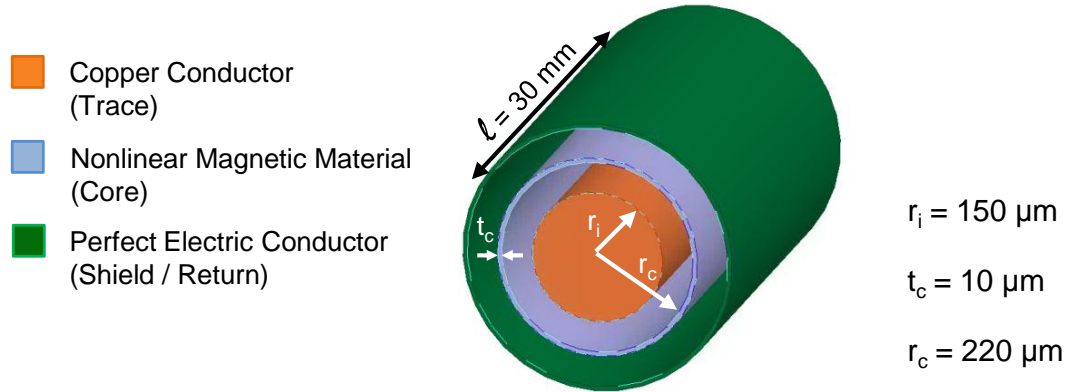


Figure A.1: Dimensional and material information for simple coaxial inductor shorted at the far end.

$$M = M_S \tanh(gH). \quad (\text{A.1})$$

In (A.1) H is the magnetic field intensity magnitude in A/m, M is the magnetization magnitude in A/m, $M_S = 9.08 \times 10^5$ A/m is the saturation magnetization and $g = 3.16 \times 10^{-4}$ m/A is a scaling term. In this model we are ignoring hysteresis, Ferro-Magnetic Resonance/Relaxation (FMR), and electric field effects. Therefore, the “measurements” are made with a magnetoquasistatic simulation of an microinductor which simultaneously includes the effects of magnetic saturation and eddy currents. This is simulated with a PEEC solver, although many other field solvers would also be appropriate.

A.2 First Order Physics-Based Model

While the field-solver “measurements” are solutions to a Partial Differential Equation (PDE), the physics-based model we are constructing is described by a first order Ordinary Differential Equation (ODE). Such a first order model is only capable of capturing the low-frequency eddy currents in the core and thus ignores the skin-effect. The inner conductor is described by its internal DC resistance and inductance, ignoring end effects, given by

$$R_0 = \frac{\ell}{\sigma \pi r_i^2} \quad (\text{A.2a})$$

$$L_0 = \frac{\mu \ell}{8\pi}. \quad (\text{A.2b})$$

In the above, ℓ is the length of the coax and r_i is the radius of the inner conductor (see Fig. A.1) [152]. For most currents the internal inductance of the inner conductor and the external inductance to the core is eclipsed by the inductance of the magnetic material region which is boosted by its relative permeability. Therefore, in what follows we will make the approximation $L_0 = 0$ and ignore any inductance due to the dielectric regions. This is necessary to have only one inductor and thus a 1st order model (i.e. one independent reactive element).

A first order physics-based model of a coaxial microinductor with nonlinear magnetic material can be rather involved. The hyperbolic tangent static nonlinearity of (A.1) makes considering the difference in magnetic path length along the

inner and outer surface of the core difficult. Fortunately, this difference is small compared to the average magnetic path length, so we will consider a uniform magnetic field for the inductance calculation. The first step is to find the effective magnetic path length and magnetic flux area. We take the magnetic path length to be the circumference at the center of the core, that is

$$l_{core} = 2\pi \left(r_c + \frac{t_c}{2} \right). \quad (\text{A.3})$$

See Fig. A.1 for definition of variables in (A.3). The cross-sectional area normal to the flux-density is the magnetic flux area

$$A_{core} = \ell t_c. \quad (\text{A.4})$$

Using Ampere's Law with the magnetic path length as the integration path, we have by symmetry

$$H = \frac{i_L}{l_{core}}, \quad (\text{A.5})$$

where i_L is the current through the inner conductor. Substituting (A.1) and (A.5) in to the definition of flux ($\Phi = BA$) gives

$$\Phi_{core} = BA_{core} = \mu_0 A_{core} (H + M(H)) \quad (\text{A.6})$$

$$\Phi_{core} = \mu_0 A_{core} \left(\frac{i_L}{l_{core}} + M_S \tanh \left(\frac{g i_L}{l_{core}} \right) \right). \quad (\text{A.7})$$

The small-signal inductance of the core can then be found using the chain rule of calculus

$$v_L = \frac{d\Phi_{core}}{dt} = \frac{d\Phi_{core}}{di_L} \frac{di_L}{dt} = L(i_L) \frac{di_L}{dt}, \quad (\text{A.8})$$

where v_L is the voltage across the inductor. Performing differentiation with respect to i_L on (A.7) gives the expression for the small-signal nonlinear inductance of the core as

$$L(i_L) = \frac{\mu_0 A_{core}}{l_{core}} + \frac{\mu_0 A_{core} M_S g}{l_{core}} \text{sech}^2 \left(\frac{g i_L}{l_{core}} \right). \quad (\text{A.9})$$

Using (A.3) and (A.4) gives the inductance based on physical dimensions as

$$L(i_L) = \frac{\mu_0 \ell t_c}{2\pi \left(r_c + \frac{t_c}{2} \right)} + \frac{\mu_0 \ell t_c M_S g}{2\pi \left(r_c + \frac{t_c}{2} \right)} \text{sech}^2 \left(\frac{g i_L}{2\pi \left(r_c + \frac{t_c}{2} \right)} \right). \quad (\text{A.10})$$

The next consideration of the physics-based core model are eddy currents. Eddy currents are generated when time varying magnetic flux gives rise to an induced electromotive force in a conductive material. For eddy currents it is more important to know the variation in magnetic field in the core,³ so consider the core to have a small-signal permeability of $\mu(i_{bias})$, where i_{bias} is the DC bias current to the microinductor. Ampere's law can be used to obtain the small-signal flux from r to $r_c + t_c$ as

³When compared to their importance in calculating the inductance

$$\Phi_{core}(r) = \frac{\ell i_L \mu (i_{bias})}{2\pi} \ln\left(\frac{r_c + t_c}{r}\right), \quad (\text{A.11})$$

where i_L is the amplitude of the small-signal sinusoidal microinductor current. In the coaxial model, since the perfect electric conductor enforces a zero electric field at the outer edge of the coaxial configuration, we can consider the path length for Faraday's law to be ℓ , thus

$$E_{core}(r) = \frac{j\omega\Phi_{core}(r)}{\ell} = \frac{j\omega i_L \mu (i_L)}{2\pi} \ln\left(\frac{r_c + t_c}{r}\right). \quad (\text{A.12})$$

In (A.12) ω is the radian frequency of the small-signal sinusoidal microinductor current. Using Ohm's law and integrating over the core's volume to obtain ohmic power loss, gives

$$P_{eddy} = \ell \int_{r_c}^{r_c+t_c} \frac{\sigma_{core} |E_{core}(r)|^2}{2} 2\pi r dr. \quad (\text{A.13})$$

Evaluating the integral, we arrive at

$$P_{eddy} = \frac{\ell i_L^2 \sigma_{core} \omega^2 \mu^2 (i_{bias})}{16\pi} \left[2r_c t_c + t_c^2 - 2r_c^2 \left(\ln^2\left(\frac{r_c + t_c}{r_c}\right) + \ln\left(\frac{r_c + t_c}{r_c}\right) \right) \right]. \quad (\text{A.14})$$

The voltage across the nonlinear inductor is $j\omega\Phi_{core}(r_c)$, therefore the parallel resistance due to eddy currents is

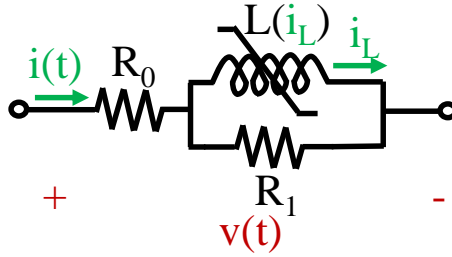


Figure A.2: First order physics-based model of coaxial nonlinear microinductor of Fig. A.1.

Table A.1: Element values of circuit given in Fig. A.2 for first order physics-based model.

Element	Formula	Value
R_0	(A.2a)	7.1 m Ω
$L(i_L)$	(A.10)	$0.27 + 77 \cdot \text{sech}^2(0.22 \cdot i_L)$ nH
R_1	(A.15)	6.5 Ω

$$R_1 = \frac{\omega^2 \Phi_{core}^2(r_c)}{2P_{eddy}} = \frac{2\ell}{\pi \sigma_{core}} \frac{\ln^2\left(\frac{r_c+t_c}{r_c}\right)}{\left(2r_c t_c + t_c^2 - 2r_c^2 \left(\ln^2\left(\frac{r_c+t_c}{r_c}\right) + \ln\left(\frac{r_c+t_c}{r_c}\right)\right)\right)}. \quad (\text{A.15})$$

Thus, our final model for the low-frequency core eddy currents and nonlinear inductance is a parallel combination of $L(i_L)$ described by (A.10) and R_1 described by (A.15). Together, these elements form the first order physics-based model shown in Fig. A.2 modeling the coaxial microinductor of Fig. A.1. The specific element values for the dimensions and materials used are given in Table A.1 and their scalable formulas are given in Appendix A.

A.3 First Order Behavioral Model

Behavioral models are based on a simplified mathematical descriptions of the physical device. One quite general way to describe a nonlinear ordinary differential equation is through the state-space description. Let us consider the Nth order state-space representation of a general P-port system:

$$\dot{\mathbf{x}}(t) = \mathbf{f}(\mathbf{x}(t), \mathbf{u}(t), t) \quad (\text{A.16a})$$

$$\mathbf{y}(t) = \mathbf{g}(\mathbf{x}(t), \mathbf{u}(t), t). \quad (\text{A.16b})$$

In (A.16) **bold** letters represent vector functions or quantities. $\mathbf{x}(t)$ is a $N \times 1$ vector of state variables as a function of time, t and $\dot{\mathbf{x}}(t)$ is their time derivative vector. The state variables in our case typically represent fluxes or currents through microinductors. The input $P \times 1$ vector, $\mathbf{u}(t)$, captures the voltages and/or currents applied to the model and $\mathbf{y}(t)$ is the $P \times 1$ vector of output currents and/or voltages. The system evolves according to the N state-derivative functions organized into a $N \times 1$ vector of functions, $\mathbf{f}(\cdot)$. The output variables are then obtained from the P output functions organized into a $P \times 1$ vector of functions, $\mathbf{g}(\cdot)$. The goal of behavioral modeling is to accurately reproduce the functions $\mathbf{f}(\cdot)$ and $\mathbf{g}(\cdot)$, and thus the device's behavior.

First, we will consider the state-space description of the physics-based model (Fig. A.2). The physics-based model is first order and a single port, so we have ($N=1$ and $P=1$). Considering the time-dependent terminal voltage, $v(t)$, as our

input and the microinductor current, $i_L(t)$, as our state, it can be shown using Kirchoff's Laws/circuit analysis that the state derivative function is

$$f_{physics}(i_L(t), v(t)) = \frac{di_L(t)}{dt} = \frac{R_1(v(t) - R_0 i_L(t))}{(R_0 + R_1)L(i_L(t))}. \quad (\text{A.17})$$

Also, using basic circuit analysis, the terminal “output” current can be found from the state and input giving $g(\cdot)$ as

$$g_{physics}(i_L(t), v(t)) = i(t) = \frac{v(t) + R_1 i_L(t)}{R_0 + R_1}. \quad (\text{A.18})$$

Now that we have the state-space description of our physics-based circuit, let us consider some behavioral/mathematical modeling approaches. To reproduce the behavior of the coaxial microinductor we need to approximate the functions $f(\cdot)$ and $g(\cdot)$. To simplify, we will use the physics-based model's linear $g(\cdot)$, (A.18), and focus on the nonlinear state function $f(\cdot)$. To completely specify our example, we will be using the values given in Table A.1 for the elements. The PEEC field-solver state-function is obtained by harmonic balance simulations for ten bias currents from -8 Amps to 8 Amps each performed at ten logarithmically-spaced frequencies from 100 kHz to 5 MHz. The applied large-signal sinusoidal voltage had amplitude $1.4 \times 10^{-6} \cdot f$ so as to not cause huge currents at low frequencies. A rectangular domain over ± 7 Amps and ± 4 Volts is then obtained by removing points outside the domain. The state-function is generated over this domain from the terminal characteristics ($i(t)$, $v(t)$, and $\frac{di(t)}{dt}$) by using (A.18) and its time derivative.

Two common ways to estimate $\mathbf{f}(\cdot)$ are a canonical form for the Volterra series [153] and Artificial Neural Networks (ANNs) [154]. For a first order network, [153] gives $\mathbf{f}(\cdot)$ as the sum of two polynomials α and β

$$f_{poly}(i_L(t), v(t)) = \sum_{m=1}^M (\alpha_m i_L(t)^m) + \sum_{n=0}^N (\beta_n v(t)^n). \quad (\text{A.19})$$

where α_m and β_n are the coefficients of the polynomial. A linear least squares fitting of (A.19) with order $M=7$, $N=7$ to the PEEC field-solver data is used as our polynomial behavioral model. The state functions for the PEEC field solver and this behavioral model are shown in Fig. A.3(a) and (b), respectively, over the domain $i_L \in [-4.7, 4.7]$ and $v \in [-2.35, 2.35]$. The L2-norm error⁴ for the polynomial behavioral model is 2.6%. Expanding the domain by 70% and calculating the difference between the two models shows that the polynomial approximation does a poor job of extrapolation (See Fig. A.3(c)). This is expected since polynomials may grow fast outside their fitting domain, and the PEEC field-solver data remains relatively flat. The L2-norm error jumps to 34% over the expanded domain for the polynomial behavioral model.

The artificial neural network approach is more involved [154]. For example, the state function is formulated as

$$f_{ANN}(i_L(t), v(t)) = -i_L(t) + \tau h_{ANN}(i_L(t), v(t), w). \quad (\text{A.20})$$

⁴The L2-norm error for a bivariate function is defined as $100\% \cdot \sqrt{\sum_i \sum_j |\tilde{f}(x_i, y_j) - f(x_i, y_j)|^2} / \sqrt{\sum_i \sum_j |f(x_i, y_j)|^2}$ where \tilde{f} is the approximation being compared to the reference f .

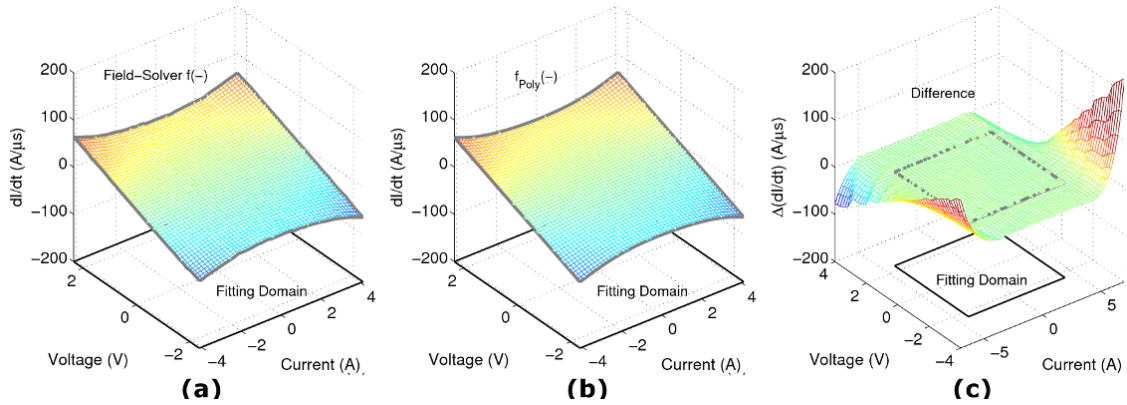


Figure A.3: State-function for field-solver measurements ($f(\cdot)$) (a), the polynomial fit to the state-function (f_{poly}) (b), and the difference between the two on an extended domain (c).

In (A.20), τ is a constant scaling parameter to a feed-forward Multi-Layer Perceptron (MLP) neural network, h_{ANN} with constant weighting parameters w [155]. Using ten hidden neurons that have hyperbolic tangent activation functions, the neural network was trained to the PEEC field-solver data. The comparison between the PEEC field-solver data and the trained neural network behavioral model on the same domain as the polynomial behavioral model is shown in Fig. A.4(a) and (b). The L2-norm error over this domain is just 2.2%. The difference on a 70% expanded domain is shown in Fig. A.4(c), where we see that the artificial neural network also poorly extrapolates, with an L2-norm error of 39% on the expanded domain.

The physics-based model from Appendix A.1 is not trained or fitted to the field-solver data. Their comparison is shown in Fig. A.5 (a) and (b). The L2-norm error on the original domain is actually larger than the fitted functions, i.e.

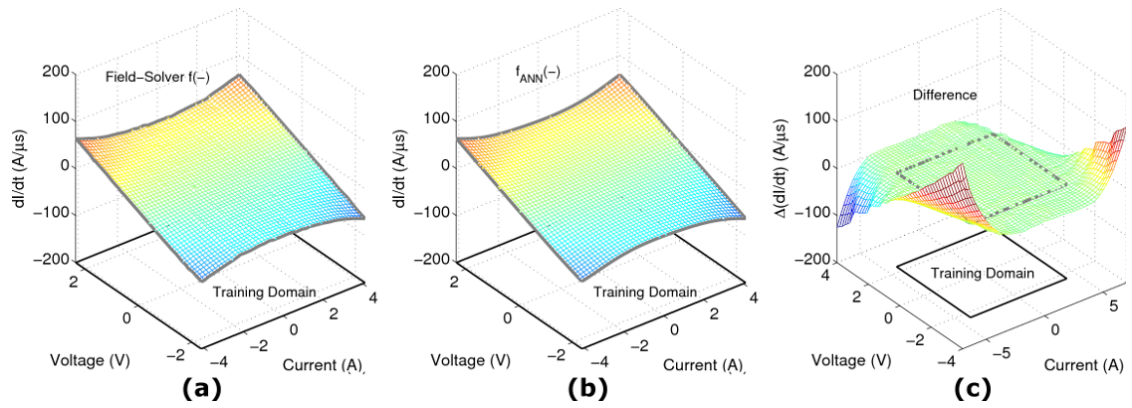


Figure A.4: State function for field-solver measurements ($f(\cdot)$) (a), the artificial neural network fit to the state function (b), and the difference between the two on an extended domain (c).

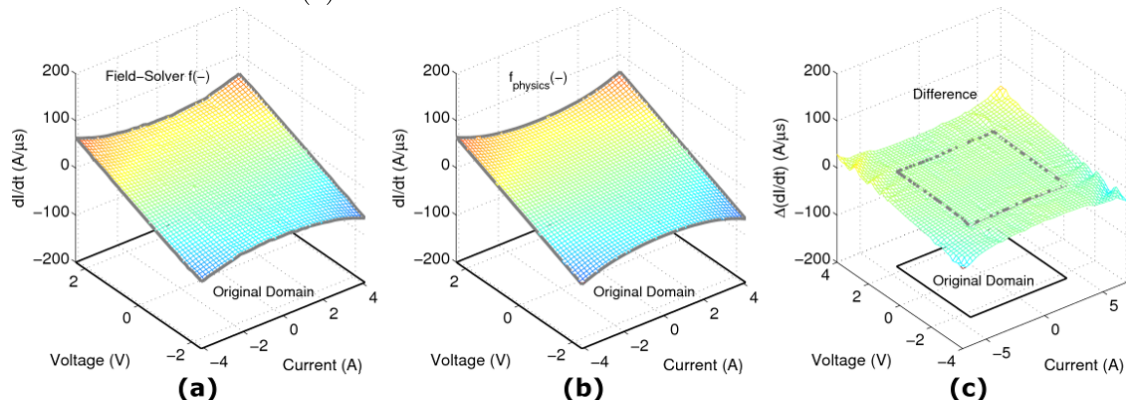


Figure A.5: State function for field-solver measurements ($f(\cdot)$) (a), the physics-based state function (b), and the difference between the two on an extended domain (c).

4.5%. However, as shown in Fig. A.5 (c) on the expanded domain the error is much lower at 8.2% than for the behavioral models. We believe the errors in the physics-based model are due to ignoring higher-order eddy current-effects in the core and conductor.

Appendix B – Magnetic Domain and Inductance

B.1 Magnetic Circuits

The word circuit is from the Latin *circuitus*, which literally means “a going around,” or more mathematically, “something making a closed path.” Electrical circuits are made of closed paths of elements as evidenced by the ability to apply Kirchoff’s Voltage Law (KVL). As we will see, magnetic circuits, too, form closed paths and obey their respective Kirchoffian laws. For an electric circuit, Kirchoff’s laws are

$$\sum_k^K I_k = 0 \quad (\text{B.1a})$$

$$\sum_n^N V_n = 0. \quad (\text{B.1b})$$

Equation (B.1a) is Kirchoff’s Current Law (KCL), and (B.1b) is Kirchoff’s Voltage Law, where I_k are the K currents flowing into a particular node, and V_n are the voltages across the N elements around a particular closed loop (a mesh). Kirchoff’s laws are related to Maxwell’s equations. If we regard $\frac{d\Phi}{dt}$ as a lumped voltage source giving rise to V_s in an otherwise passive circuit, then the integral form of Faraday’s Law becomes

$$0 = -V_s + \oint_C \mathbf{E} \cdot d\mathbf{l} \approx -V_s + \sum_n^N E_n l_n = -V_s + \sum_n^N V_n, \quad (\text{B.2})$$

which is KVL. Similarly, consider the integral form of the continuity equation with $\frac{dq}{dt} = 0$, this is the case for a circuit node. If there is a build up of charge, a capacitance needs to be additionally placed at the node. The integral form of the continuity equation thus becomes

$$0 = \oiint_S \mathbf{J} \cdot d\mathbf{A} \approx \sum_k^K J_k A_k = \sum_k^K I_k, \quad (\text{B.3})$$

where we have used the lumped circuit approximation of wire area A_k for current I_k and transformed the equation to KCL.

It is instructive to see that magnetic circuits also follow KVL and KCL, where in an analogous way, voltage (electromotive force) is replaced by magnetomotive force, and current is replaced by magnetic flux. Instead of Faraday's law and the continuity equation, we will be starting from Ampere's law and Gauss's law for magnetism.

$$0 = -I_{tot} + \oint_C \mathbf{H} \cdot d\mathbf{l} \approx -I_{tot} + \sum_n^N H_n l_n = -I_{tot} + \sum_n^N \mathcal{F}_n \quad (\text{B.4a})$$

$$0 = \oiint_S \mathbf{B} \cdot d\mathbf{A} \approx \sum_k^K B_k A_k = \sum_k^K \Phi_k. \quad (\text{B.4b})$$

Note the analogy between (B.2) and (B.4a), also (B.3) and (B.4b). From this form of KCL and KVL we can see that the magnetomotive force (MMF) can either be

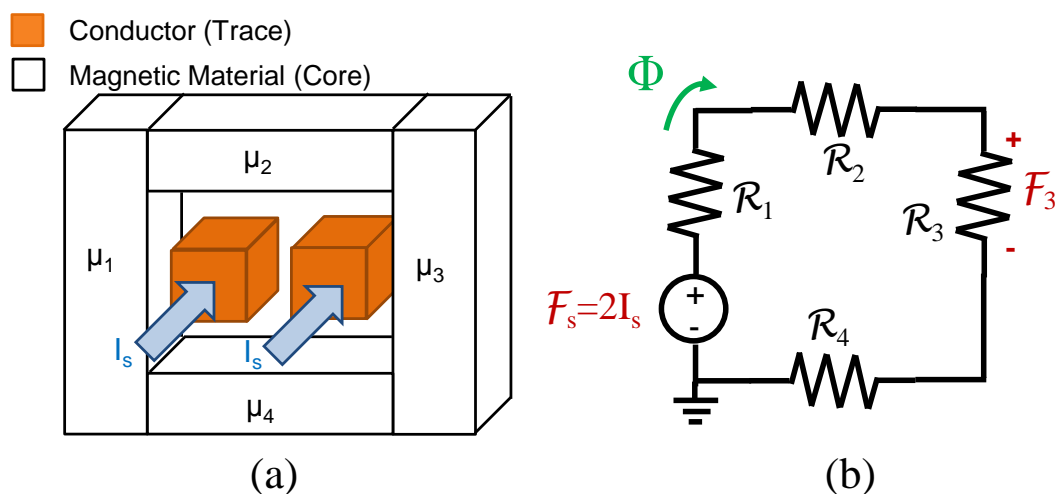


Figure B.1: Simple diagram of a section of a microinductor (a), and its corresponding magnetic circuit (b)

described by the magnetic field integrated over a path, or the enclosed current creating said field (see (B.4a)). In either case, the general unit of MMF is the ampere-turn (At). The flow term of the magnetic circuit should be more familiar, it is the magnetic flux, Φ , and has the unit weber (Wb).¹

Let us consider the microinductor illustrated in Fig. B.1(a). Application of (B.4a) produces

$$0 = -2I_s + \sum_n^4 H_n l_n = -2I_s + \sum_n^4 \Phi \frac{l_n}{\mu_n A_n}, \quad (\text{B.5})$$

where I_s is the source current, l_n is the length of section n , and A_n is the area of section n . From (B.5) it can be seen that Φ is multiplied by a factor very similar to resistance with σ replaced by μ . In fact, this term is the analog of resistance

¹Named after German physicist Wilhelm Eduard Weber

called reluctance. Our magnetic KVL equation becomes

$$0 = -2I_s + \sum_n^4 \Phi \mathcal{R}_n, \quad (\text{B.6})$$

where \mathcal{R}_n is the n th reluctance of the magnetic circuit (see Fig. B.1 (b)).

Now that we have established the basics of magnetic circuits, how can the concept of a magnetic circuit be applied to formation of electric circuits? One way is to convert a magnetic circuit to an electric circuit using Slemon's dual [94]. Slemon's dual derives from the fact that magnetic current (Φ) gives rise to electric voltage ($Nd\Phi/dt$) and magnetic voltage (\mathcal{F}) is created from electric current (NI), where N is the number of turns. In general this dual relationship between voltage and current is described by a generalized impedance inverter [156]. Thus, parallel combinations of reluctances in the magnetic domain, are the dual of series combinations of inductances. Likewise, series combinations of reluctances become parallel inductances. To transform from a magnetic circuit to electric, one simply needs to generate the dual circuit where parallel and series combinations are switched.

In reference [94] Slemon presents a method to form the dual network graphically. First, consider the magnetic circuit in Fig. B.2(a). Instead of individually converting parallel and series connections, label the mesh openings with letters A, B, and C (don't forget the "opening" C on the outside of the circuit). Next, for each element, make a connection from one opening to the other through the element (dashed blue lines in Fig. B.2(a)). In the dual circuit the opening A becomes

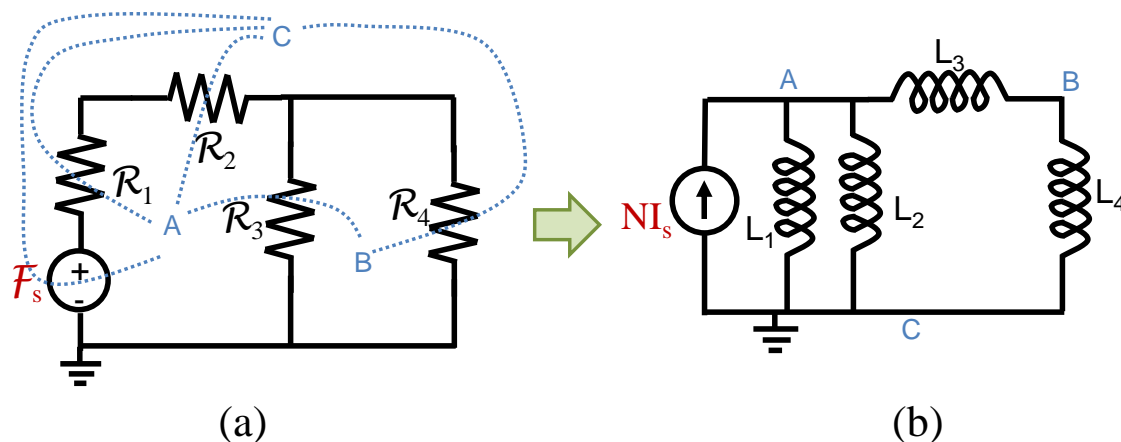


Figure B.2: Example of a magnetic circuit (a) being converted to an electric circuit (b).

node A, and a dashed line from A to B through \mathcal{R}_3 is a connection from node A to node B with element L_3 , see Fig. B.2(b). In this way, the complete dual network is formed from the original network.

Unfortunately, the conversion from a magnetic circuit to an purely electric circuit cannot always be done, specifically for non-planar magnetic circuits. To handle this scenario impedance inverters [156] such as the gyrator [157], or the magnetoelectric differential gyrator [89], can be employed. Using the gyrator, the reciprocal of reluctance, known as permeance, is replaced by a capacitor in the magnetic circuit. Next, the winding interface to the electric domain is replaced by the gyrator. In the magneto-electric differential gyrator, which we will be using, the magnetic circuit is represented more intuitively, with resistance replacing reluctance and the winding being modeled by the differential gyrator. The differential gyrator has the relationship between its two domains of

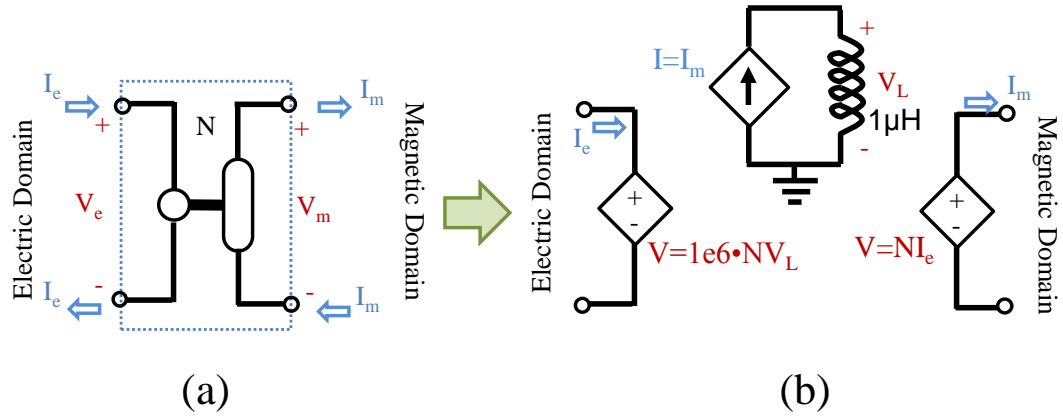


Figure B.3: Magnetolectric differential gyrator symbol adopted from [89] (a) and an example subcircuit implementation (b).

$$V_e = N \frac{d\Phi}{dt} = N \frac{dI_m}{dt} \quad (\text{B.7a})$$

$$\mathcal{F} = V_m = NI_e, \quad (\text{B.7b})$$

where the subscript m indicates the magnetic domain, and e indicates the electric domain. The magnetolectric differential gyrator symbol is shown in Fig. B.3(a) and can be implemented in common circuit simulators using controlled sources and a memory element such as an inductor. An example of such a circuit using a $1\ \mu\text{H}$ inductor is shown in Fig. B.3(b).

With the conversion equations between domains in place, it is possible to determine how a complex magnetic impedance transforms to the electric domain. Consider a general impedance in the magnetic domain,

Table B.1: Conversion of equations and elements between domains.

Electric Domain		Magnetic Domain	
Faraday's Law	$\nabla \times \mathbf{E} = \frac{\partial \mathbf{B}}{\partial t}$	Ampere's Law	$\nabla \times \mathbf{H} = \frac{\partial \mathbf{J}}{\partial t}$
Continuity Equation	$\nabla \cdot \mathbf{J} = -\frac{\partial \rho}{\partial t} = 0$	Gauss's Law	$\nabla \cdot \mathbf{B} = 0$
Electromotive Force	$V = V_e$	Magnetomotive Force	$\mathcal{F} = V_m$
Electric Current	$I = I_e$	Magnetic Flux	$\Phi = I_m$
Inductance	$L = \frac{N^2}{\mathcal{R}}$	Reluctance	$\mathcal{R} = \frac{N^2}{L}$
Resistance	$R = \frac{N^2}{\mathcal{L}}$	Magnetic Inductance	$\mathcal{L} = \frac{N^2}{R}$
Impedance	$Z_e = \frac{j\omega N^2}{Z_m}$	Magnetic Impedance	$Z_m = \frac{j\omega N^2}{Z_e}$

$$V_m = I_m Z_m. \quad (\text{B.8})$$

Using phasors and the fact that the operator d/dt is multiplication by $j\omega$, we can replace the magnetic domain terms with the electric domain terms from (B.7) and simplify.

$$NI_e = \frac{1}{Nj\omega} V_e Z_m \quad (\text{B.9a})$$

$$Z_e = \frac{V_e}{I_e} = \frac{N^2 j\omega}{Z_m}, \quad (\text{B.9b})$$

where $j = \sqrt{-1}$. From (B.9b), we see that magnetic resistance (inductance) behaves in the electric domain as an inductance (resistance). Table B.1 summarizes the analogy between the electric and magnetic circuit domains.

B.2 Nonlinear Inductance Definitions

Corresponding to the two domains discussed in Appendix B.1 (electric and magnetic) are two different implementations of nonlinear inductors. We first consider an implementation in the electric domain. The linear electric circuit definition of inductance is $v = L \cdot di/dt$, if we were to define a linearized inductance at each current which satisfied this relationship, we would have what is known as the small-signal, or incremental inductance, i.e.

$$v(t) = L_{ss}(i(t)) \frac{di(t)}{dt}, \quad (\text{B.10})$$

where $L_{ss}(i(t))$ is the small-signal inductance. The small-signal inductance can be implemented with controlled sources in the electric domain. It also can be related to the magnetic domain. Consider Faraday's Law and the chain rule of calculus.

$$v(t) = \frac{Nd\Phi(t)}{dt} = \frac{Nd\Phi(i(t))}{di} \frac{di(t)}{dt}. \quad (\text{B.11})$$

We see from comparing (B.11) to (B.10), that the definition of small-signal inductance in terms of magnetic circuit quantities is

$$L_{ss}(i) = \frac{Nd\Phi(i)}{di}. \quad (\text{B.12})$$

Instead of performing the differentiation of Φ with respect to i , which amounts to the slope of the tangent line of $\Phi(i)$ at i , we can take the slope of the secant line from $(0, 0)$ to (i, Φ) , i.e.

$$L_{ls}(i) = \frac{N\Phi(i)}{i}, \quad (\text{B.13})$$

where $L_{ls}(i)$ is known as the secant or large-signal inductance. Regardless of the definition of inductance used, we see that it may be implemented in the magnetic domain as a voltage controlled current source or, equivalently, a nonlinear reluctance, in essence, $\Phi(i)$.

We have seen the two definitions of inductance for a single inductor, what about two or more coupled inductors, as in a transformer? Consider the arrangement of two toroidal conductors shown in Fig. B.4. Φ_{10} is the flux flowing through coil 1, but not coupled to any other coil, likewise with Φ_{20} and coil 2. Φ_{12} is the flux generated by coil 2 linking to coil 1, and Φ_{21} is the flux generated by coil 1 linking to coil 2. All of these terms in a nonlinear magnetic configuration are functions of all the source currents. We can, therefore, write the equations for the total flux through coil 1 (Φ_1) and coil 2 (Φ_2) as

$$\Phi_1(I_1, I_2) = \Phi_{10}(I_1, I_2) + \Phi_{12}(I_1, I_2) + \Phi_{21}(I_1, I_2) \quad (\text{B.14a})$$

$$\Phi_2(I_1, I_2) = \Phi_{20}(I_1, I_2) + \Phi_{21}(I_1, I_2) + \Phi_{12}(I_1, I_2). \quad (\text{B.14b})$$

Similar to the single inductor case, we can divide by the current generating the flux and get the secant, or large-signal inductance matrix, $\mathbf{M}_{ls}(I_1, I_2)$.

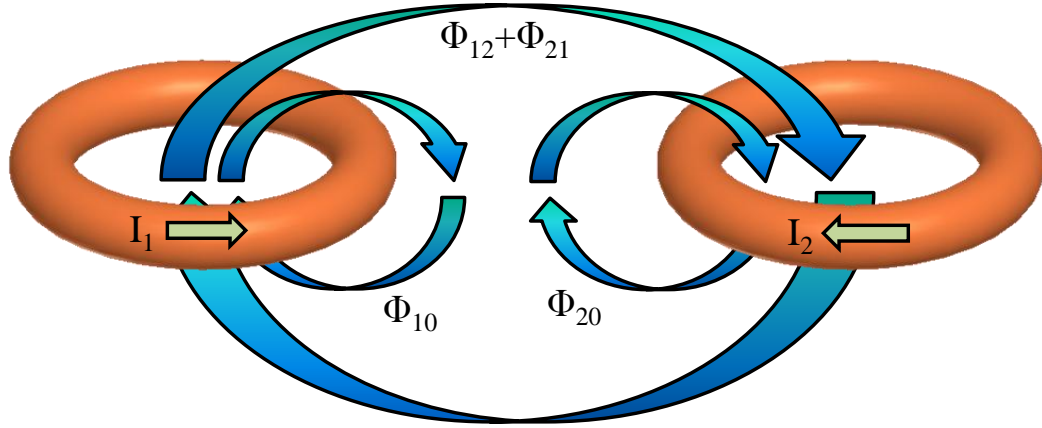


Figure B.4: Two magnetically coupled toroidal conductors with labeled fluxes.

$$\begin{bmatrix} \Phi_1 \\ \Phi_2 \end{bmatrix} = \begin{bmatrix} \frac{\Phi_{10} + \Phi_{12}}{I_1} & \frac{\Phi_{21}}{I_2} \\ \frac{\Phi_{12}}{I_1} & \frac{\Phi_{20} + \Phi_{21}}{I_2} \end{bmatrix} \begin{bmatrix} I_1 \\ I_2 \end{bmatrix} = \mathbf{M}_{ls}(I_1, I_2) \mathbf{I}. \quad (\text{B.15})$$

The incremental, or small-signal inductance is used to calculate voltage rather than flux. Instead of a vector of currents on the right-hand-side of the matrix, we have a vector of their time derivatives. The multi-variable chain rule informs us the matrix components to create the voltage are $\partial\Phi_i/\partial I_j$ so the definition of the small-signal inductance matrix, $\mathbf{M}_{ss}(I_1, I_2)$ is

$$\begin{bmatrix} V_1 \\ V_2 \end{bmatrix} = \begin{bmatrix} \frac{d\Phi_1}{dt} \\ \frac{d\Phi_2}{dt} \end{bmatrix} = \begin{bmatrix} \frac{\partial\Phi_1}{\partial I_1} & \frac{\partial\Phi_1}{\partial I_2} \\ \frac{\partial\Phi_2}{\partial I_1} & \frac{\partial\Phi_2}{\partial I_2} \end{bmatrix} \begin{bmatrix} \frac{dI_1}{dt} \\ \frac{dI_2}{dt} \end{bmatrix} = \mathbf{M}_{ss}(I_1, I_2) \frac{d\mathbf{I}}{dt}. \quad (\text{B.16})$$

If there are N_i turns to coil i , simply replace Φ_i by $N_i\Phi_i$ in (B.15) and (B.16). For more details, including how to convert between the forms, see [158], where the small-signal inductance is referred to as “differential inductance.”

Appendix C – Passivity

The enforcement of passive behavior for the passive components in this thesis is important. Passivity implies that no net energy is generated by the device. When power is a critical parameter of many of the devices, it is apparent that it is undesirable for power to be generated by our device, for this non-physical effect would alter the accurate modeling of power loss. Less apparent, is the the benefits of having a passive circuit, such as causality, and aiding in stability [71]. Also, in general, since we are generating physics-based models it is good for them to have physically appropriate properties such as passivity. In this section we demonstrate that both the electrical nonlinear inductor used in the microinductor model, and the magnetic nonlinear reluctance used in the microtransformer model and microfluxgate model are passive with the proper choice of parameters.

C.1 Electric Domain

The model of Fig. 3.5 has all linear lumped elements, except for the N nonlinear inductors, L_{cn} . Since series and parallel combinations of passive elements creates a passive circuit, if all of these elements can be proven to be passive, then the total circuit of Fig. 3.5 would be passive. The algorithm presented in Section III guarantees that all of the linear lumped elements are positive, thus all that remains

is to show that the N nonlinear inductors, L_{cn} , are also passive.

The definition of passivity for any element is that the energy absorbed is always non-negative. Thus, using passive sign convention, we require

$$\int_{\tau \rightarrow -\infty}^t v(\tau) i(\tau) d\tau \geq 0. \quad (\text{C.1})$$

In (C.1) v is the voltage across the nonlinear inductor and i is the current through the inductor. Next, we replace the voltage with the expression for the voltage across a small-signal nonlinear inductor.

$$\int_{\tau \rightarrow -\infty}^t L_{cn}(i) \frac{di}{d\tau} i d\tau \geq 0 \quad (\text{C.2})$$

Changing our integration variable, with the assumption that $\lim_{\tau \rightarrow -\infty} i(\tau) = 0$ gives

$$\int_{\lambda=0}^i L_{cn}(\lambda) \lambda d\lambda \geq 0. \quad (\text{C.3})$$

If L_{cn} is non-negative for all currents, then the integrand of (C.3) is either in quadrant I or III and the integral is non-negative for any i . It is a sufficient condition for passivity that the small-signal inductance be non-negative and thus the circuit of Fig. 3.5 is passive with appropriate choice of circuit parameters.

C.2 Magnetic Domain

For the magnetic domain, it is helpful to convert the condition for passivity from the electric to the magnetic side of a magneto-electric differential gyrator. It then

becomes apparent that the transformed passivity condition is met for the nonlinear reluctance and linear magnetic inductor we are using in the magnetic domain. Since the transformed condition for passivity for series and parallel connections is preserved in the magnetic domain, this shows that the total networks of Fig. 4.4 and Fig. 5.2 are passive.

On the electric domain side of a differential gyrator the condition for passivity is (C.1). Using the conversion to the magnetic domain of $v = Nd\Phi/dt$ and $\mathcal{V}_m = Ni$ from (B.7a) and (B.7b) gives:

$$\int_{\tau \rightarrow -\infty}^t \frac{1}{N} \mathcal{V}_m(\tau) \frac{Nd\Phi}{d\tau} d\tau \geq 0. \quad (\text{C.4})$$

Changing the integration variable and simplifying, while assuming $\lim_{\tau \rightarrow -\infty} \Phi(\tau) = 0$ gives

$$\int_{\Psi=0}^{\Phi} \mathcal{V}_m(\Psi) d\Psi \geq 0. \quad (\text{C.5})$$

Equation (C.5) is employed to evaluate if the elements on the magnetic side of the differential gyrator preserve passivity. Consider first the linear magnetic inductor representing loss. Its equation is $\mathcal{V}_m = \mathcal{L}d\Phi/dt$, rewriting this expression with differentials and the exchange of variable $\Psi = \Phi$ yields

$$d\Psi = \frac{\mathcal{V}_m}{\mathcal{L}} dt. \quad (\text{C.6})$$

Inserting this expression into (C.5) and making the exchange of variables back to time, reveals

$$\int_{\tau \rightarrow -\infty}^t \frac{(\mathcal{V}_m(\tau))^2}{\mathcal{L}} d\tau \geq 0. \quad (\text{C.7})$$

It is clear from (C.7) that the integrand (and thus integral) is always positive for positive magnetic inductance, \mathcal{L} .

We now use (C.5) to evaluate if the nonlinear reluctance we have created is also passive. The expression for a nonlinear reluctance is $\Phi(\mathcal{V}_m)$; notice that this is the inverse of the integrand in (C.5). So what can be said about the relationship between MMF and Flux based on passivity? If the integrand of (C.5) is a one-to-one function and is always in quadrants I or III, then the integral will always be positive, and the nonlinear reluctance is passive. This is true for our shifted hyperbolic tangent nonlinear reluctance if, the x-axis shifts, slopes, and y-axis scalings for each term are always positive. Our optimization routine is only fit over positive parameter values, thus we guarantee the nonlinear reluctance is passive.

Appendix D – Sample Device Models

This appendix catalogs the specific ideal element values and parameters of the models generated throughout this thesis.

D.1 Microinductor Device Models

Microinductor device 1 (see Section 3.5.1) has parameters given in Table D.1, device 2 (see Section 3.5.2) has parameters given in Table D.2 and device 3 (see Section 3.5.3) has parameters given in Table D.3. The circuit topology for all three is given in Fig. 3.5.

Table D.1: Extracted circuit element values and nonlinear inductance parameters for microinductor device 1.

R_s	555 Ω	C_s	291 pF				
L_{t1}	1.71 nH	R_{t1}	897 m Ω	L_{t2}	6.19 nH	R_{t2}	638 m Ω
R_{c1}	867 Ω	R_{c2}	82 Ω	R_{c3}	103 Ω	R_{c4}	507 Ω
α_{11}	0.287	α_{21}	-1.30 A^{-1}	α_{31}	0.232 A	α_{41}	-15.7
L_{01}	27.9 pH						
α_{12}	0.556	α_{22}	-2.56 A^{-1}	α_{32}	0.639 A	α_{42}	-14.5
L_{02}	23.2 fH						
α_{13}	0.778	α_{23}	-4.66 A^{-1}	α_{33}	0.355 A	α_{43}	-14.4
L_{03}	2.52 nH						
α_{14}	0.593	α_{24}	-2.64 A^{-1}	α_{34}	1.00 A	α_{44}	-13.5
L_{04}	1.40 nH						

Table D.2: Extracted circuit element values and nonlinear inductance parameters for microinductor device 2.

R_s	101 m Ω	C_s	305 fF				
L_{t1}	7.05 nH	R_{t1}	16.4 m Ω	L_{t2}	5.31 nH	R_{t2}	15.0 m Ω
R_{c1}	133 Ω	R_{c2}	4.29 Ω	R_{c3}	31.7 Ω	R_{c4}	13.5 Ω
α_{11}	0.598	α_{21}	-0.702 A^{-1}	α_{31}	2.84 A	α_{41}	-15.7
L_{01}	367 aH						
α_{12}	0.889	α_{22}	-1.03 A^{-1}	α_{32}	5.32 A	α_{42}	-12.4
L_{02}	1.42 fH						
α_{13}	0.289	α_{23}	-1.16 A^{-1}	α_{33}	1.68 A	α_{43}	-15.8
L_{03}	444 aH						
α_{14}	0.301	α_{24}	-0.412 A^{-1}	α_{34}	2.15 A	α_{44}	-17.1
L_{04}	2.58 nH						

Table D.3: Extracted circuit element values and nonlinear inductance parameters for microinductor device 3.

R_s	103 Ω	C_s	11.1 pF				
L_{t1}	166 nH	R_{t1}	1.06 k Ω	L_{t2}	4.47 nH	R_{l2}	73.8 Ω
R_{c1}	35.8 k Ω	R_{c2}	26.9 k Ω	R_{c3}	54.8 k Ω	R_{c4}	30.1 k Ω
α_{11}	0.893 A	α_{21}	$-1.08 \times 10^3 A^{-1}$	α_{31}	10.6 mA	α_{41}	-2.75
L_{01}	135 pH						
α_{12}	0.963 A	α_{22}	$-1.13 \times 10^3 A^{-1}$	α_{32}	12.3 mA	α_{42}	6.41×10^{-3}
L_{02}	58.7 pH						
α_{13}	0.963 A	α_{23}	$-1.09 \times 10^3 A^{-1}$	α_{33}	12.4 mA	α_{43}	-0.498
L_{03}	49.0 pH						
α_{14}	0.322 A	α_{24}	-247 A^{-1}	α_{34}	12.9 mA	α_{44}	-10.8
L_{04}	1.64 nH						

D.2 Microtransformer Device Models

Microtransformer device 1 (see Section 4.5.1) has parameters given in Table D.4, device 2 (see Section 4.5.2) has parameters given in Table D.5 and device 3 (see Section 4.5.3) has parameters given in Table D.6. The circuit topology for all three is given in Fig. 4.4.

Table D.4: Extracted circuit element values and nonlinear reluctance parameters for microtransformer device 1.

N_1	2	N_2	2	\mathcal{R}_{lin}	$1.55 \times 10^9 H^{-1}$		
C_{s1}	0 F	R_{s1}	$\infty \Omega$	C_{s2}	0 F	R_{s2}	$\infty \Omega$
C_{top}	0 F	R_{top}	$\infty \Omega$	C_{bot}	0 F	R_{bot}	$\infty \Omega$
R_{a1}	782 m Ω	R_{a2}	703 m Ω	R_{a3}	746 m Ω		
L_{a1}	897 pH	L_{a2}	998 pH	L_{a3}	2.05 nH		
R_{b1}	955 m Ω	R_{b2}	542 m Ω	R_{b3}	918 m Ω		
L_{b1}	797 pH	L_{b2}	1.51 nH	L_{b3}	868 pH		
\mathcal{L}_{c1}	24.8 m \mathcal{U}	\mathcal{L}_{c2}	295 m \mathcal{U}	\mathcal{L}_{c3}	97.1 m \mathcal{U}	\mathcal{L}_{c4}	41.1 m \mathcal{U}
$\beta_{0,1}$	3.76 pH	$\beta_{1,1}$	1.83 nWb	$\beta_{2,1}$	1.31 nH	$\beta_{3,1}$	542 pWb
$\beta_{4,1}$	780 pH	$\beta_{5,1}$	678 mAt				
$\beta_{0,2}$	32.5 pH	$\beta_{1,2}$	886 pWb	$\beta_{2,2}$	1.42 nH	$\beta_{3,2}$	663 pWb
$\beta_{4,2}$	1.99 nH	$\beta_{5,2}$	749 mAt				
$\beta_{0,3}$	24.1 pH	$\beta_{1,3}$	1.31 nWb	$\beta_{2,3}$	1.42 nH	$\beta_{3,3}$	1.43 nWb
$\beta_{4,3}$	2.53 nH	$\beta_{5,3}$	1.37 At				
$\beta_{0,4}$	12.0 pH	$\beta_{1,4}$	1.82 nWb	$\beta_{2,4}$	1.48 nH	$\beta_{3,4}$	1.07 nWb
$\beta_{4,4}$	549 pH	$\beta_{5,4}$	2.29 At				

Table D.5: Extracted circuit element values and nonlinear reluctance parameters for microtransformer device 2.

N_1	3	N_2	3	\mathcal{R}_{lin}	$7.77 \times 10^8 H^{-1}$		
C_{s1}	0 F	R_{s1}	$\infty \Omega$	C_{s2}	0 F	R_{s2}	$\infty \Omega$
C_{top}	0 F	R_{top}	$\infty \Omega$	C_{bot}	0 F	R_{bot}	$\infty \Omega$
R_{a1}	4.64 Ω	R_{a2}	738 m Ω				
L_{a1}	6.98 nH	L_{a2}	8.09 nH				
R_{b1}	5.48 Ω	R_{b2}	780 m Ω				
L_{b1}	9.04 nH	L_{b2}	5.88 nH				
\mathcal{L}_{c1}	3.69 m V	\mathcal{L}_{c2}	3.86 m V	\mathcal{L}_{c3}	4.79 m V	\mathcal{L}_{c4}	3.12 m V
$\beta_{0,1}$	1.00 aH	$\beta_{1,1}$	1.38 nWb	$\beta_{2,1}$	566 pH	$\beta_{3,1}$	1.57 nWb
$\beta_{4,1}$	470 pH	$\beta_{5,1}$	5.49 At				
$\beta_{0,2}$	23.8 pH	$\beta_{1,2}$	276 pWb	$\beta_{2,2}$	298 pH	$\beta_{3,2}$	3.18 nWb
$\beta_{4,2}$	1.44 nH	$\beta_{5,2}$	2.34 At				
$\beta_{0,3}$	32.3 pH	$\beta_{1,3}$	1.18 nWb	$\beta_{2,3}$	565 pH	$\beta_{3,3}$	376 pWb
$\beta_{4,3}$	488 pH	$\beta_{5,3}$	3.15 At				
$\beta_{0,4}$	21.9 pH	$\beta_{1,4}$	246 pWb	$\beta_{2,4}$	233 pH	$\beta_{3,4}$	2.28 nWb
$\beta_{4,4}$	1.77 nH	$\beta_{5,4}$	1.42 At				

Table D.6: Extracted circuit element values and nonlinear reluctance parameters for microtransformer device 3.

N_1	1	N_2	1	\mathcal{R}_{lin}	$1.46 \times 10^9 H^{-1}$		
C_{s1}	9.88 pF	R_{s1}	44.9 Ω	C_{s2}	10.7 pF	R_{s2}	79.1 Ω
C_{top}	122 fF	R_{top}	346 m Ω	C_{bot}	122 fF	R_{bot}	346 m Ω
R_{a1}	6.71 Ω	R_{a2}	9.01 Ω				
L_{a1}	57.8 nH	L_{a2}	54.4 nH				
R_{b1}	5.00 Ω	R_{b2}	23.7 Ω				
L_{b1}	63.6 nH	L_{b2}	34.3 nH				
\mathcal{L}_{c1}	5.79 m \mathcal{U}	\mathcal{L}_{c2}	722 $\mu\mathcal{U}$	\mathcal{L}_{c3}	312 $\mu\mathcal{U}$	\mathcal{L}_{c4}	810 $\mu\mathcal{U}$
$\beta_{0,1}$	840 pH	$\beta_{1,1}$	372 pWb	$\beta_{2,1}$	3.52 nH	$\beta_{3,1}$	1.79 nWb
$\beta_{4,1}$	18.6 nH	$\beta_{5,1}$	75.0 mAt	$\beta_{6,1}$	1.76 nWb	$\beta_{7,1}$	23.2 nH
$\beta_{8,1}$	174 mAt						
$\beta_{0,2}$	86.2 pH	$\beta_{1,2}$	813 pWb	$\beta_{2,2}$	8.13 nH	$\beta_{3,2}$	377 pWb
$\beta_{4,2}$	9.11 nH	$\beta_{5,2}$	83.3 mAt	$\beta_{6,2}$	1.28 nWb	$\beta_{7,2}$	8.24 nH
$\beta_{8,2}$	250 mAt						
$\beta_{0,3}$	107 pH	$\beta_{1,3}$	1.69 nWb	$\beta_{2,3}$	8.08 nH	$\beta_{3,3}$	412 pWb
$\beta_{4,3}$	8.59 nH	$\beta_{5,3}$	297 mAt	$\beta_{6,3}$	1.35 nWb	$\beta_{7,3}$	13.1 nH
$\beta_{8,3}$	232 mAt						
$\beta_{0,4}$	1 aH	$\beta_{1,4}$	1.89 nWb	$\beta_{2,4}$	7.86 nH	$\beta_{3,4}$	519 pWb
$\beta_{4,4}$	8.99 nH	$\beta_{5,4}$	392 mAt	$\beta_{6,4}$	3.27 nWb	$\beta_{7,4}$	20.2 nH
$\beta_{8,4}$	292 mAt						

D.3 Microfluxgate Device Models

Microfluxgate device 1 (see Section 5.5.1) has parameters given in Table D.7, device 2 (see Section 5.5.2) has parameters given in Table D.8. The circuit topology for both is given in Fig. 5.2.

Table D.7: Extracted circuit element values and nonlinear reluctance parameters for microfluxgate device 1.

N_D	50	N_S	50	ℓ_c	1.05 mm		
L_D	6.34 nH	R_D	4.15 Ω	L_S	11.0 nH	R_S	17.2 Ω
$\beta_{0,C}$	1 aH	$\beta_{1,C}$	13.2 pWb	$\beta_{2,C}$	38.9 pH	$\beta_{3,C}$	22.1 pWb
$\beta_{4,C}$	97.6 pH	$\beta_{5,C}$	199 mAt	$\beta_{6,C}$	1.88 pWb	$\beta_{7,C}$	18.7 pH
$\beta_{8,C}$	331 mAt						
$\beta_{0,A}$	1 aH	$\beta_{1,A}$	13.2 pWb	$\beta_{2,A}$	39.5 pH	$\beta_{3,A}$	22.1 pWb
$\beta_{4,A}$	99.1 pH	$\beta_{5,A}$	196 mAt	$\beta_{6,A}$	1.88 pWb	$\beta_{7,A}$	19.0 pH
$\beta_{8,A}$	326 mAt						
$\beta_{0,link}$	1 aH	$\beta_{1,link}$	3.70 pWb	$\beta_{2,link}$	47.1 pH	$\beta_{3,link}$	13.0 pWb
$\beta_{4,link}$	190 pH	$\beta_{5,link}$	11.0 mAt	$\beta_{6,link}$	30.3 pWb	$\beta_{7,link}$	41.2 pH
$\beta_{8,link}$	270 mAt						

Table D.8: Extracted circuit element values and nonlinear reluctance parameters for microfluxgate device 2.

N_D	50	N_S	50	ℓ_c	1.05 mm		
L_D	116 nH	R_D	5.91 Ω	L_S	113 nH	R_S	25.3 Ω
$\beta_{0,C}$	1 aH	$\beta_{1,C}$	12.1 pWb	$\beta_{2,C}$	38.9 pH	$\beta_{3,C}$	7.60 pWb
$\beta_{4,C}$	8.00 pH	$\beta_{5,C}$	680 mAt	$\beta_{6,C}$	18.4 pWb	$\beta_{7,C}$	98.9 pH
$\beta_{8,C}$	328 mAt						
$\beta_{0,A}$	1 aH	$\beta_{1,A}$	12.1 pWb	$\beta_{2,A}$	132 pH	$\beta_{3,A}$	7.60 pWb
$\beta_{4,A}$	27.2 pH	$\beta_{5,A}$	200 mAt	$\beta_{6,A}$	18.4 pWb	$\beta_{7,A}$	336 pH
$\beta_{8,A}$	96.3 mAt						
$\beta_{0,link}$	1 aH	$\beta_{1,link}$	5.76 pWb	$\beta_{2,link}$	33.8 pH	$\beta_{3,link}$	33.9 pWb
$\beta_{4,link}$	152 pH	$\beta_{5,link}$	65.9 mAt	$\beta_{6,link}$	2.27 pWb	$\beta_{7,link}$	62.3 pH
$\beta_{8,link}$	74.7 mAt						

